ORNL/NUREG-9

Test of 6-in.-thick Pressure Vessels Series 3: Intermediate Test Vessel V-7A Under Sustained Loading

R. H. Bryan
T. M. Cate
P. P. Holz
T. A. King
J. G. Merkle
G. C. Robinson
G. C. Smith
J. E. Smith
G. D. Whitman

Prepared for the U.S. Nuclear Regulatory Commission
Office of Nuclear Regulatory Research
Under Interagency Agreements ERDA 40-551-75 and 40-552-75

BLANK PAGE

Printed in the United States of America. Available from
National Technical Information Service
U.S. Department of Commerce
5285 Port Royal Road, Springfield, Virginia 22161
Price: Printed Copy $11.00; Microfiche $3.00
12.50

ORNL/NUREG-9
Dist. Category NRC-5

Contract No. W-7405-eng-26

Engineering Technology Division

TEST OF 6-IN.-THICK PRESSURE VESSELS SERIES 3: INTERMEDIATE TEST VESSEL V-7A UNDER SUSTAINED LOADING

R. H. Bryan
T. M. Cate
P. P. Holz
T. A. King
J. G. Merkle
G. C. Robinson
G. C. Smith
J. E. Smith
G. D. Whitman

Manuscript Completed — February 1, 1978

Date Published: February 1978

Prepared for the
U.S. Nuclear Regulatory Commission
Office of Nuclear Regulatory Research
Under Interagency Agreements ERDA 40-551-75 and 40-552-75

Prepared by the
OAK RIDGE NATIONAL LABORATORY
Oak Ridge, Tennessee 37830
operated by
UNION CARBIDE CORPORATION
for the
DEPARTMENT OF ENERGY

CONTENTS

BLANK PAGE

FOREWORD

The work reported here was performed mostly at Oak Ridge National Laboratory (ORNL) under sponsorship of the U.S. Nuclear Regulatory Commission's (NRC) Heavy-Section Steel Technology (HSST) Program, which is directed by ORNL. The program is conducted as part of the ORNL Pressure Vessel Technology Program, of which G. D. Whitman is manager. The manager for the NRC is E. K. Lynn.

This report is designated Heavy-Section Steel Technology Program Technical Report No. 45. Prior reports in this series are listed below.

1. S. Yukawa, *Evaluation of Periodic Proof Testing and Warm Prestressing Procedures for Nuclear Reactor Vessels*, HSSTP-TR-1, General Electric Company, Schenectady, N.Y. (July 1, 1969).

2. L. W. Loechel, *The Effect of Section Size on the Transition Temperature in Steel*, MCR-69-189, Martin Marietta Corporation, Denver, Colo. (Nov. 20, 1969).

3. P. N. Randall, *Gross Strain Measure of Fracture Toughness of Steels*, HSSTP-TR-3, TRW Systems Group, Redondo Beach, Calif. (Nov. 1, 1969).

4. C. Visser, S. E. Gabrielse, and W. VanBuren, *A Two-Dimensional Elastic-Plastic Analysis of Fracture Test Specimens*, WCAP-7368, Westinghouse Electric Corporation, PWR Systems Division, Pittsburgh, Pa. (October 1969).

5. T. R. Mager, F. O. Thomas, and W. S. Hazelton, *Evaluation by Linear Elastic Fracture Mechanics of Radiation Damage to Pressure Vessel Steels*, WCAP-7328 (ev.), Westinghouse Electric Corporation, PWR Systems Division, Pittsburgh, Pa. (October 1969).

6. W. O. Shabbits, W. H. Pryle, and E. T. Wessel, *Heavy Section Fracture Toughness Properties of A533 Grade B Class 1 Steel Plate and Submerged Arc Weldment*, WCAP-7414, Westinghouse Electric Corporation, PWR Systems Division, Pittsburgh, Pa. (December 1969).

7. F. J. Loss, *Dynamic Tear Test Investigations of the Fracture Toughness of Thick-Section Steel*, NRL-7056, U.S. Naval Research Laboratory, Washington, D.C. (May 14, 1970).

8. P. B. Crosley and E. J. Ripling, *Crack Arrest Fracture Toughness of A533 Grade B Class 1 Pressure Vessel Steel*, HSSTP-TR-8, Materials Research Laboratory, Inc., Glenwood, Ill. (March 1970).

9. T. R. Mager, *Post-Irradiation Testing of 2 T Compact Tension Specimens*, WCAP-7561, Westinghouse Electric Corporation, PWR Systems Division, Pittsburgh, Pa. (August 1970).

10. T. R. Mager, *Fracture Toughness Characterization Study of A 533, Grade B, Class 1 Steel*, WCAP-7578, Westinghouse Electric Corporation, PWR Systems Division, Pittsburgh, Pa. (October 1970).

11. T. R. Mager, *Notch Preparation in Compact Tension Specimens*, WCAP-7579, Westinghouse Electric Corporation, PWR Systems Division, Pittsburgh, Pa. (November 1970).

12. N. Levy and P. V. Marcal, *Three-Dimensional Elastic-Plastic Stress and Strain Analysis for Fracture Mechanics, Phase I: Simple Flawed Specimens*, HSSTP-TR-12, Brown University, Providence, R.I. (December 1970).

13. W. O. Shabbits, *Dynamic Fracture Toughness Properties of Heavy Section A533 Grade B, Class 1 Steel Plate*, WCAP-7623, Westinghouse Electric Corporation, PWR Systems Division, Pittsburgh, Pa. (December 1970).

14. P. N. Randall, *Gross Strain Crack Tolerance of A 533-B Steel*, HSSTP-TR-14, TRW Systems Group, Redondo Beach, Calif. (May 1, 1971).

15. H. T. Corten and R. H. Sailors, *Relationship Between Material Fracture Toughness Using Fracture Mechanics and Transition Temperature Tests*, T&AM Report 346, University of Illinois, Urbana, Ill. (Aug. 1, 1971).

16. T. R. Mager and V. J. McLoughlin, *The Effect of an Environment of High Temperature Primary Grade Nuclear Reactor Water on the Fatigue Crack Growth Characteristics of A533 Grade B Class 1 Plate and Weldment Material*, WCAP-7776, Westinghouse Electric Corporation, PWR Systems Division, Pittsburgh, Pa. (October 1971).

17. N. Levy and P. V. Marcal, *Three-Dimensional Elastic-Plastic Stress and Strain Analysis for Fracture Mechanics, Phase II: Improved Modeling*, HSSTP-TR-17, Brown University, Providence, R.I. (November 1971).

18. S. C. Grigory, *Six-Inch-Thick Flawed Tensile Tests, First Technical Summary Report, Longitudinal Specimens 1 through 7*, HSSTP-TR-18, Southwest Research Institute, San Antonio, Tex. (June 1972).

19. P. N. Randall, *Effects of Strain Gradients on the Gross Strain Crack Tolerance of A 533-B Steel*, HSSTP-TR-19, TRW Systems Group, Redondo Beach, Calif. (May 1, 1972).

20. S. C. Grigory, *Tests of Six-Inch-Thick Flawed Tensile Specimens, Second Technical Summary Report, Transverse Specimens Numbers 8 through 10, Welded Specimens Numbers 11 through 13*, HSSTP-TR-20, Southwest Research Institute, San Antonio, Tex. (June 1972).

21. L. A. James and J. A. Williams, *Heavy Section Steel Technology Program Technical Report No. 21, The Effect of Temperature and Neutron Irradiation Upon the Fatigue-Crack Propagation Behavior of ASTM A533, Grade B, Class 1 Steel*, HEDL-TME-72-132, Hanford Engineering Development Laboratory, Richland, Wash. (September 1972).

22. S. C. Grigory, *Tests of Six-Inch-Thick Flawed Tensile Specimens, Third Technical Summary Report, Longitudinal Specimens Number 14 through 16, Unflawed Specimen Number 17*, HSSTP-TR-22, Southwest Research Institute, San Antonio, Tex. (October 1972).

23. S. C. Grigory, *Tests of Six-Inch-Thick Flawed Tensile Specimens, Fourth Technical Summary Report, Tests of One-Inch-Thick Flawed Tensile Specimens for Size Effect Evaluation*, HSSTP-TR-23, Southwest Research Institute, San Antonio, Tex. (June 1973).

24. S. P. Ying and S. C. Grigory, *Tests of Six-Inch-Thick Tensile Specimens, Fifth Technical Summary Report, Acoustic Emission Monitoring of One-Inch and Six-Inch-Thick Tensile Specimens*, HSSTP-TR-24, Southwest Research Institute, San Antonio, Tex. (November 1972).

25. R. W. Derby et al., *Test of 6-Inch-Thick Pressure Vessels. Series 1: Intermediate Test Vessels V-1 and V-2*, ORNL-4895 (February 1974).

26. W. J. Stelzman and R. G. Berggren, *Radiation Strengthening and Embrittlement in Heavy Section Plates and Welds*, ORNL-4871 (June 1973).

27. P. B. Crosley and E. J. Ripling, *Crack Arrest in an Increasing K-Field*, HSSTP-TR-27, Materials Research Laboratory, Glenwood, Ill. (January 1973).

28. P. V. Marcal, P. M. Stuart, and R. S. Bettes, *Elastic-Plastic Behavior of a Longitudinal Semi-Elliptical Crack in a Thick Pressure Vessel*, Brown University, Providence, R.I. (June 1973).

29. W. J. Stelzman, Characterization of HSST Plates 01, 02, and 03 (in preparation).

30. D. A. Canonico, Characterization of Heavy Section Weldments in Pressure Vessel Steels (in preparation).

31. J. A. Williams, *The Irradiation and Temperature Dependence of Tensile and Fracture Properties of ASTM A533, Grade B, Class 1 Steel Plate and Weldment*, HEDL-TME 73-75, Hanford Engineering Development Laboratory, Richland, Wash. (August 1973).

32. J. M. Steichen and J. A. Williams, *High Strain Rate Tensile Properties of Irradiated ASTM A533 Grade B Class 1 Pressure Vessel Steel*, HEDL-TME 73-74, Hanford Engineering Development Laboratory, Richland, Wash. (July 1973).

33. P. C. Riccardella and J. L. Swedlow, *A Combined Analytical-Experimental Fracture Study*, WCAP-8224, Westinghouse Electric Corporation, PWR Systems Division, Pittsburgh, Pa. (October 1973).

34. R. J. Podlasek and R. J. Eiber, *Final Report on Investigation of Mode III Crack Extension in Reactor Piping*, Battelle Columbus Laboratories, Columbus, Ohio (May 1974).

35. T. R. Mager et al., *Interim Report on the Effect of Low Frequencies on the Fatigue Crack Growth Characteristics of A533 Grade B Class 1 Plate in an Environment of High-Temperature Primary Grade Nuclear Reactor Water*, WCAP-8256, Westinghouse Electric Corporation, Pittsburgh, Pa. (December 1973).

36. J. A. Williams, *The Irradiated Fracture Toughness of ASTM A533, Grade B, Class 1 Steel Measured with a Four Inch Thick Compact Tension Specimen*, HEDL-TME 75-10, Hanford Engineering Development Laboratory, Richland, Wash. (January 1975).

37. R. H. Bryan et al., *Test of 6-in.-thick Pressure Vessels, Series 2: Intermediate Test Vessels V-3, V-4, and V-6*, ORNL-5059 (November 1975).

38. T. R. Mager, S. E. Yanichko, and L. R. Singer, *Fracture Toughness Characterization of HSST Intermediate Pressure Vessel Material*, WCAP-8456, Westinghouse Electric Corporation, Pittsburgh, Pa. (December 1974).

39. J. G. Merkle, G. D. Whitman, and R. H. Bryan, *An Evaluation of the HSST Program Intermediate Pressure Vessel Tests in Terms of Light-Water Reactor Pressure Vessel Safety*, ORNL/TM-5090 (November 1975).

40. J. G. Merkle et al., *Test of 6-in.-thick Pressure Vessels. Series 3: Intermediate Test Vessel V-7*, ORNL/NUREG-1 (August 1976).

41. J. A. Davidson, L. J. Cheschini, R. P. Shogan, and G. V. Rao, *The Irradiated Dynamic Fracture Toughness of ASTM A533, Grade B, Class 1 Steel Plate and Submerged-Arc Weldment*, WCAP-8775, Westinghouse Electric Corp., Pittsburgh, Pa. (October 1976).

42. R. D. Cheverton, *Pressure Vessel Fracture Studies Pertaining to a PWR LOCA-ECC Thermal Shock: Experiments TSE-1 and TSE-2*, ORNL/NUREG/TM-3 (September 1976).

43. J. G. Merkle, G. C. Robinson, P. P. Holz, and J. E. Smith, *Test of 6-Inch-Thick Pressure Vessels. Series 4: Intermediate Test Vessels V-5 and V-9 with Inside Nozzle Corner Cracks*, ORNL/NUREG-7 (August 1977).

44. John A. Williams, The Ductile Fracture Toughness of Heavy Section Steel Plate, Hanford Engineering Development Laboratory, Richland, Wash. (in preparation).

Copies of these reports may be obtained from Laboratory Records Department, Oak Ridge National Laboratory, P.O. Box X, Oak Ridge, Tenn. 37830

ACKNOWLEDGMENTS

The authors wish to thank the many persons who made essential contributions to the preparation and testing of vessel V-7A: D. A. Canonico, C. E. Childress, R. S. Crouse, H. D. Curtis, K. K. Klindt, J. L. Redford, R. Smith, and W. J. Stelzman of Oak Ridge National Laboratory; L. I. Schlemper of the Computer Science Division of Union Carbide Corporation, Nuclear Division; J. F. Bampfield and P. Peckham of White Oak Laboratory; and M. P. Kelly and R. J. Schlamp of Dunegan/Endevco. Individual contributions are noted in the text of the report where practicable.

TEST OF 6-IN.-THICK PRESSURE VESSELS. SERIES 3: INTERMEDIATE TEST VESSEL V-7A UNDER SUSTAINED LOADING

R. H. Bryan T. A. King G. C. Smith
T. M. Cate J. G. Merkle J. E. Smith
P. P. Holz G. C. Robinson G. D. Whitman

ABSTRACT

HSST intermediate test vessel V-7 was repaired after being tested hydrostatically to leakage and was retested pneumatically as vessel V-7A. Except for the method of applying the load, the conditions in both tests were nearly identical. In each case, a sharp outside surface flaw 547 mm long (18 in.) by about 135 mm deep (5.3 in.) was prepared in the 152-mm-thick (6-in.) test cylinder of A533, grade B, class 1 steel. The inside surface of vessel V-7A was sealed in the region of the flaw by a thin metal patch so that pressure could be sustained after rupture. Vessel V-7A failed by rupture of the flaw ligament without burst, as expected. Rupture occurred at 144.3 MPa (20.92 ksi), after which pressure was sustained for 30 min without any indication of instability. The rupture pressure of vessel V-7A was about 2% less than that of vessel V-7. The test demonstrated (1) that the pneumatically sustained loading did not significantly affect the behavior of the flaw, and (2) that the repair of the original V-7 flaw, made by the half-bead welding technique without stress relief, was capable of withstanding pressures up to two times design pressure. The report includes pretest analyses and a complete set of test data.

1. INTRODUCTION

The United States electric power industry adopted nuclear power as an economically competitive source of energy during the 1960–1970 decade. Plans were made and construction was started for boiling-water reactor (BWR) and pressurized-water reactor (PWR) nuclear generating stations in increasing numbers. The international energy crisis has intensified the pressure to utilize these types of nuclear power plants.

With the competitive commercialization of BWRs and PWRs, the predominant capacity ratings of these plants increased to about 1100 MW(e) with an attendant demand for larger, thicker reactor pressure vessels. The

BLANK PAGE

Heavy-Section Steel Technology (HSST) Program was instituted during this period of industrial change to accelerate investigations initiated by the industry of thick-section vessels for water-cooled nuclear reactor service. The program is especially concerned with developing the information necessary for assessing the influence of flaws on the safety and serviceability of the thick-section components of reactor pressure vessels. The program has developed data on the characteristics of plates, welds, and forgings in terms of mechanical properties, toughness, inherent flaws, and homogeneity. A major objective is to develop methods by which better estimates can be made of the effects of flaws on the service life and strength of vessels.

Methods of analysis, as well as experimental methods, are being developed for fracture evaluation of structures. A wide variety of specimen types and sizes have been tested under a wide range of loading conditions. Considerable progress has been made in understanding the behavior of flawed structures and in the application of results of tests of small specimens to the analysis and evaluation of large structures.

The importance of the size of test specimens and structures in the proper characterization of behavior has been demonstrated in many parts of the program. The confidence in methods of analysis so important in safety evaluation of nuclear vessels can be attained only in proportion to the degree to which theoretical methods have been tried by experience or experiment with appropriately sized structures under loading conditions of interest. Consequently, the HSST program includes simulated service tests, of which the intermediate vessel tests are a part.

The aim of simulated service testing is to provide, through a series of experiments, a connection between the behavior of structures observed in a laboratory environment and the behavior of full-size components under the wide variety of conditions that constitute the real operating environment. The main effort of this task is to determine, if not already known, which factors or conditions are important and then to carry out tests with the particular combinations of conditions that will contribute significant information on behavior of structures in service. Factors of concern include material properties; flaw location, orientation, shape, size, and sharpness; and loading and environmental conditions. If expense, resources,

safety, and time were of no importance, the significance of these factors could be studied under actual service conditions imposed on vessels in a large number of experiments with vessels as large as, or larger than, reactor pressure vessels. Since such an approach is completely impractical, each factor is studied separately or in combination with others on as simple a scale as practicable.

The objective of each simulated service test is to determine the ability of analytical methods to predict actual fracture behavior of a flawed structure under known conditions of material properties and loading. In the planned progression of such tests, analytical methods are confirmed, improved, or their limitations revealed. The testing of intermediate vessels in conjunction with tests of flawed tensile specimens of similar material and flawed models of the intermediate vessels permits consideration of many variables. Thus the intermediate vessel tests are a part of a structural test program that covers ranges of flaw size, section thickness, temperature, and stress state. The effects of differences in transverse restraint, toughness, plastic strain, biaxiality, and stress concentration can be observed and analyzed.

The original objectives emphasized in the simulated service task were (1) to demonstrate capability to predict the "vessel transition temperature" for a selected crack configuration using the material of interest (ASTM A533, grade B, class 1 plate; ASTM A508, class 2 forging); and (2) to demonstrate, for the materials of interest, capability to predict various combinations of load (pressure), temperature, and crack configuration in full-thickness walls 152 mm or more (6 in.) that will not cause fracture, and finally, a combination that will cause fracture for both frangible and tough fracture conditions.

The intermediate vessel tests have been subdivided into four series:

1. flaws in cylindrical vessels, A508, class 2 forging steel — two vessels;
2. flaws in cylindrical vessels with longitudinal submerged-arc weld seams, A508, class 2 forging steel — three vessels;
3. flaws in cylindrical vessels with longitudinal submerged-arc weld seams, A533, grade B, class 1 plate steel — two vessels;

4. cylindrical vessels with radially attached nozzles; vessels of A508 class 2 forging steel and A533, grade B, class 1 plate steel; nozzles of A508, class 2 forging steel – three vessels.

Reports have been prepared on tests in all four series. The report[1] on the first series contains a comprehensive description of the pertinent factors considered in the design of the vessels and construction of the test facility and those leading to the tests of series 1, as well as a documentation of test results and fracture predictions. Emphasis is placed on providing the test results in such a manner that they form a resource for any investigators interested in the problem of fracture. The report[2] on series 2 documents comprehensive information on the characteristics of three test vessels, material properties, conditions of testing, and results so as to facilitate further analysis. The reports also describe the use of fracture toughness measurements based on equivalent-energy concepts. These measurements and the investigations of crack growth by tests of both large tensile specimens and model vessels provided the bases for analytical predictions of rupture conditions. The report[3] on series 4 presents similar details on the two vessels with nozzles that have been tested.

Intermediate test vessel V-7 has been tested three times in series 3. This vessel has the same cylindrical geometry as the five vessels of the first two series. However, vessel V-7 contained a flaw that was much larger and deeper than those of any other vessel tested. The first test was preceded by tests of steel scale models of V-7 and by analyses, which all together indicated that the mode of failure would be the rupture of the thin ligament along the base of the flaw. Vessel V-7 failed as predicted, the first test being necessarily terminated by the leakage of the pressurizing fluid. The vessel as a structure and the flaw itself remained stable throughout the test. Results of the first test were reported (Ref. 4) while the vessel was being prepared for the second test with the designation V-7A. The latter test is the subject of this report.

The pneumatic test of vessel V-7A was initially conceived and planned as a replication of the hydrostatic test of vessel V-7. It was thought that this test would serve two purposes: (1) to demonstrate the effects of sustained pressure loading on the behavior of a large cracklike flaw

in a thick pressure vessel and (2) to try out certain means of performing later crack propagation and arrest tests in this or other intermediate-size vessels. Vessel V-7A was tested essentially as planned. Loading was sustained prior to rupture through the use of nitrogen as the pressurizing fluid and after rupture by a thin metal membrane welded to the inside surface of the vessel in the area of the flaw. The crack behaved as predicted, with the rupture pressure differing from that in the V-7 test by 2%.

References

1. R. W. Derby et al., *Test of 6-in.-Thick Pressure Vessels. Series 1: Intermediate Test Vessels V-1 and V-2*, ORNL-4895 (February 1974).

2. R. H. Bryan et al., *Test of 6-in.-Thick Pressure Vessels. Series 2: Intermediate Test Vessels V-3, V-4, and V-6*, ORNL-5059 (November 1975).

3. J. G. Merkle et al., *Test of 6-in.-Thick Pressure Vessels. Series 4: Intermediate Test Vessels V-5 and V-9 with Inside Nozzle Corner Cracks*, ORNL/NUREG-7 (August 1977).

4. J. G. Merkle et al., *Test of 6-in.-Thick Pressure Vessels. Series 3: Intermediate Test Vessel V-7*, ORNL/NUREG-1 (August 1976).

2. PRETEST PLANNING AND ANALYSIS

2.1 Background

The test of vessel V-7A was designed primarily to study the prerupture and postrupture stability of a large deep surface flaw in the wall of a thick pressure vessel. Eight HSST intermediate vessel tests had been carried out before preparations for this test commenced. The information derived from those eight previous tests confirmed that one could predict the conditions for initiation of unstable crack extension on the basis of well-characterized flaw geometry, material properties, and loading. At the same time there was an interest[1] in extending the scope of the HSST program to include an investigation of vessel failure modes under conditions of sustained loads in order to more accurately model the behavior of reactor primary coolant systems. Furthermore, some questions were raised about the applicability of the results of the intermediate vessel tests to reactor pressure vessels, since rapid depressurization upon rupture was characteristic of the tests. These concerns led to studies of the influence of the pressurizing medium on crack behavior. Two types of experimental investigations of flawed vessels ensued: (1) demonstration of the effect of sustained loading on the initiation of unstable crack extension (in V-7A) and (2) study of crack propagation and arrest in thick vessels under sustained load (in progress).

2.2 Fluid Mechanics Effects

2.2.1 Pressure-time behavior during loss of fluid

Pressurized- and boiling-water-reactor (PWR and BWR) primary coolant systems contain sufficient energy to maintain pressure of the system essentially constant for a long time after a small rupture occurs. The pressure-time behavior of intermediate test vessels under hydraulic loading is quite different, in that pressure drops rapidly even for small breaks.

The pressure-time behavior of a vessel with a rupture of a given size is dependent on the effective compliance of the entire pressurized system,

with account taken of the compliance of the pressure boundary itself and the volumes and compressibilities of all contained fluids. The compliance of the pressure boundary is a minor factor for the cases of interest. The pressure-time behavior of a homogeneous system is governed for adiabatic-reversible processes by the equation[2]

$$\frac{dp}{dt} = \frac{c_p}{c_v \kappa m} \frac{dm}{dt} , \tag{1}$$

where p is pressure, t is time, κ is compressibility, c_p and c_v are specific heat at constant pressure and constant volume, respectively, and m is the mass contained in volume V. The mass flow rate, dm/dt, through a crack in the vessel is given, for cases of interest, by the critical flow relationship

$$\frac{dm}{dt} = \frac{AC_0}{v_0} , \tag{2}$$

where A is the area of the throat of the opening at which local sonic velocity, C_0, is attained in the fluid with local specific volume, v_0. Values of C_0 and v_0 are entirely dependent upon the thermodynamic properties and initial state of the fluid. The flow process was assumed to be isentropic.

From these relationships, pressure decay curves were constructed for a reference design PWR under various conditions, as shown in Figs. 2.1 and 2.2. These curves agreed well with results calculated by the RELAP-4 computer code,[3,4] as Fig. 2.1 shows. In the long term, PWR pressure would change by about 1/2% for a leak the size of the V-7 rupture.

Pressure decay in an intermediate test vessel was calculated for both water and nitrogen for vessel V-7 test conditions. High-pressure properties of water and nitrogen were taken from Refs. 5 to 7. As shown in Fig. 2.3, pressure decreases linearly with time for a short time interval, since the mass, mass flow rate, and thermodynamic parameters in Eq. (1) change very little.

These analyses show that pressure in a ruptured pneumatically loaded intermediate test vessel would decrease more rapidly than it would in a

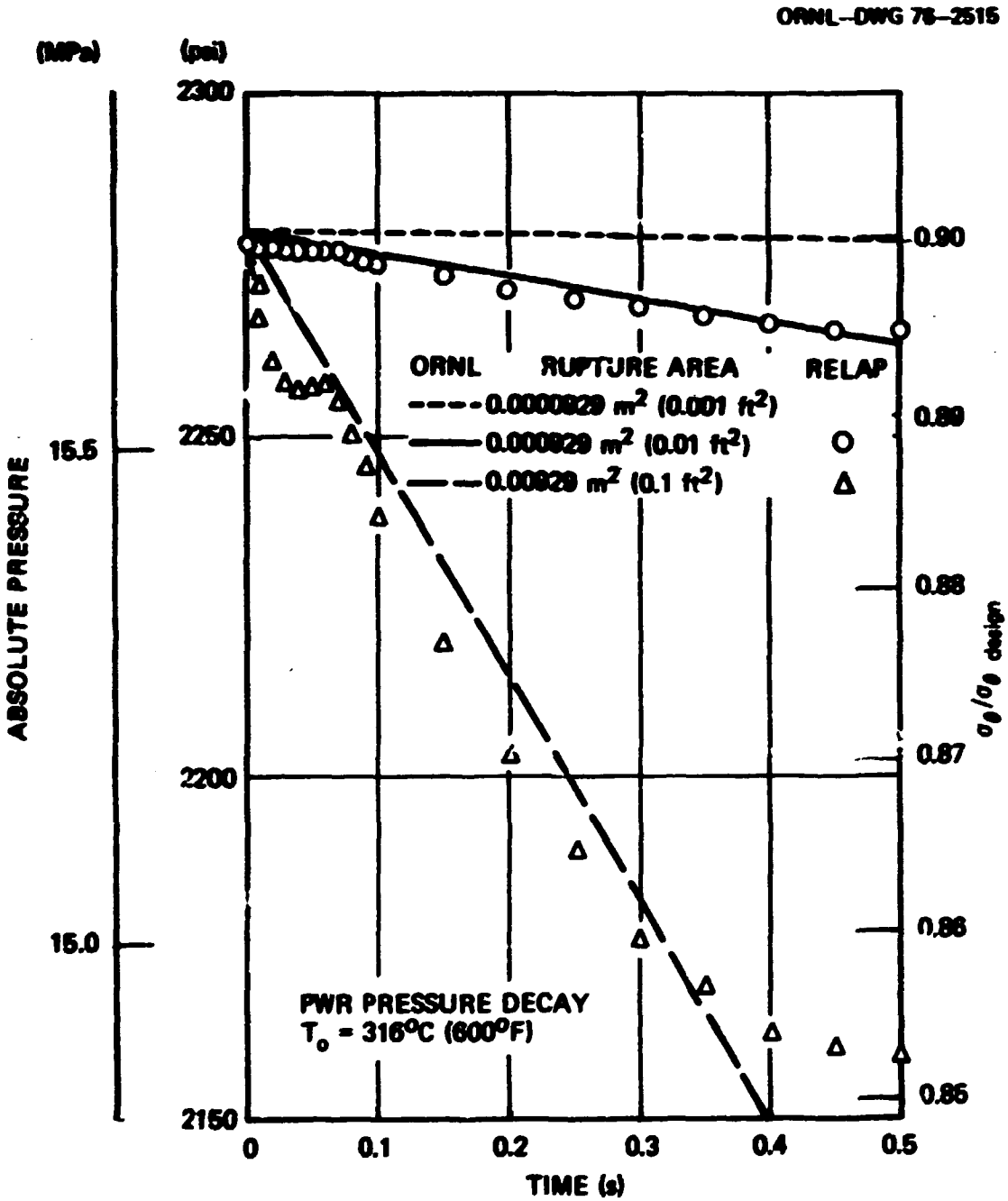

Fig. 2.1. Pressure and circumferential stress vs time for a PWR initially under normal operating conditions.

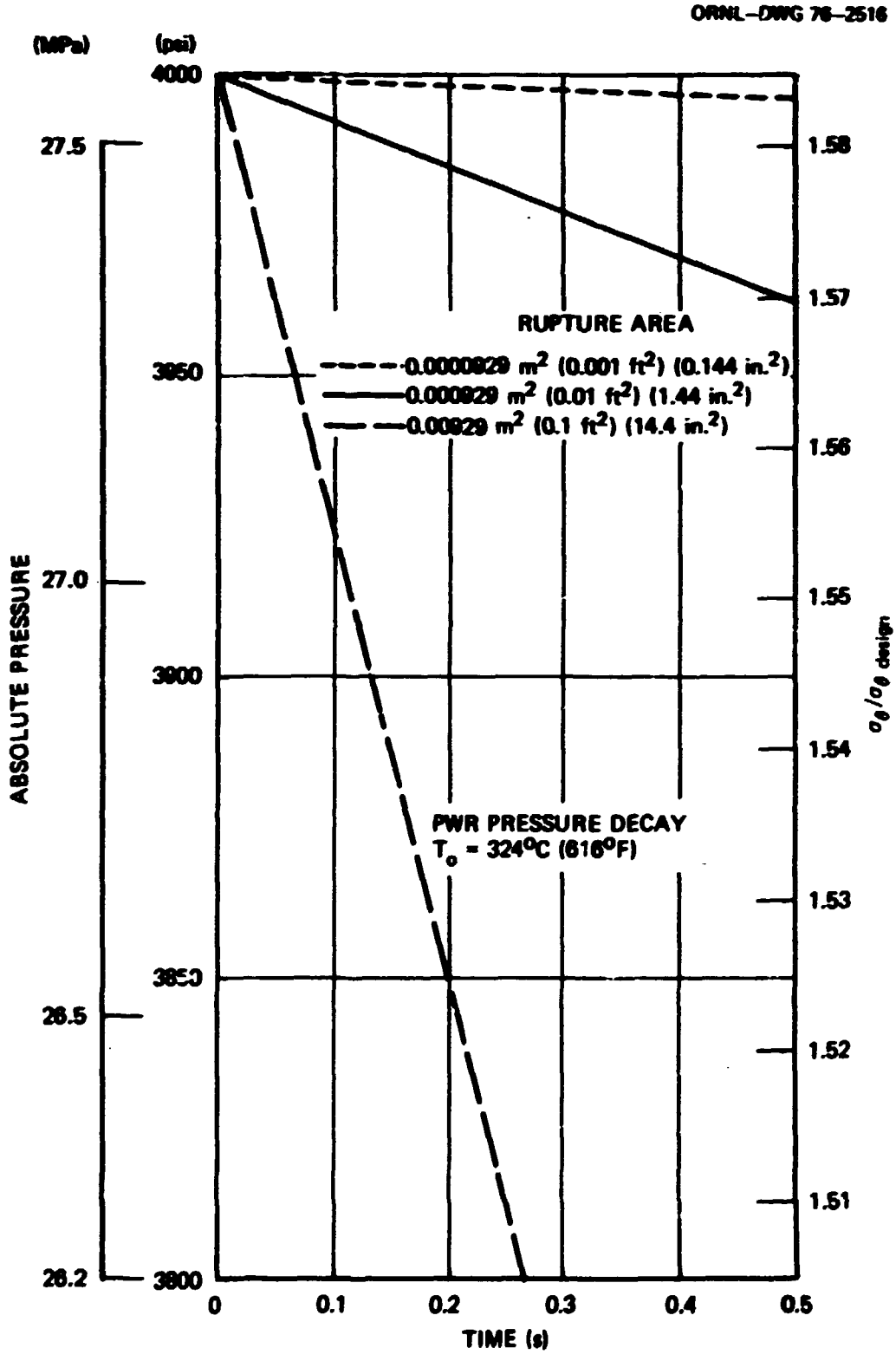

Fig. 2.2. Pressure and circumferential stress vs time for a PWR initially under abnormal operating conditions.

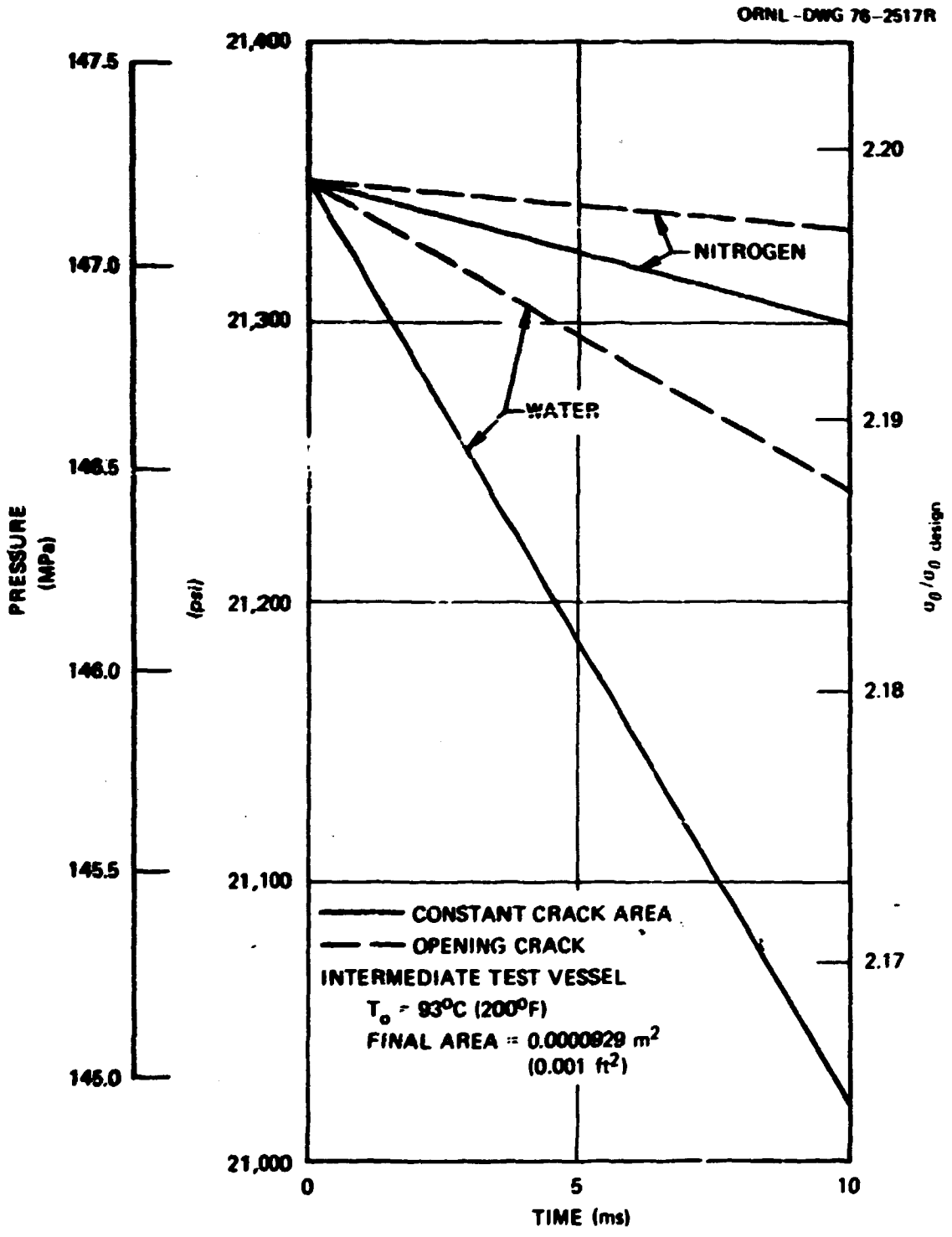

Fig. 2.3. Pressure and circumferential stress vs time for an intermediate test vessel at 93°C (200°F).

PWR vessel with the same size opening. Although the load dropoff in the test vessel would not seriously impair some fast crack propagation tests, which may last only a few microseconds, slowly developing changes would be affected. Consequently, a leak-retarding patch was installed in vessel V-7A so that long-term post-ligament-rupture behavior could be observed.

2.2.2 Load changes prior to rupture

Several quasi-static and dynamic processes affect the capability of a test system to sustain the load on a cracked vessel prior to rupture. They are summarized in Table 2.1. The changes in the state of the pressurizing fluid result in changes in the pressure load and are caused either by deformations of the vessel of by perturbations of the testing system. With the possible exception of highly localized and rapid deformation of the membrane near the flaw (a special case of change A, cause 2 in Table 2.1), all the changes take place slowly enough for the resultant pressure change to be uniformly distributed over the inside surface of the vessel. Accordingly, they have been evaluated as quasi-static changes in pressure. A conservative model of rapid deformation near the crack has been used to estimate the upper limits on the potential dynamic effect on crack-zone stresses.

Table 2.1. Fluid mechanics processes affecting crack-zone stresses prior to rupture

Change in fluid state	Causes
A. Change in volume of fluid inside vessel	1. General elastic or plastic dilation of shell
	2. Local plastic deformation of membrane as crack opens or grows
B. Change in fluid mass inside vessel	3. Compliance, leakage, and cooling of pressurizing system
C. Change in temperature of fluid	4. Change in vessel temperature
	5. Change in rate of heat input to the vessel and fluid masses

The testing procedure calls for increasing the pressure as rapidly as the pumping system allows. The pressurization rate was about 350 kPa/min (50 psi/min) for the pneumatic system used for vessel V-7A and about 5000 kPa/min (700 psi/min) in the hydraulic intermediate vessel tests. The vessel dilates with increasing pressure; and after yielding, there is a continued slow dilation for some time after pumping stops. In the tests at 55°C (130°F) and above (vessels V-1, -3, -5, -6, and -7), substantial stable crack growth was observed as pressure increased. Pressure increments and crack growth are attended by changes in crack-opening displacement (COD) and small movements of the inside surface of the vessel. If this surface, which is in contact with the pressurizing fluid, moves slowly during a crack jump, the pressure will change uniformly throughout the vessel. In this case, the effect on load and crack-zone stresses can be estimated from the change in fluid volume.

Volume changes. The expansion of vessel V-7 and the distortion of the inside surface near the flaw were estimated from strain data from the first test and posttest measurements of the flaw zone. The parameters used in this analysis are given in Table 2.2. The relationships governing pressure changes for isothermal and adiabatic-reversible conditions are, respectively,[2]

$$(dp)_T = -\frac{dV}{\kappa V} , \tag{3}$$

and

$$(dp)_s = -\frac{c_p}{\kappa c_v}\frac{dV}{V} . \tag{4}$$

The changes in volume are sufficiently small that variation of the thermodynamic variables and V with pressure can be neglected. Furthermore, it is conservative to assume that entropy, s, is constant, since its actual increase would diminish the pressure drop by $\beta T/\kappa c_v\, ds$, where T is temperature and β is the coefficient of thermal expansion of the fluid.

The isothermal equation [Eq. (3)] is less conservative, because it does not include the factor c_p/c_v, which is always greater than 1.

Table 2.2. Calculated pressure changes in vessels V-7 and V-7A due to ligament necking, crack region bulging, and uniform vessel strain

Internal volume of vessel, m^3 (ft^3)	0.696 (24.6)
Initial pressure, MPa (psi)	138 (20,000)
Initial temperature, °C (°R)	87.8 (190)
Necked ligament	
Length, mm (in.)	125 (4.92)
Average width, mm (in.)	25 (0.98)
Maximum depth, mm (in.)	13 (0.51)
Displaced volume, m^3 (ft^3)	2.03×10^{-5} (7.17×10^{-4})
Δp, kPa (psi)	
H_2O (V-7)	−106 (15.3)
N_2 (V-7A)	−15.3 (2.2)
Bulging	
Length, 2L, mm (in.)	330 (13)
Width, 2W, mm (in.)	540 (21)
Maximum depth, mm (in.)	4.0 (0.16)
Displaced volume, m^3 (ft^3)	1.2×10^{-4} (4.2×10^{-3})
Δp, kPa (psi)	
H_2O (V-7)	−620 (−90)
N_2 (V-7A)	−90 (−13)
Uniform dilation	
Nominal final circumferential strain, %	0.13
Nominal final axial strain, %	0.03
Displaced volume, m^3 (ft^3)	1.43×10^{-3} (5.05×10^{-2})
Δp, MPa (psi)	
H_2O (V-7)	−7.46 (−1082)
N_2 (V-7A)	−1.08 (−156)

Furthermore, isothermal conditions could not be maintained during the rapid change in pressure that we wish to evaluate.

Volume changes resulting from ligament necking, bulging, and uniform dilation of vessel V-7 were estimated separately. These changes took place generally throughout the last part of the test according to the actual strain, COD, and ultrasonic measurements.[8] Figures 4.11, 4.12, and 4.15 of Ref. 7 indicate that most of the deformation took place at high pressure, generally above 124 MPa (18,000 psi). It is plausible that necking

and bulging, in some instances, advanced in rapid jumps of such small magnitude that the discontinuous nature of the events could not be detected. In order to evaluate the possible contribution such events might have made to pressure decay during the test, we calculated the pressure drops that would have resulted if all the deformations had occurred in one rapid jump. The results are given in Table 2.2 for V-7 (the H_2O cases) together with predictions for V-7A (the N_2 cases).

Necking parameters were estimated by visual inspection of the deformed inside surface of V-7 after the initial test. (See Fig. 4.19 of Ref. 8.) Uniform dilation was based upon average strains in the cylindrical part of the vessel, as shown in Table 2.2.

The volume change resulting from bulging was estimated from the COD and ligament strains measured at maximum pressure in the V-7 test. (See Figs. 4.12 and 4.14 of Ref. 8.) The angular rotation, α, of the crack face was estimated from these data. Bulging of the inside surface was assumed to be confined to an area of axial length, 2L, and circumferential width, 2W, with the flaw at the center. The bulging displacement, w, was assumed to vary with circumferential distance, x, and axial distance, y, from the center of the flaw as

$$w = \frac{\alpha}{2LW} (L - |y|) (W - |x|)^2 . \qquad (5)$$

The calculated pressure drops given in Table 2.2 are far too small to account for the pressure-time behavior of vessel V-7 during pauses in pumping. In that test, pressure drops of 2000 to 3000 kPa (300 to 400 psi) were typical for pauses at pressures above 70 MPa (10 ksi). The COD and strain changes during these pauses were small in comparison with the total changes — about 10% of the total in the worst case. We concluded that the quasi-static changes in internal volume affected pressure during pauses only to a minor degree in the hydraulic test and that pressure drops induced by such changes contributed negligibly to changes in the crack-zone stress field.

Test system changes. The test system used for the hydraulic intermediate vessel tests is capable of raising the vessel pressure rapidly, by about 4000 kPa/min (600 psi/min) at low pressure and 6000 kPa/min

(900 psi/min) at high pressure. When pumps are stopped, there are two factors that may contribute to a gradual and continued decline in pressure. First, leakage past pump seals and check valves would cause a continued slow decline in pressure. Second, stopping the pressurizing pumps is an occurrence which produces a discontinuity in the rate at which the fluid in the vessel is heated. During constant pumping, a steady-state fluid temperature tends to be established through a balance of the energy input from compressive work and heat loss from the fluid to the vessel and its environs. The decrease in energy input upon cessation of pumping causes the fluid temperature to decline toward a new steady state dependent entirely upon the vessel heating system. In this case, pressure would decline approximately in proportion to absolute temperature and also approach a steady value. The pressure in the nitrogen system is quite sensitive, at 138 MPa (20,000 psi), to a change in temperature, since

$$\left(\frac{\partial p}{\partial T}\right)_v \approx 500 \text{ kPa/K } (\sim 40 \text{ psi/°R}) \ .$$

The variation of pressure with time was not measured with enough precision in the V-7 test to determine whether the pressure declined linearly with time or tended to approach a steady value. In the V-7A test, pressure did tend to level off after a few minutes with total pressure drops equivalent to a 1 to 2.5 K (1.8 to 4.5°F) drop in average temperature of the gas.

Rapid change in pressure. When a crack pops in or runs unstably, there is an attendant local movement of the inside surface of the vessel. The recession of the pressure boundary, illustrated in Fig. 2.4, will generate a local decompression wave affecting the load on the boundary and, as a consequence, the stress field near the flaw. The decrease in pressure on the receding boundary is immediate, while the effect at a distance is delayed. In both locations, the magnitude of the change is determined by the speed of the receding boundary and the thermodynamic properties of the pressurizing medium.

ORNL DWG 78-52

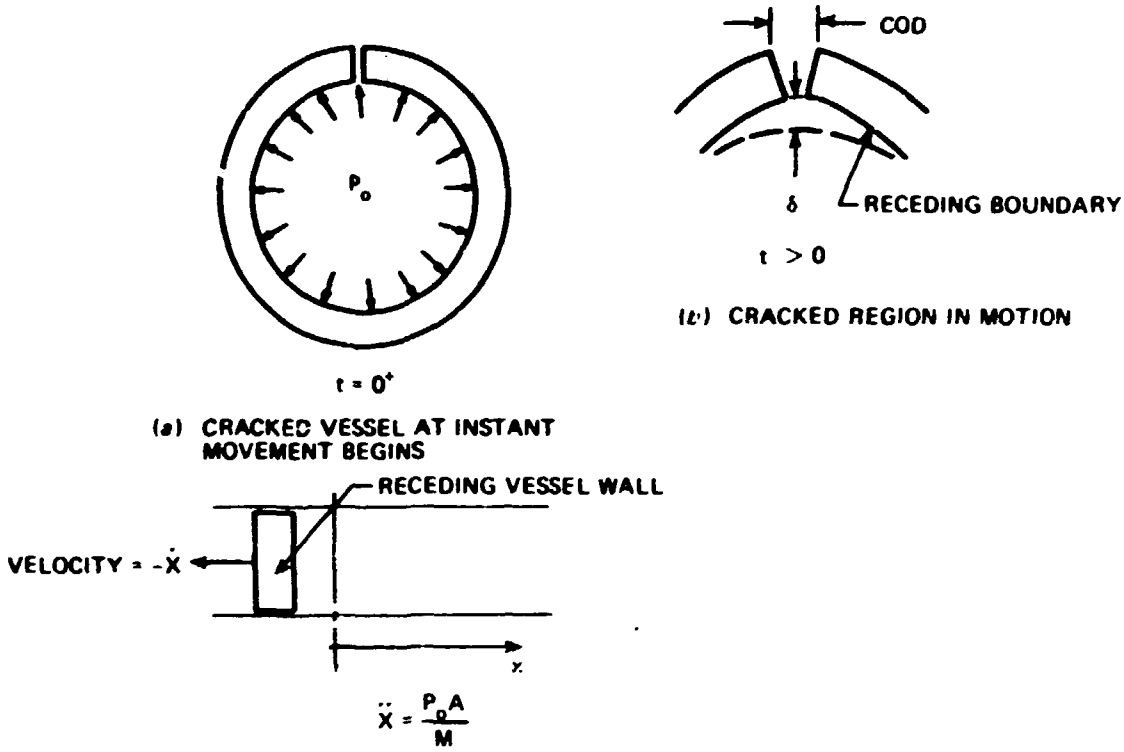

Fig. 2.4. Receding boundary problem.

In order to estimate the dynamic effect of a local displacement of the boundary, a one-dimensional idealization of the problem has been analyzed. In this idealization the following assumptions were made:

1. The receding boundary (Fig. 2.4b) is a plane moving as a piston away from the initially static fluid.

2. The vessel wall accelerates continuously without restraint under the influence of a constant (initial) pressure.

The geometry of the simplified problem is defined in Fig. 2.4c; given the motion of the boundary prescribed by assumption 2, the task is to find the change in pressure on the boundary itself and at distant points representative of the wall of the pressure vessel remote from the crack. The

calculated changes in pressure will be extreme overestimates, since assumption 2 completely ignores the strength of the vessel.

Behavior of the fluid next to a receding boundary is described[9] by the nonlinear partial differential equations,

$$\left[\frac{\partial}{\partial t} + (\bar{u} \pm \bar{c}) \frac{\partial}{\partial x}\right] (\bar{u} \pm F) = 0 , \tag{6a}$$

where $\bar{u}$ and $\bar{c}$ are fluid particle and sound velocities, respectively, and F is the thermodynamic variable,

$$F = \int_{p_o}^{p} \frac{dp'}{\rho \bar{c}} . \tag{6b}$$

Thus, F is a function of p and p_o. The fluid dynamic process was assumed to be isentropic; the thermodynamic state and F at any point is then completely defined by the initial state and one variable, such as p in Eq. (6b). Alternatively, F may also be defined in terms of $\bar{c}$.

The boundary conditions for the problem are

(1) $\bar{u} = \dot{X}$ on the moving boundary; and

(2) at $t = 0$: $\bar{u} = 0$, $\bar{c} = \bar{c}_o$, and $p = p_o$ everywhere. (6c)

The solution to the problem obtained by the method of characteristics is that on each characteristic, C_i^+ (a line in the $x - t$ plane in Fig. 2.5), defined by

$$\frac{dx}{dt} = \bar{u}_i + \bar{c}_i = \text{constant} , \tag{7}$$

originating at point X_i, the variable F is a constant given by

$$F_i = \dot{X}_i . \tag{8}$$

Thus, the C^+ characteristics are straight lines, illustrated in Fig. 2.5, along which F, p, and $\bar{c}$ are constant (but generally different from one characteristic to another).

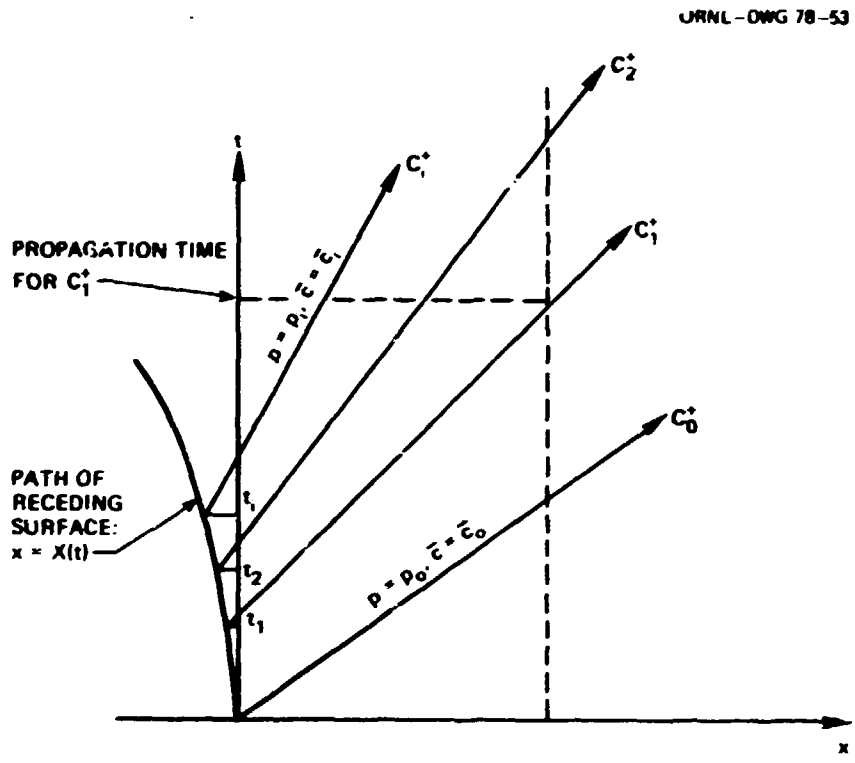

Fig. 2.5. Solution to receding boundary problem.

Calculations were made with nitrogen data from Stewart et al.[7] Results shown in Table 2.3 give the time and decompression on the moving boundary and on the characteristics for boundary displacements up to the maximum bulge analyzed statically, that is, 4.0 mm (0.16 in.). Initial conditions are as shown in Table 2.2. Table 2.3 also gives the time required for a pressure change of a given magnitude to propagate a distance representative of the average distance from the crack to the remote wall of the cylinder.

The results indicate that the local decompression is substantial (about 10%) for a displacement of 4 mm under the stated assumptions. However, it is important to note that it requires substantially longer for the disturbance to start to unload the major portion of the structure than the running time of a fast pop-in. In view of these results, it was concluded that it is unlikely that pop-ins would be arrested as a result of the dynamic interaction of the vessel boundary, the fluid, and the structure.

Table 2.3. Results of calculations of the effects of a moving boundary[a]

Boundary displacement (mm)	Dispiacement time (msec)	Pressure change (MPa)	Travel time to x = 4r/π (msec)
First signal			0.46
1	0.145	−7.6	0.48
2	0.205	−10.8	0.49
3	0.251	−13.2	0.50
4	0.290	−15.2	0.50

[a]Conversion factors: 1 MPa = 145.04 psi; 1 mm = 0.0394 in.

2.3 Reevaluation of Burst Calculations

2.3.1 Interpretation of previous test results

The result of the test of vessel V-7 was clearly a leak without a burst.[8] This test result was implied by pretest calculations indicating that, at the ligament separation pressure, the ends of the crack would not extend axially because of the increase in fracture toughness caused by the through-thickness contraction of the vessel cylinder.[8] However, this is not the only cause to which the test result could be attributed. It could also be postulated, but not proven, that had the vessel been loaded pneumatically rather than hydraulically, a fracture instability rather than a leak would have resulted because of the greater compliance of a pneumatic system. While we did not subscribe to the latter hypothesis, it became necessary to conduct a pneumatic experiment (vessel V-7A) in order to remove any doubt about the reasons for the original (vessel V-7) test result.

The leak-without-burst implication of the pretest calculations for vessel V-7 mentioned above was primarily the result of assuming that the fracture toughness resisting the axial extension of the through crack that existed after ligament separation would be elevated above its plane

strain value because of through-thickness contraction. This was demonstrated by an identical calculation, based on the assumption of plane strain conditions, which indicated that the plane strain toughness itself was insufficient to resist the axial extension of the crack at the ligament separation pressure. Thus, the effect of decreasing transverse restraint along the through-thickness portions of the crack front appeared to be the most important physical factor governing the postleak behavior of the flaws in vessels V-7 and V-7A.

A rational hypothesis concerning transverse restraint effects had been developing gradually during the testing of the intermediate vessels. The development of this hypothesis was particularly aided by the test results obtained from vessels V-5 and V-7 and by a successful partial transverse restraint analysis of the first seven surface-flawed intermediate tensile specimens tested earlier.[10] Simply stated, the hypothesis is that the strain tangent to the crack front, in the plane of the crack, is the primary agent of transverse restraint and that this strain can be inferred from the nominal strain that would occur in the uncracked structure, in the same direction, at the location of the crack. The development of this hypothesis is described in Appendix E of Ref. 10, and the partial transverse restraint analysis of the intermediate tensile specimens is given in Appendix H of Ref. 10. The application of the same hypothesis to the inside nozzle corner cracks in vessels V-5 and V-9 is described in Ref. 11. According to this hypothesis, an axially oriented surface crack in the cylindrical region of a pressure vessel should always be subjected to full transverse restraint, because the axial strain in the cylindrical part of the vessel is always nearly zero, even after yielding occurs. However, neither an inside nozzle corner crack nor a through-thickness crack in the cylindrical part of a vessel should be subject to plane strain conditions, because substantial contraction strains occur in the directions tangent to both crack fronts. The results obtained from all the intermediate vessels tested to date tend to support this hypothesis.

Although a rational explanation for the leak-without-burst performance of vessel V-7 had been developed in terms of transverse restraint effects, little if any experimental data from pneumatic tests were available to support the hypothesis. This is because the few pneumatic tests

of flawed vessels that had been done before the test of vessel V-7, including three model tests of vessel V-7 done at Oak Ridge National Laboratory (ORNL), had resulted in burst failures rather than leak failures.[8] This situation could have been resolved if there had been one generally accepted method of analysis for explaining why the prior tests had produced burst failures while vessel V-7 had produced a leak failure. However, instead of one method, there were several semiempirical methods available for analyzing the burst pressure of thin cylinders containing long axial through-wall flaws, and the one that was the most appropriate for the case at hand had not been established. Thus, it became necessary to select the most appropriate method for estimating burst pressures and, as a prerequisite to the pneumatic testing of vessel V-7A, to show why it and vessel V-7 should produce leak failures whereas the previous tests had produced burst failures.

2.3.2 Preliminary examination of burst formulas

Equations based on the strip yield model. Three formulas for calculating the burst pressures of thin cylindrical shells containing long axial cracks were examined in some detail. The first two formulas are intended to be applied to through-thickness cracks, and both are generalizations of the strip yield equation to account for the effects of cylindrical geometry. The third formula is applicable to deep part-through surface cracks and assumes that the fracture toughness is sufficiently high so that failure is caused by the onset of plastic instability in the region surrounding the flaw.

The strip yield equation, as originally derived, is applicable to a through-thickness crack in a wide plate under uniform tensile loading. The equation is[12]

$$\delta = \frac{8\sigma_Y c}{\pi E} \ln \sec\left(\frac{\pi\sigma}{2\sigma_Y}\right), \tag{9}$$

where δ is the COD at the real crack tips, c is the half-crack length, σ_Y is the yield stress, and σ is the remotely applied tensile stress.

Equation (9) can be rewritten in the form

$$\delta = \frac{4\sigma_Y c}{\pi E} \ln\left[1 + \tan\left(\frac{\pi\sigma}{2\sigma_Y}\right)\right], \tag{10}$$

which, for small values of σ/σ_Y, reduces to

$$\delta = \frac{\sigma^2 \pi c}{E\sigma_Y} . \tag{11}$$

Using

$$K_I^2 = E\sigma_Y\delta , \tag{12}$$

Eq. (11) then gives

$$K_I = \sigma\sqrt{\pi c} , \tag{13}$$

which agrees with the linear elastic fracture mechanics (LEFM) formula for a through crack in a wide plate. The corresponding expression for a longitudinal through crack in a cylinder[13] is

$$K_I = M\sigma\sqrt{\pi c} , \tag{14}$$

where the bulging factor M accounts for the increase in K_I due to the lateral deflections of the crack region caused by internal pressure.

Since Eq. (13) is a special case of Eq. (9) for through cracks in flat plates, it has been assumed that Eq. (14) is a special case of an equation having the same form as Eq. (9) but containing the bulging factor M so as to be applicable to longitudinal through cracks in pressurized cylinders. This assumption seems rational as a semiempirical approach, but it leaves unanswered the question of where to locate the bulging factor M in the general expression for δ. Consequently, two formulas have been proposed. In the first, by Wells[14] and Cowan and Kirby,[15] the factor M is applied to the flaw size, c, giving

$$\delta = \frac{8\sigma_Y M^2 c}{\pi E} \ln \sec\left(\frac{\pi\sigma}{2\sigma_Y}\right) . \tag{15}$$

In the second, by Hahn, Sarrate, and Rosenfield,[16] the factor M is applied to the stress, σ, giving

$$\delta = \frac{8\sigma_Y c}{\pi E} \ln \sec\left(\frac{\pi M \sigma}{2\sigma_Y}\right). \tag{16}$$

Although Refs. 15 and 16 do not agree on the subject of where to locate the bulging factor M in the equation for δ, Ref. 15 does acknowledge (in fact, by referring to Ref. 16) that the stress at which plastic instability commences, which is the stress at which the value of δ becomes infinitely large, corresponds more closely to

$$\sigma = \frac{\sigma_Y}{M}, \tag{17}$$

as predicted by Eq. (16), rather than to

$$\sigma = \sigma_v, \tag{18}$$

as predicted unconservatively by Eq. (15). Thus, since Eqs. (15) and (16) agree closely for small values of σ/σ_Y, but Eq. (16) provides the better estimate of the stress at which plastic instability commences, Eq. (16) appears to be the better choice of an equation for analyzing the burst pressures of cylinders containing axial through-wall cracks. A derivation will be given later to further support this choice.

The Battelle Memorial Institute (BMI) plastic instability formula for a part-through crack. Reference 17 gives a formula for estimating the pressure at which plastic instability will develop in the ligament beneath an external part-through surface flaw in a pressurized pipe, assuming that a toughness-controlled fracture does not occur first. Although the equation appears to produce reasonable estimates of ligament plastic instability pressures, no derivation was given in Ref. 17 or elsewhere, so the one discussed below was developed.

Referring to Fig. 2.6, it is assumed that (1) the ligament, shown shaded in Fig. 2.6. will fail by plastic instability at an average stress

ORNL DWG 78 54

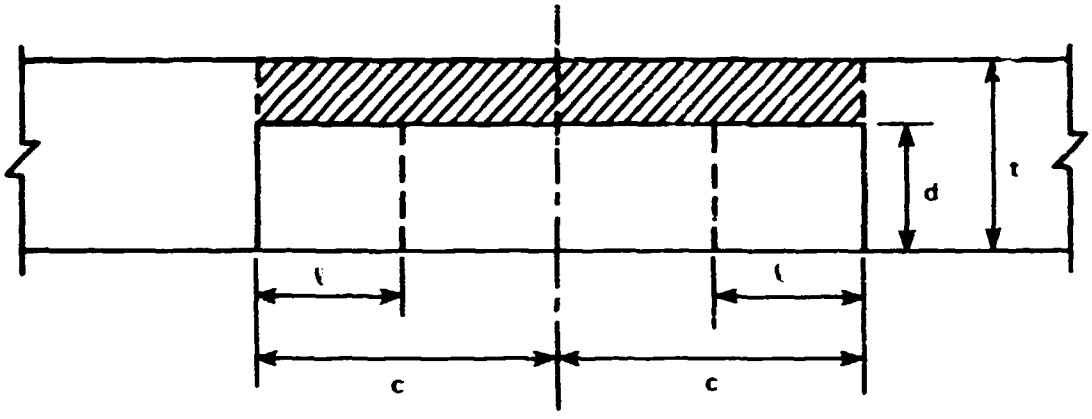

Fig. 2.6. Upper-shelf ligament plastic instability model for a part-through surface crack in a pressurized cylinder.

equal to the flow stress, σ_f; and (2) the load that would have been transmitted across the crack area, in the absence of the crack, within a distance ℓ from each end of the crack, is redistributed laterally beyond the ends of the crack and is not transferred to the ligament. Thus, at ligament separation,

$$\sigma_{PTC}A - \sigma_{PTC}\frac{\ell}{c}A_c = \sigma_f\,(A - A_c)\ , \tag{19}$$

where σ_{PTC} is the average unflawed hoop stress at ligament separation,

$$A = 2ct\ , \tag{20}$$

and

$$A_c = 2cd\ . \tag{21}$$

Assuming that

$$\frac{\ell}{c} = \frac{\sigma_{TC}}{\sigma_f}\ , \tag{22}$$

where σ_{TC} is the burst stress for a through crack of length 2c, substituting Eq. (22) into Eq. (19) and rearranging gives

$$\frac{\sigma_{PTC}}{\sigma_f} = \frac{A - A_c}{A - A_c\,(\sigma_{TC}/\sigma_f)} \quad . \tag{23}$$

Based on test data,[17] σ_Y in Eq. (17) is replaced by σ_f to give

$$\frac{\sigma_{TC}}{\sigma_f} = \frac{1}{M} \quad , \tag{24}$$

where M is the bulging factor for a through crack of length 2c. Then, substituting Eqs. (20), (21), and (24) into Eq. (23) gives[17]

$$\frac{\sigma_{PTC}}{\sigma_f} = \frac{1 - (d/t)}{1 - (d/t)(1/M)} \quad . \tag{25}$$

For an infinitely long crack, $M = \infty$ and

$$\frac{\sigma_{PTC}}{\sigma_f} = 1 - (d/t) \quad , \tag{26}$$

which provides a lower bound to the stress for ligament failure by plastic instability. Also, for a leak to occur,

$$\frac{\sigma_{PTC}}{\sigma_f} \leq \frac{1}{M} \quad , \tag{27}$$

so that, combining Eqs. (25) and (27),

$$\frac{\sigma_{PTC}}{\sigma_f} \leq \frac{1 - (d/t)}{1 - (d/t)(\sigma_{PTC}/\sigma_f)} \quad . \tag{28}$$

Rearranging Eq. (28) gives

$$\frac{d}{t} \geq \frac{1}{1 + (\sigma_{PTC}/\sigma_f)} \quad . \tag{29}$$

Figure 2.7 shows plots of Eq. (25) for four different values of 1/M (1.0, 0.9, 0.5, and 0) and the curve defined by Eq. (29), shown dashed, which separates leak conditions from burst conditions. Also plotted in Fig. 2.7 are two points representing the failure conditions for intermediate test vessels V-6 and V-7, as listed in Table 2.4. The failure modes of both vessels agree with the figure. Note that Fig. 2.7 implies that all cracks with depths less than half the vessel wall thickness will produce burst failures under overload, neglecting the effects of stable crack growth.

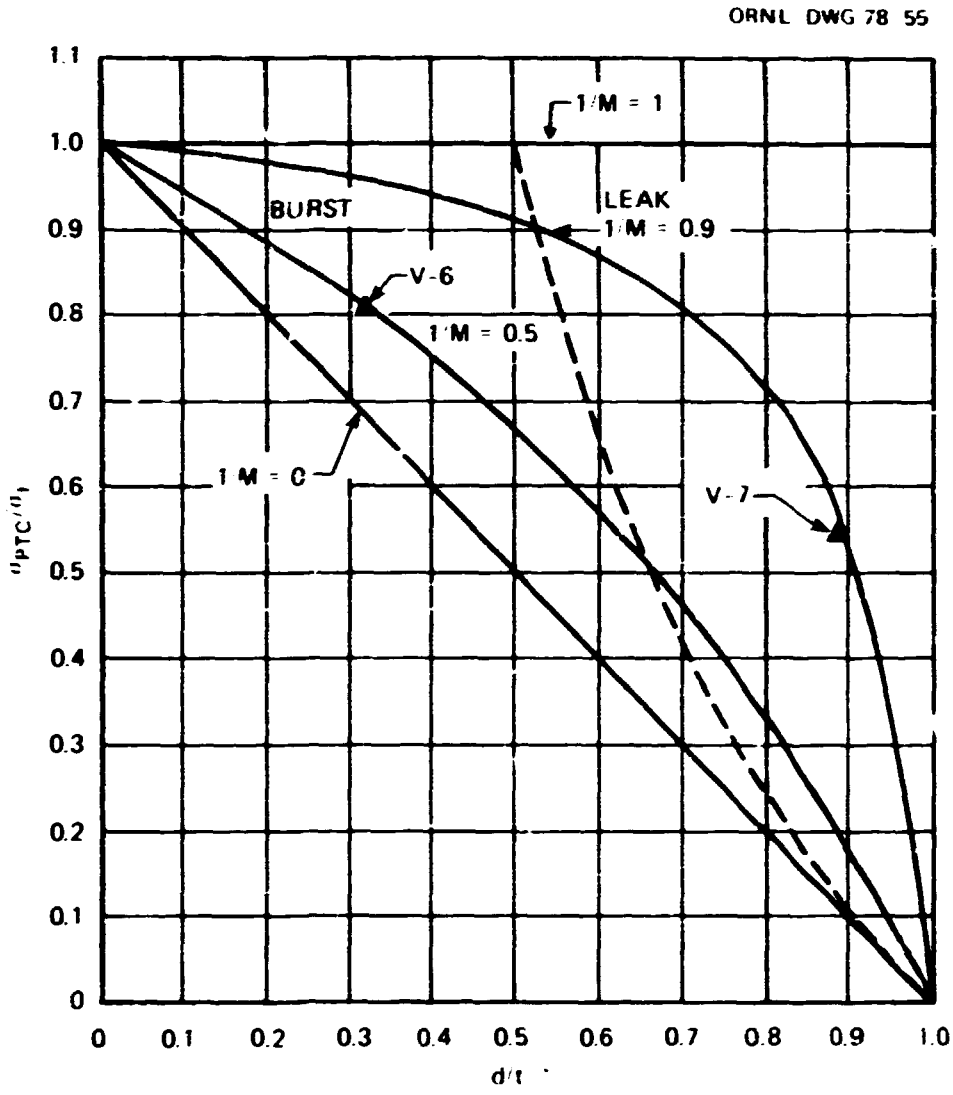

Fig. 2.7. Diagram of failure conditions as predicted by the BMI upper-shelf ligament plastic instability model for part-through surface cracks in pressurized cylinders.

Table 2.4. Upper-shelf failure conditions for intermediate test vessels V-6 and V-7, based on σ_f = 609 MPa (88.3 ksi)

Vessel	Test temperature [°C (°F)]	d/t ratio	Failure conditions			
			Pressure [MPa (ksi)]	$\sigma_{PTC} = 2.25\ p$ [MPa (ksi)]	σ_{PTC}/σ_f	Mode of failure
V-6	88 (190)	0.313	220 (31.9)	495 (71.8)	0.813	Burst
V-7	91 (196)	0.883	148 (21.4)	332 (48.2)	0.545	Leak

Trial calculations (analysis performed by G. T. Hahn, Battelle Memorial Institute, Columbus, Ohio). For purposes of illustration and comparison, sample calculations were made by the BMI modification to the strip yield equation, Eq. (16), for both an intermediate test vessel and a typical reactor pressure vessel, with various assumed through-wall crack sizes and fracture toughnesses. Using Eq. (12) and replacing the yield stress, σ_Y, with the flow stress, σ_f, Eq. (16) gives, after rearranging,

$$\sigma_{TC} = \frac{2\sigma_f \cos^{-1}\left\{\exp\left[-\frac{\pi}{8}\left(\frac{K_c}{\sigma_f}\right)^2\right]\right\}}{M\pi} . \tag{30}$$

The bulging factor M was estimated from[16]

$$M = \sqrt{1 + 1.61\ [(c/t)^2]\ (t/R)} , \tag{31}$$

in which the value of R was taken as the inside radius of the vessel cylinder, although it is usually taken as the mean radius. The flow stress, σ_f, was taken as 586 MPa (85 ksi). In these calculations, Eq. (30) was simplified to

$$\sigma_{TC} = \frac{\sigma_f}{M} \tag{32}$$

whenever

$$\left(\frac{K_c}{\sigma_f}\right)^2 \frac{1}{c} \geq 7 \ . \tag{33}$$

The calculations are listed in Table 2.5. Assuming a leak to occur in the reactor pressure vessel at a pressure of 2.2 times the code design pressure as it did in intermediate test vessel V-7, the margin to burst appears to be considerably less in the case of an intermediate test vessel with a crack half-length of 200 mm (8 in.) than in a reactor pressure vessel. This is because the bulging factor M increases with decreasing R for a given value of (c/t), but the comparison is somewhat exaggerated by using the inside radius rather than the mean radius for computing M. Also, the lowest apparent margins to burst are the result of choosing toughness values not much above the plane strain value of 460 $MN \cdot m^{-3/2}$ (419 $ksi\sqrt{in.}$) and assuming large effective crack half-lengths. Nevertheless, all the calculations summarized in Table 2.5 predict a leak rather than a burst, because the through-crack failure pressure, p_f, always exceeds the assumed ligament separation pressure, $2.2p_d$.

Discussion. From the preceding information, it was clear that establishing the reliability of an estimate of the margin of pressure between leak and burst for the pneumatic test of vessel V-7A depended on the following factors: (1) the fracture toughness resisting the axial extension of a longitudinal through crack, especially as it is increased above the plane strain value by through-thickness contraction; (2) the rationality of the BMI-modified strip yield equation, Eq. (16), for predicting the burst pressure of a cylindrical shell containing a longitudinal through-thickness crack; and (3) the effective length of a trapezoidal through crack. Therefore, additional studies concerning each of these factors were performed, as discussed below, following which final calculations were made to estimate the pressure margin between leak and burst for vessel V-7A.

2.3.3 Comparisons between COD and K_c measures of toughness

In the pretest calculations for vessel V-7, it was estimated that the effective fracture toughness resisting the axial extension of a through

Table 2.5. Trial burst pressure calculations for an intermediate test vessel and a typical reactor pressure vessel considering long through-wall flaws based on σ_f = 586 MPa (85 ksi)

C [mm (in.)]	K_c [$MN \cdot m^{-3/2}$ (ksi$\sqrt{in.}$)]	$\left(\frac{K_c}{\sigma_f}\right)^2 \cdot \frac{1}{c}$	M	σ_{TC} [MPa (ksi)]	p_f [MPa (ksi)]	$\frac{p_f}{2.2p_d}$
	Sample calculations for HSST IVT; R = 343 mm (13.5 in.), t = 152 mm (6.0 in.), p_d = 67 MPa (9.71 ksi)					
152 (6)	≥769 (≥700)	11.3	1.31	448 (65)	200 (29)	1.36
178 (7)	≥769 (≥700)	9.7	1.40	421 (61)	186 (27)	1.26
203 (8)	≥769 (≥700)	8.5	1.51	386 (56)	172 (25)	1.17
203 (8)	659 (600)	6.2	1.51	365 (53)	165 (24)	1.12
203 (8)	549 (500)	4.3	1.51	345 (50)	152 (22)	1.03
229 (9)	≥769 (≥700)	7.5	1.62	359 (52)	159 (23)	1.07
	Sample calculations for full-scale vessel; R = 2.16 m (85 in.), t = 21.6 cm (8.5 in.), p_d = 17.2 MPa (2.5 ksi)					
178 (7)	≥769 (≥700)	9.7	1.05	558 (81)	56 (8.1)	1.47
203 (8)	≥769 (≥700)	8.5	1.07	545 (79)	54 (7.9)	1.44
229 (9)	≥769 (≥700)	7.5	1.09	538 (78)	54 (7.8)	1.42

crack could be as high as 2863 $MN \cdot m^{-3/2}$ (2610 $ksi\sqrt{in.}$) because of through-thickness contraction.[8] This toughness value corresponds to a K_c/K_{Ic} ratio of 6.23. At first glance, this may look like an excessively high value of toughness, but it does have some experimental justification. Although direct experimental measurements of fracture toughness values this high, in terms of J_c of K_c, have not been made, some strong inferences can be obtained from measurements of large COD values in the fully plastic range. Two dynamic tear (DT) specimens of A533, grade B, class 1 steel were tested to incomplete separation by the U.S. Naval Research Laboratory.[18] One was the 162-mm-thick (6 3/8-in.) DT specimen shown in Figs. 2.8 and 2.9, which was tested at 77°C (170°F) and developed a COD of ~13 mm (1/2 in.). The other was the 254-mm (10-in.) net section thickness DT specimen shown in Fig. 2.10, which was tested at 102°C (215°F) and developed a COD of ~38 mm (1.5 in.). In addition, intermediate tensile specimen 14, a 152-mm-thick (6-in.) surface-cracked tensile specimen tested at 93°C (200°F) by the Southwest Research Institute,[19] developed a COD of 30.5 mm (1.2 in.) at failure. The load vs COD curve for specimen 14 is shown in Fig. 2.11. Converting the latter COD value to an equivalent K_c value, by means of Eq. (12), but replacing σ_Y with σ'_{ult}, to allow for strain hardening, gives

$$K_c = \sqrt{E\,\sigma'_{ult}\,\delta} = 2066\ MN \cdot m^{-3/2}\ (1880\ ksi\sqrt{in.})\ ,$$

where $E = 20.7 \times 10^4$ MPa (3×10^4 ksi) and $\sigma'_{ult} = 676$ MPa (98.1 ksi). Furthermore, as mentioned previously, partial restraint elastic-plastic fracture strength calculations have been made for the first seven intermediate tensile specimens by means of the tangent modulus method, and these calculations also give evidence of upper-shelf toughness values of approximately the same magnitude.[10] Thus, K_c values approaching 2200 $MN \cdot m^{-3/2}$ (2000 $ksi\sqrt{in.}$) appear to be physically possible, under conditions of less than full transverse restraint, on the upper shelf. Consequently, there is good reason to believe that the through-crack burst pressure of vessel V-7A should be close to the pressure required for crack-induced plastic instability.

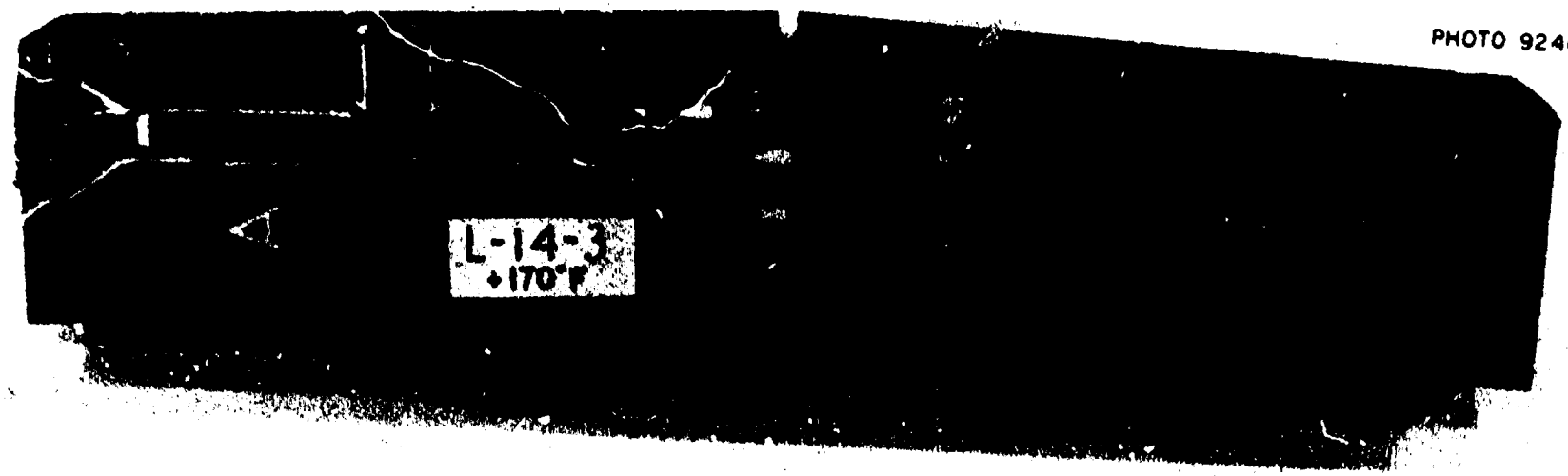

Fig. 2.8. View of 162-mm-thick (6 3/8-in.) dynamic tear specimen of A533, grade B, class 1 steel tested to incomplete separation by the U.S. Naval Research Laboratory at 77°C (170°F).

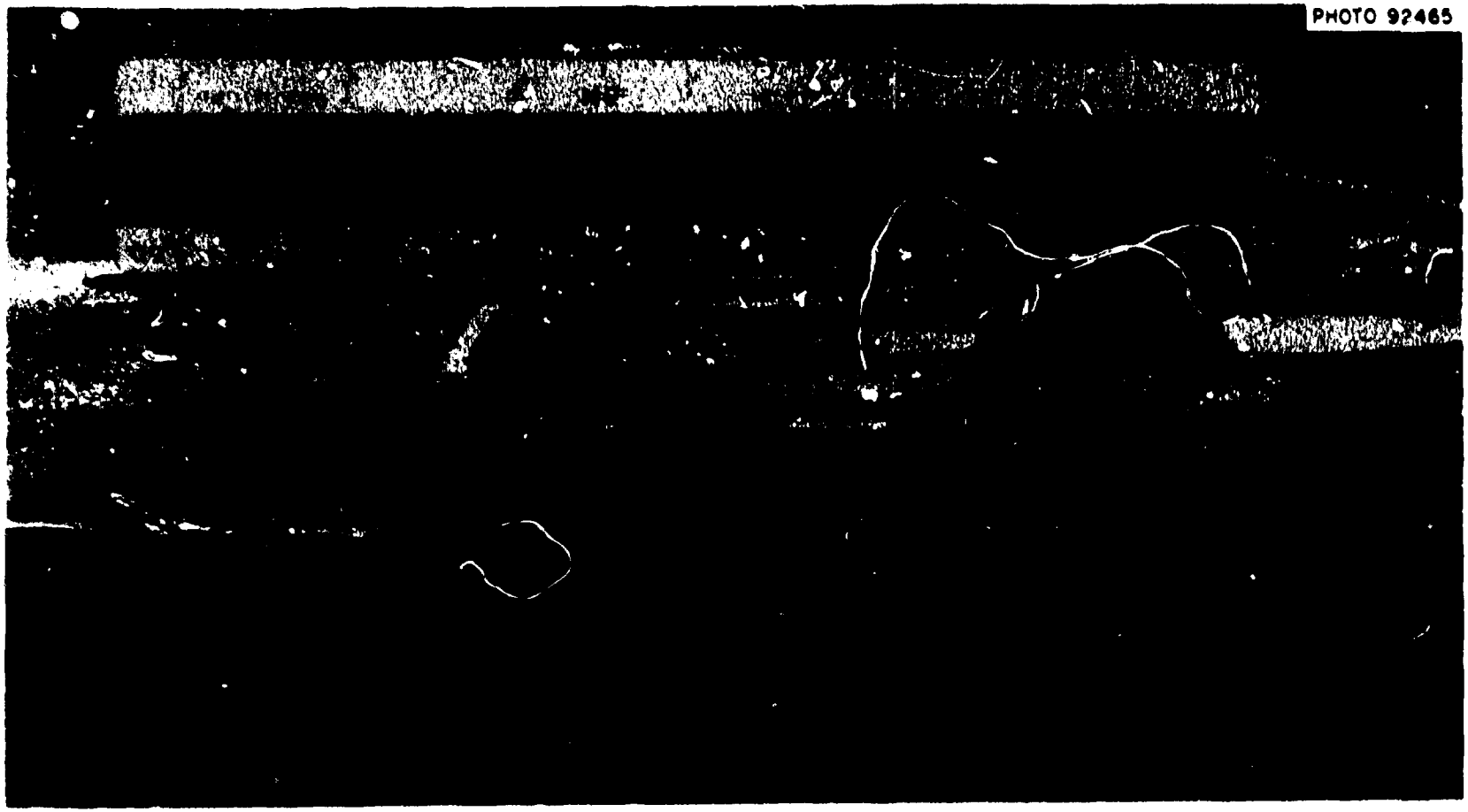

Fig. 2.9. Close-up view of crack region in 162-mm-thick (6 3/8-in.) dynamic tear specimen tested to incomplete separation at 77°C (170°F); a general view of the same specimen is shown in Fig. 2.8.

PHOTO 7365-77

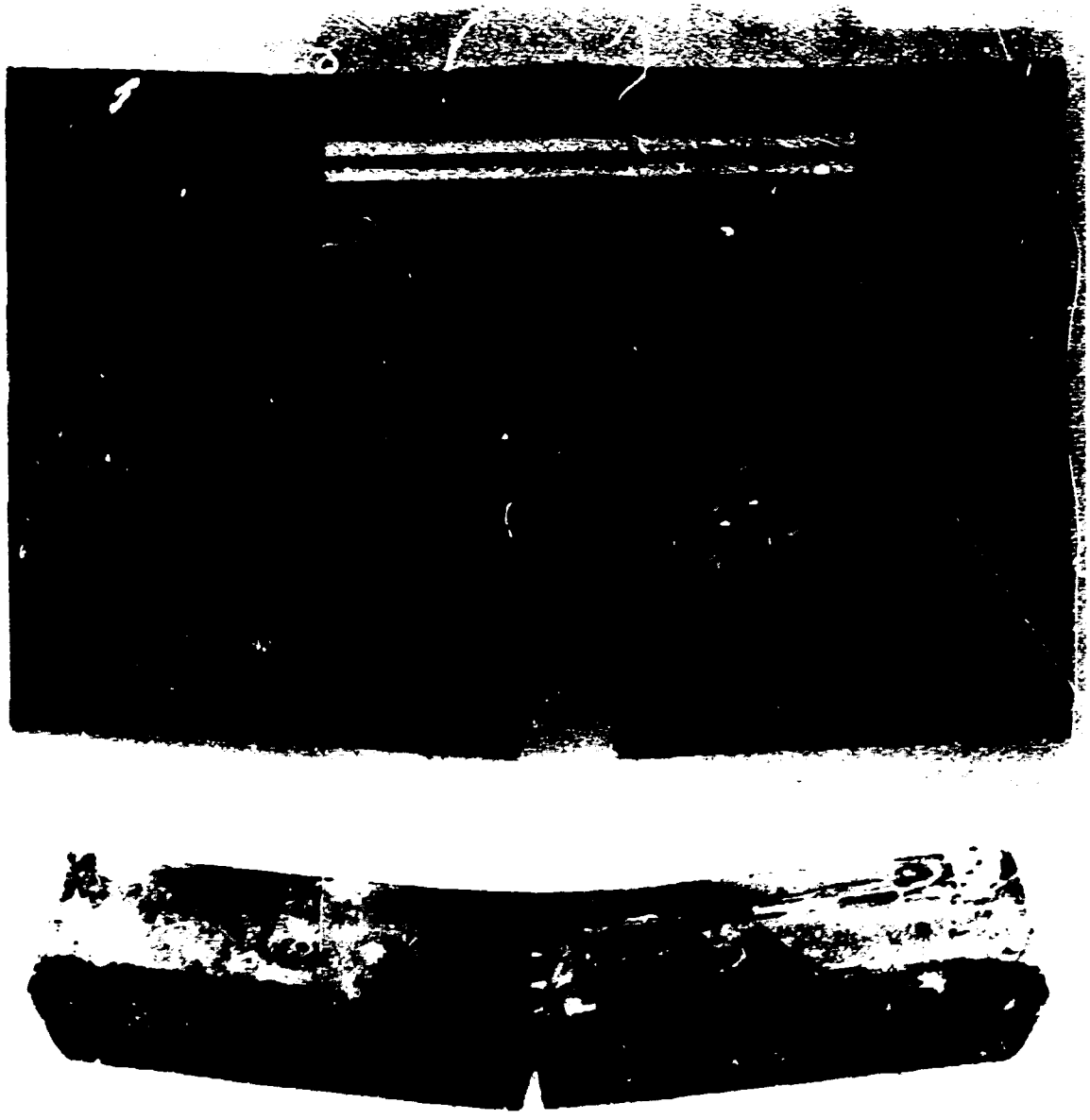

Fig. 2.10. View of 254-mm (10-in.) net section thickness dynamic tear specimen of A533, grade B, class 1 steel tested to incomplete separation by the U.S. Naval Research Laboratory at 102°C (215°F).

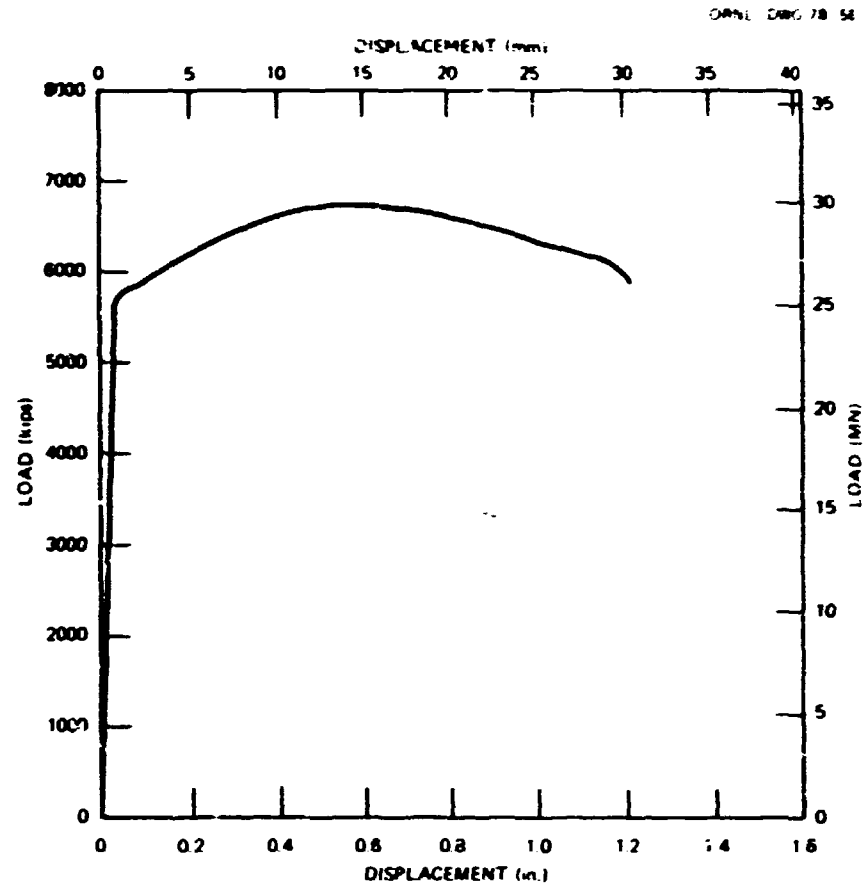

Fig. 2.11. Load vs crack-opening displacement (crack mouth clip gage) for 152-mm-thick (6-in.) surface-flawed intermediate tensile specimen 14 of A533, grade B, class 1 steel tested at 93°C (200°F) by the Southwest Research Institute.

2.3.4 Examination of the BMI modified strip yield equation

Plastic-zone-size expression. A first step in the examination of the BMI modified strip yield equation, Eq. (16), is the derivation of a plastic-zone-size expression based on elastic analysis. This derivation can be accomplished by means of the Irwin equation[20,21] for a through crack subjected to a symmetrically varying remote tensile stress. The stress-intensity factor for such a crack is given by[21]

$$K_I = D\sqrt{w}\int_0^{\pi/2} \sigma \, d\beta \, , \tag{34}$$

where

$$D = \frac{2\sqrt{2}}{\pi} M \left(\tan \frac{\pi c}{2w}\right)^{1/2} , \tag{35}$$

and

$$\beta = \cos^{-1}\left[\frac{\sin (\pi\lambda/2w)}{\sin (\pi c/2w)}\right]. \tag{36}$$

In Eqs. (34) through (36), c is the crack half-length, w is specimen half-width measured in the direction parallel to the crack plane, λ is the distance from the crack centerline to a point on the crack line, and M is an elastic bulging factor which has a value of 1.0 for a through crack in a flat plate. (Note that in Ref. 20 the distances λ and $c - \lambda$ were inadvertently reversed.) When w is large compared to c, Eqs. (34) and (35) can be combined and reduced to

$$K_I = \frac{M\sqrt{\pi c}}{\pi/2} \int_0^{\pi/2} \sigma \, d\beta , \tag{37}$$

where

$$\beta = \cos^{-1} (\lambda/c) . \tag{38}$$

Note that w has been eliminated from Eq. (37) and that $\beta = 0$ corresponds to the crack tip. Following the usual procedure for the strip yield model,[12,22] a plastic zone of length ρ is added to the crack length, c, so that the yield stress closure tractions acting across the plastic zone cause the elastically calculated value of K_I at the tip of the plastic zone to be zero. Thus, infinite stresses at the fictitious crack tip are eliminated. Therefore, for σ = const.,

$$K_I = 0 = \frac{M\sigma\sqrt{\pi(c + \rho)}}{\pi/2} \int_0^{\pi/2} d\beta - \frac{\sigma_Y\sqrt{\pi(c + \rho)}}{\pi/2} \int_0^{\cos^{-1}[c/(c+\rho)]} d\beta . \tag{39}$$

Note that in Eq. (39) the factor M is not applied to the crack surface tractions in the plastic zone because no additional geometry effects are associated with these stresses. From Eq. (39),

$$M\sigma = \frac{\sigma_Y}{\pi/2} \cos^{-1}\left(\frac{c}{c+\rho}\right) \tag{40}$$

or

$$\frac{c}{c+\rho} = \cos\left(\frac{M\sigma}{\sigma_Y} \cdot \frac{\pi}{2}\right). \tag{41}$$

Note that the bulging factor M appears with the stress σ. Furthermore, Eq. (41) implies that $\rho = \infty$, which is a crack-induced plastic instability condition, occurs when $M\sigma = \sigma_Y$ in agreement with Eq. (17). This means that crack-induced plastic instability can occur before general yielding for $M > 1$.

Derivation of the expressions for the crack tip and centerline crack-opening displacements. Because the derivation of the plastic-zone-size equation, Eq. (41), for the strip yield model involves setting the stress-intensity factor at the fictitious crack tip equal to zero, it might appear that the calculated COD should also remain zero. This might be the case if the crack tip remained fixed and the yield stress traction zone progressed back toward the crack centerline with each load increment. However, that is not the physical model being used here. The essential feature of the strip yield model, as shown in Fig. 2.12, is that the tangent modulus associated with the yield stress tractions is zero. This includes the tractions acting within the plastic zone already formed and those acting within the incremental distance $d\rho$, shown in Fig. 2.12, which is added to the plastic zone with the application of the stress increment $d\sigma$. Therefore, the incremental CODs caused by the stress increment $d\sigma$ should be as calculated by an elastic analysis. On this basis, the pattern of incremental CODs due to a stress increment $d\sigma$ should be elliptical,[23] so that

$$\left(\frac{d\delta}{d\delta_0}\right)^2 + \left(\frac{\lambda}{c+\rho}\right)^2 = 1 , \tag{42}$$

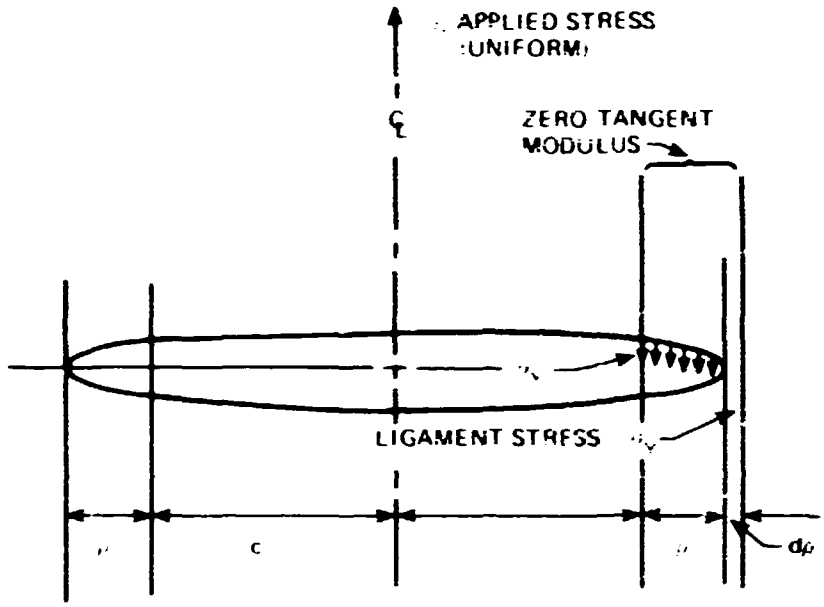

Fig. 2.12. Diagram of the strip yield model.

where $d\delta_0$ is the incremental COD at the crack centerline and $d\delta$ is the incremental COD occurring at a distance λ from the crack centerline. At the real crack tip, $\lambda = c$. Therefore, by substituting c for λ in Eq. (42) and then using Eq. (41),

$$d\delta = d\delta_0 \sin \beta_1 \ , \tag{43}$$

where

$$\beta_1 = \frac{\pi M\sigma}{2\sigma_Y} \ . \tag{44}$$

Furthermore, based on the Green and Sneddon analysis,[23]

$$d\delta_0 = \frac{4M(c + \rho)d\sigma}{E} \ . \tag{45}$$

Therefore, using Eqs. (41) and (44), Eq. (45) becomes

$$d\delta_0 = \frac{4Mc\ d\sigma}{E} \ \frac{1}{\cos \beta_1} \ . \tag{46}$$

Thus, combining Eqs. (43) and (46) gives

$$d\delta = \frac{4Mc}{E} \tan \beta_1 \, d\sigma \ . \tag{47}$$

From Eq. (44),

$$d\sigma = \frac{2\sigma_Y}{M\pi} \, d\beta_1 \ , \tag{48}$$

so that substituting Eq. (48) into Eq. (47) gives

$$d\delta = \frac{8\sigma_Y c}{\pi E} \tan \beta_1 \, d\beta_1 \ . \tag{49}$$

Note that the bulging factor M has been eliminated by cancellation from the first factor in Eq. (49) and therefore appears only in the term β_1. Integrating Eq. (49) and then using Eq. (44) thus gives

$$\delta = \frac{8\sigma_Y c}{\pi E} \ln \sec \left(\frac{\pi M \sigma}{2\sigma_Y} \right) , \tag{16}$$

which is the BMI modified strip yield equation for the COD at the real crack tip.[16]

The equation for the COD at the crack centerline can also be derived in the same manner. From Eq. (46),

$$d\delta_0 = \frac{4Mc}{E} \sec \beta_1 \, d\sigma \ . \tag{50}$$

Substituting Eq. (48) into Eq. (50) gives

$$d\delta_0 = \frac{8\sigma_Y c}{\pi E} \sec \beta_1 \, d\beta_1 \ . \tag{51}$$

Then, integrating Eq. (51) and using Eq. (44) gives

$$\delta_0 = \frac{8\sigma_Y c}{\pi E} \ln \tan \left(\frac{\beta_1}{2} + \frac{\pi}{4} \right) . \tag{52}$$

Since

$$\tan\left(\frac{\beta_1}{2} + \frac{\pi}{4}\right) = \left(\frac{1 + \sin \beta_1}{1 - \sin \beta_1}\right)^{1/2} , \tag{53}$$

it follows, by the use of identities, that Eq. (52) can be rewritten in the form

$$\delta_0 = \frac{8\sigma_Y c}{\pi E} \tanh^{-1}\left[\sin\left(\frac{\pi M\sigma}{2\sigma_Y}\right)\right], \tag{54}$$

which agrees with the expression given by Goodier and Field[12] for M = 1.

The foregoing derivations imply that the proper place for the elastic bulging factor M to appear in a modification of the strip yield equation is with the stress rather than the crack size. Consequently, approaches to elastic-plastic fracture analysis that are based on applying the bulging factor to the crack size rather than to the stress should be reexamined, especially with regard to the occurrence of crack-induced plastic instability prior to general yielding, for M > 1. An example of this phenomenon was given in Ref. 16, using data obtained by Almond et al.[24] The test specimen was a 127-mm-ID (5-in.), 12.7-mm-thick (0.5-in.) cylinder made of a mild steel with a yield stress of 315 MPa (45.7 ksi) and containing a longitudinal through crack of half-length equal to 28.58 mm (1.125 in.). At a nominal hoop stress of 241 MPa (35 ksi), the measured crack-tip-opening displacement was 2.007 mm (0.079 in.). For these test data, a point can be plotted in the coordinates of the normalized COD curve proposed by Burdekin and Dawes[25] as a design curve, based on the same effective flaw size concept used in Eq. (15). From Eq. (31), the bulging factor M is 1.58, so that

$$\bar{a} = M^2 c = (25.4)(1.58)^2(1.125) = 70.9 \text{ mm } (2.79 \text{ in.}) .$$

Therefore, referring to Fig. 2.13, the normalized COD is given by

$$\Phi = \frac{\delta}{2\pi\varepsilon_Y \bar{a}} = \frac{7.90 \times 10^{-2}}{(2\pi)(1.52 \times 10^{-3})(2.79)} = 2.96 .$$

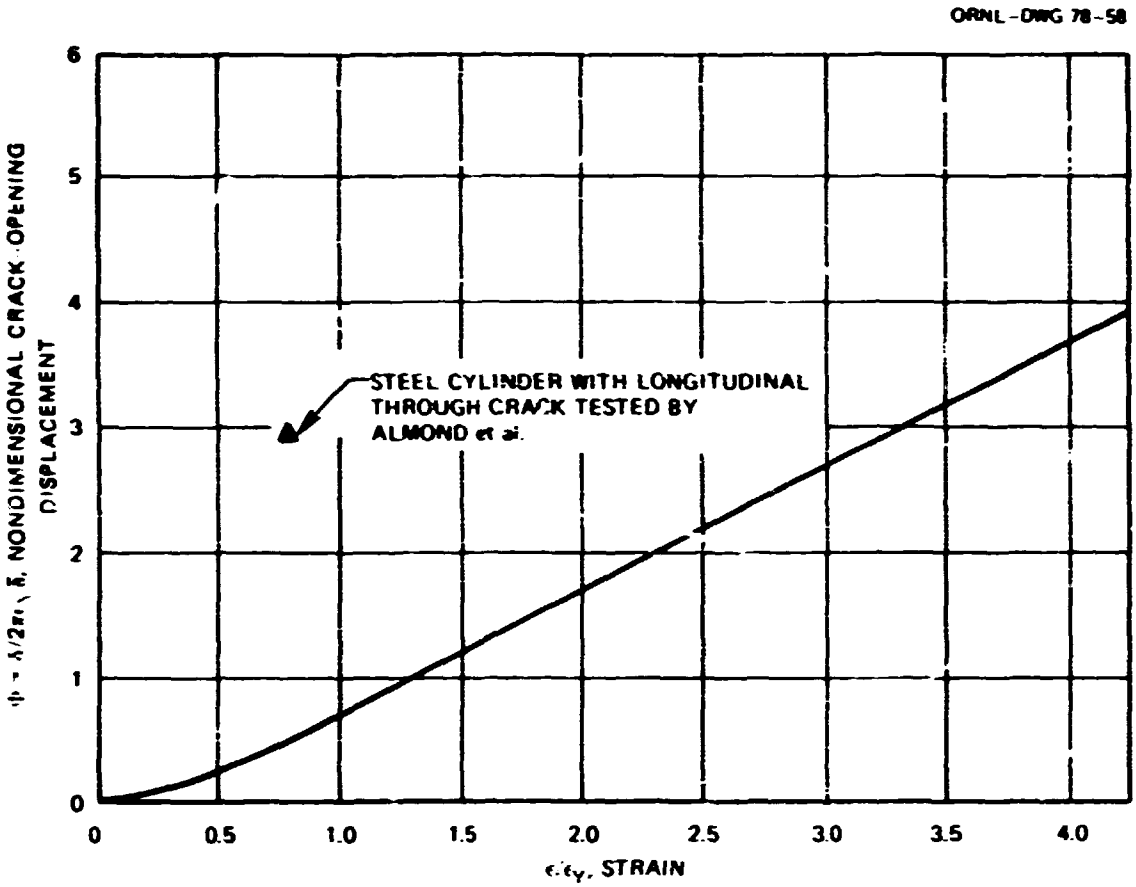

Fig. 2.13. Normalized crack-opening displacement diagram and plotted point for a through-cracked pressurized pipe test.

Since the applied stress is less than the yield stress, $\varepsilon/\varepsilon_Y = \sigma/\sigma_Y = 35.0/45.7 = 0.766$. As shown in Fig. 2.13, the resulting plotted point lies well above the normalized COD curve, indicating a nonconservative prediction, based on the normalized curve, for this test.

Comparison of LEFM and the BMI modified strip yield equation. Since the strip yield model leads to a plastic-zone-size adjusted linear elastic analysis, it is of interest to compare its results with those of a conventional plane stress plastic-zone-size adjusted LEFM analysis. The latter is developed by replacing the crack half-length, c, in Eq. (14)

with $c + r_y$, where, for plane stress,

$$r_y = \frac{1}{2\pi}\left(\frac{K_I}{\sigma_Y}\right)^2 . \tag{55}$$

The result is

$$K_I = \frac{M\sigma\sqrt{\pi c}}{\sqrt{1 - \frac{M^2}{2}\left(\frac{\sigma}{\sigma_Y}\right)^2}} . \tag{56}$$

From Eq. (12),

$$\left(\frac{K_I}{\sigma_Y}\right)^2 = \frac{\delta}{\varepsilon_Y} , \tag{57}$$

and substituting Eq. (57) into Eq. (56) gives, after some rearrangement,

$$\Phi_1 = \frac{\frac{1}{2}\left(M\frac{\sigma}{\sigma_Y}\right)^2}{1 - \frac{1}{2}\left(M\frac{\sigma}{\sigma_Y}\right)^2} , \tag{58}$$

where

$$\Phi_1 = \frac{\delta}{2\pi\varepsilon_Y c} . \tag{59}$$

Note that Φ_1 is based on the actual crack half-length, c, rather than an "effective" crack half-length, M^2c. The corresponding equation for the BMI modified strip yield equation, from Eq. (16), is

$$\Phi_1 = \frac{4}{\pi^2} \ln \sec\left(\frac{\pi M\sigma}{2\sigma_Y}\right) . \tag{60}$$

The curves of Φ_1 vs $M\sigma/\sigma_Y$ for both Eqs. (58) and (60) shown in Fig. 2.14

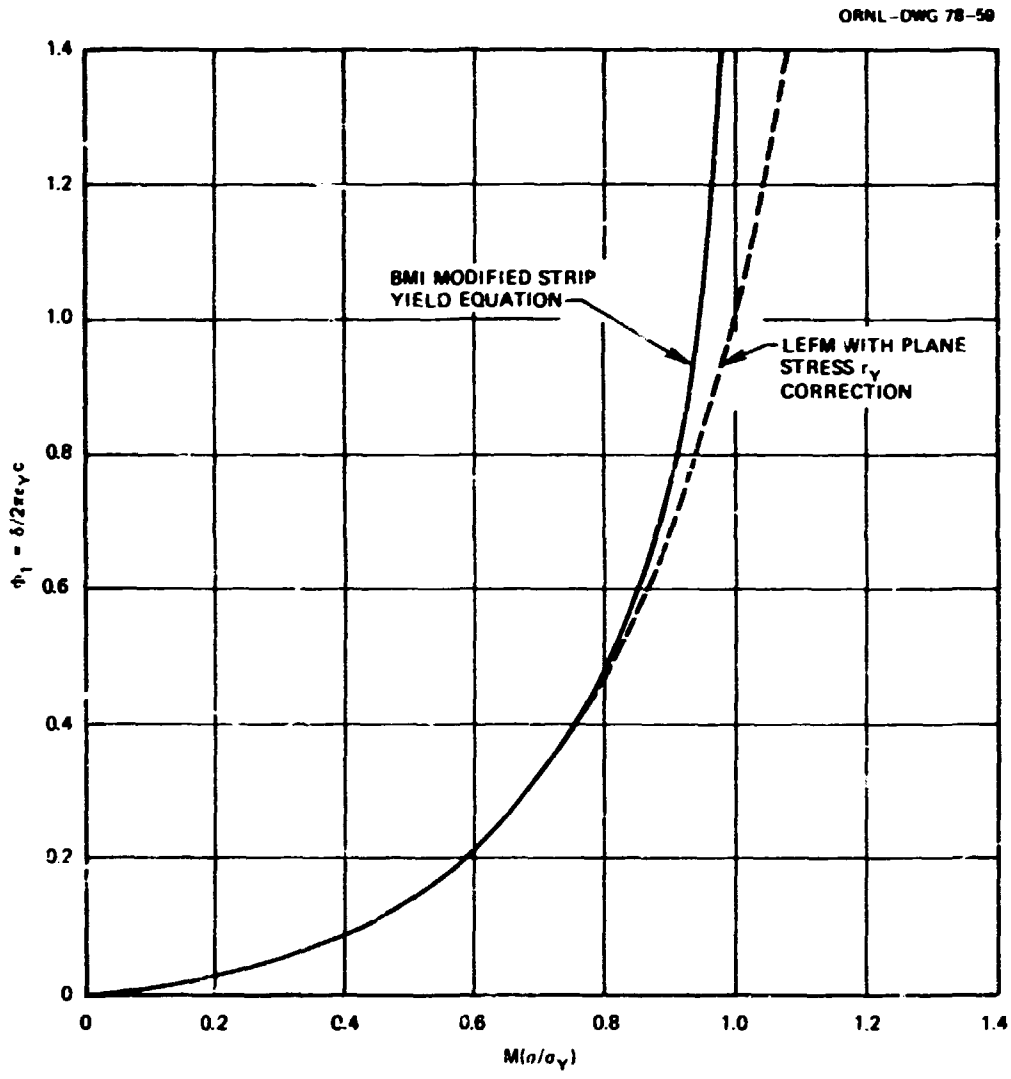

Fig. 2.14. Comparison of crack-opening displacements predicted by the BMI modified strip yield equation and by linear elastic fracture mechanics (LEFM) with a plane stress plastic-zone-size (r_y) correction.

indicate that there is no significant difference between the two expressions for loads less than 75% of the limit load predicted by the BMI modified strip yield equation.

2.4 Elastic Bulging Factor Studies

The bulging factor M, which was used to extend the strip yield model to include cylindrical geometries, was derived for thin shallow shells

with axial flaws of uniform through-thickness lengths. Intermediate test vessel V-7A clearly does not qualify as a thin shell. However, Hahn et al.[16] present data indicating that the strip yield model equation for burst remains valid even for a vessel with a radius to wall thickness ratio of 5, which is well below that normally associated with thin shallow shells. The trapezoidal shape of the V-7A flaw is also at variance with the assumptions made in the bulging factor derivation. It was initially proposed that the trapezoidal shape of the flaw be ignored and that a bulging factor based on the average V-7A flaw length be used in the strip yield model. This study was made to examine that proposal.

Catanach and Erdogan[26] have also considered the problem of a cylinder with an axial, uniform-length, through-thickness flaw. Their solution, involving several terms of a series expansion, makes a distinction between the bulging factors at points on the outer and inner surfaces of the cylinder. Their results are shown as the solid lines in Fig. 2.15. Also plotted in Fig. 2.15, as a dashed line, is the commonly used Folias bulging factor,[16] which is given by the following expression:

$$M = (1.0 + 1.61\ c^2/Rt)^{1/2} , \tag{31}$$

where R is the mean cylinder radius, c is the crack half-length, and t is the cylinder wall thickness. It is of interest to note from Fig. 2.15 that the stress-intensity factor is greater for the outer surface than for the inner, even though the circumferential stress would be higher at the inner surface of an unflawed vessel. This difference reflects the bulging in the shell due to the coupling of the extensional and bending stresses that occurs in curved surfaces.

In order to assess the effect of the departure of the trapezoid-shaped V-7A flaw from the constant-length flaw considered in the derivation of the bulging factor, a finite-element code was used to model the V-7A flaw and vessel and to infer the bulging factor from nodal displacements. The method relies on the plane strain, near-crack-tip relationship between the stress-intensity factor K and the normal displacement u of a point on the crack surface at a distance r from the crack tip, and is given by

$$u = \frac{2K}{G}(1 - \nu)\left(\frac{r}{2\pi}\right)^{1/2} , \tag{61}$$

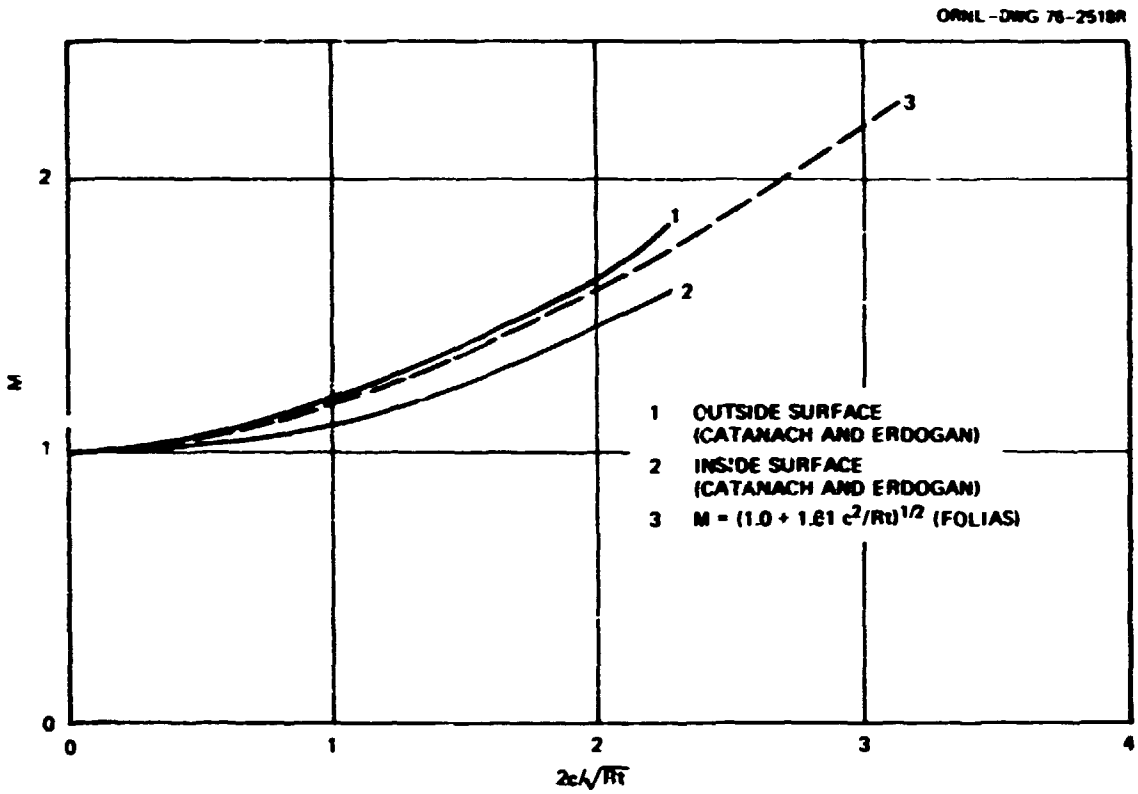

Fig. 2.15. Theoretical bulging factors as a function of cylinder geometry.

where G and ν are the shear modulus and Poisson's ratio, respectively. Kobayashi[27] discusses the degree of refinement necessary in the finite-element mesh size near the crack tip and an upper and lower bound on the distance from the crack tip that should be used in conjunction with Eq. (61). For the work discussed here, the characteristic mesh size near the crack tip was 1/100 of the crack length, and the distance r from the crack tip was taken to be approximately 3/100 of the crack length. Several problems of interest were solved by this method, using the finite-element program STATIC SAP. The elements for the analyses reported here consisted of eight-node bricks. Typically, the problems had one layer of elements through the thickness and 1100 degrees of freedom.

The first three problems that will be discussed were intended as a check of the analysis method, since the finite-element models were taken to be just within the requirements discussed by Kobayashi[27] in order to

minimize computer costs. The first problem that was solved consisted of a large flat plate with a center slit. The stress-intensity factor determined by the finite-element approach was found to be 1.27% above the theoretical value for an infinite plate; that is, $K_I = \sigma\sqrt{\pi c}$, where σ is the far field stress and c is the crack half-length. The numerically determined value normalized by the theoretical value is shown in Fig. 2.16 as a triangle. Since a flat plate can be thought of as the limiting case of a cylinder with a radius of curvature equal to infinity, the flat plate point is plotted with an abscissa value of zero. Figure 2.16 also shows the results for the inner and outer surface values of the bulging factor determined from the finite-element results for cylinders with mean radius to wall thickness ratios of 50 and 100. At an abscissa value of 2.25, the

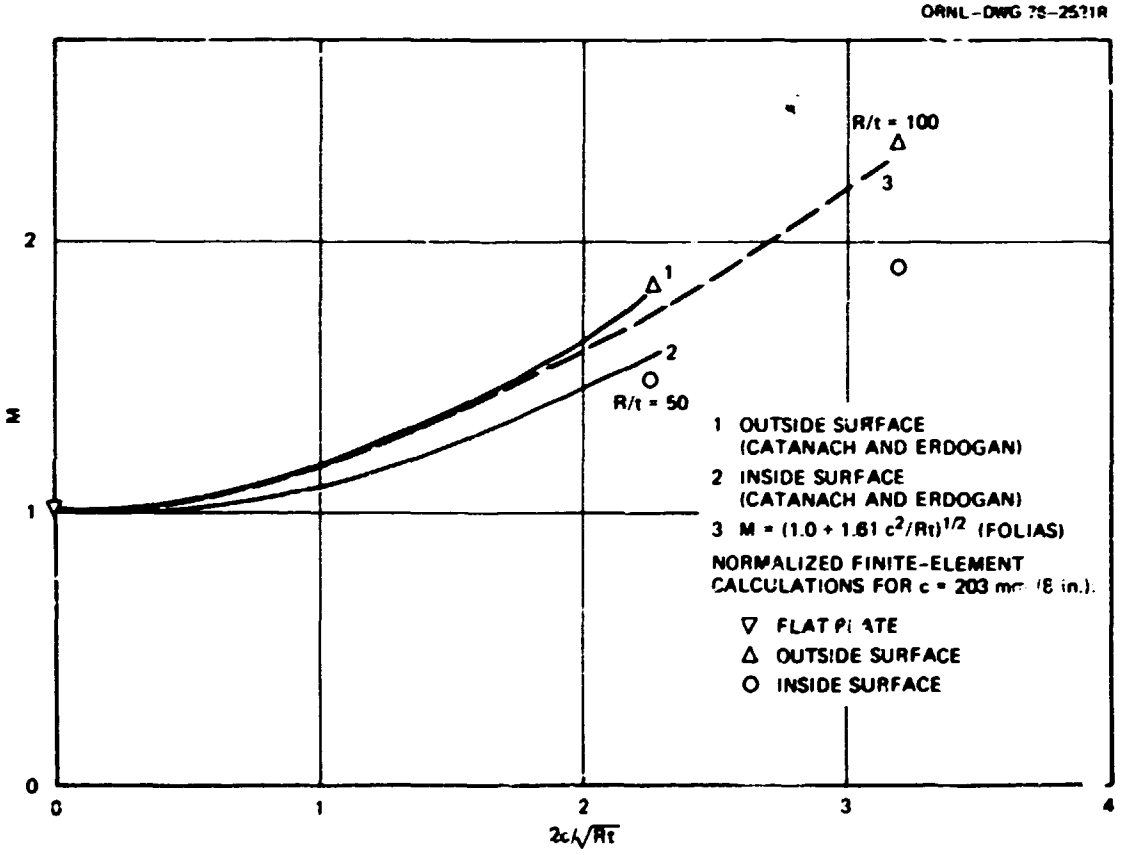

Fig. 2.16. Bulging factor test cases for a flat plate and two thin shallow shells.

bulging factor compares favorably with the results given by Catanach and Erdogan.[26] At an abscissa value of 3.2, which was beyond the domain of convergency for the eight terms used by Catanach and Erdogan,[26] the value of the bulging factor seems reasonable.

As a first step in understanding the effect of nonuniform longitudinal crack length, the stress-intensity factors for tapered cracks in two flat plates with different thicknesses but with the same inside and outside surface crack lengths as V-7A (as shown in Fig. 2.17) were calculated using the finite-element method. The plate thicknesses that were considered were 152.4 mm (6 in.) and 76.2 mm (3 in.). The objective in analyzing the flat plates was to establish a basis by which the results for a cylinder with a variable-length crack could be better interpreted. The calculated flat plate stress-intensity factors, evaluated at each surface and normalized by the stress-intensity factor for a crack of uniform length equal to the average tapered crack length of 165.1 mm (6.5 in.), are shown in Fig. 2.18. Again, the flat plate values correspond to an abscissa of zero. The 76.2-mm-thick (3-in.) plate values are the extreme values plotted on the ordinate in Fig. 2.18, and the largest value (1.42) pertains to the surface of the plate which has the 101.6-mm (4-in.) crack half-length. The 152.4-mm-thick (6-in.) plate displays the same general character as the thinner plate, except that the difference between the values at the two

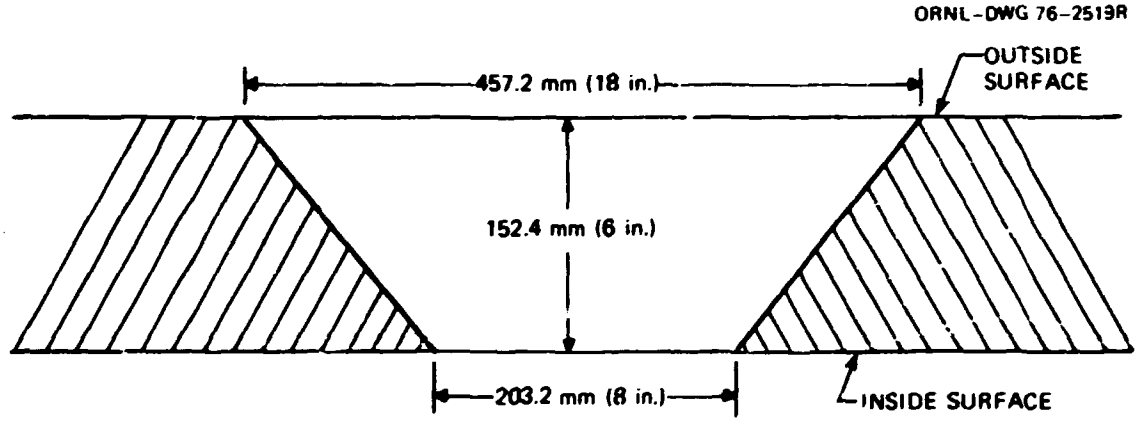

Fig. 2.17. Intermediate test vessel V-7 crack geometry used for finite-element analysis.

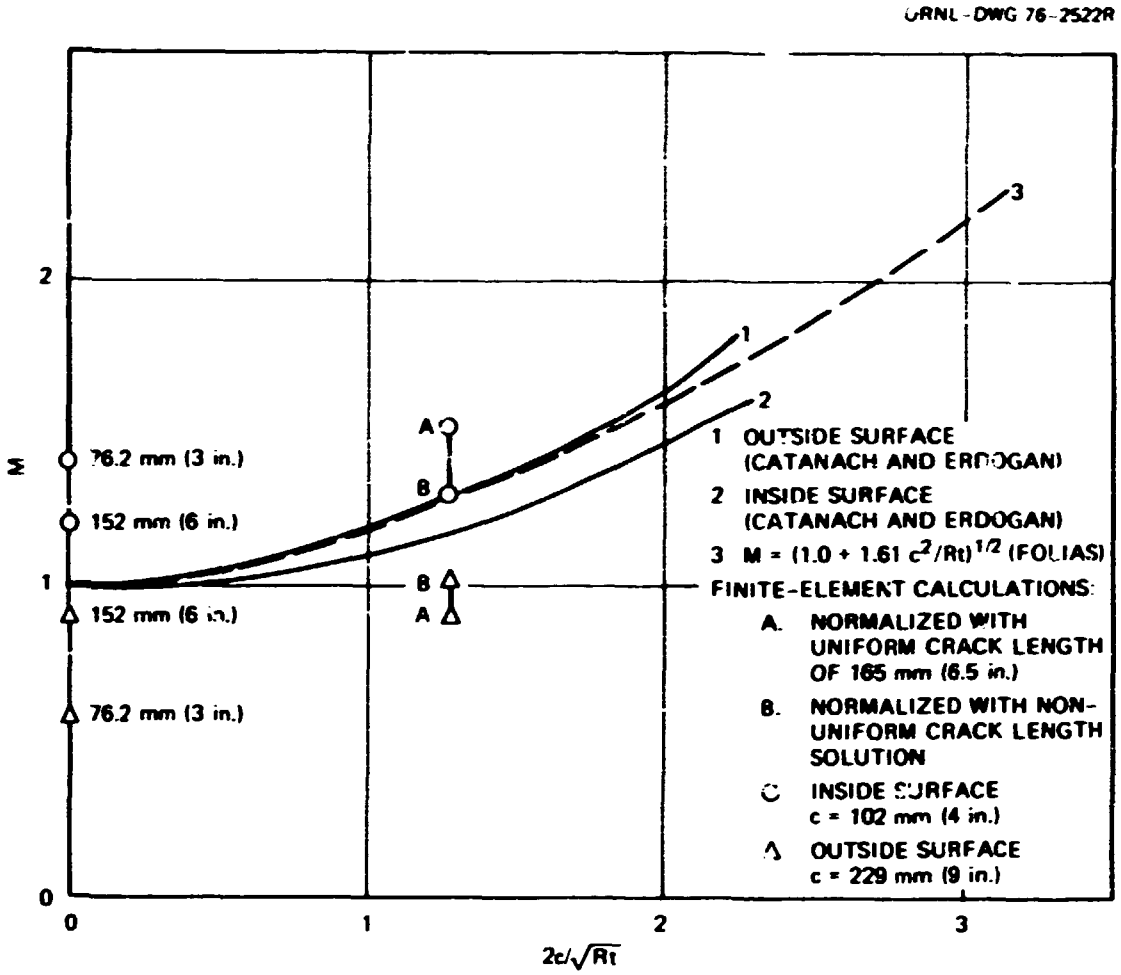

Fig. 2.18. Bulging factors for nonuniform crack length in flat plates and V-7A.

surfaces is less. It can be concluded from these examples that the varying crack length tends to redistribute the load in the structure, and this in turn has a significant effect on the stress-intensity factors developed at points corresponding to the shortest and longest longitudinal crack lengths.

Results of an analysis of the same variable-length crack in the V-7A vessel are shown in Fig. 2.18, where the value of $2c/\sqrt{Rt}$ was determined to be 1.61, using the mean crack length and mean radius. The bulging factor for each surface was determined using two different flat plate stress-intensity factors for normalization. The extreme values of the bulging factor in the range shown were determined by using a uniform 165.1-mm

(6.5-in.) crack half-length, while the points closer to the value predicted by the Folias formula were determined by using the corresponding stress-intensity factors from the finite-element solution of the comparable flat plate problem with a nonuniform crack length.

The elastic analysis results shown in Fig. 2.18 indicate that the bulging factor for a trapezoid-shaped flaw can deviate from the value given by the Folias formula. The deviation, by analogy to the flat plate case, is apparently due to the stress-concentrating nature of the nonuniform crack length. In the case of the actual vessel, the deviation may be less than that indicated by the elastic analysis as a result of load redistribution resulting from either (or both) yielding and tearing at the inner surface where the crack length is the shortest. Because of these factors, the crack would probably tend to behave as a straight-through crack, and the upper and lower surface bulging factors would tend toward the value given by the Folias formula at an average crack length. Since there was evidence of tearing and yielding from the V-7 test, the difference between the bulging factor found from the finite-element analysis and that given by the Folias equation was not considered significant when the average crack length was used.

2.5 Estimate of the Pressure Margin Between Leak and Burst for Vessel V-7A

The modified strip yield model proposed by Hahn, Sarrate, and Rosenfield[16] as a relationship for predicting the burst pressure of a flawed cylindrical vessel was discussed in a previous section. The good correlation of that equation with experimental data (see, for example, Kiefner et al.[17]) led to its acceptance for predicting the burst pressure of intermediate test vessel V-7A. This section contains a discussion of the pretest calculation of the burst pressure vs crack length for V-7A and a similar calculation for a small pneumatically loaded model specimen. In the model experiment, the vessel was intentionally pressurized to failure. The test results for vessel V-7 and for the model thus give leak and burst conditions that the modified strip yield model correctly predict.

The governing equation for predicting burst, which is obtained by combining Eqs. (12) and (16) and replacing the yield stress, σ_Y, with the flow stress, σ_f, is given by

$$\sigma = \frac{2\sigma_f \cos^{-1} \exp\left\{\left[-\frac{\pi}{8}\left(\frac{K_c}{\sigma_f}\right)^2\right]\right\}}{M\pi} , \tag{30}$$

where

σ = the hoop stress at failure,

σ_f = the flow stress of the material,

M = the bulging factor,

2c = the length of the through-wall flaw,

K_c = the effective fracture toughness of the material.

The effective fracture toughness, K_c, was determined from an empirical relationship, given by Irwin et al.,[28] between effective K_c and the plane strain fracture toughness K_{Ic}; namely,

$$K_c^2 = K_{Ic}^2 \left(1 + 1.4\ \beta_{Ic}^2\right) , \tag{62}$$

where

$$\beta_{Ic} = \frac{1}{t}\left(\frac{K_{Ic}}{\sigma_Y}\right)^2 , \tag{63}$$

σ_Y = yield stress, and t = thickness.

For the V-7A vessel, this expression gives high toughness values on the order of those discussed in the previous section comparing COD and K_c measures of toughness. The value of the flow stress was taken to be the nominal hoop stress at plastic instability for an unflawed cylinder with closed ends under internal pressure (see Appendix C of Ref. 29) and is given by

$$\sigma_f = 1.07\ \frac{(\sigma_Y + \sigma'_{ult})}{2} . \tag{64}$$

Taking a yield stress of 448 MPa (65 ksi) and an engineering ultimate stress, σ'_{ult}, of 479 MPa (84 ksi) from Fig. 5.2 of Ref. 30, the flow stress is found to be 550 MPa (80 ksi). If a pressure greater than the vessel gross yield pressure was calculated from Eq. (30), then the gross yield pressure was substituted for the calculated value. In the case of vessel V-7A, the gross yield pressure was taken to be 183 MPa (26.5 ksi), which was the gross yield pressure for intermediate test vessels V-5 and V-9 (Ref. 11). At 196°F, a lower-bound estimate of the plane strain fracture toughness is 460 $MN \cdot m^{-3/2}$ (419 $ksi\sqrt{in.}$).[30,31] For purposes of presentation, the burst stress in Eq. (30) was replaced by the nominal vessel burst pressure, p_{burst}, given by

$$p_{burst} = \frac{t}{R_{in}} \sigma \ , \tag{65}$$

where

t = thickness,

R_{in} = vessel inside radius,

σ = hoop stress at burst.

Equations (30) and (62) to (65) were used to calculate the V-7A burst pressure for different crack lengths and for different values of plane strain fracture toughness. These results plus the V-7 experimental point are plotted in Fig. 2.19. The experimental point corresponds to the pressure at which leaking was detected for the V-7 test based on a nominal crack length of 343 mm (13.5 in.), which was discussed in the previous section concerning the bulging factor correction. The predicted margin against burst is thus the difference between the leak pressure from the V-7 test and the burst pressure determined from the curve for a nominal crack length of 343 mm (13.5 in.). This margin is approximately 36 MPa (5200 psi). The curve corresponding to a toughness of 460 $MN \cdot m^{-3/2}$ (419 $ksi\sqrt{in.}$) is nearly coincident with a limit curve that would be found if the toughnesses were assumed to tend toward an infinite value (i.e., the upper curve in Fig. 2.19 is essentially independent of toughness). For comparison purposes, burst calculations based on an arbitrary plane strain fracture toughness of 275 $MN \cdot m^{-3/2}$ (250 $ksi\sqrt{in.}$) were also made and are shown in Fig. 2.19.

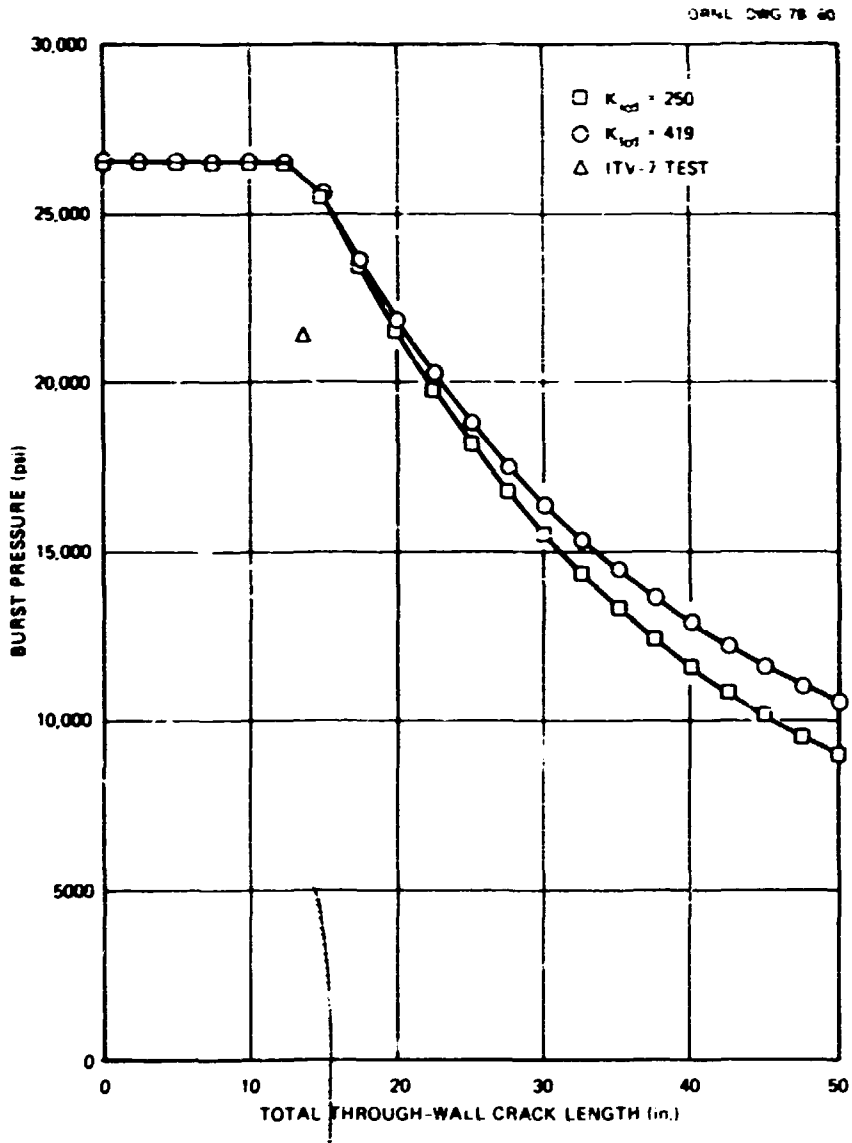

Fig. 2.19. Burst pressure vs crack length for intermediate vessel tests V-7 and V-7A (1 in. = 25.4 mm; 1 psi = 6895 kPa).

One can conclude that the margin against burst is relatively insensitive to the scatter that may exist in the plane strain toughness data.

Burst calculations were also carried out for the pneumatically loaded model test No. 10 which is described on pages 51–55 of Ref. 8. The results of those calculations are shown in Fig. 2.20. As in the case of vessel V-7, the curve associated with the appropriate toughness, estimated to be 137

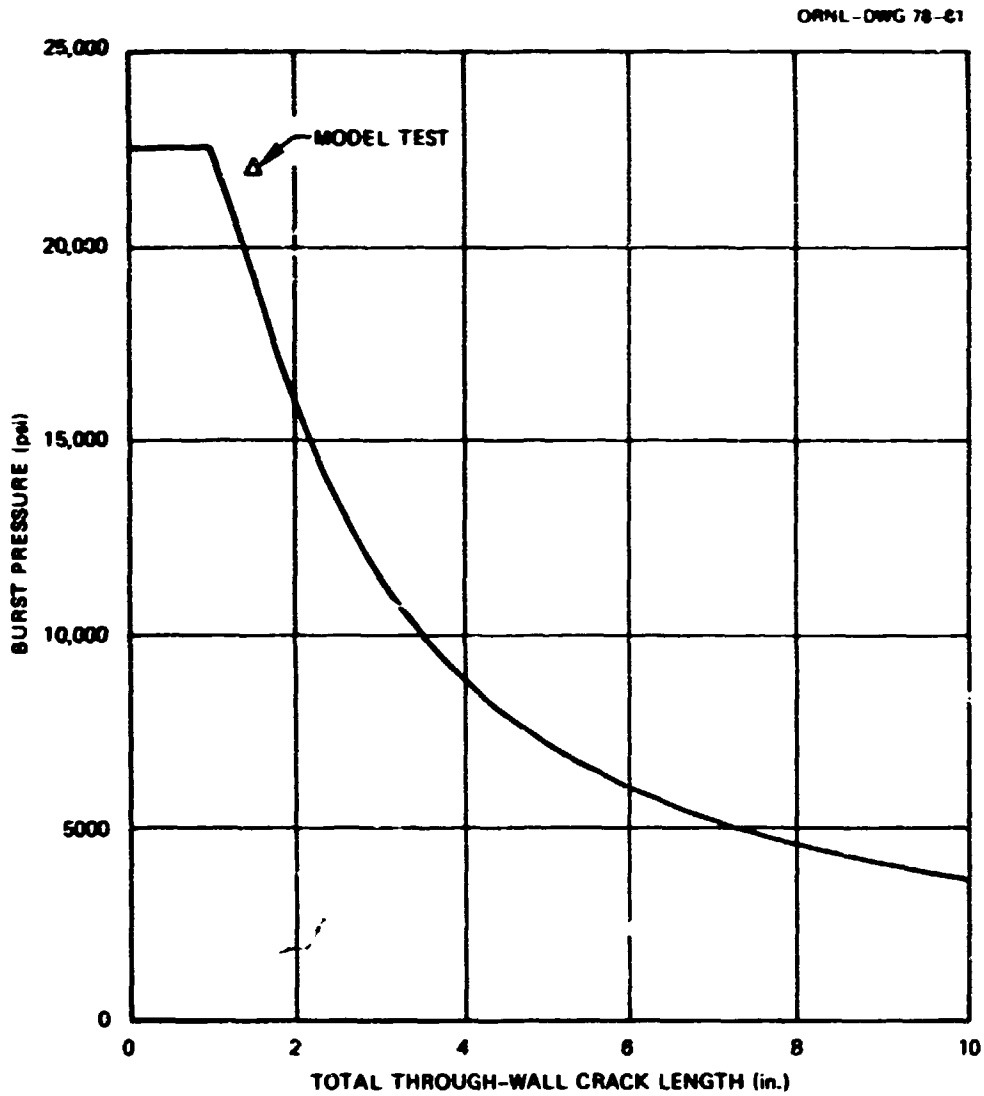

Fig. 2.20. Burst pressure vs crack length for a small-scale model (1 in. = 25.4 mm; 1 psi = 6895 kPa).

$MN \cdot m^{-3/2}$ (150 $ksi\sqrt{in.}$), is nearly coincident with the limit case where the toughness is sufficiently high so that the burst pressure is insensitive to further increases in toughness. The model was loaded until it burst. The experimentally determined burst pressure lies slightly above the curve which is the region where burst instead of leakage should occur, according to the strip yield model.

References

1. Letter from R. F. Fraley, Executive Secretary, Advisory Committee on Reactor Safeguards, to M. Shaw, Mar. 8, 1971; Subject: ACRS Comments on the HSST Program.

2. J. B. Jones and G. A. Hawkins, *Engineering Thermodynamics*, John Wiley and Sons, New York, 1960.

3. H. Sullivan, Nuclear Regulatory Commission, personal communication to R. H. Bryan, Oak Ridge National Laboratory, December 1975.

4. Nuclear Regulatory Commission, Division of Technical Review, *WREM: Water Reactor Evaluation Model* (Revision 1) (May 1975).

5. C. L. Segaser, *System Design Description of the Intermediate Vessel Tests for the Heavy-Section Steel Technology Program*, ORNL/TM-2849 (June 1970), revised July 1973.

6. F. Din, *Temperature-Entropy Diagram for Nitrogen*, British Oxygen Research and Development, Ltd., London (1958).

7. R. B. Stewart, R. T. Jacobsen, and A. F. Myers, *The Thermodynamic Properties of Oxygen and Nitrogen*, University of Idaho (Aug. 31, 1972).

8. J. G. Merkle et al., *Test of 6-in.-Thick Pressure Vessels. Series 3: Intermediate Test Vessel V-7*, ORNL/NUREG-1 (August 1976).

9. P. A. Thompson, *Compressible-Fluid Dynamics*, McGraw-Hill Book Company, New York, 1972.

10. R. H. Bryan et al., *Test of 6-in.-Thick Pressure Vessels. Series 2: Intermediate Test Vessels V-3, V-4, and V-6*, ORNL-5059 (November 1975).

11. J. G. Merkle, G. C. Robinson, P. P. Holz, and J. E. Smith, *Test of 6-in.-Thick Pressure Vessels. Series 4: Intermediate Test Vessels V-5 and V-9 with Inside Nozzle Corner Cracks*, ORNL/NUREG-7 (August 1977).

12. J. N. Goodier and F. A. Field, "Plastic Energy Dissipation in Crack Propagation," pp. 103–18 in *Fracture of Solids*, edited by D. C. Drucker and J. J. Gilman, Interscience, 1962.

13. E. S. Folias, "An Axial Crack in a Pressurized Cylindrical Shell," *Int. J. Fract. Mech.* 1, 104–13 (1965).

14. A. A. Wells, "Fracture Control of Thick Steels for Pressure Vessels," *Br. Weld. J.* 15, 221 (1968).

15. A. Cowan and N. Kirby, "Fracture Initiation in Low Strength Steel Pressure Vessels," *Trans. ASME, Ser. B, J. Eng. Ind.* 92(1), 79–85 (1970).

16. G. T. Hahn, M. Sarrate, and A. R. Rosenfield, "Criteria for Crack Extension in Cylindrical Pressure Vessels," *Int. J. Fract. Mech.* 5, 187–210 (1969).

17. J. F. Kiefner et al., "Failure Stress Levels of Flaws in Pressurized Cylinders," pp. 461–81 in *Progress in Flaw Growth and Fracture Toughness Testing*, ASTM STP-536, American Society for Testing and Materials, 1973.

18. F. J. Loss, *Dynamic Tear Test Investigations of the Fracture Toughness of Thick-Section Steel*, NRL Report 7056 (also HSSTP-TR-7), U.S. Naval Research Laboratory (May 14, 1970).

19. S. C. Grigory, *Tests of 6-In.-Thick Flawed Tensile Specimens. Third Technical Summary Report, Longitudinal Specimens Numbers 14 through 16, Unflawed Specimen Number 17*, HSSTP-TR-22, Southwest Research Institute (October 1972).

20. PVRC Ad Hoc Group on Toughness Requirements, *PVRC Recommendations on Toughness Requirements for Ferritic Materials*, WRC Bulletin 175, Welding Research Council (August 1972).

21. J. G. Merkle, "Approximate Stress-Intensity Factor Calculations for Continuous Inside-Surface Circumferential Cracks in a Cylinder Under Thermal Loading," pp. 3–15 in *HSST Program Quarterly Progress Report for January–March 1976*, ORNL/NUREG/TM-28 (July 1976).

22. F. M. Burdekin and D. E. W. Stone, "The Crack Opening Displacement Approach to Fracture Mechanics in Yielding Materials," *J. Strain Anal.* 1(2), 145–53 (1966).

23. A. E. Green and I. N. Sneddon, "The Distribution of Stress in the Neighborhood of a Flat Elliptical Crack in an Elastic Solid," in *Proc., Cambridge Phil. Soc.* 46, 159–63 (1950).

24. E. A. Almond et al., "The Fracture of Pressurized Laminated Cylinders," *J. Iron Steel Inst., London*, 207, 1319–23 (1969).

25. F. M. Burdekin and M. G. Dawes, "Practical Use of Linear Elastic and Yielding Fracture Mechanics with Particular Reference to Pressure Vessels," pp. 28–37 in *Practical Application of Fracture Mechanics to Pressure-Vessel Technology*, Institution of Mechanical Engineers, London, 1971.

26. W. M. Catanach, Jr., and F. Erdogan, *Fatigue Crack Propagation in Cylindrical Shells*, NASA-CR-1197 (October 1968).

27. A. S. Kobayashi (ed.), *Experimental Techniques in Fracture Mechanics*, Society for Experimental Stress Analysis, Westport, Conn., 1973.

28. G. R. Irwin et al., *Basic Aspects of Crack Growth and Fracture*, NRL Report 6598, U.S. Naval Research Laboratory (November 1967).

29. R. W. Derby et al., *Test of 6-In.-Thick Pressure Vessels. Series 1: Intermediate Test Vessels V-1 and V-2*, ORNL-4895 (February 1974).

30. W. J. Stelzman, "Characterization of Intermediate Test Vessels," *HSST Quarterly Progress Report for April–June 1974*, ORNL/TM-4655 (August 1974).

31. F. J. Witt and T. R. Mager, *A Procedure for Determining Bounding Values on Fracture Toughness K_{Ic} at Any Temperature*, ORNL/TM-3894 (October 1972).

3. DESCRIPTION OF TEST VESSEL

3.1 Background

Vessel V-7 was fabricated of 150-mm-thick (6-in.) A 533, grade B, class 1 steel plate.[1] A long, deep outside surface flaw was formed in the test section of the vessel, and the vessel was tested under hydraulic loading at 91°C (196°F) until it leaked at 147 MPa (21,350 psi).[2] (The fabrication history is described in Ref. 1, and the condition of the vessel after the test is described in detail in Ref. 2.) Subsequently, the vessel was repaired and prepared for retesting with the designation V-7A.

Vessel V-7A was the first of the intermediate test vessels to be prepared for testing by repairing a vessel that had been previously tested to the point of failure. It was suitable for further testing because, in the initial test, the vessel had developed a rupture through the wall only immediately beneath the prepared flaw, and gross residual distortion of the vessel was limited to the region of the flaw. Thus, distortion did not affect the removal and resealing of the head or the repair of the flaw itself.

The cylindrical test section in regions remote from the flaw had reached strains of 0.29 to 0.47% on the inside surface and about 0.1% on the outside. The strain distributions in Figs. 3.1 and 3.2 show measured outside and inside circumferential strains near the maximum pressure in the test of V-7. A permanent set in the vessel prior to weld repair is indicated by the residual strain distributions also shown in these two figures. A location 135° from the original V-7 flaw was selected for the V-7A flaw to minimize the influence of the repair weld and residual strain on the test. The V-7A flaw location relative to the old flaw is shown in Fig. 3.3.

3.2 Weld Repair

The original flaw in vessel V-7 was a 25-mm-wide (1-in.) machined notch sharpened by a cracked electron-beam (EB) weld bead. The cross section of the flaw, shown in Fig. 3.4, lay in a radial-axial plane of the test section 180° from the longitudinal submerged-arc weld in the vessel.

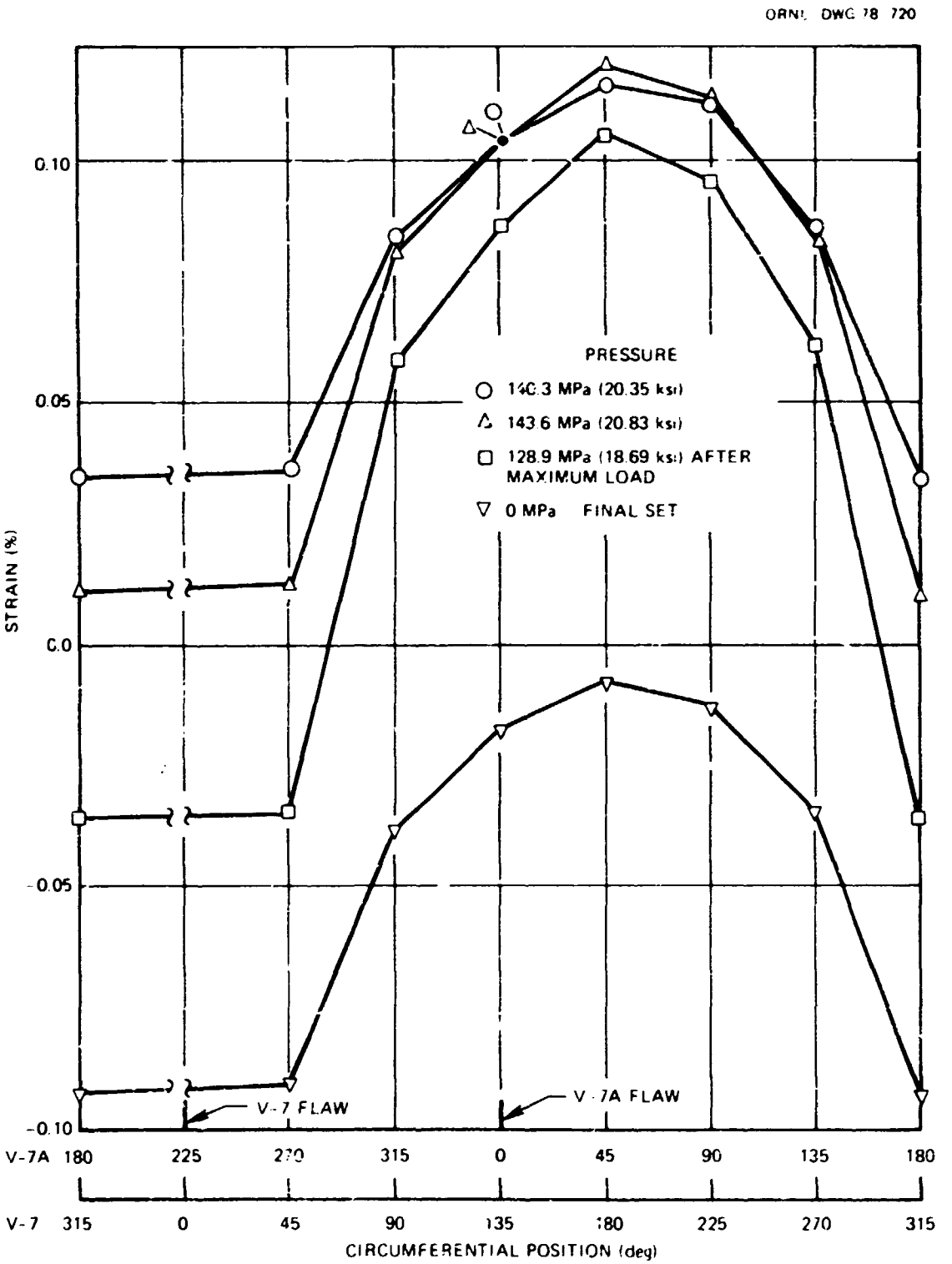

Fig. 3.1. Outside circumferential strain distribution at midplane of vessel V-7 near maximum pressure and after depressurization.

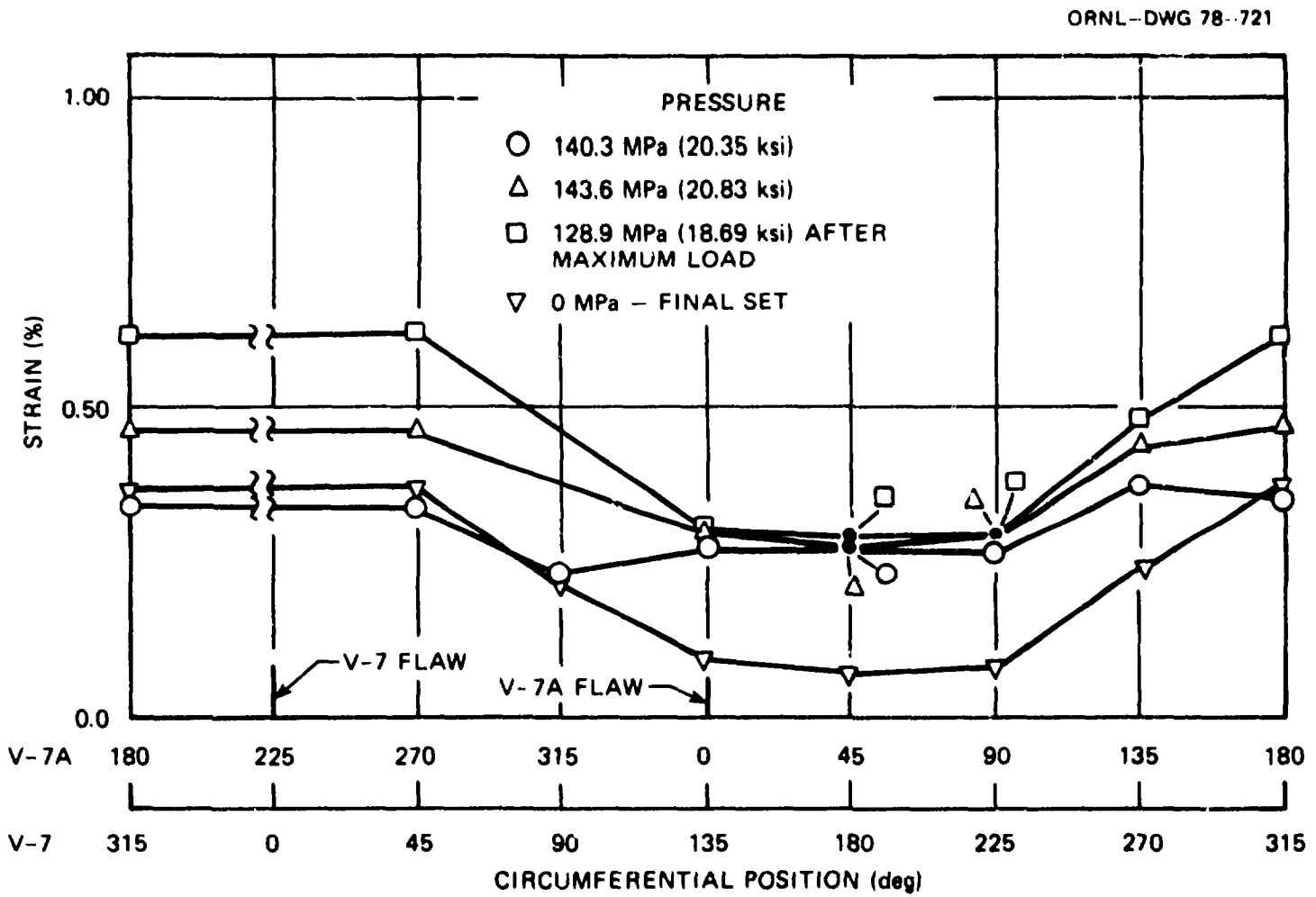

Fig. 3.2. Inside circumferential strain distribution at midplane of vessel V-7 near maximum pressure and after depressurization.

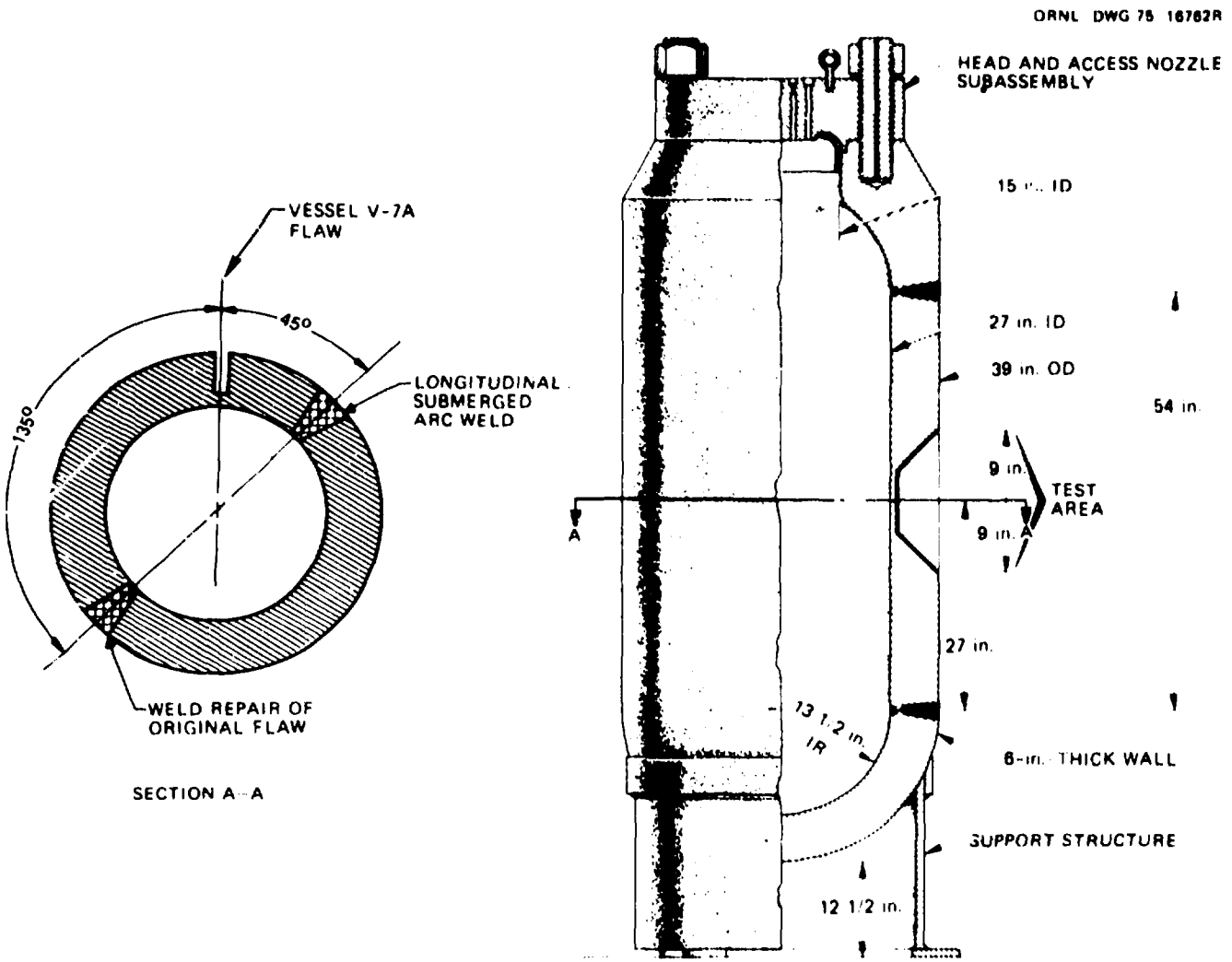

Fig. 3.3. Intermediate test vessel V-7A (1 in. = 25.4 mm).

ORNL-DWG 76-7962

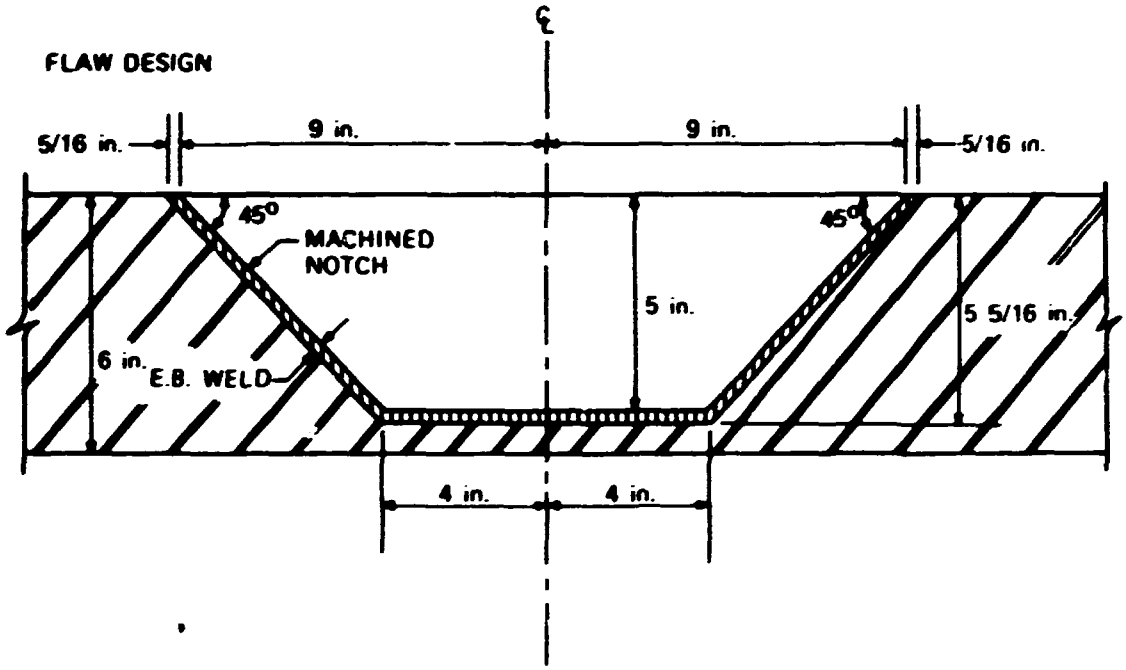

Fig. 3.4. Flaw design for vessels V-7 and V-7A (1 in. = 25.4 mm).

Consideration was given to making a repair of the fracture zone by the most economical means consistent with the objectives of the subsequent test. Alternatively, the vessel could have been repaired by procedures applicable to nuclear vessels. The latter course was chosen, since the test being planned for V-7A would be a rare opportunity to test a repair weldment to a high overload.

A repair weldment was designed for vessel V-7 to utilize the half-bead procedure prescribed by Subsubarticle IWB-4420 of Section XI of the *ASME Boiler and Pressure Vessel Code*[3] (hereafter referred to as the Code). This procedure is intended for use in repair of components for which it is impractical to perform the usual postweld heat treatment at 590 to 620°C (1100 to 1150°F). The ORNL Welding Specification No. W-HB100, based upon this procedure in the Code, was written especially for the repair of vessel V-7.

The welding procedures incorporated in the specifications were developed with the advice of the Pressure Vessel Research Committee's (PVRC's)

Advisory Task Group on Weld Repair of Pressure Vessels, under the chairmanship of E. Landerman of Westinghouse Electric Corporation. The Electric Power Research Institute (EPRI) participated in this effort by funding the repair, which was made by Combustion Engineering, Inc. (CE) at no cost to the government. R. E. Smith was project leader for EPRI, and W. D. Goins of CE directed the weld preparations, procedure qualification, repair welding, and nondestructive examination. A detailed account of work of CE is given in Ref. 4, and the welding specifications are given in Appendix A.

Section XI of the Code requires the preparation of a welding procedure qualification piece similar to the repair weldment. The cylindrical prolongation of intermediate test vessel V-9 was chosen for this purpose, since it was fabricated from the same heat as vessel V-7 (Ref. 1). The V-7 prolongation had already been cut up for material characterization. Since vessel V-7 was not a "Code" vessel in the strict sense and its future use in fracture tests did not demand a Section XI repair, the procedure qualification piece was not tested as required by the Code for the purpose of qualifying the procedure used on the vessel. The vessel and the prolongation were prepared and welded concurrently. The prolongation was eventually sectioned for material property studies and for the measurement of residual stresses.

The prolongation was instrumented with weldable strain gages in the region of the repair weld by ORNL at the locations shown in Fig. 3.5. Two additional circumferential gages, one on the inside surface and one on the outside surface, were placed 180° from the repair cavity. Thermocouples were installed at each strain gage location to ensure that the temperature limitation for the gages was not exceeded. Ailtech type SG425 gages were used within 50.8 mm (2 in.) of the cavity, and type SG125 gages were used at locations corresponding to gages 3, 4, 7, and 8 on the prolongation. Strain observations were made at several stages of the repair process and were used subsequently in the residual stress study described in Section 3.3.

The material that had to be removed from the flawed region to prepare the vessel for welding is shown in Figs. 3.6 and 3.7, respectively. This material was removed to the nominal dimensions shown in Fig. 3.8 by using the conventional manual air-carbon-arc process followed by grinding.[5] In

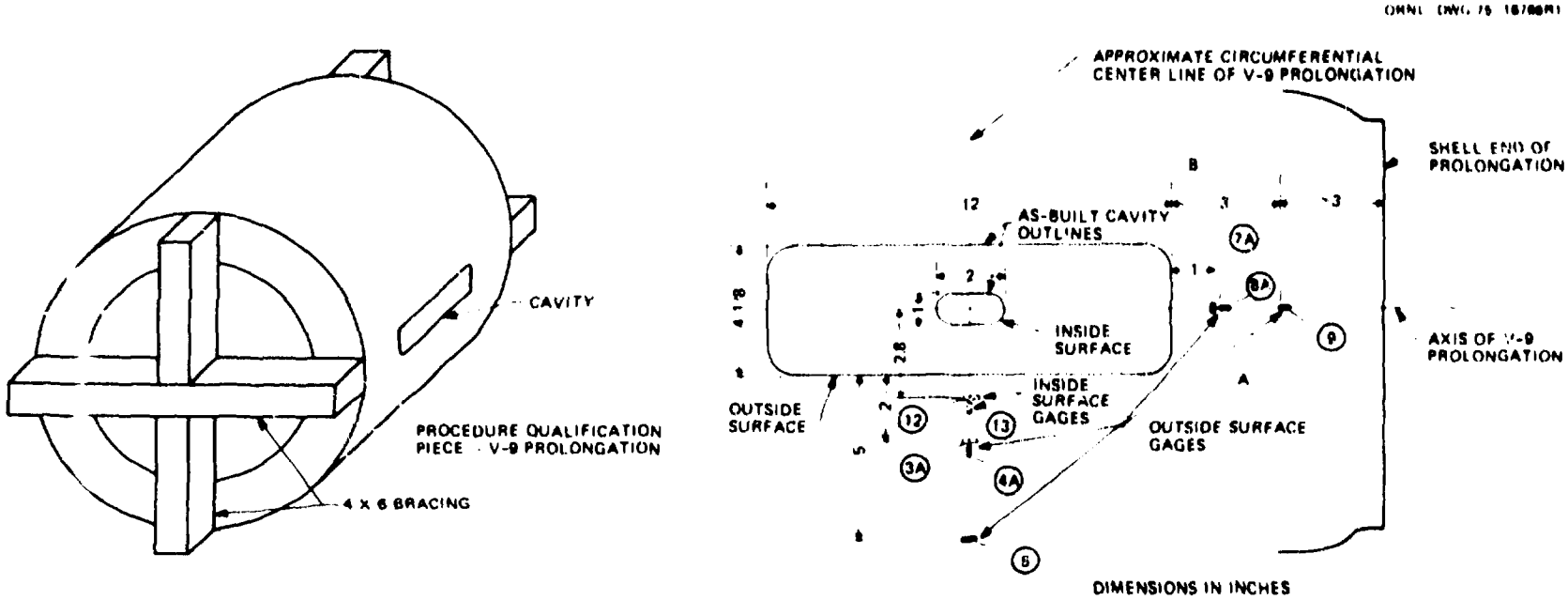

Fig. 3.5. Strain gage layout for V-9 prolongation used for V-7 repair weld procedure qualification (1 in. = 25.4 mm).

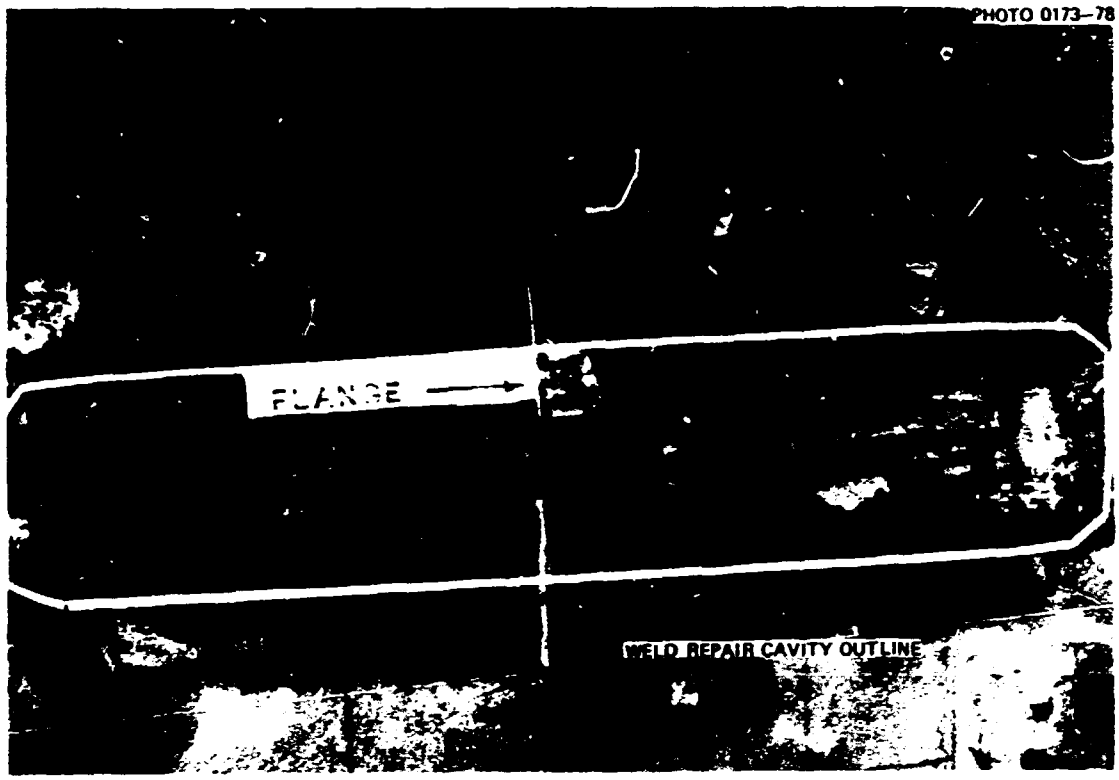

Fig. 3.6. Outside view of flaw in vessel V-7 after test showing material to be removed to prepare the vessel for welding.

this process, a direct current arc is maintained between the work piece and a copper-coated carbon electrode. The molten material is blown away by high-velocity jets of compressed air. The final air-arc-produced surface of the cavity is shown in Fig. 3.9.

A minimum of 6.4 mm (1/4 in.) of metal was removed by grinding to ensure complete removal of the air-carbon-arc surface and any heat-affected zone resulting from the air-carbon-arc process. After grinding, the cavities in both the vessel and the prolongation were given liquid-penetrant and magnetic-particle (MT) examination to ensure that the cavity surfaces were crack-free. The final ground surface of the vessel cavity in shown in Fig. 3.10.

Electrical resistance heaters were used to preheat the vessel and the prolongation for air-arc gouging and welding. The welding preheat temperature range was 177 to 260°C (350 to 500°F).

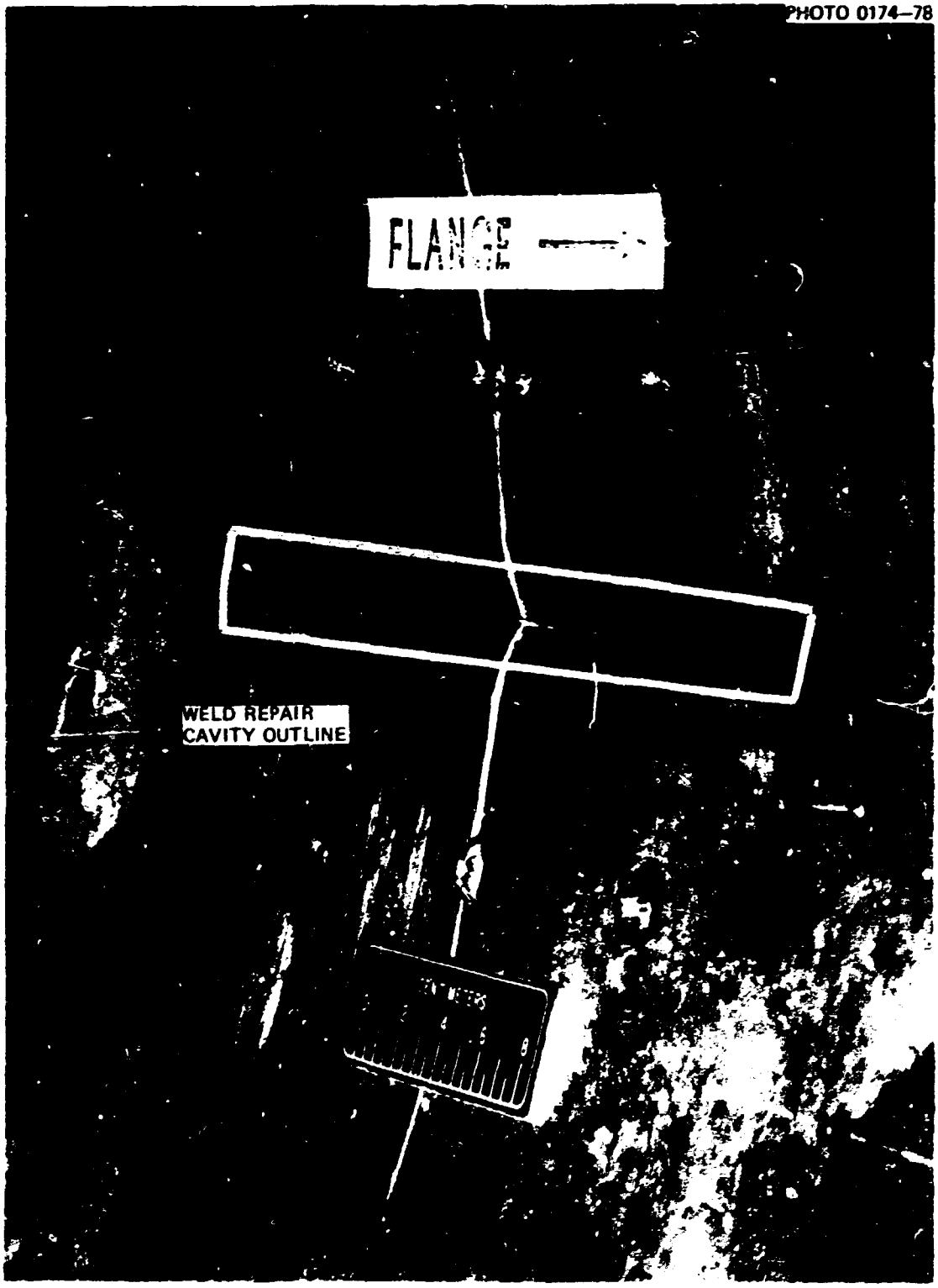

Fig. 3.7. Inside view of vessel V-7 in area of rupture showing material to be removed to prepare the vessel for welding.

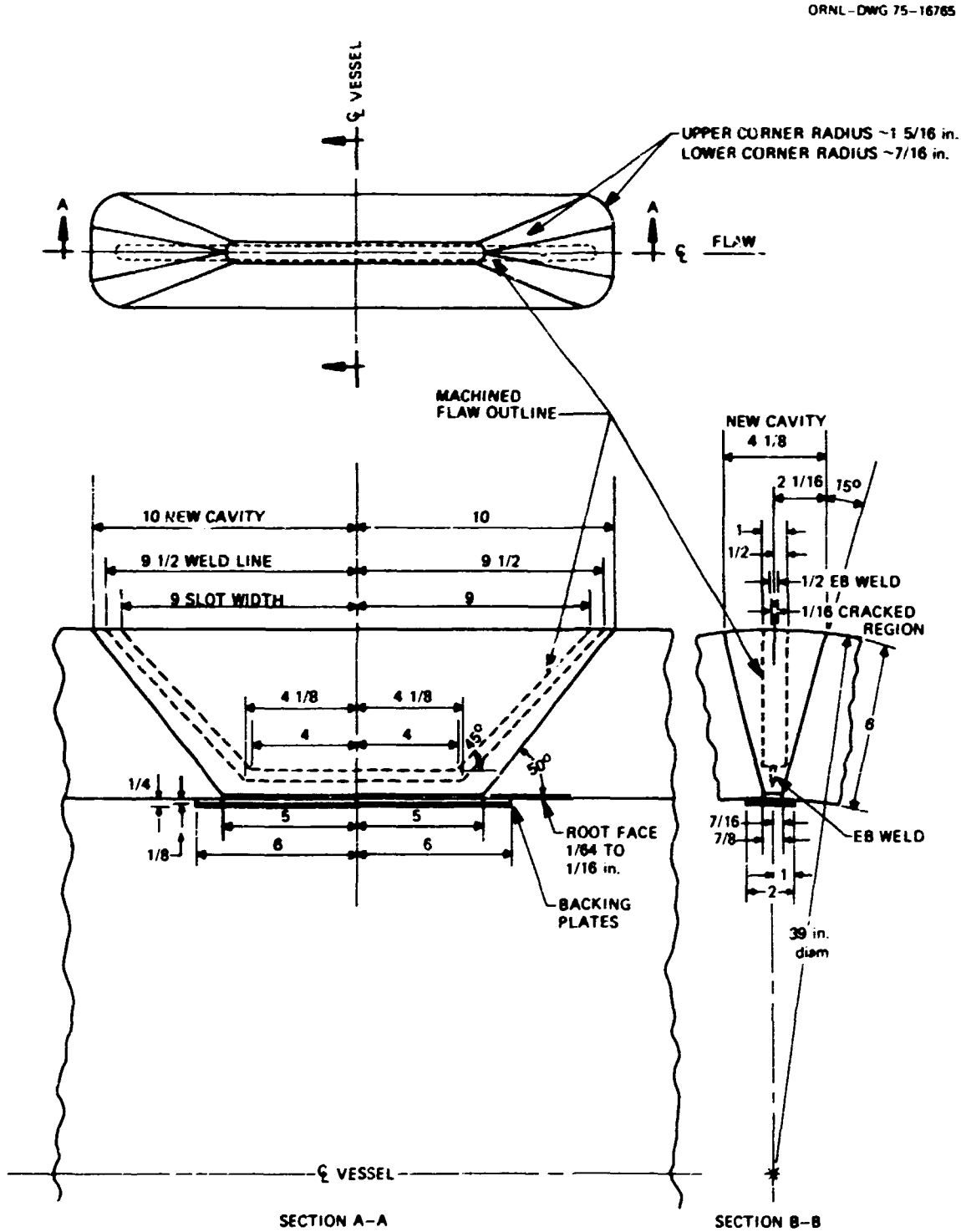

Fig. 3.8. Design of repair-preparation cavity in vessel V-7 (1 in. = 25.4 mm).

Fig. 3.9. Vessel weld-repair cavity after air-arc gouging. Photograph courtesy of Combustion Engineering, Inc.

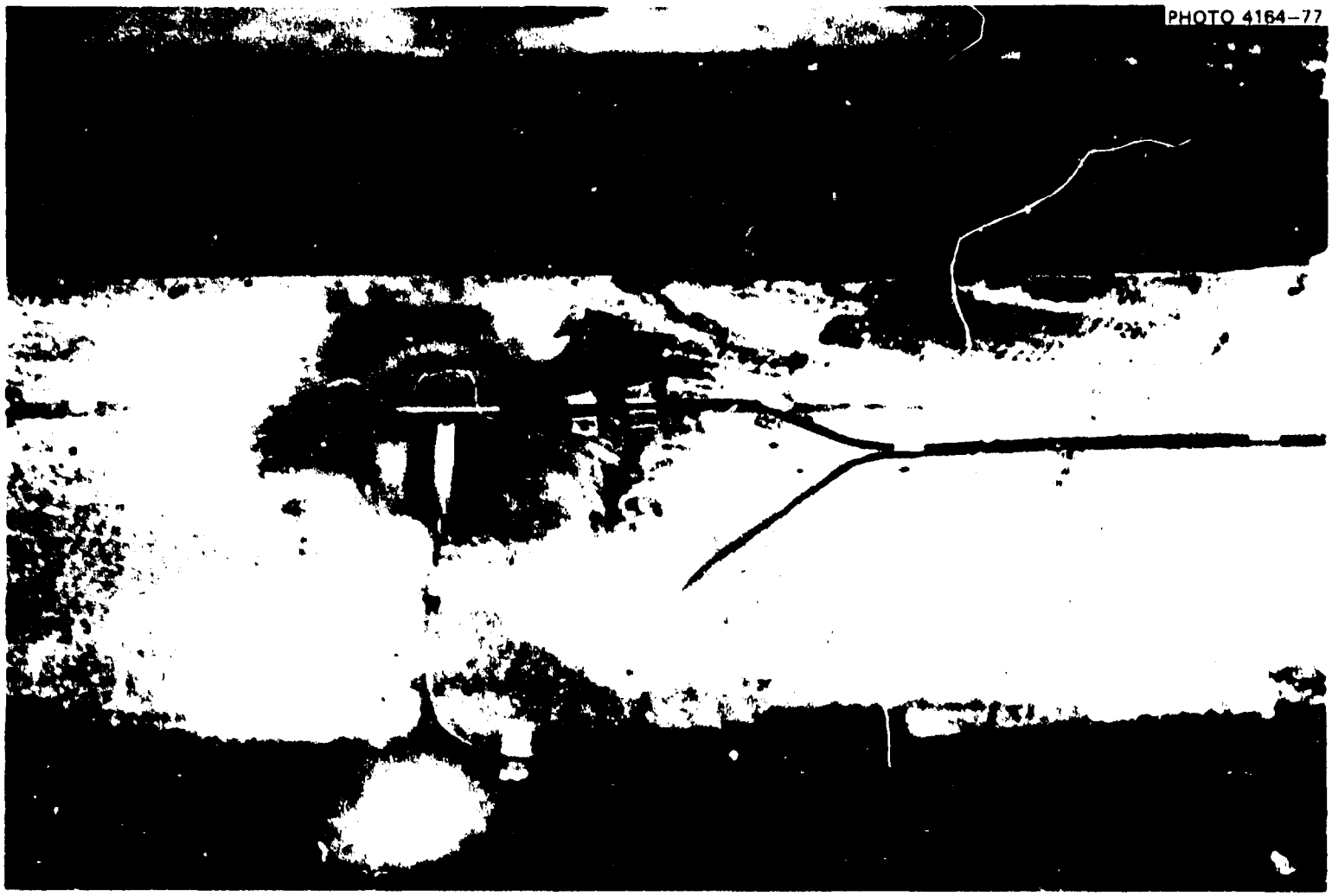

Fig. 3.10. Vessel weld-repair cavity after grinding to final dimensions before welding. Photograph courtesy of Combustion Engineering, Inc.

Welding was accomplished by the manual shielded-metal-arc process. The weld cavity surfaces were "buttered" with 2.38-mm-diam (3/32-in.) electrodes. The bead sequence is indicated in Fig. 3.11. The vessel and prolongation were oriented so that most of the beads were deposited in the horizontal position. Approximately half of the "buttered" layer was ground off, and the cavities were then given an MT examination. A second weld

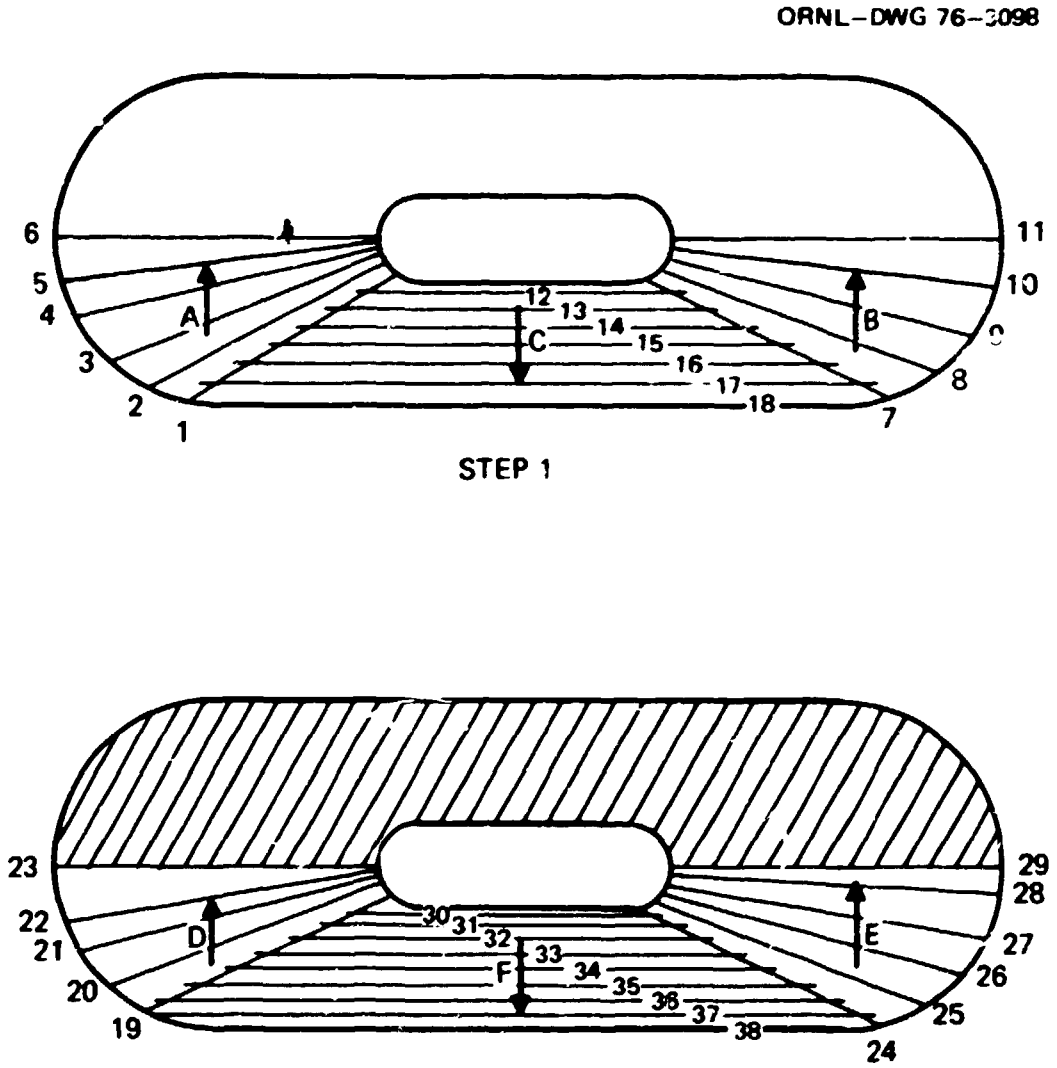

Fig. 3.11. Cavity "buttering" weld bead sequence for repair of vessel V-7.

layer was deposited over the cavity surfaces with a 3.18-mm-diam (1/8-in.) electrode. The weld bead sequence used to deposit the second layer was the same as that used to deposit the first one. After the second layer was completed and MT inspected, the cylinders were rotated so that the cavities would be at the 12 o'clock position. Each cavity was then filled with 3.18- and 3.97-mm-diam (1/8- and 5/32-in.) electrodes. The first bead deposited in each vertical layer was placed next to the cavity side wall, and subsequent beads were sequenced inward toward the center. MT inspection was performed on alternate layers and on the final ground layer. There were no MT indications detected in either cavity during any of the inspections. Figure 3.12 shows the vessel cavity partially welded.

After the welding was completed, the welds were heat treated in the temperature range of 232 to 288°C (450 to 550°F) for 4 hr. The temperatures of the vessel and prolongation repair weld regions were controlled within ±11 K (20°F) of the average temperatures at all times. The heat-up and cool-down rates were approximately 14 K/hr (25°F/hr).

The entire weld and the adjacent base metal within a distance of one-half the thickness of the cylinder (1/2T) of both the vessel and the prolongation were examined ultrasonically in accordance with the requirement of paragraph IWA-2232 and Appendix I of Section XI (Ref. 3). The required examination was performed three times: (1) as soon as the vessel and prolongation surfaces reached room temperature; (2) 48 hr after both surfaces returned to room temperature; and (3) approximately 4 weeks later. There were no recordable indications detected during any of these inspections.

Radiographic examination was performed with a 7 1/2-MeV Varian linear accelerator and Kodak M film in accordance with the requirements of paragraph IWA-2231 of Section XI. No defects were found in the vessel repair weld. Porosity was detected near the inside surface of the weld in the prolongation, and it is believed to be related to the restricted access available to the welder in the deep, narrow portion of the prolongation cavity.

In order to provide sufficient material for characterizing the properties of the weld metal, two test plates, shown in Fig. 3.13, were welded and heat treated with the same parameters that were used to repair the vessel. MT examination and radiography revealed no rejectable indications

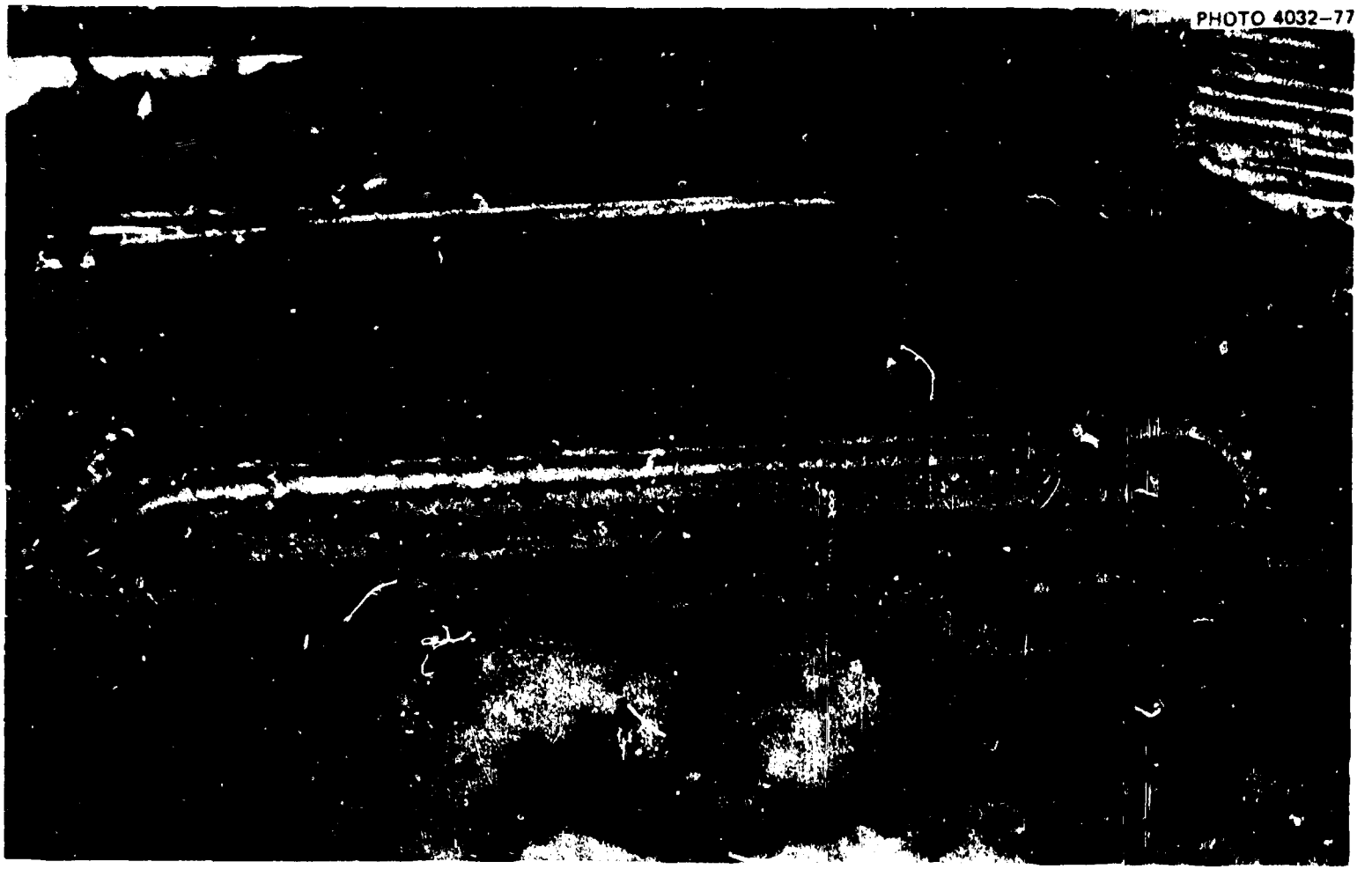

Fig. 3.12. Vessel cavity with second buttered layer complete and cavity partially filled with weld metal. Photograph courtesy of Combustion Engineering, Inc.

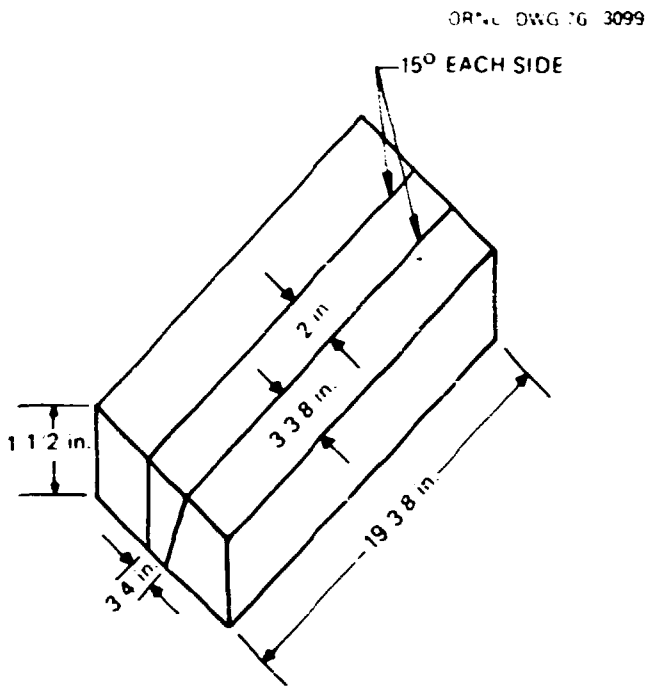

TEST PLATE A

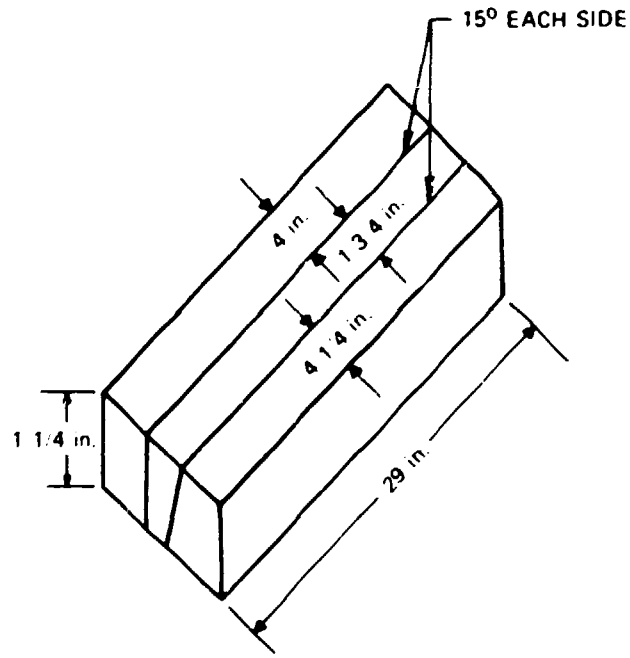

TEST PLATE B

Fig. 3.13. Weld metal test plates (1 in. = 25.4 mm).

in the test plates. The base material in these plates came from the 3/4T depth of section 02FH of HSST plate 02 (Refs. 6 and 7).

Recommendations on this type of weld repair were included in the report prepared by Goins and Butler of CE.[4]

3.3 Repair Weld Characterization

The welding procedure qualification piece (that is, the V-9 prolongation) and one of the two weld metal test plates prepared by CE were used for characterizing the properties of the weld repair zone and for investigating the through-the-thickness residual stress in the V-7A weldment.

3.3.1 Material properties

W. J. Stelzman and D. A. Canonico of the Metals and Ceramics Division of ORNL determined the material properties of the weld repair zone. Since the repair zone in vessel V-7A was not to be flawed, an extensive investigation of the fracture properties of the material in this zone was deemed unnecessary. However, ultimate and yield stresses, Charpy energies, and lower-bound fracture toughnesses of the weld metal were measured.

Material property specimens were machined from test plate B, shown in Fig. 3.13. A cross section of this weldment, designated W-1, is shown in Fig. 3.14. Tensile specimens of the W orientation (specimen axis perpendicular to the welding direction and parallel to the plate surface) were tested in the temperature range from −73 to 232°C (−100 to 450°F), and the results are presented in Table 3.1 and Fig. 3.15.

Charpy V specimens from weldment W-1 were tested in the WL orientation (specimen axis perpendicular to the welding direction with the crack propagating in the welding direction). The notches were located at the weld centerline. The Charpy V impact properties of weldment W-1 are given in Fig. 3.16. Precracked Charpy specimens of the same orientation were tested statically, and the results are shown in Fig. 3.17.

Yield and ultimate strengths of W-1 weld metal differ slightly from those previously measured for HSST plate 02 (Ref. 7). The yield strength of W-1 weld metal is about 50 MPa (7 ksi) higher than that of the midsection region of the V-7 base material.[1] Generally, the weld exhibited higher

Fig. 3.14. Cross section of shielded metal-arc weldment in test plate B.

Table 3.1. Tensile values from W-oriented specimens[a] from shielded metal-arc weldment W-1 (test plate B)

Location[b]	Test temperature [°C (°F)]	Strength			Elongation (%)		Reduction in area (%)
		Upper yield [MPa (ksi)]	Lower yield[c] [MPa (ksi)]	Ultimate [MPa (ksi)]	Uniform	Total	
0.71	−73.3 (−100)	585 (84.9)	543 (78.8)	655 (95.0)	8	18	72
0.29	23.3 (74)	543 (78.8)	510 (73.9)	590 (85.6)	5	14	76
0.35	24.4 (76)		488 (70.8)	586 (85.0)		18[d]	72
0.35	24.4 (76)		491 (71.2)	589 (85.4)		18[d]	72
0.71	65.6 (150)	507 (73.5)	479 (69.5)	563 (81.6)	6	15	71
0.29	121 (250)		490 (71.0)	582 (84.4)	2	7	39[e]
0.71	177 (350)		490 (71.1)	659 (95.6)	5	10	58
0.29	232 (450)		497 (72.1)	622 (90.2)	4	10	64

[a]Unless noted, data are from 4.52-mm (0.178-in.) gage diameter specimens with a gage length to diameter ratio of 7 and $\dot{\varepsilon} = 0.016\ min^{-1}$.

[b]Fractional depth from top surface of the weld.

[c]Absence of upper yield denotes 0.2% yield.

[d]Standard 12.8-mm (0.505-in.) gage diameter specimens with gage length to diameter ratio of 4 and $\dot{\varepsilon} = 0.22\ min^{-1}$.

[e]Low due to lack of fusion and entrapped slag in the fracture zone.

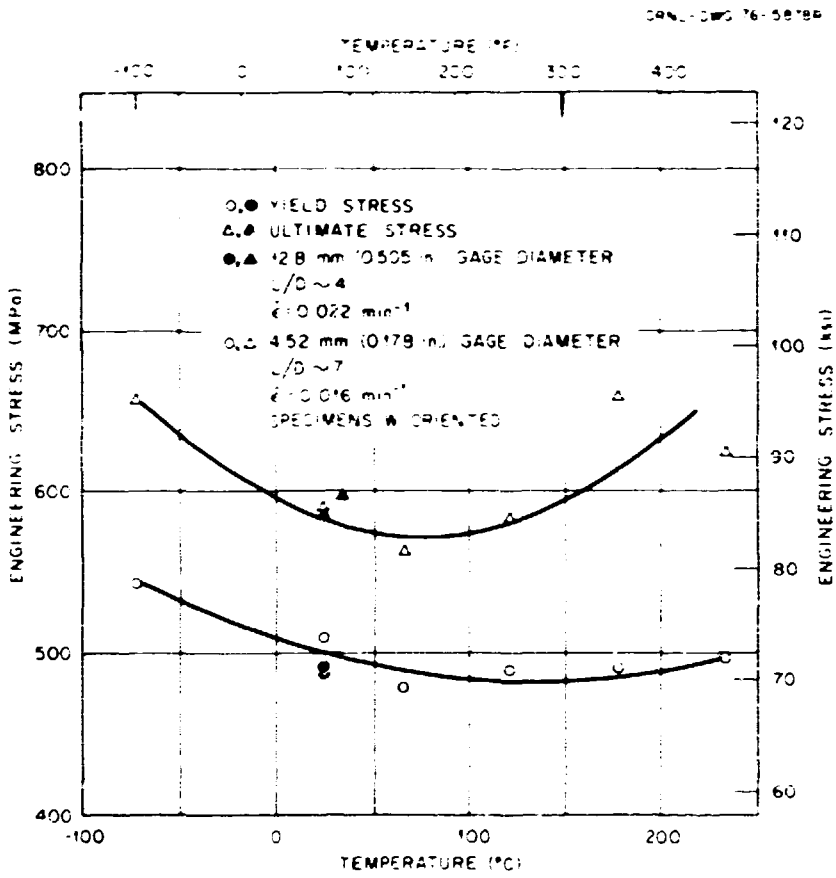

Fig. 3.15. Variation of tensile properties with temperature for test weldment W-1.

upper-shelf Charpy V impact energy values than either plate 02 or vessel V-7, while the transition temperature at the 41-J (30-ft-lb) level of the weld [−34°C (−30°F)] is within the range of values measured in V-7 material at various depths and orientations.

The V-9 prolongation (Fig. 3.5) that was used as the welding procedure qualification piece was sectioned to provide additional material for studying the properties of the repair zone. After the braces were cut from the ends of the prolongation, the remaining cylinder was sawed into two pieces along the circumferential centerline labeled in Fig. 3.5. Subsequently, the shell-end half was sawed approximately along the axial centerline of the repair weld cavity, and the quadrant of the repair zone labeled "B" in Fig. 3.5 was used for material properties studies. The circumferential

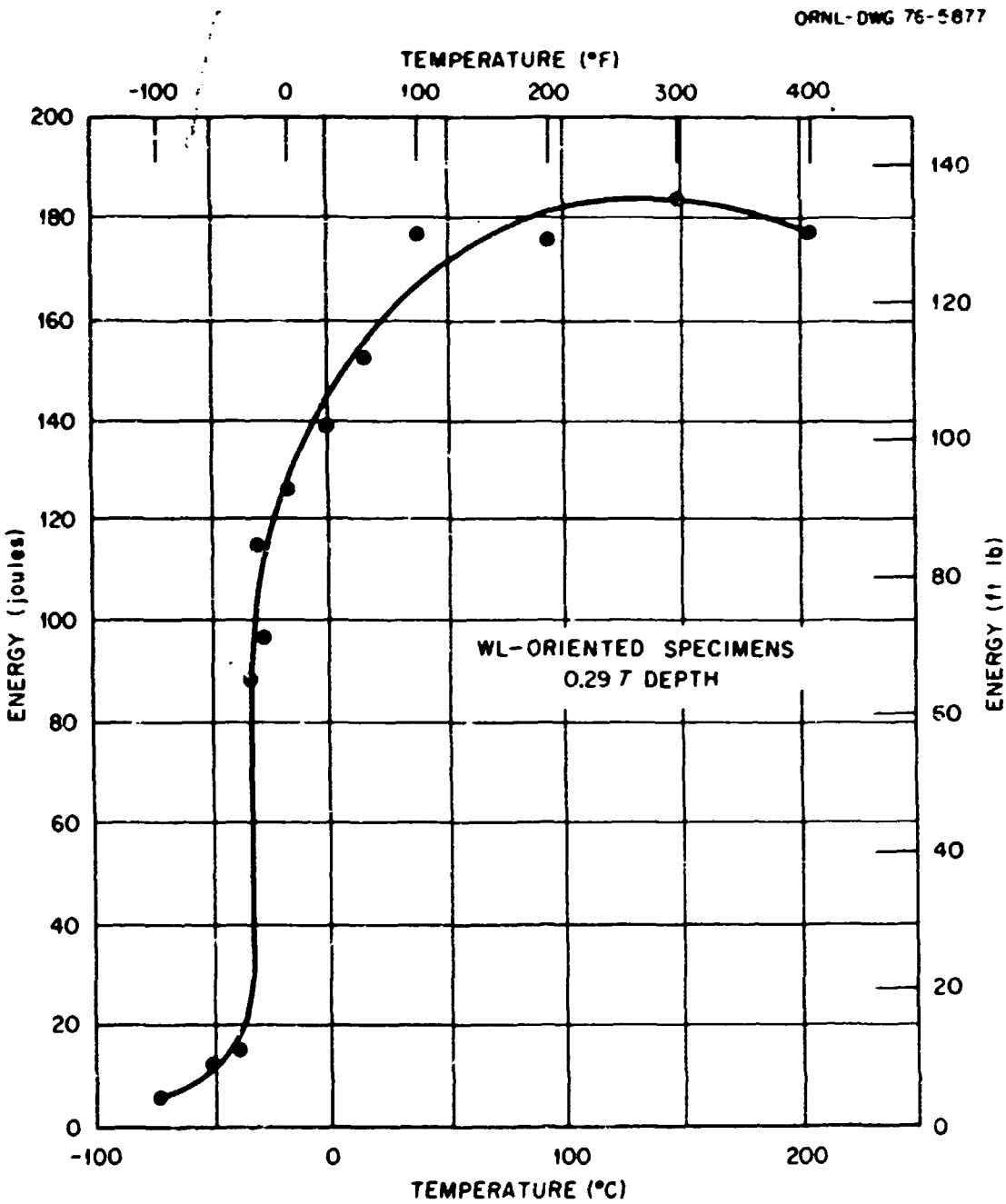

Fig. 3.16. Variation of Charpy V impact energy with temperature for test weldment W-1.

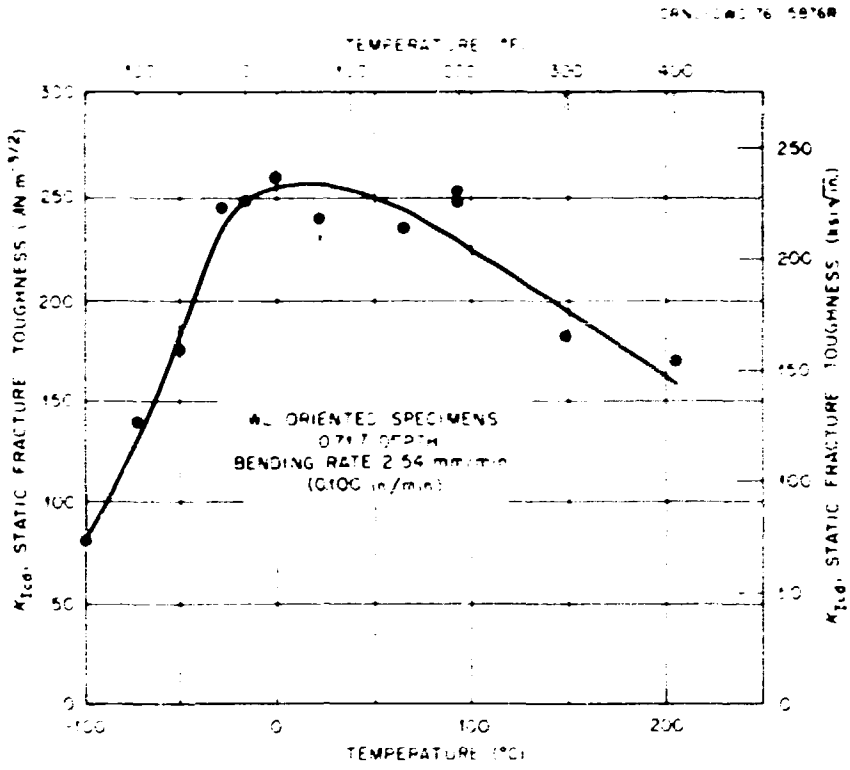

Fig. 3.17. Variation of fracture toughness with temperature as determined from slow-bend tests of precracked Charpy specimens from test weldment W-1.

slice of part B shown in Fig. 3.18 was etched to reveal the weld–base metal interface and the heat-affected zone (HAZ) in the base metal.

Microhardness measurements were made in the vicinity of the HAZ. The location of one such region is shown in Fig. 3.19. The circumferential-radial face was traversed by three sets of hardness penetrations in a region approximately 25 mm (1 in.) from the outside cylindrical surface, as indicated in that figure. Dimensional details of the traverses are given in Fig. 3.20 and the results in Fig. 3.21. Hardness values are consistently higher in the dark etched band of the HAZ, with the highest value measured in this repair weldment being 310 diamond pyramid hardness (DPH). The relationship between hardness and ultimate tensile strength for steel[8] implies an ultimate tensile strength of the HAZ as high as 1000 MPa (145 ksi).

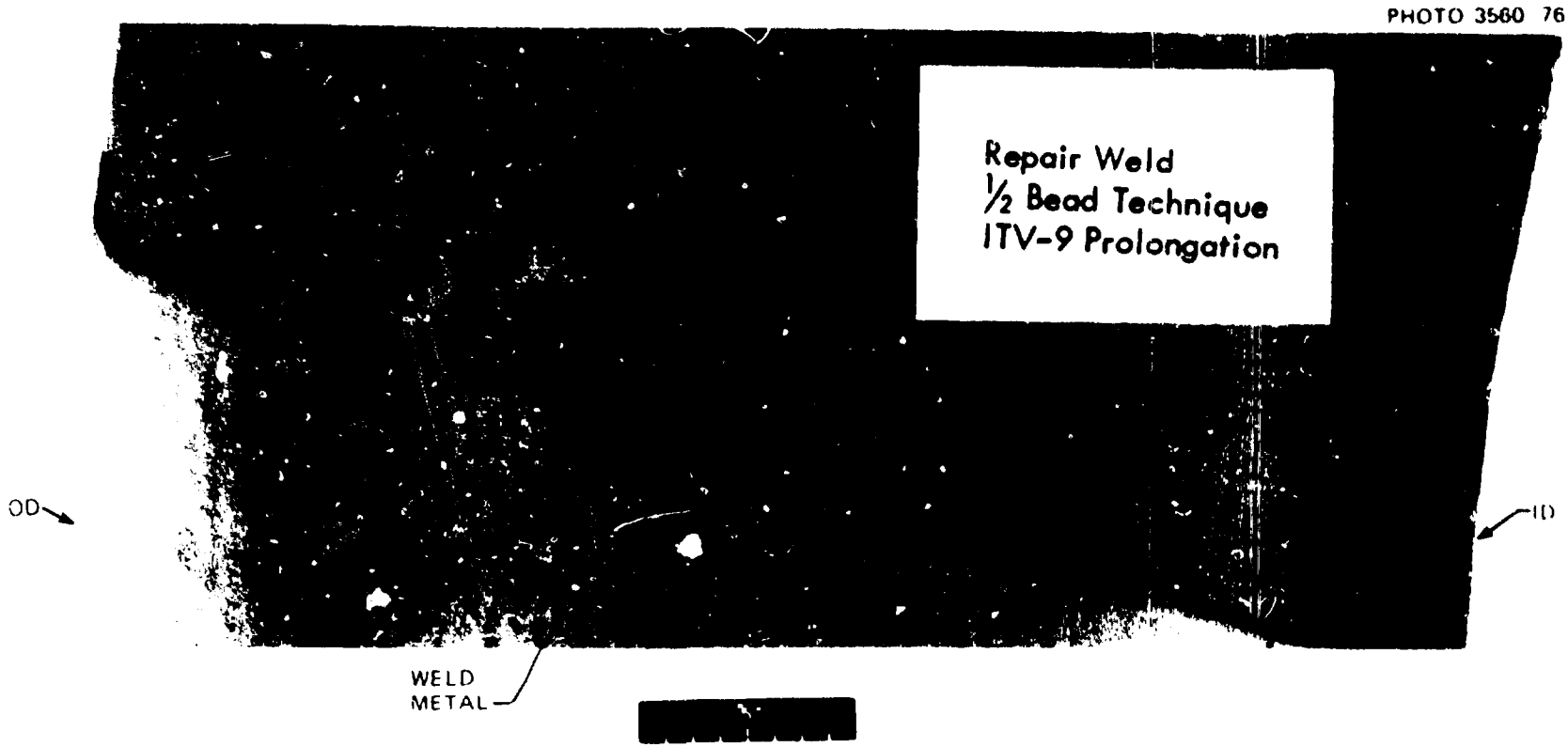

Fig. 3.18. Circumferential cross section of the repair weldment taken from part B of the V-9 prolongation.

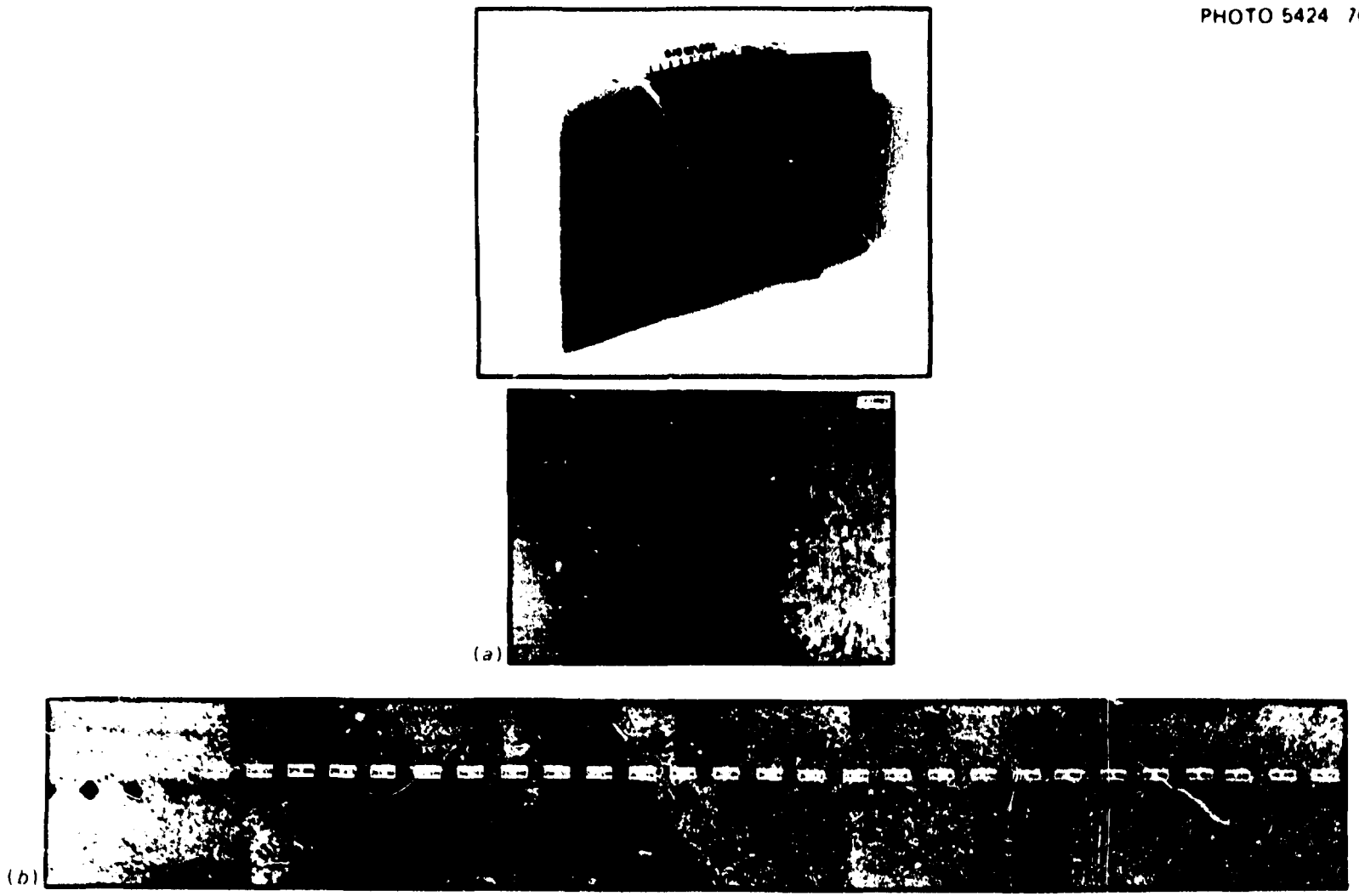

Fig. 3.19. Microhardness traverses on a circumferential-radial section of the repair zone of the V-9 prolongation. The 100× montage in (b) shows the center traverse.

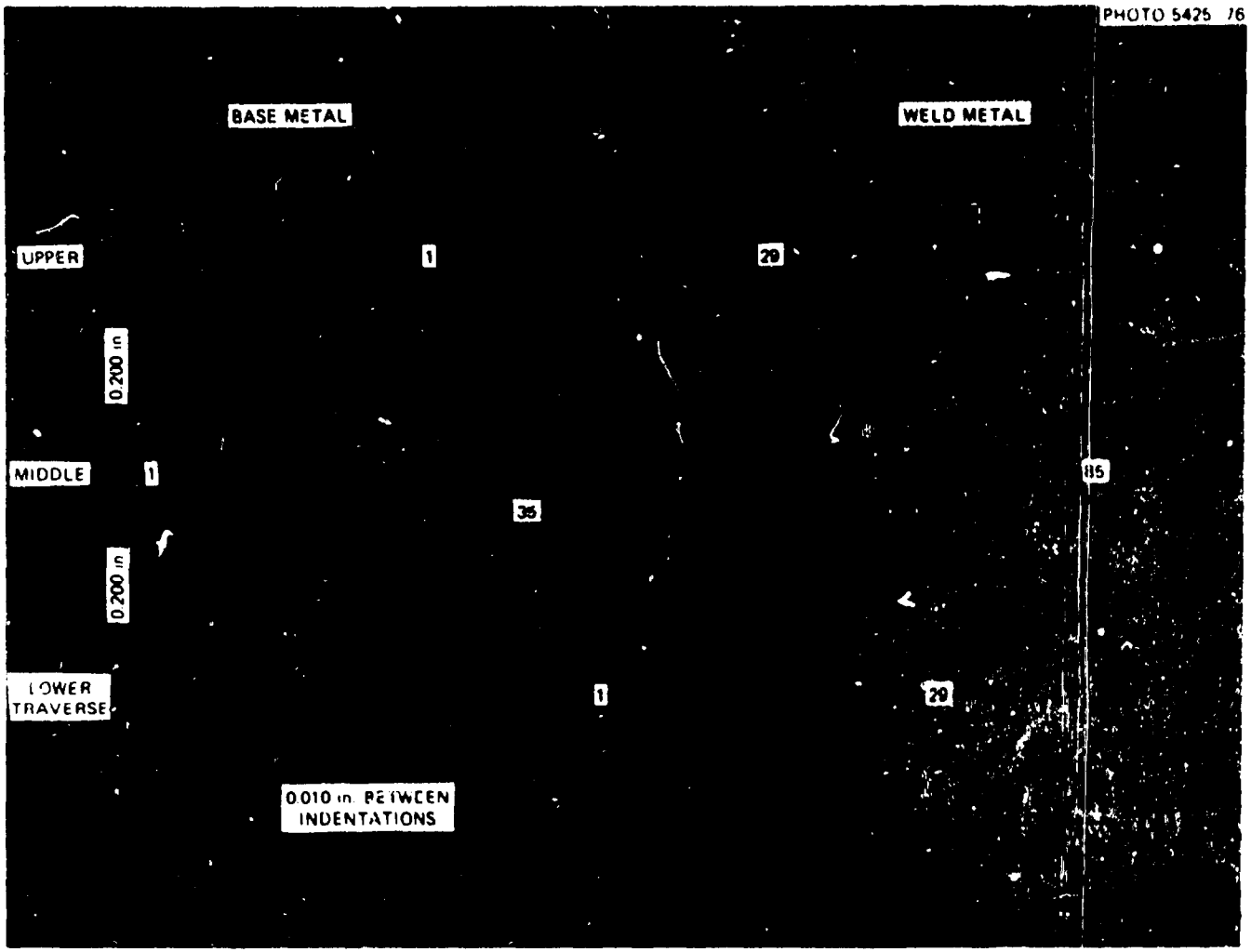

Fig. 3.20. Location of diamond pyramid hardness indentations across the heat-affected zone and adjacent areas of a cross section of the weld repair of the V-9 prolongation. 5×. (1 in. = 25.4 mm.)

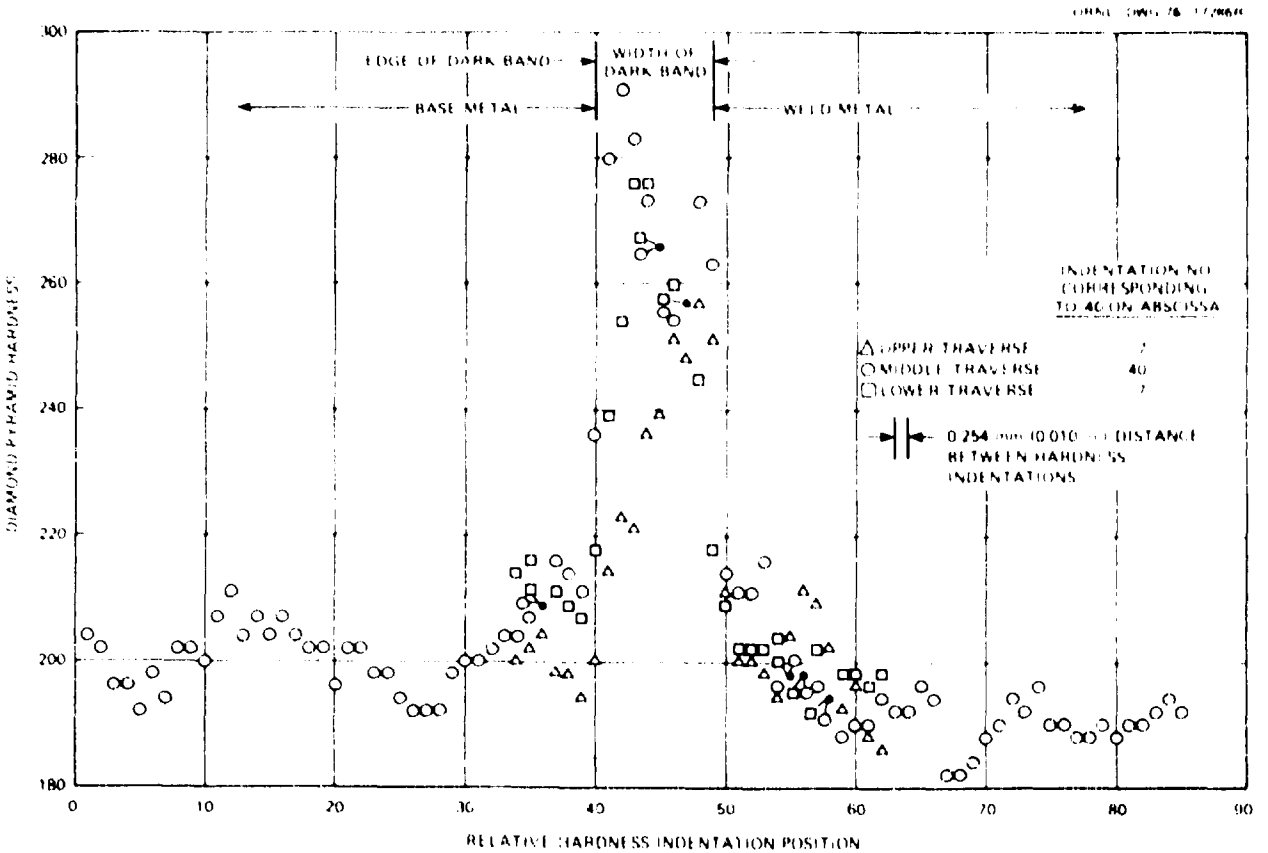

Fig. 3.21. Hardness traverses of the heat-affected zone and adjacent areas of a cross section of the weld repair of the V-9 prolongation. Positions of hardness indentations of the three traverses have been normalized so that the indentation at base metal edge of the dark etched band in each traverse is assigned to position 40 on the abscissa.

Charpy specimens oriented perpendicular to the fusion plane were cut from part B of the prolongation in the vicinity of the hardness measurements. The blanks were notched and fatigue-precracked in or near the HAZ so that the crack would run in the welding direction. The results of six static and dynamic tests are presented in Table 3.2. The broken halves of the specimens, re-etched to show the fracture path relative to the weld location, are shown in Figs. 3.22 and 3.23. These photographs show that, for specimens precracked in the HAZ, the crack advanced away from the original crack plane and into weld metal. For specimens in which the precrack resided in weld metal, the crack extensions remained in that material. It appears that the repair weld metal and HAZ are as tough as, or tougher than, the V-7 base metal.

Table 3.2. Static and dynamic fracture toughness values for material in and near the HAZ of the half-bead weld repair of the V-9 prolongation; data obtained from precracked Charpy specimens tested at 21°C (70°F)

Notch location	Fracture toughness	
	Static, K_{Icd} [$MN \cdot m^{-3/2}$ (ksi$\sqrt{in.}$)]	Dynamic, K_{Idd} [$MN \cdot m^{-3/2}$ (ksi$\sqrt{in.}$)]
HAZ	316 (288)	459 (418)
Weld metal–HAZ	271 (247)	319 (290)
Weld metal–HAZ	264 (240)	380 (346)

3.3.2 Residual stresses

Measurements were made on both the vessel and the cylindrical prolongation used for welding procedure qualification in order to estimate the magnitude of the residual stresses induced by the weld repair.

The initial set of residual stress measurements was made by using weldable strain gages attached to the weld qualification piece and to vessel V-7. These gages were monitored during the welding operation, and estimates of the residual stresses induced by the repairs were made from the change in strain between the start and completion of the repair. The

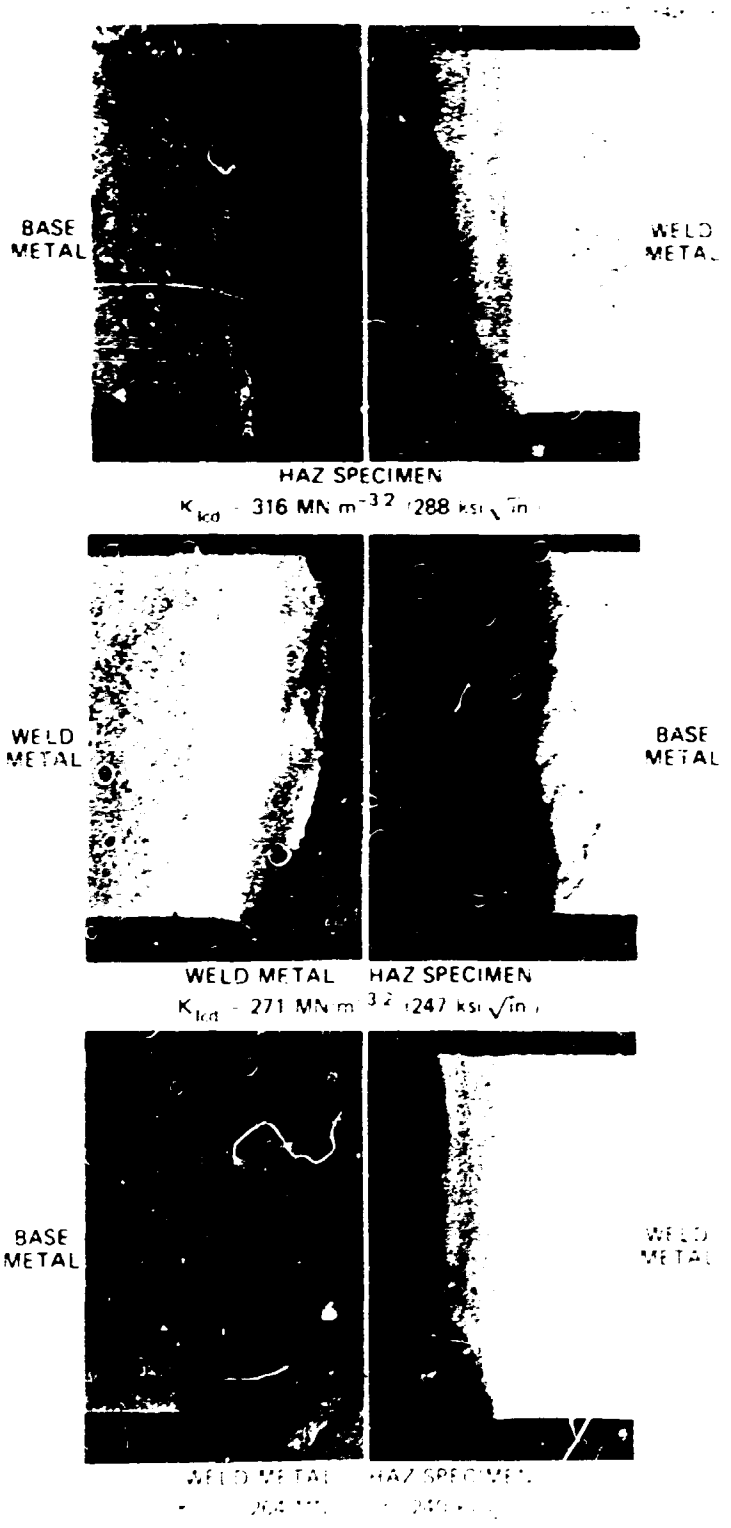

Fig. 3.22. Macrophotographs showing the fracture path of statically tested precracked Charpy V specimens from the HAZ of the weld repair of the V-9 prolongation.

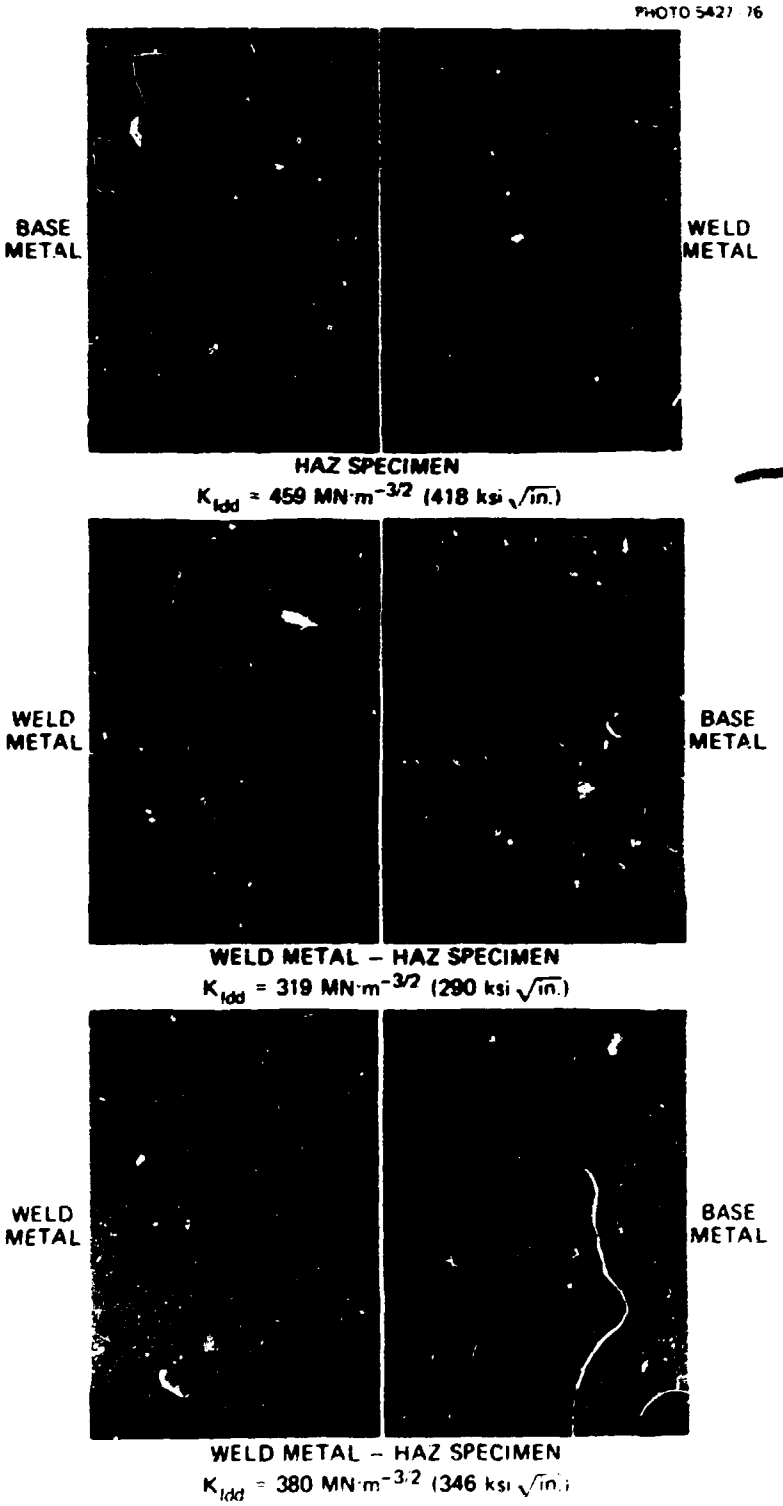

Fig. 3.23. Macrophotographs showing the fracture path of dynamically tested precracked Charpy V specimens from the HAZ of the weld repair of the V-9 prolongation.

locations of the strain gages near the weld cavity on the qualification piece are shown in Fig. 3.5; in addition, gages 19 and 20 were placed circumferentially on the outside and inside surfaces, respectively, of the cylinder 180° from the cavity. Four gages, numbered 3, 4, 7, and 8 were placed on the outside surface of vessel V-7 at locations, relative to the nearest edges and centerlines of the cavity, identical to those of gages 3A, 4A, 7A, and 8A on the qualification piece. The orientations of the gages were also identical to those on the qualification piece. Strains measured at various states during the repair are shown in Table 3.3.

Table 3.3. Microstrain with temperature (°F) of strain gage during weld repair of V-7 and V-9 prolongation

Gage No.	Step No.[a]						
	1	2	3	4	5	6	7
				Vessel			
3	0	−651 (450)	−1456 (475)	−1498 (525)	−604 (87)		
4	0	−1134 (450)	+106 (475)	+25 (525)	+1216 (87)		
7[b]	0	−898 (400)					
8	0	−596 (400)	+259 (465)	213 (515)	+838 (85)		
				Prolongation			
7A	0	−872 (365)	−2141 (383)	−2338 (500)	−1044 (78)	−1206 (90)	−1187
8A	0	−902 (365)	+90 (383)	−185 (500)	+787 (78)	+822 (90)	811
3A	−7	+267 (360)	−914 (383)	−832 (502)	−1110 (78)	−1083 (86)	−1070
4A	−3	+97 (360)	+1507 (383)	+1443 (502)	+1327 (78)	1291 (86)	1275
5	+4	+239 (360)	−580 (388)	−505 (502)	−760 (78)	−753 (86)	−721
9	+3	+243 (360)	+637 (385)	+564 (495)	+172 (78)	+283 (92)	273
12	−3	+37 (380)	−25 (398)	−57 (502)	+29 (78)	+15 (85)	92
13	−3	−85 (380)	−66 (398)	−40 (502)	+48 (78)	+156 (85)	40
19	−3	−53 (190)	−46 (232)	−55 (285)	+11 (78)	−51 (90)	−69
20	−8	+239 (180)	+294 (230)	+365 (282)	+63 (78)	+231 (90)	207

[a]Steps:

1. Prior to the application of preheat (reading taken at room temperature).
2. After the vessel reaches the specified preheat range, but before any welding is started.
3. After all welding was completed, but prior to the postweld heat treatment.
4. After the postweld heat treatment, but before cooling to room temperature.
5. After the weld repair temperature was at ambient temperature for a minimum of 2 hr, but before removal of bracing and restraints.

6, 7. After removal of all bracing and restraints.

[b]Damaged gage.

The strain indications used in estimating induced stresses were observed with the vessel and qualification piece at room temperature (steps 1 and 7, Table 3.3). The resulting estimates are listed in Table 3.4.

Table 3.4. Strains and stresses induced by the weld repair operation

Gage	Orientation	Microstrain	Stress[a,b] (MPa)		
			σ_A	σ_C	σ
		Vessel V-7			
3	Axial	−642	−67		
4	Circumferential	1151		211	
8	Axial	817			163
		Weld qualification piece (V-9 prolongation)			
3A	Axial	−1063	−151		
4A	Circumferential	1278		212	
5	Axial	−725			−145
7A	Circumferential	−1187		−207	
8A	Axial	811	102		
9	Axial	270			54
12	Axial	95	24		
13	Circumferential	43		15	
19	Circumferential	−66			−13
20	Circumferential	215			43

[a] For gage pairs: $\sigma_A = \frac{E}{1-\nu^2}(\varepsilon_A + \nu\,\varepsilon_C)$; $\sigma_C = \frac{E}{1-\nu^2} \times (\varepsilon_C + \nu\,\varepsilon_A)$. For isolated gages: $\sigma = E\varepsilon$.

[b] 1 MPa = 145.038 psi.

A second set of residual stress measurements was made on the V-9 prolongation by means of the hole-drilling technique. The cylinder was sectioned by sawing so as to expose the two planes of symmetry of the weld on which measurements were to be made. Ten strain gage rosettes were attached to the section to be studied (part A, shown in Fig. 3.5)

before any cuts were made. The dimensions of part A and the rosette locations are shown in Fig. 3.24.

The strain changes measured by the rosettes were used to estimate the axial and circumferential stresses throughout the body that are relieved by cutting. A stress distribution that is linear in Z and quadratic in X and Y was assumed; X, Y, and Z are defined in Fig. 3.24. The quadratic form of X and Y presumes two planes of symmetry bisecting the weld repair, which is suggested by the work reported by Ferrill, Juhl, and Miller.[9] The inferred stress distributions were then used to adjust the residual stresses measured on the cut sections through the weldment.

A subcontract was let to Westinghouse Research Laboratories to make 40 residual stress measurements on the part of the prolongation shown in Fig. 3.24. The two faces that bisect the weld were prepared by using the

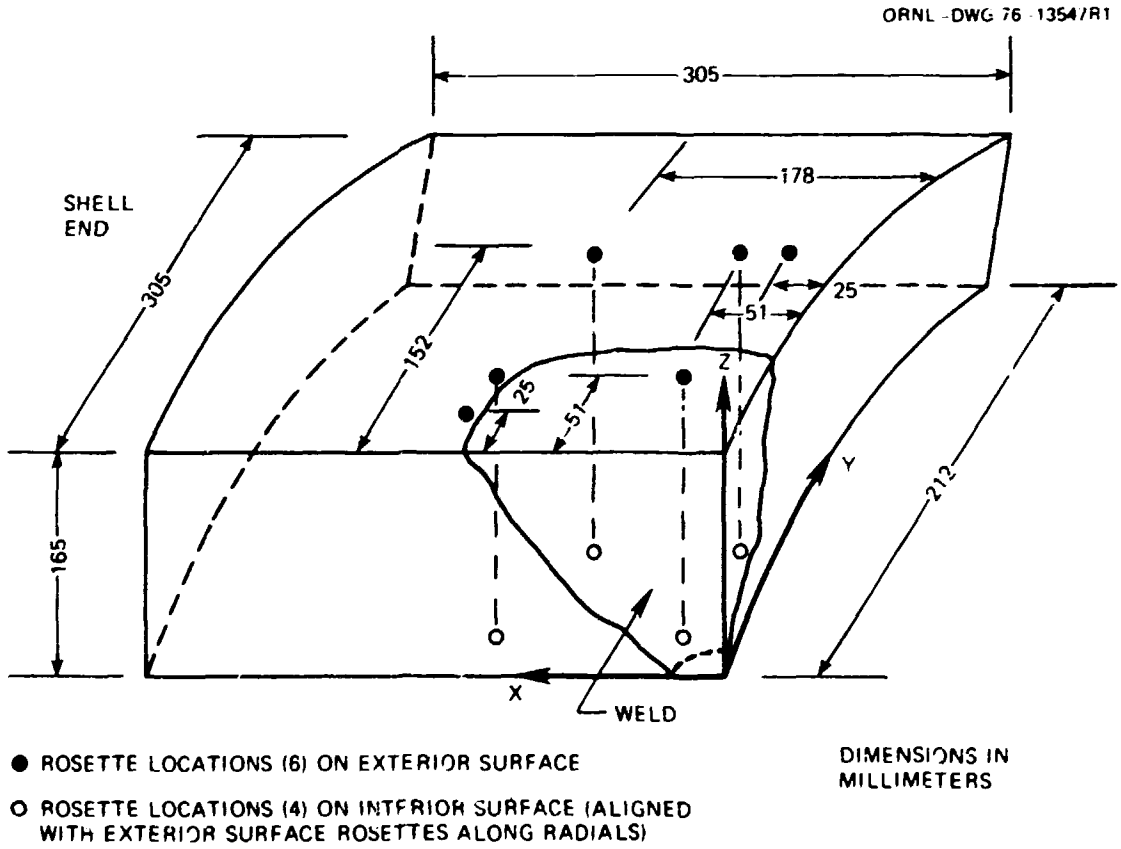

Fig. 3.24. Schematic of section removed from weld procedure qualification piece for residual stress measurements (1 mm = 0.03937 in.).

"gentle" grind technique suggested by Nowikowski, Maranchik, and Field.[10] This technique minimizes surface residual stresses induced from the cutting operation. The work at Westinghouse was performed under the direction of A. J. Bush. The residual stresses were determined from hole-drilling-type measurements for which an air-abrasive device was used to machine the holes.[11] Elastic relaxation stresses resulting from cutting the cylinder were calculated for each location at which a residual stress was measured, and the inverses of the relaxation stresses were added to the directly measured residual stresses. The resulting best estimates of the original residual stresses that existed through the thickness of the weld repair before the cylinder was cut are shown in Figs. 3.25 and 3.26. Also shown

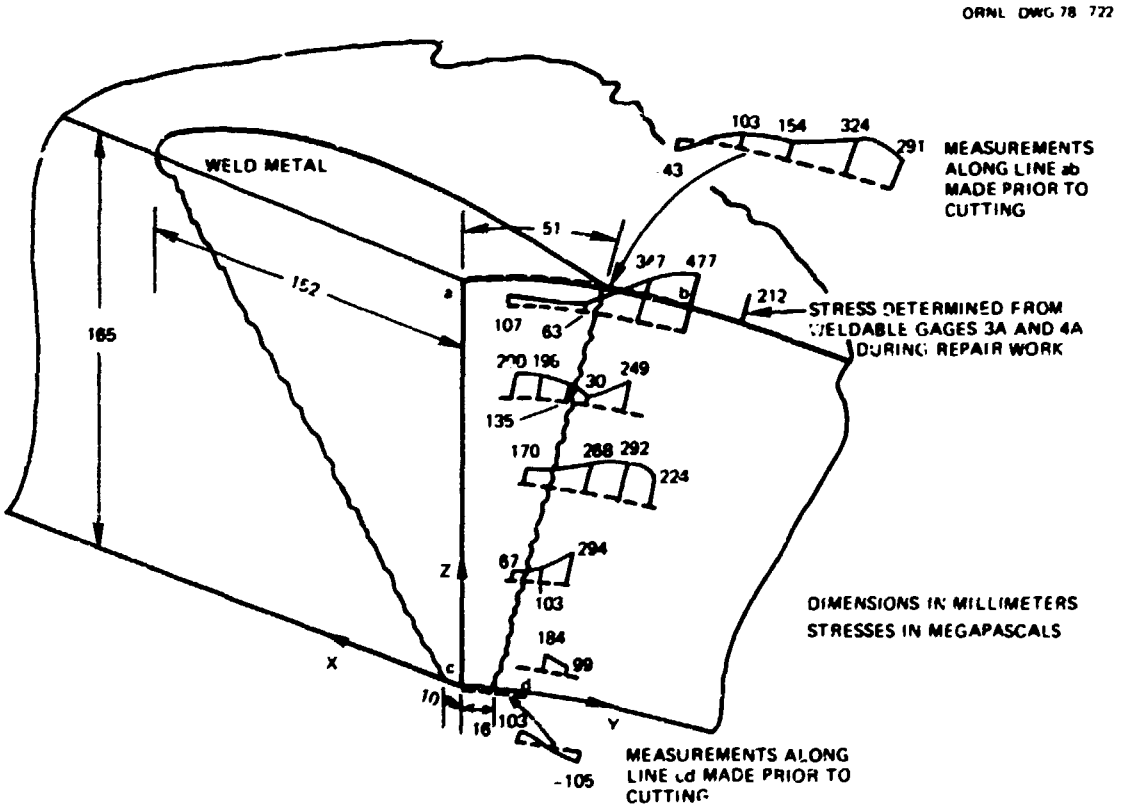

Fig. 3.25. Circumferential residual stresses in the V-9 prolongation weldment made for qualification of the welding procedure used in repair of vessel V-7. Values on the cut plane (Y–Z) have been adjusted to account for the relief of stresses during cutting. (1 mm = 0.03937 in.; 1 MPa = 145 psi.)

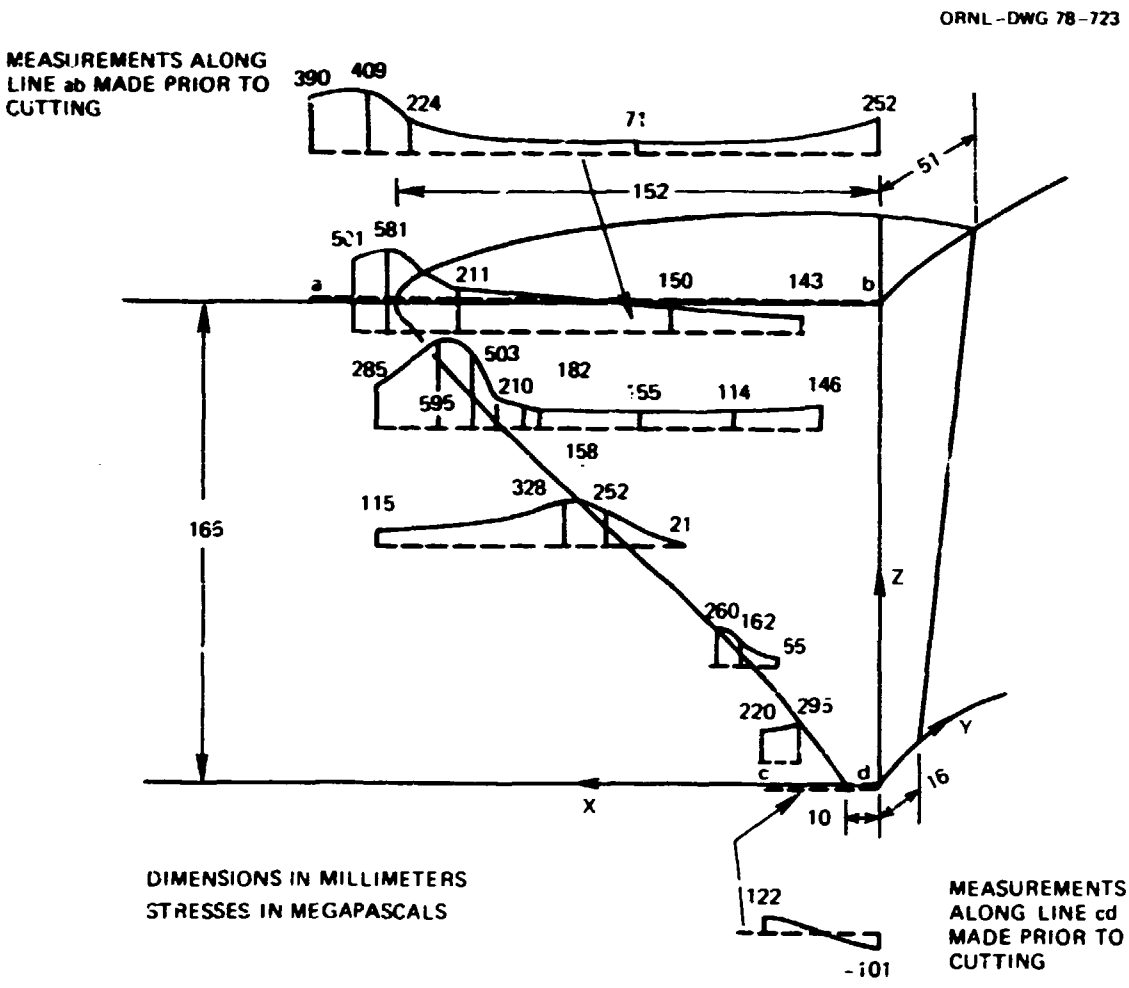

Fig. 3.26. Axial residual stresses in the V-9 prolongation weldment made for qualification of the welding procedure used in repair of vessel V-7. Values on the cut plane (X-Z) have been adjusted to account for the relief of stresses during cutting. (1 mm = 0.03937 in.; 1 MPa = 145 psi.)

in these figures are results of surface measurements made before the cylinder was cut. Additional details of the residual stress measurements are presented in Ref. 12.

3.4 Flaw Preparation

The repaired vessel, designated V-7A, was flawed in Union Carbide Corporation-Nuclear Division (UCC-ND) facilities at Oak Ridge by the same means and with the same flaw design as used in preparing vessel V-7

for testing.[2] The location of the V-7A flaw in base plate material is shown in Fig. 3.3. The flaw consists of a flat-bottom machined slot extended to a sharp edge by hydrogen charging an EB weld bead that had been laid along the base. The slot was milled in a radial-axial plane of the test cylinder to the trapezoidal contour shown in Fig. 3.4 by a Giddings and Lewis horizontal boring mill.

EB welding was performed in the large Sciaky weld chamber used in the preparation of vessel V-7 for the original test. The resulting EB weld bead in the V-7A notch, shown in Fig. 3.27, was laid in three segments, the deepest segment being laid first. The welding parameters used previously for the V-7 flaw to obtain and EB weld crack depth of 7.9 mm (5/16 in.) were again employed for the V-7A flaw. They are as follows:

Power: 40 kV with 180 mA on horizontal surface (deepest portion of notch) and 185 mA on the two slopes

Speed of beam: 2.3 m/min (90 in./min)

Vacuum chamber pressure: 0.67×10^{-3} Pa (5×10^{-6} torr)

Average bead cross section: surface width 3 mm (1/8 in.); depth of penetration 7.9 mm (5/16 in.)

In the machined notch of vessel V-7A, a high magnetic flux density, up to 6×10^{-3} T (60 G), was encountered. This condition had not been experienced in vessel V-7 preparations, for which flux densities were about 3×10^{-4} T (3 G). It is believed that the polarity (negative ground) of the direct current arc welding electrode and the location of the attachment of the ground during repair welding account for the magnetization observed.

EB welding experiments on magnetized prototype test pieces had provided earlier indications that high and nonuniform magnetic flux density in the notch to be welded would cause significant deflection of the electron beam. Under such conditions, the deflected beam is not normal to the bottom surface of the groove. Severe transverse beam deflection can also cause attachment of the beam to the side wall of the machined groove. It is also possible that a longitudinally deflected beam will lose sharp focus, which adversely affects depth of penetration. Earlier experimentation had indicated beam distortion problems with magnetic flux densities of 5×10^{-4} T (5 G) or more.

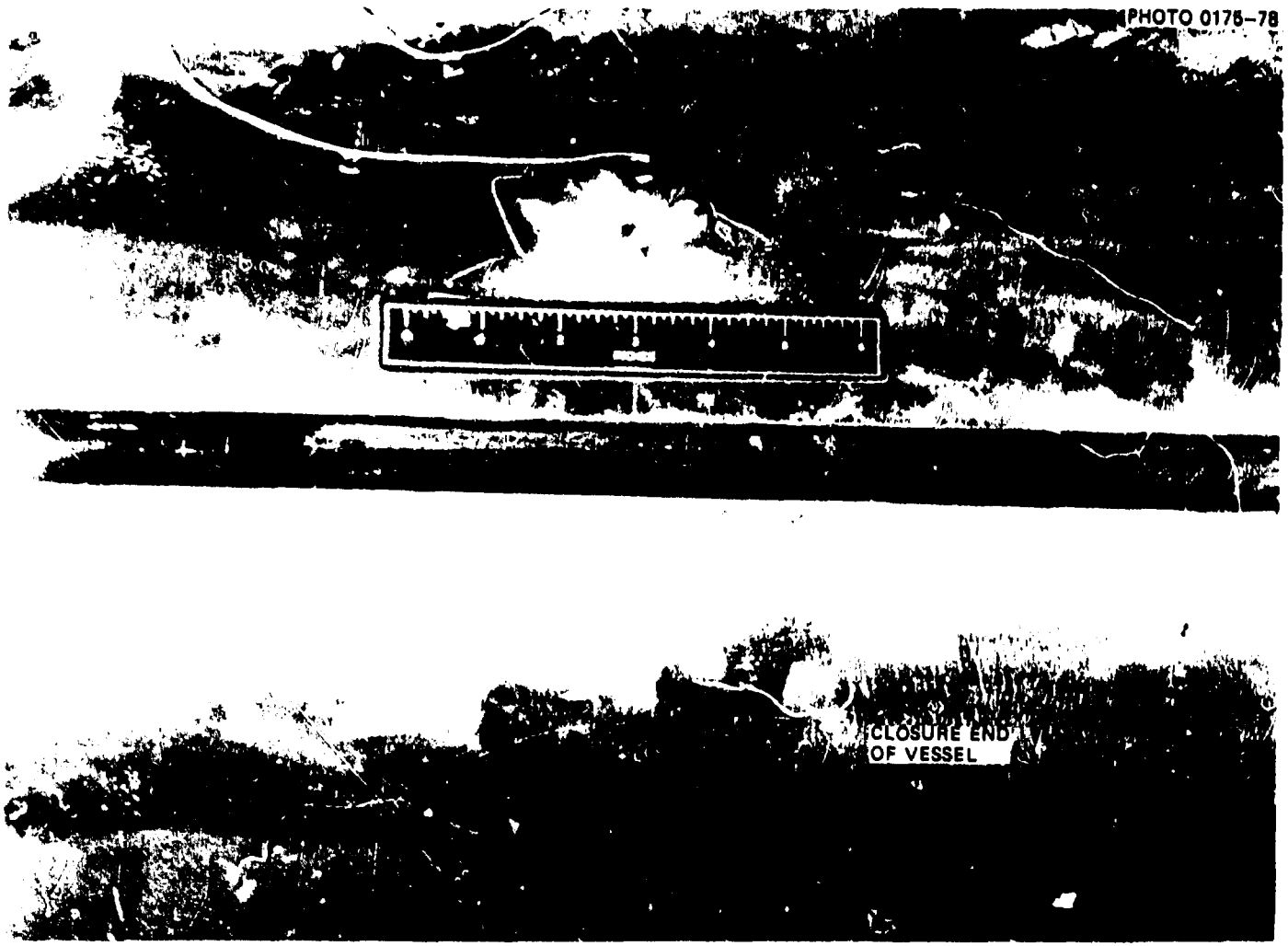

Fig. 3.27. Pretest photograph of notch in vessel V-7A showing the electron-beam weld bead along the base of the notch.

Many attempts were made to degauss the vessel and reduce the residual magnetic field before placing the vessel into the weld chamber. Both alternating current and direct current degaussing procedures were used. Results with direct current were highly unpredictable; flux increases were noted on some occasions. Effective degaussing was achieved by wrapping a 150-m (500-ft) No. 2 weld cable in continuous coils in three perpendicular planes about the vessel. Alternating current voltages were applied to generate up to 250 A. Magnetic flux densities in the vicinity of the vessel slot were reduced to 25% of initial values, or to about 15×10^{-4} T (15 G) maximum and about 8×10^{-4} T (8 G) average. Two 0.1-T (1000-G) permanagnets were used during EB welding for flux trimming so as to keep the weld beam centered along the longitudinal axis of the notch.

After the EB welding was completed, the exposed weld bead was hydrogen charged by the process previously used[2] until a sharp crack was formed around the entire periphery of the notch. In this process, the surface of the notch, except for the bead, is masked by an insulating material. The notch is then filled with an electrolyte, a 10% aqueous solution of H_2SO_4. A current of about 8×10^{-4} A/mm^2 of exposed weld bead is passed through the solution in order to release hydrogen at the weld bead. The crack gradually formed along the entire bead over a period of about 8.5 hr of charging.

3.5 Leak-Retarding Patch

As discussed in Section 2.2 and shown in Fig. 2.3, the pressure decay in an intermediate test vessel after a small rupture develops is sufficiently rapid that slowly developing changes at the time of rupture would be inhibited by the drop in pressure. One of the measures adopted for enhancing the capability of the testing system to record the behavior of a vessel under sustained load was a leak-retarding membrane, or patch, attached to the inside surface of the test vessel in the vicinity of the prepared flaw.

The patch concept introduced two complications to the test plan. First, it was desired to place several strain gages and ultrasonic transducers on the inside surface of the vessel near the flaw, as was done for

the V-7 test.[2] The patch would have to accommodate these devices or they would be eliminated. Initial attempts to design a patch device that would house ultrasonic transducers and their electrical penetrations were discontinued for lack of confidence that a reliable design could be proven within a reasonable time. Furthermore, preliminary trials by K. K. Klindt and his group to locate a buried crack tip with the ultrasonic transducer mounted on the cracked side of the specimen (corresponding to the outside of the notch in V-7A) were promising. The patch development then shifted to the use of a thin membrane fillet-welded at the edge to the inside of the vessel.

The second complication of using a leak-retarding device is the problem of reliably determining whether the wall of the vessel has ruptured and, if it has, the precise time of rupture. If the patch performs as desired, there is neither leakage nor pressure drop to mark the occurrence of vessel rupture. An instrumented patch pressurization system, for which Fig. 3.28 is a simplified schematic, was designed and tested to indicate vessel rupture.

The general scheme is to maintain the pressure beneath the patch (i.e., between the patch and the inside surface of the vessel) at the same

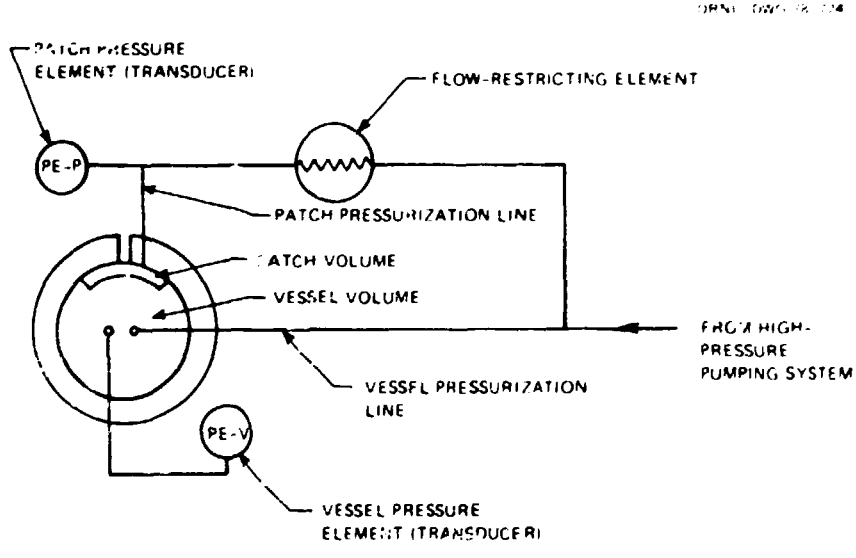

Fig. 3.28. Simplified schematic diagram of the patch pressurization system for vessel V-7A.

pressure as that throughout the vessel as long as the vessel wall is intact. The pressures in the vessel and in the system communicating with the volume beneath the patch are measured with a flow restriction between the points of measurement. When the vessel ligament ruptures, the pressure in the patch system will drop rapidly, provided there is adequate communication between the point of rupture and the patch pressurization system.

The patch is a 406 × 610 × 1.59 mm (16 × 24 × 1/16 in.) sheet of type 304L stainless steel rolled to conform to the inside surface of the vessel and welded by the tungsten–inert gas process around the edge with INCO 82 filler (see Figs. 3.29 and 3.30). The patch pressurization line is attached to the vessel by a 6.4-mm (1/4-in.) type 316 stainless steel high-pressure nipple installation as shown in Fig. 3.31.

The design of the patch and pressurization system was based upon a series of mockup tests performed to determine the performance of each element of the system and the complete system. Details of this work, which was necessary to ensure the integrity of the patch and the adequacy of the leak-detection system, are described in Appendix F.

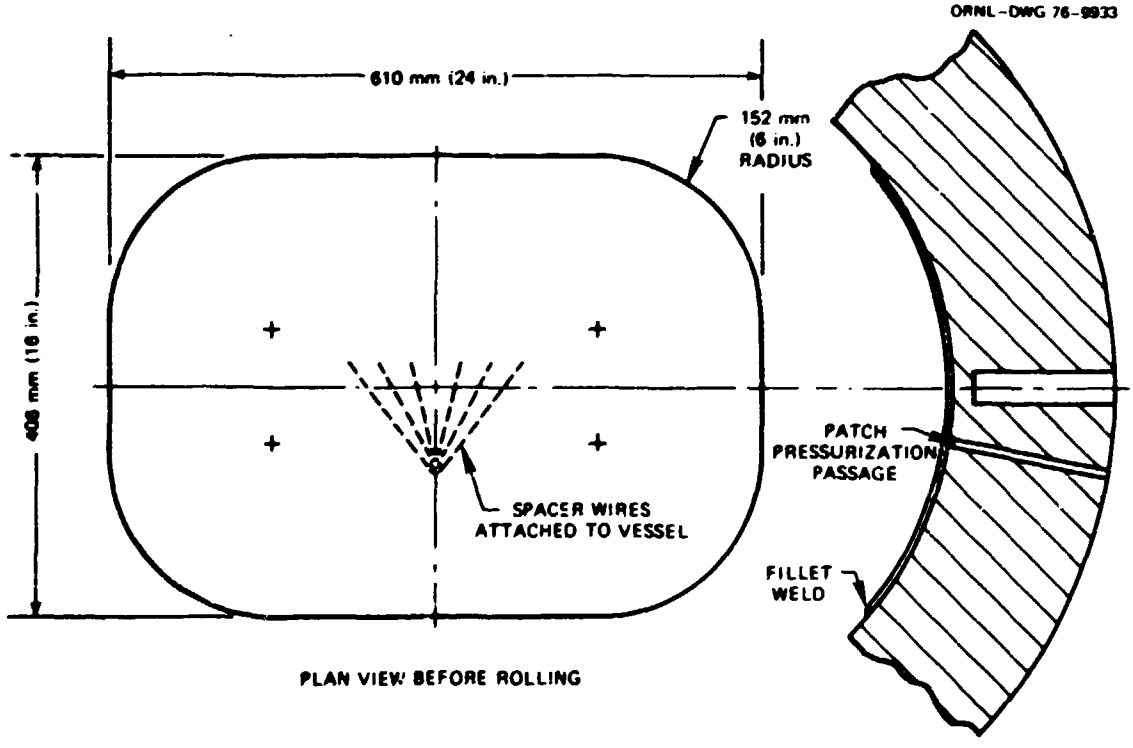

Fig. 3.29. Design of leak-retarding patch for vessel V-7A.

Fig. 3.30. Stainless steel patch installed in vessel V-7A.

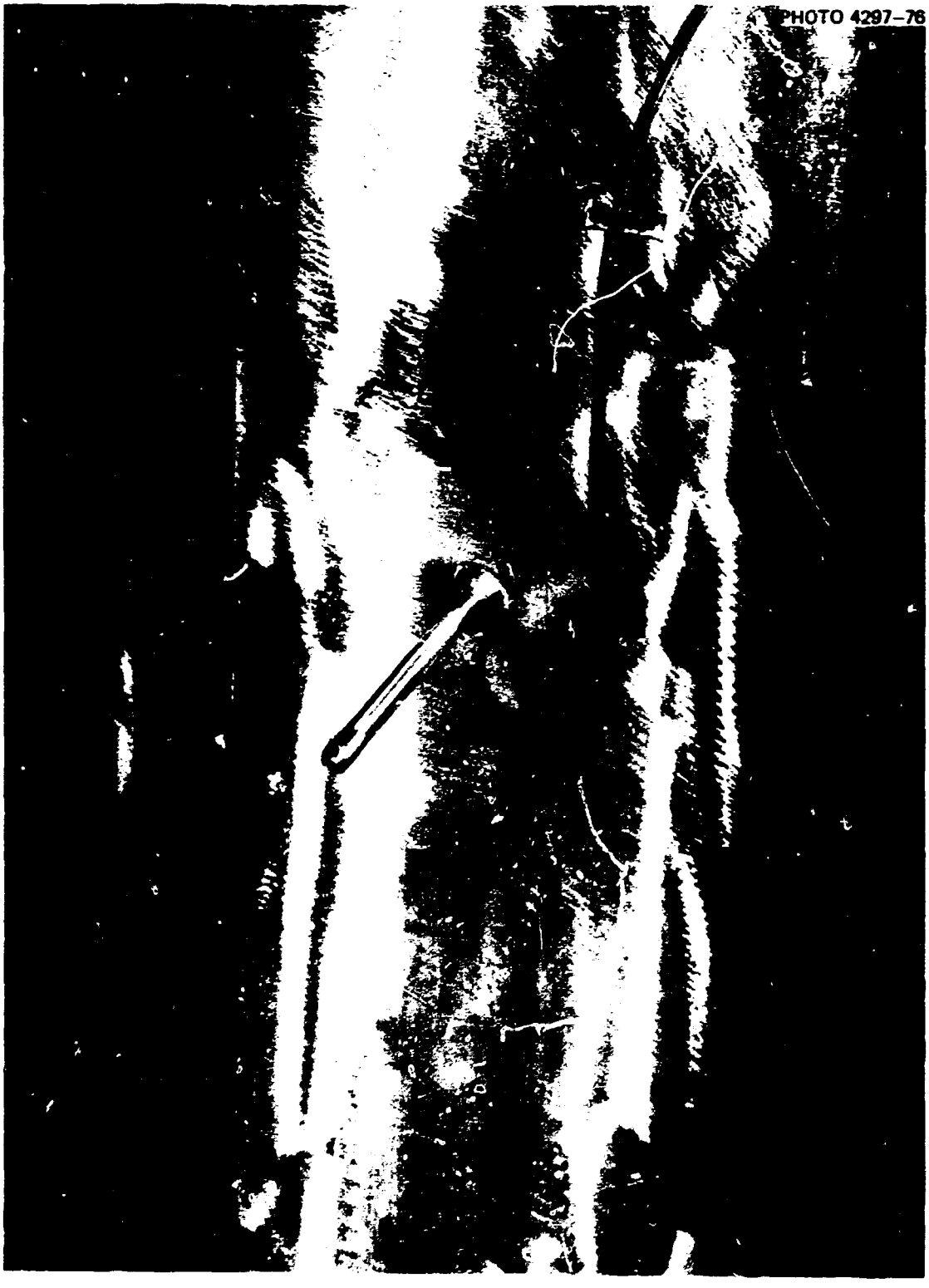

Fig. 3.31. Patch pressurization system nipple-welded to vessel V-7A.

References

1. C. E. Childress, *Fabrication and Mechanical Test Data for the Four 6-Inch-Thick Intermediate Test Vessels Made from Steel Plate for the Heavy Section Steel Technology Program*, Documentary Report 5, ORNL/TM-5074 (January 1976).

2. J. G. Merkle et al., *Test of 6-in.-thick Pressure Vessels. Series 3: Intermediate Test Vessel V-7*, ORNL/NUREG-1 (August 1976).

3. "Rules for Inservice Inspection of Nuclear Power Plant Components," *ASME Boiler and Pressure Vessel Code*, Section XI, 1974 edition with Summer and Winter 1974 addenda, American Society of Mechanical Engineers, New York.

4. W. D. Goins and D. L. Butler, *Weld Repair of Heavy Section Steel Technology Program Vessel V-7*, EPRI NP-179, (ORNL/Sub/88242-76/1), Combustion Engineering Inc., Chattanooga, Tenn. (August 1976).

5. S. T. Walker (ed.), *Welding Handbook*, 6th ed., Section 3A, pp. 43.10 and 42.56, American Welding Society, 1970.

6. C. E. Childress, *Fabrication History of the First Two 12-in.-Thick ASTM A-533 Grade B, Class 1 Steel Plates of the Heavy Section Steel Technology Program*, Documentary Report 1, ORNL-4313 (February 1969).

7. D. A. Canonico and R. G. Berggren, *Tensile and Impact Properties of Thick-Section Plate and Weldments*, ORNL/TM-3211 (January 1971).

8. *Metals Handbook, Vol. 1, Properties and Selections of Metals*, 8th ed., p. 1234, American Society for Metals, 1961.

9. D. A. Ferrill, P. B. Juhl, and D. R. Miller, "Measurement of Residual Stresses in a Heavy Weldment," *Weld. J. (Miami), Suppl.*, 45(11), 504S–514S (1966).

10. L. J. Nowikowski, J. Maranchik, Jr., and M. Field, "Distortion and Residual Surface Stress in Grinding and Milling of High Strength Steels," Paper 340L, presented at 1961 SAE National Aeronautic Meeting, New York, N.Y., April 4–7, 1971; a condensed version appears in *SAE J.* 69(8): 41–45 (August 1961).

11. A. J. Bush and F. J. Kromer, "Simplification of the Hole-Drilling Method of Residual Stress Measurement," *ISA Trans.* 12(3), 249–59 (1973).

12. G. C. Smith and P. P. Holz, Repair Weld Induced Residual Stresses in Thick-Walled Steel Pressure Vessels, ORNL/NUREG/TM-153 (to be published).

4. TEST FACILITY DESIGN AND PERFORMANCE

4.1 Introduction

The decision to test a large vessel pneumatically introduced several problems that had not been encountered in the previous hydraulic intermediate vessel tests. Suitable pressurizing gas and equipment had to be selected. A new test site had to be developed; and the design of the electrical, mechanical, and instrumentation systems had to be reexamined and altered to meet the new test conditions.

The test plan and facility design developed at the inception of the intermediate vessel test program were the basis for many of the pneumatic test facility design requirements. The design requirements for the existing test facility in the K-25 Power House had been carefully determined for hydraulic testing.[1] The test cell was designed to contain fragments produced in a hydraulic test, but the stored energy in a pneumatic test is far greater than the energy this facility can accommodate. The stored energy in the pneumatic fluid at 140 MPa (20 ksi) was estimated conservatively to be about 200 MJ (1.5×10^8 ft-lb), about 80 times the energy stored in the same volume of water at that pressure.

In view of the unusual safety requirements imposed by the large potential energy release, considerations of economics led to the decision to look for a test site outside the Oak Ridge area that was already developed and suitable for testing explosives. The Naval Surface Weapons Center (NSWC) was chosen because it had such a site with the particular facilities and pressurization equipment needed for the pneumatic test.

The use of a remote site necessitated that the vessel be prepared for testing and all of the associated heating equipment, instrumentation, and data-acquisition equipment be installed and tested before shipment from ORNL. The instrumented vessel and the data-acquisition system (DAS) also had to be protectively enclosed for shipment by common carrier.

Completion of as many preparations as practicable in Oak Ridge appeared to be the most economical procedure for attaining a high level of confidence that the testing systems would perform satisfactorily. The equipment used in instrumenting the vessel and in preparing and installing

seals is specialized; therefore, it was not expected that emergency repairs or adjustments could be effected at the test site without major delays. The computer-controlled data-acquisition system (CCDAS), for which there was no satisfactory redundancy, was of such vital importance that specialists in the use and repair of that equipment were included in the test team and kept on standby for troubleshooting and emergency repairs.

The pneumatic sustained-loading conditions made it desirable to include some instrumentation and data-recording equipment not used previously. Accordingly, instrumentation was installed to measure crack propagation velocity in case of burst and to record the associated transient pressures and strains. A magnetic tape recorder furnished by the NSWC was used for recording data for intermediate transients; fast digital recording apparatus, also furnished by NSWC, was included for recording a very fast burst.

4.2 Test Site

The test facility for vessel V-7A is located at the Explosives Experimental Area of the Dahlgren (Virginia) Laboratory of the NSWC. The Oak Ridge Operations Office of the Energy Research and Development Administration (ERDA)* entered into an interagency agreement† with the NSWC to provide the following facilities and services:

1. a site with protective personnel shelters, weather enclosure for test vessel, and utilities for the support of ORNL test equipment;
2. a high-pressure nitrogen pressurization system;
3. equipment and personnel for handling the test vessel assembly and the ORNL data-acquisition system (DAS) trailer;
4. magnetic tape data-recording equipment;
5. high-speed digital recording apparatus;

---

*The functions of the Energy Research and Development Administration have since been transferred to the Department of Energy.

†Interagency Agreement ERDA No. EY-76-I-05-4971 [formerly E-(40-1)-4971].

6. supplementary video equipment;
7. the development and supervision of a safety plan for a hazardous test.

The test field was laid out as shown in Fig. 4.1. An overall view of the site is shown in Fig. 4.2. The vessel was enclosed in a plywood and wood frame shelter to protect personnel and equipment from rain during final preparations and testing. The vessel was separated from the manned facilities by a distance of about 100 m (330 ft). The NSWC determined this to be a reasonable distance for protection of personnel in the event of a burst, which NSWC estimated realistically would be equivalent to the detonation of about 13 kg (30 lb) of TNT.

For safety, all personnel were required to stay within the sheltered areas (Fig. 4.1) whenever the vessel pressure was high enough to be considered hazardous (i.e., above design pressure). Movement through the emergency access route was forbidden at high pressure except as permitted by the range safety officer. The NSWC maintained surveillance over and excluded people from contiguous areas of the test site and the Potomac River during high-pressure testing.

ORNL and subcontractor personnel were stationed in two locations during high-pressure testing: (1) the DAS trailer and (2) the bunker. These facilities, shown in Figs. 4.2, 4.3, and 4.4, were provided with

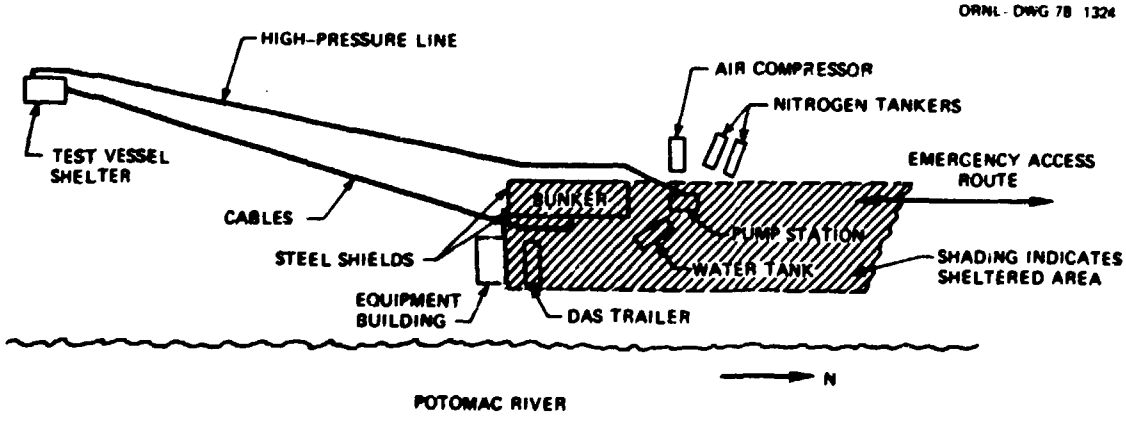

Fig. 4.1. Arrangement of the Dahlgren, Virginia, site for the pneumatic test of vessel V-7A.

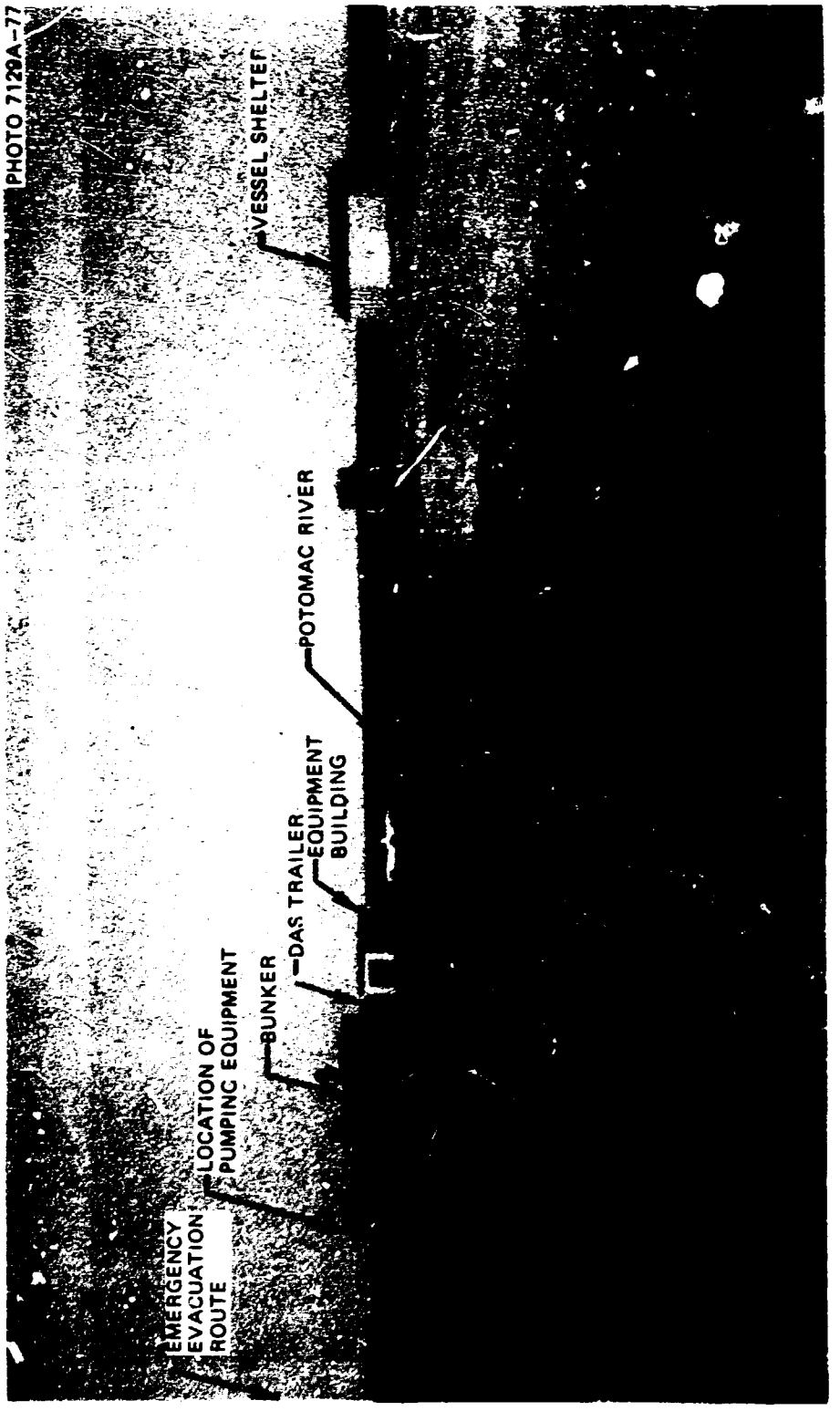

Fig. 4.2. Easterly view of V-7A test site.

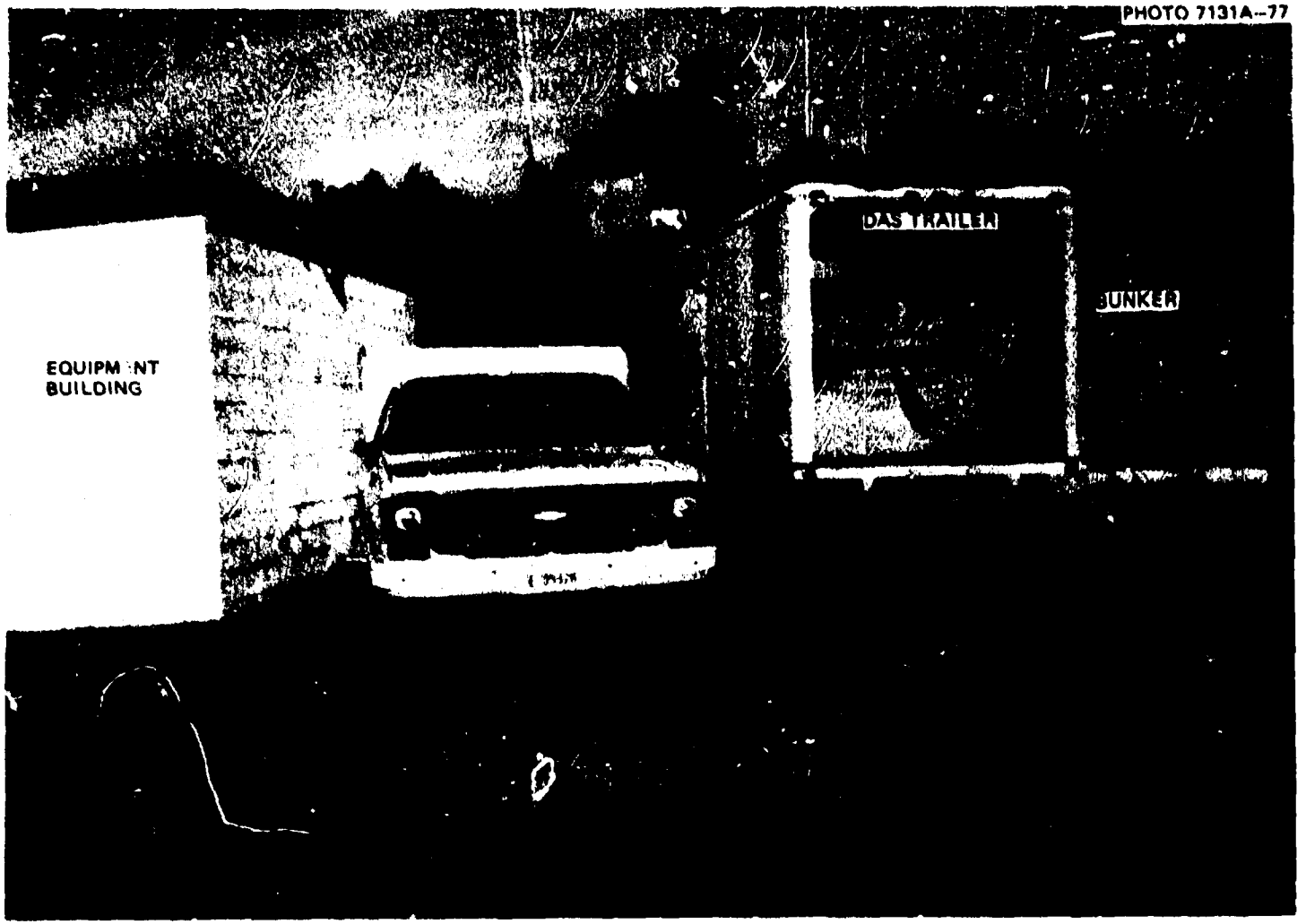

Fig. 4.3. The ORNL data-acquisition system (DAS) trailer parked beside the equipment building and bunker at the Dahlgren site.

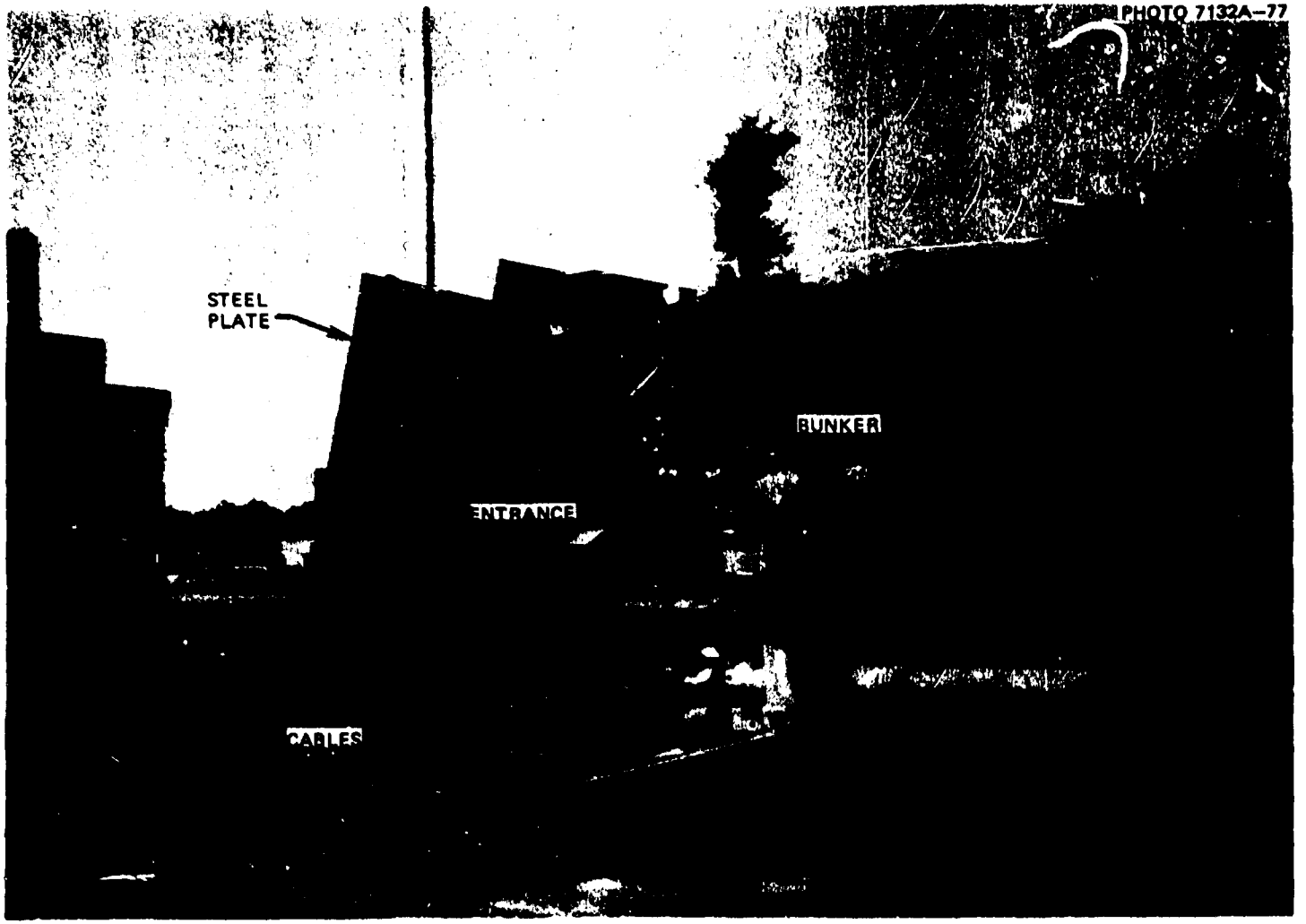

Fig. 4.4. The protective bunker at the Dahlgren site of the V-7A test.

steel, concrete, or earthen shielding against projectiles from the vessel. A steel plate was placed on top of the DAS trailer to intercept projectiles with a high trajectory, while the concrete block equipment building provided a shield against those with a flat trajectory. The NSWC operator of the pressurization equipment was shielded by the bunker, a portable steel shed, and a steel plate placed over the operating station.

High-pressure tubing was routed from the pumping station to the vessel away from inhabited areas and was also separated from the electrical and data cables to minimize the risk of damage. The tubing was staked down to inhibit whipping in the event of a failure. The vessel head was pointed away from the manned areas, since a large number of small fittings and the closure studs were potential projectiles. The axis of the vessel was pointed toward the manned area because it was assumed that the most likely direction of projection of fragments from the shell itself would be lateral. It was also thought possible that a leak through the flaw could be large enough to push the vessel off the test stand laterally.

4.3 Instrumentation and Data-Acquisition Systems

The instrumentation plans for vessel V-7A were adapted from the original (hydraulic) test of V-7 so that the original measurements could be matched with comparable measurements in the sustained-load test. Two additional types of data were required: (1) strain behavior or the Section XI weld repair zone and (2) dynamic response to pneumatic loading. in the event the vessel burst. Instrumentation sensors mounted directly on vessel V-7A consisted of 25 thermocouples, 84 strain gages, 2 crack propagation gages, 6 crack-opening displacement (COD) gages, 4 ultrasonic transducers for sensing the location of the crack tip, and 2 arrays of acoustemission (AE) transducers.

The inclusion of a patch in V-7A prevented the placement of strain gages at several important locations used in the V-7 test; it also precluded the mounting of ultrasonic transducers on the inside surface for direct determination of the crack tip location. Ultrasonic transducers were, instead, situated outside the vessel, and crack tip location involved a double reflection off the inside surface of the vessel. To

partially compensate for the loss of strain measurements on the inside surface beneath the flaw, three additional COD gages were installed within the notch about 76 mm (3 in.) below the outside surface.

Additional strain gages were located on the inside and outside surfaces in the Section XI weld repair zone.

The data-acquisition system (DAS) was designed to measure and record, in addition to the slow changes in the vessel as pressure increased, the transient response of the vessel in the event the vessel burst. If the vessel had burst, the patch would not have remained intact very long; but the pneumatic fluid would have kept the pressure from decreasing as fast as in the V-7 hydraulic test. In order to take advantage of the opportunity to observe a possible burst, several features not previously used for intermediate vessel tests were included in the V-7A DAS: (1) crack propagation gages; (2) direct recording of selected strain gage data on magnetic tape; (3) strip chart recording of COD, strain, and crack initiation data; and (4) processing of all transient data by the CCDAS and recording of digitized data on magnetic tape.

The data-acquisition requirements were developed into plans for a transportable system, which was assembled and checked out at ORNL. The CCDAS and other instrumentation, conditioning circuitry, and amplifiers for gages and test data thermocouples were located in the DAS trailer, the plan for which is shown in Fig. 4.5. Test signals were transmitted to the trailer by eight cables deployed from the vessel test assembly (described in the next section). The main features of the DAS are given in Table 4.1, and a layout of all instrumentation on the vessel test assembly is shown in Figs. 4.6 and 4.7. Details of the instrumentation and DAS are given in Appendix D.

Crack propagation data were processed and recorded by five devices. The first break was detected by a trigger module, which produced a synchronizing signal recorded by the Ampex magnetic tape recorder, strip charts, and the CCDAS. The output of both crack propagation ladders was recorded by the CCDAS (adequate for slow propagation) and by the ERDAC equipment (for fast propagation). The ERDAC is capable of continually recording data at the rate of 1 word per microsecond, with a total capcity of 4478

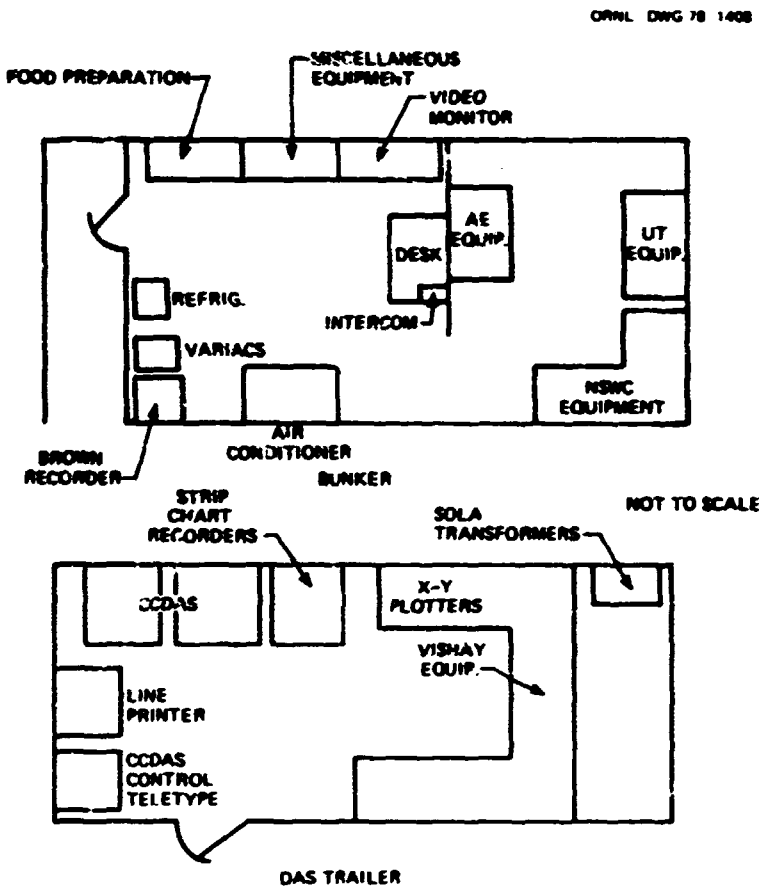

Fig. 4.5. Layout of equipment in data-acquisition system trailer and bunker.

words. The trigger signal from the first break stops the erasing of old data and recording of new data after a preset delay.

The Ampex magnetic tape recording unit recorded seven channels of strain data (see Appendix D) and the crack propagation trigger signal in the FM mode. This device has a response of 10 kHz and was included in the system to provide a good record of a rapid depressurization. Although the pressure transducers used in the test may have had an inherent capability of measuring pressure transients of interest satisfactorily, they had to be placed on a short tube attached to the head and therefore could not measure fast transient vessel pressure itself. However, the inside surface strain remote from the flaw recorded by the Ampex recorder was considered to be a good indication of pressure during unloading of the vessel.

BLANK PAGE

Table 4.1. Data-acquisition system for V-7A t

Output device	Permanent test record	Output during test	Number		
			Tempera-ture	Pressure	St
CCDAS	Digitized data on magnetic tape	(1) Line printer (full scans) (2) Digital readout of selected channel	9	3	
Vishay	Paper tape; typed record; magnetic cassette	Paper tape			
Ampex Model FR-1300 tape recorder	Direct magnetic tape record				
ERDAC	Photographic copy of CRT display	CRT display			
X-Y Plotter (data vs pressure)	Paper plot	Paper plot		1	
HP strip chart	Paper chart	Paper chart		2	
Brown recorder	Paper chart	Paper chart	16		
Ultrasonic system	Magnetic tape with voice channel	CRT display			
Acoustic-emission system	Magnetic tape	CRT display		1	
Video	Magnetic tape	TV monitors			

BLANK PAGE

Table 4.1. Data-acquisition system for V-7A test

utput during test	Number of channels by data type								
	Tempera-ture	Pressure	Strain	COD	UT	Acoustic emission	Crack propaga-tion	CP trigger	Time
) Line printer (full scans)	9	3	77	6			2	1	1
) Digital readout of selected channel									
per tape			10						
			7					1	1
T display							2		
per plot		1	1	3					
per chart		2	1	3				1	
per chart	16								
T display					4				
T display		1				2			
monitors									

BLANK PAGE

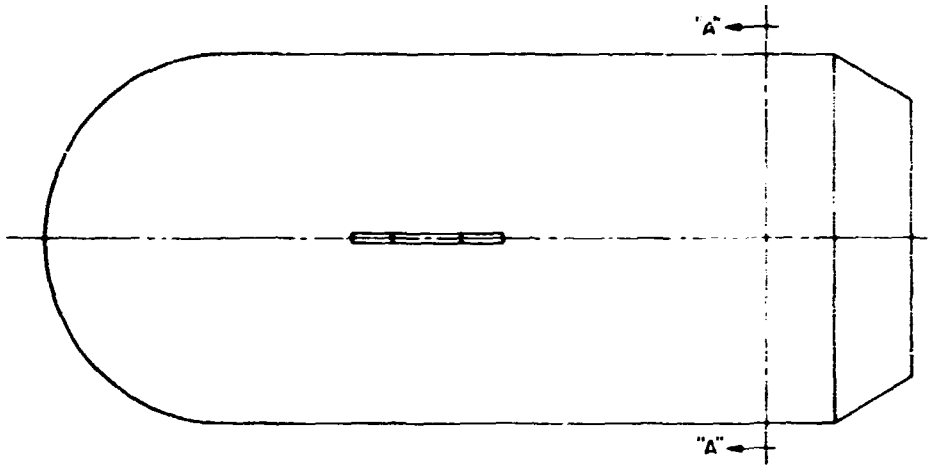

TEST VESSEL

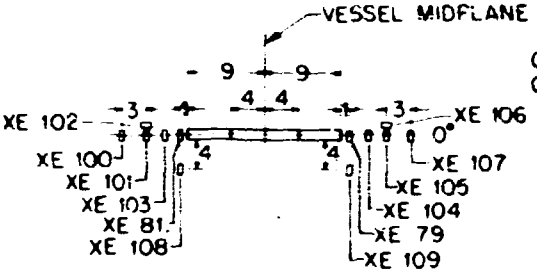

VIEW "B-B"
(SEE DETAIL A FOR OTHER SENSORS)

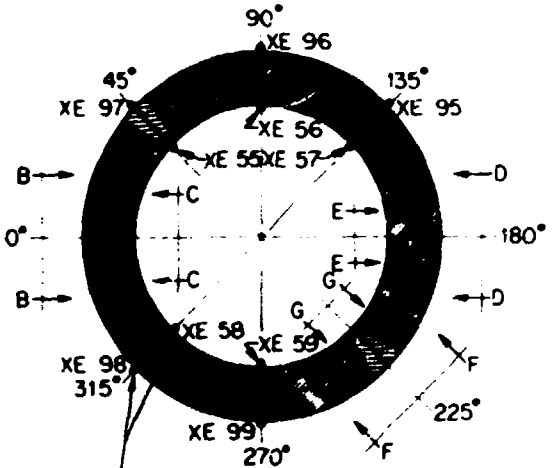

CIRCUMFERENTIAL STRAIN GAGES AT MIDPLANE OF TEST SECTION ON INSIDE AND OUTSIDE SURFACES AT 45°, 90°, 135°, 270° AND 315°

SECTION "A-A"
SEE VIEW B, C, D, E, F AND G

UNLESS SHOWN OTHERWISE, STRAIN GAGES ARE SPACED 2 in. APART

NOTE: DIMENSIONS ARE IN INCHES. 1 in. = 25.4 mm

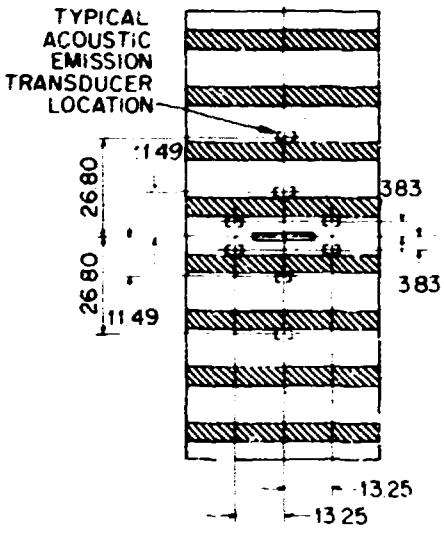

DEVELOPED VIEW - OUTSIDE SURFACE OF V-7A TEST CYLINDER

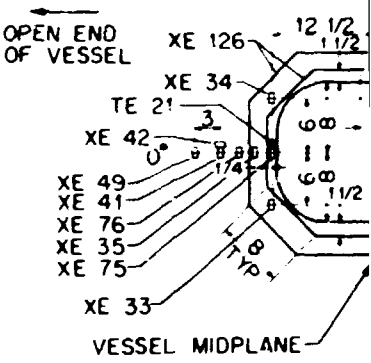

VIEW

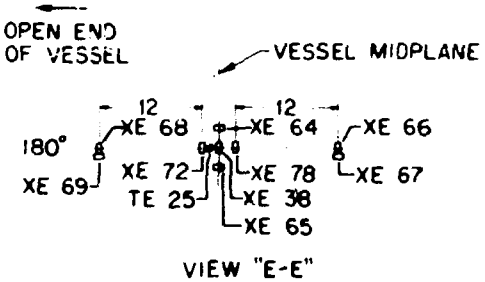

VIEW "E-E"

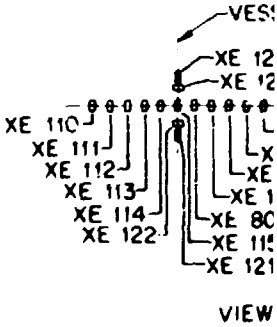

VIEW

Fig. 4.6. Instrumentation layout for vessel V-7A

BLANK PAGE

ORNL-DWG 76-14309

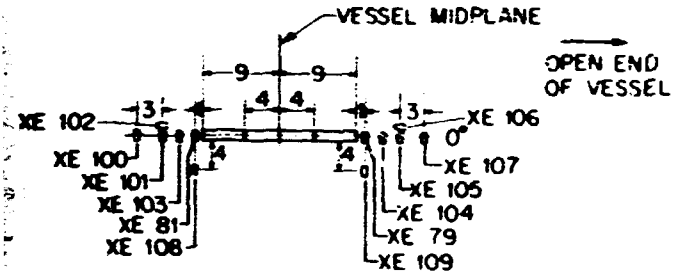

VIEW "B-B"
(SEE DETAIL A FOR OTHER SENSORS)

TYPES OF SENSORS

XE 33-XE 124	STRAIN
XE 125-XE 126	CRACK PROPAGATION
XE 140-XE 143	ULTRASONIC
ZT 127-ZT 132	COD
PE	PRESSURE
TE	TEMPERATURE

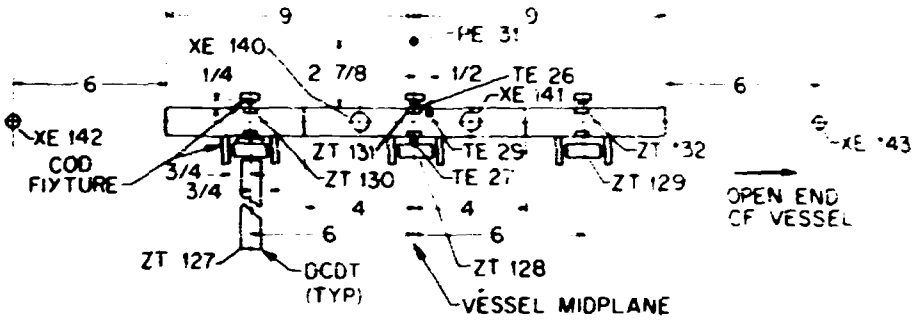

DETAIL "A"

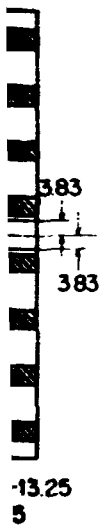

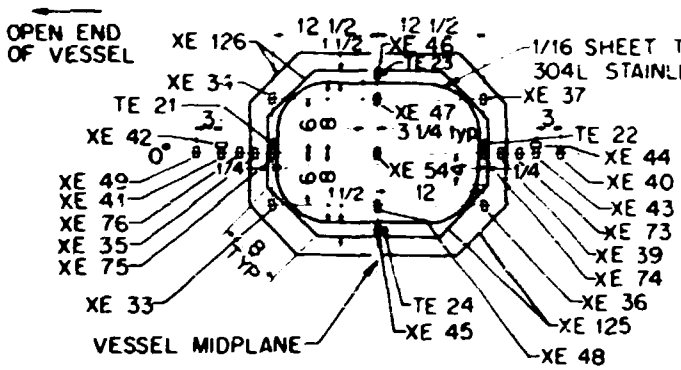

VIEW "C-C"

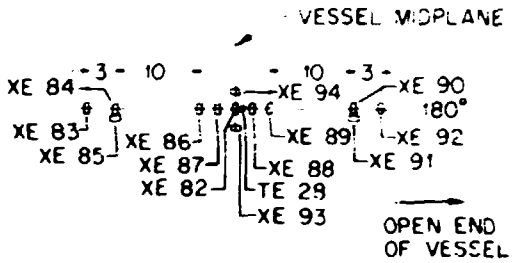

VIEW "D-D"

JTSIDE SURFACE
CYLINDER

ISEL MIDPLANE

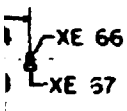

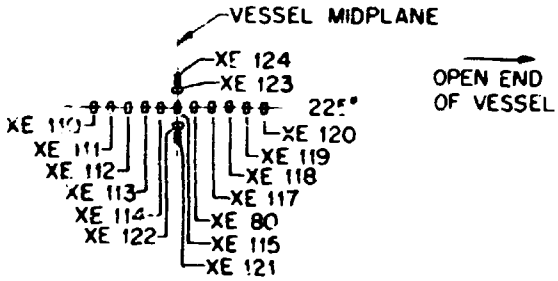

VIEW "F-F"

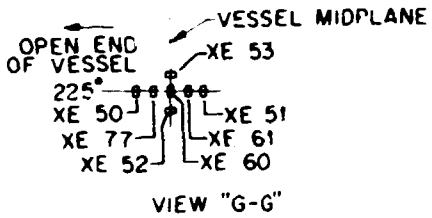

VIEW "G-G"

Instrumentation layout for Vessel V-7A.

BLANK PAGE

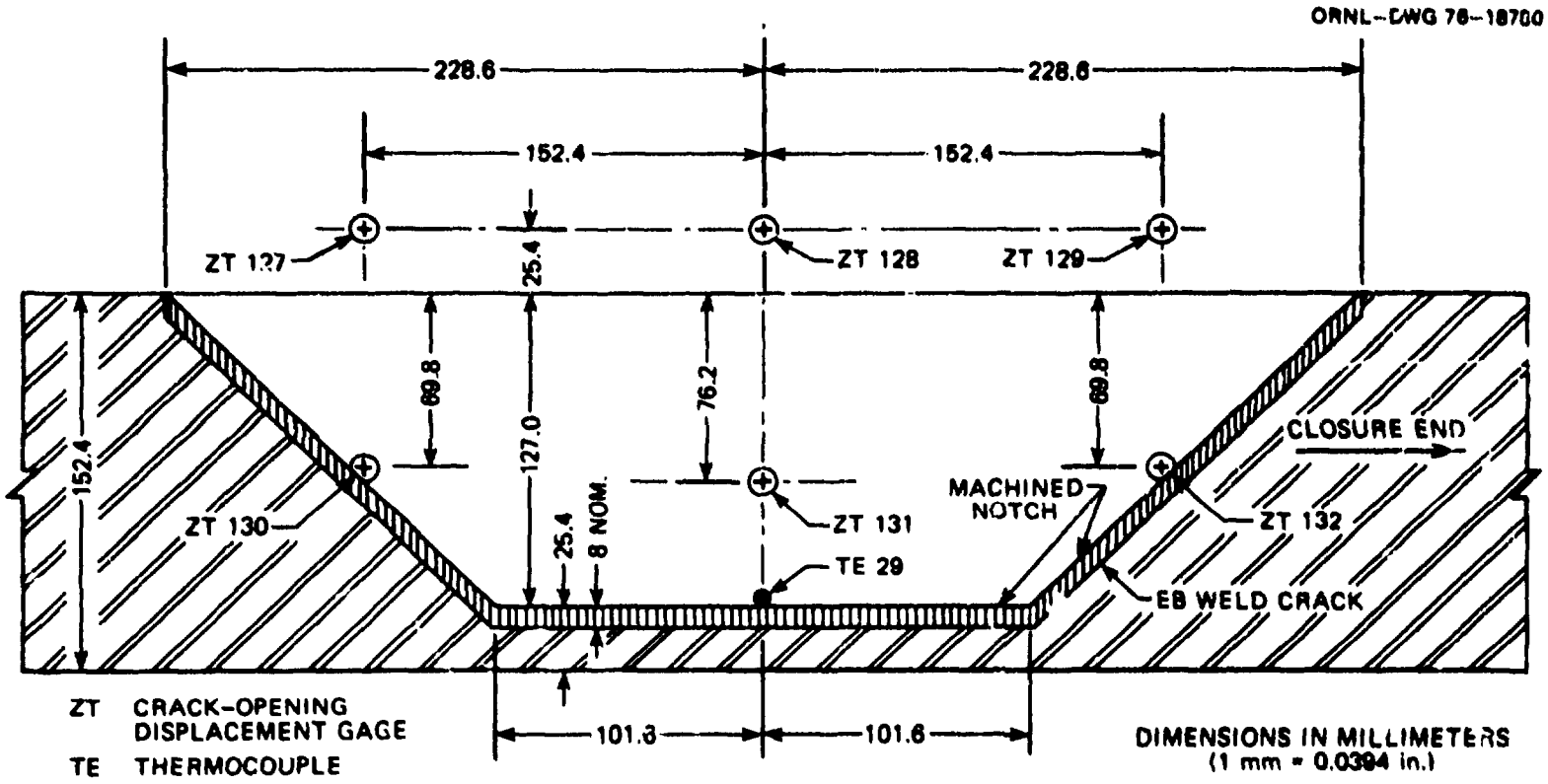

Fig. 4.7. Details of instrumentation at flaw in vessel V-7A.

BLANK PAGE

For recording slow changes in pressure and other variables, recordings were made on three strip charts at chart speeds between 1 in./min and 0.5 in./sec and on the CCDAS. See Appendix D for details. Strip chart speeds were selected during the test as necessary to resolve data for easy interpretation, while the CCDAS was preprogrammed to scan all points ten times per second. During periods of potential rapid change in data values, the CCDAS scans were recorded on magnetic tape at 1-, 2-, or 4-sec intervals. At other times scans were recorded at 1- or 5-min intervals.

The use of a patch to enable the vessel to sustain pressure after rupture necessitated the incorporation of instrumentation to detect rupture. (The principle of operation and development of the scheme of the rupture-detection system is described in detail in Appendix E.) The patch-pressurization system (PPS) was selected as the primary means of detecting rupture because of practical advantages over other possible schemes. The PPS produces a permanent record of its response with a time base, so that the events surrounding the time of rupture can be accurately correlated and evaluated after the test. Video monitoring was a backup, by which the actual rupture was first noticed. It was not considered as reliable as the PPS, because there was no way to make an objective time-based record of an event on the video recording. Furthermore, a momentary disruption of the video signal or distraction of the human monitor might result in the event being missed. Other instrumentation also provided significant information about the time of rupture, as discussed in Section 4.6.

Rupture detection by the PPS is indicated by a rapid drop in pressure in the PPS. A record of this pressure, together with vessel pressure, was made on strip chart recorder No. 1, which was monitored visually during the part of the test when rupture was most probable.

4.4 Vessel Test Assembly

A structure was designed for supporting and enclosing the instrumented vessel and associated equipment during transport. A simplified drawing of the assembly of the vessel, support, and enclosure is shown in Fig. 4.8. This structure supported the vessel, cable reels, and terminal boxes for

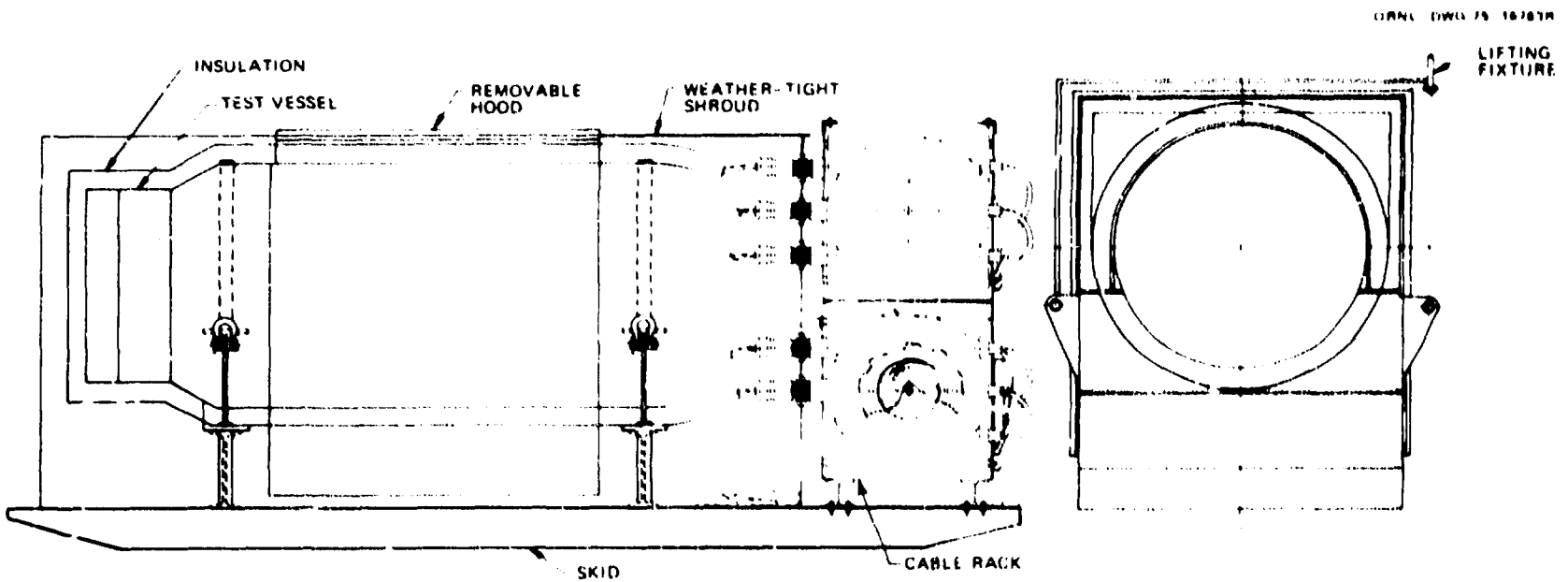

Fig. 4.8. Simplified views of vessel V-7A test assembly.

heater and instrumentation connections. The enclosure protected the instrumented vessel from weather and mechanical damage during the loading, unloading, and hauling of the vessel.

The heating system consisted of eight groups of Calrod heaters equally spaced around the vessel, as shown in Fig. 4.9. Each group was energized by a Variac and monitored by two thermocouples attached to the surface of the vessel beneath the heaters. Each group contained six 2-kW Calrod heaters connected in parallel. The space around and between the heater rods was filled with an epoxy graphite compound to improve thermal conductance between the heaters and the vessel. After instrumentation was installed, the vessel was insulated with 75-mm-thick (3-in.) glass wool. Power cables for connecting the Variacs to the heater terminal box on the vessel test assembly were supplied by the NSWC. Each Variac was rated at 28 A and 130 V and was energized by 120-V alternating current circuits. Variac controls allowed the power to be varied continuously from 0 to 3.3 kW on each group of heaters. The Brown recorder for the sixteen thermocouples monitoring the heaters was mounted in one of the two Variac cabinets that were installed in the bunker for the test.

Vessel preparation and the installation of components in the vessel test assembly were accomplished at ORNL. Strain and COD gages and thermocouples were applied by techniques developed and used on several earlier tests.[2] See Appendix D for details on the sensors in the layout in Fig. 4.6. The completed assembly is shown in Figs. 4.10 and 4.11. The vicinity of the flaw is shown in Fig. 4.12 with the strain gages and mid-depth COD gages installed. The outside surface strain gages in the weld-repair region are shown in Fig. 4.13.

The patch-pressurization system, shown schematically in Fig. 4.14, was mounted on a separate steel frame.

4.5 Pressurization System

The NSWC furnished and operated the equipment for pressurizing the intermediate test vessel with nitrogen. Figure 4.15 is a schematic diagram of this system. The arrangement allowed several modes of pressurization.

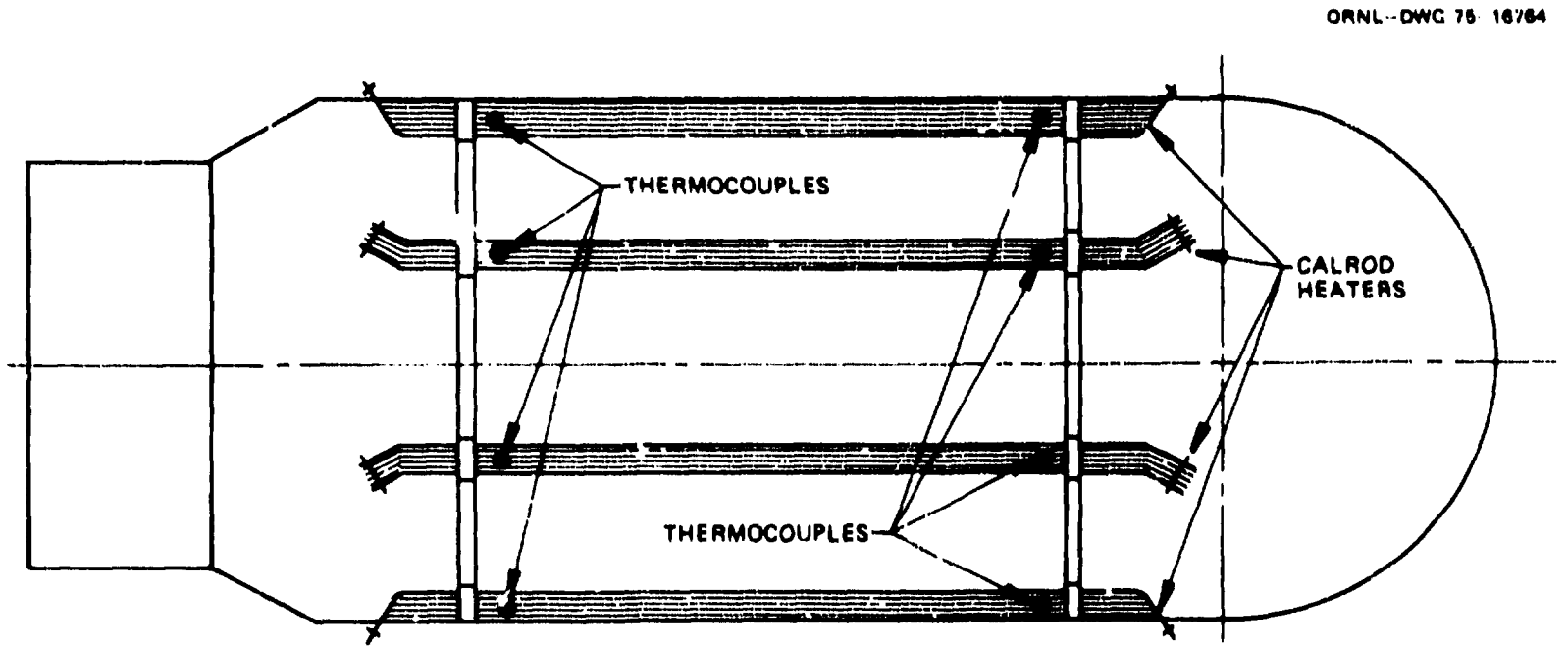

Fig. 4.9. Arrangement of electrical heaters on vessel V-7A.

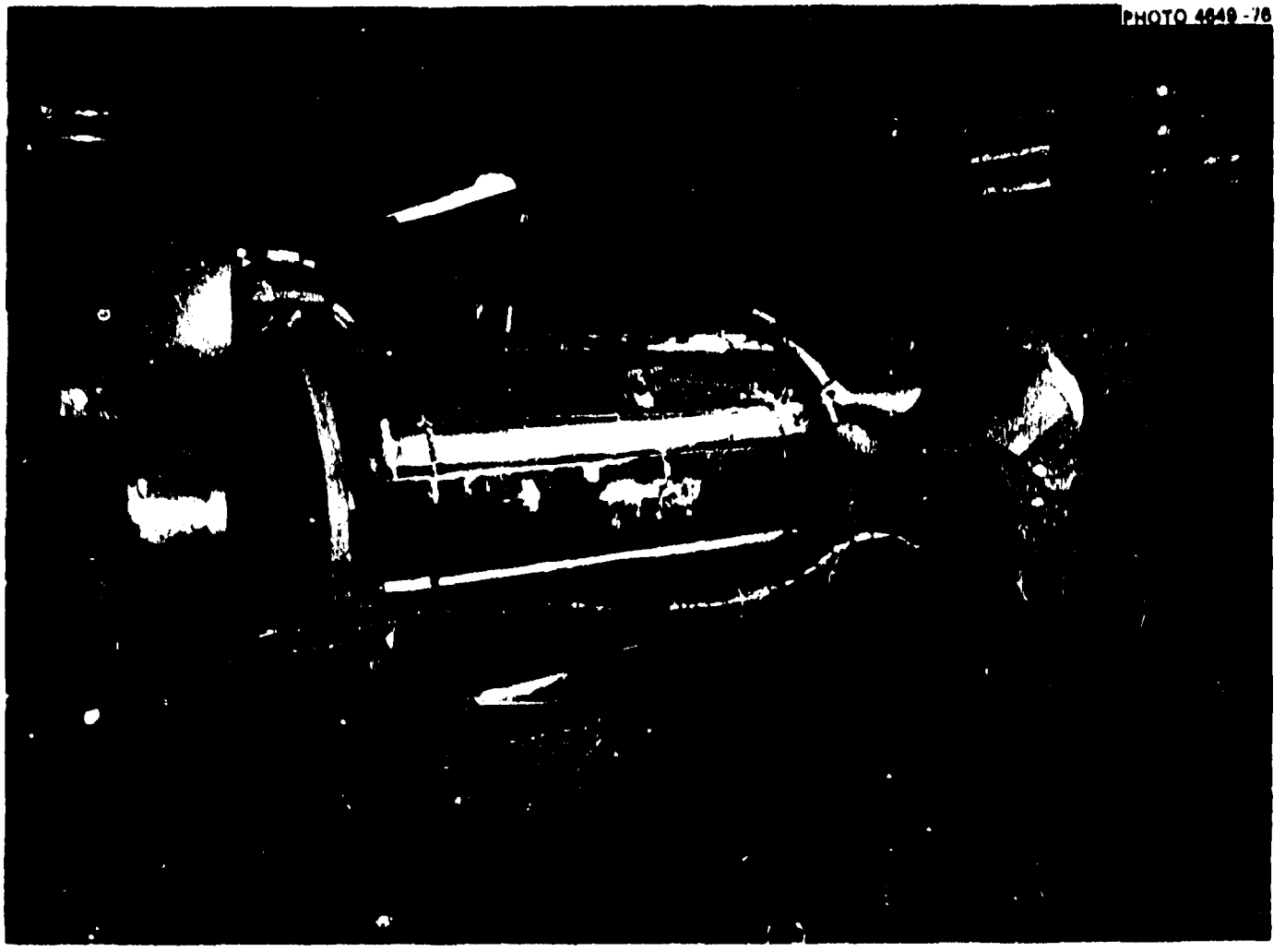

Fig. 4.10. V-7A vessel test assembly as it appeared when completed, except for installation of thermal insulation and protective cover. Photographed after test.

Fig. 4.11. Closure end view of V-7A vessel assembly showing Autoclave Engineers high-pressure penetration fittings for instrumentation cables.

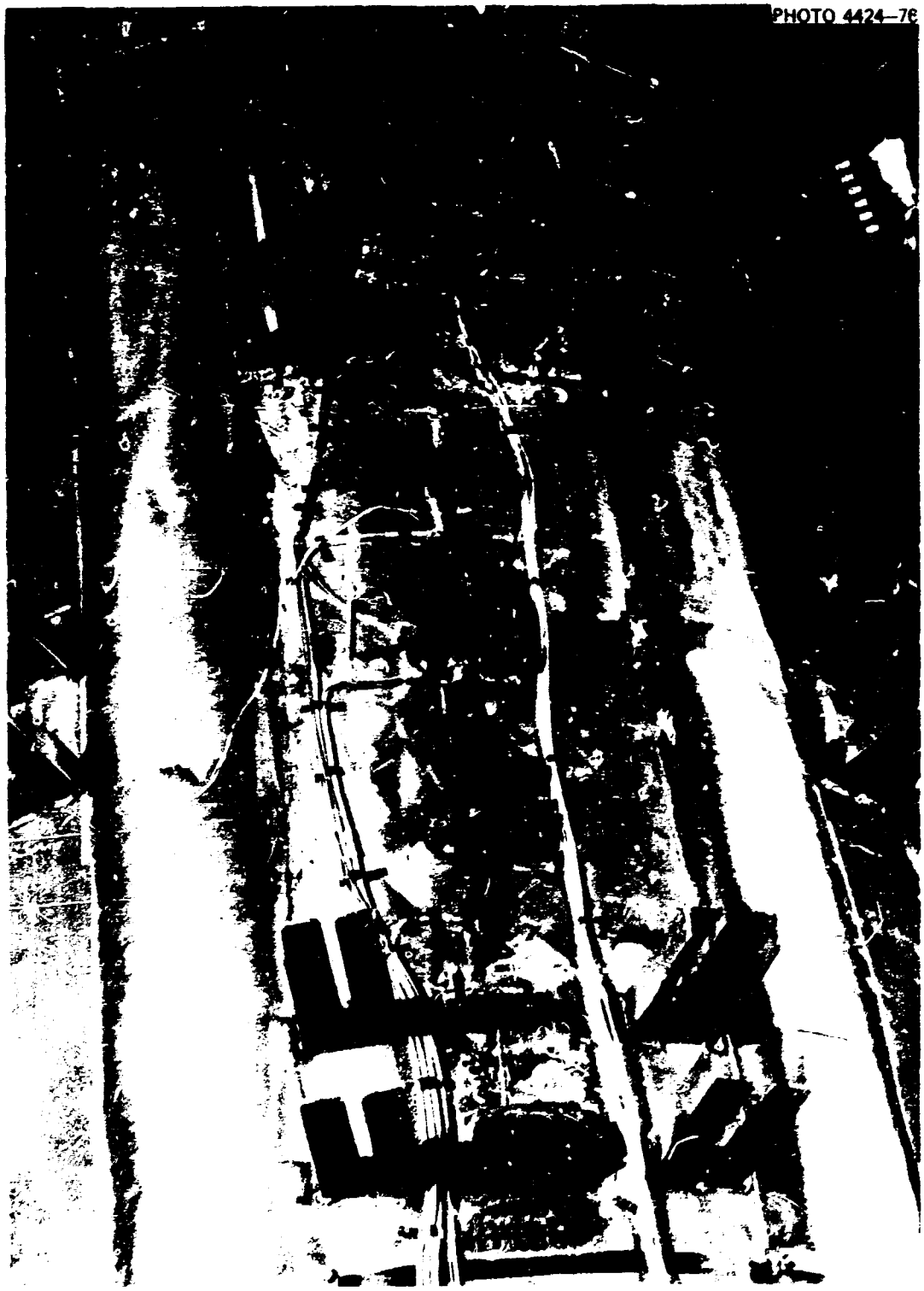

Fig. 4.12. Instrumentation in the vicinity of the notch on vessel V-7A. The guides for acoustic-emission transducers, mounts for outside COD gages, and two 45° weld bosses for ultrasonic transducers are shown without the instrumentation mounted.

Fig. 4.13. Strain gages on the outside surface of the weld-repair zone of vessel V-7A.

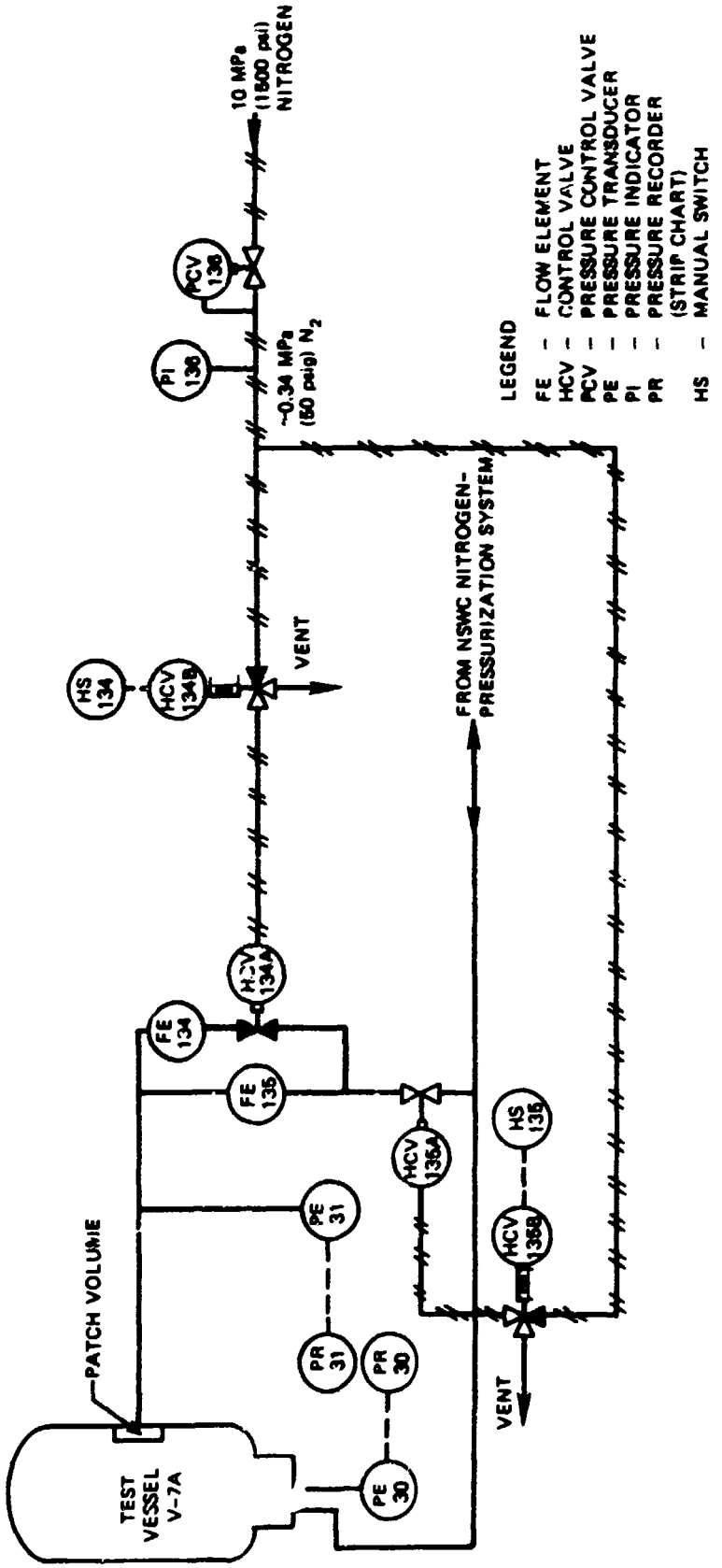

Fig. 4.14. Diagram of patch-pressurization system for V-7A.

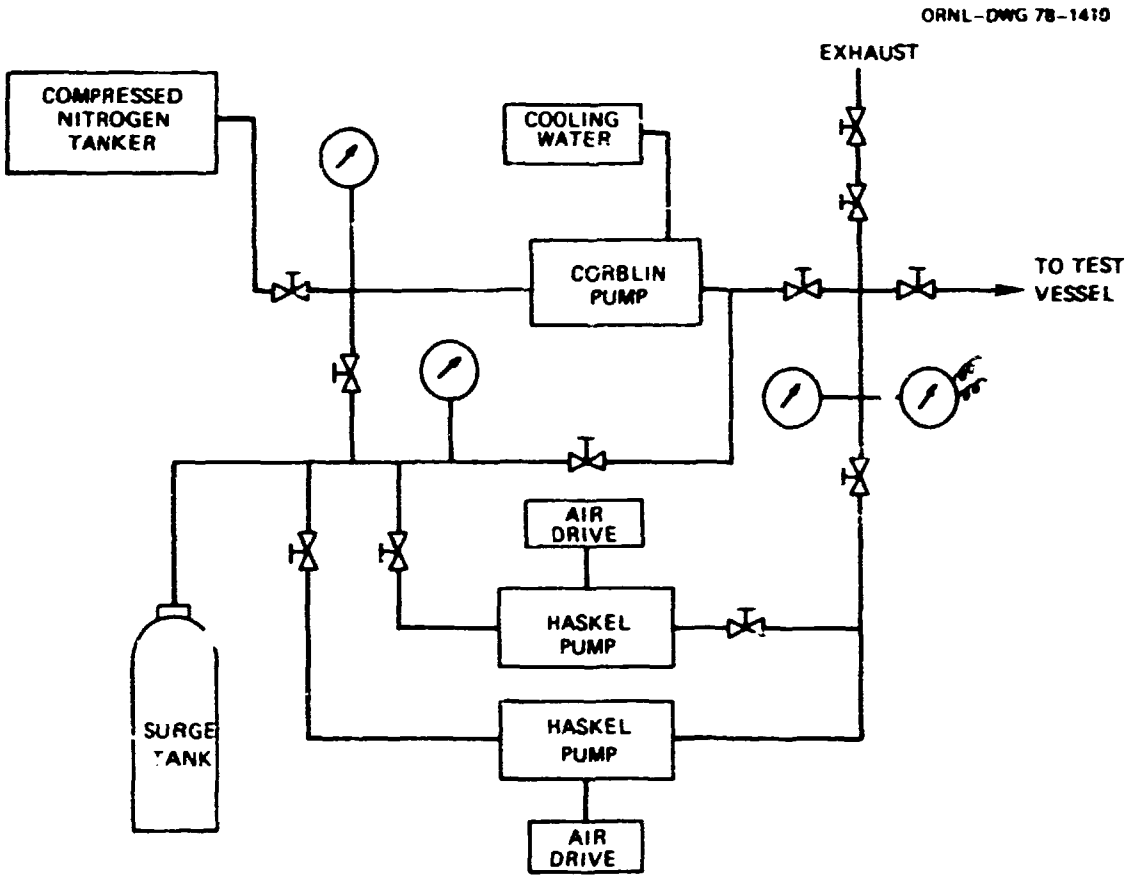

Fig. 4.15. Diagram of NSWC high-pressure nitrogen-pressurization system.

1. The test vessel could be pressurized directly by the compressed gas tank trailer up to about the pressure of the supply, 16.6 MPa (2400 psi).

2. The Corblin pump could pump directly into the test vessel up to about 62 MPa (9000 psi).

3. The two Haskel pumps could be used singly or in parallel and could be supplied directly from the tank trailer or from the Corblin pump.

During pressurization, the nitrogen could be vented to the atmosphere or to a tanker if it appeared advantageous to conserve the supply of compressed gas. Details of the pressurization system are given in Appendix H.

Figure 4.16 shows the pressurization system control station, the Corblin and Haskel pumps, the tank trailers, and the air compressor.

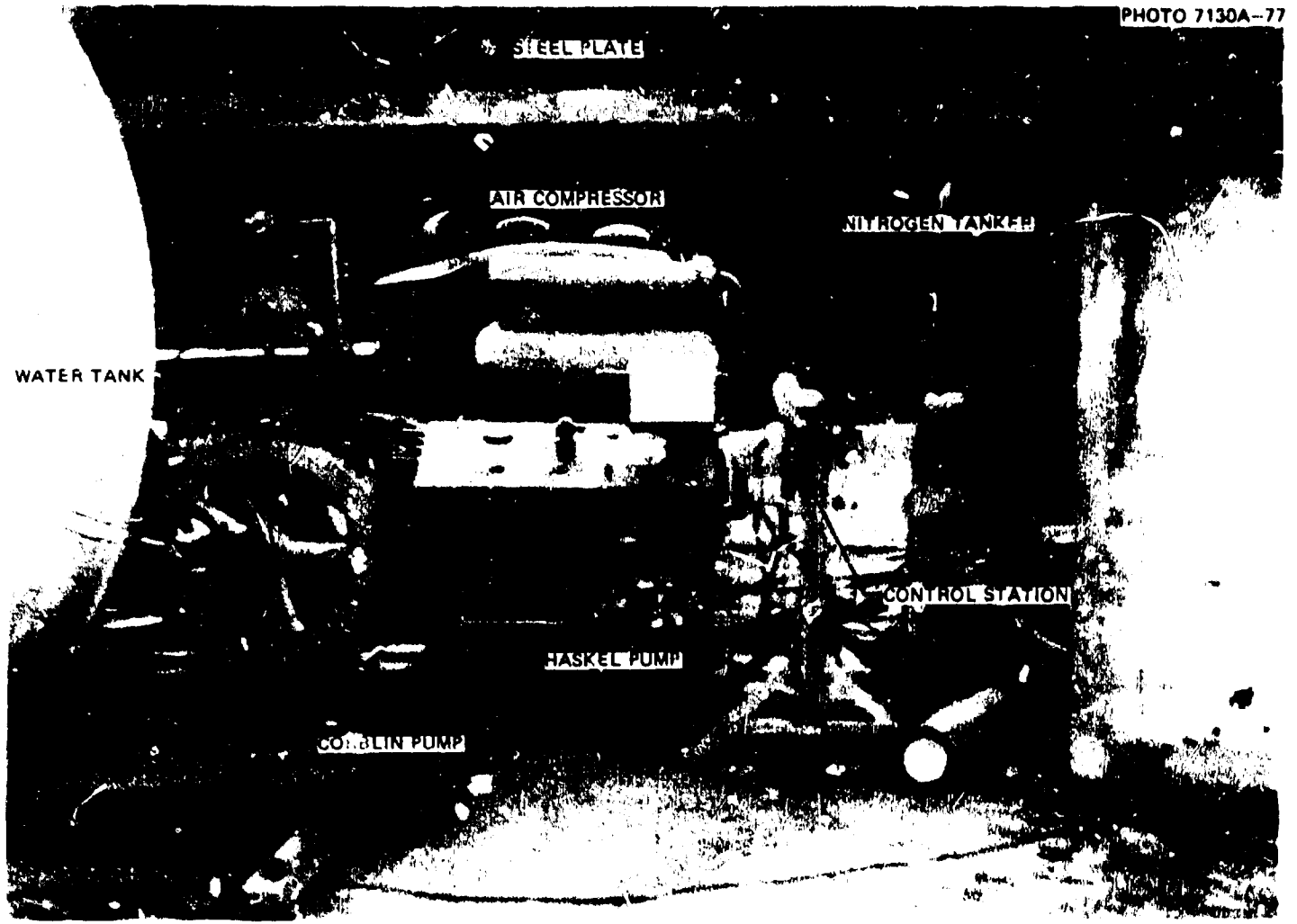

Fig. 4.16. View of NSWC pressurization control station showing cooling-water storage tank, Corblin pump, Haskel pump, air compressor, and compressed nitrogen tank trailer.

4.6 Test Operations

4.6.1 Pretest plans and preparations

The NSWC moved the principal units of the pressurization system to the test site about a month before the test date. ORNL personnel and equipment arrived on site 14 days before the test. The highest-priority goal in early test preparations was to check out the CCDAS, since it was a critical system and difficulties were not unusual. A thunderstorm the night before arrival destroyed an underground cable supplying 208/240-V, 3-phase power to the V-7A test site, and repair of the utility power feeder cable required one week. A portable engine-generator set was installed to allow preparations to proceed, and preparations other than the CCDAS checkout were not seriously affected. Pretest checks and calibrations were completed on time.

The general plan was to pressurize the test vessels several times. The necessity of having a full team of specialists present during testing made it imprudent to plan any pressurizations that would extend much beyond a normal working day. Since range safety rules permitted access to the manned areas only when test vessel pressure was not above 70 MPa (10,000 psi), the vessel was left pressurized to that level overnight between cycles, with two persons standing watch on the system.

The specific program of pressurization cycles was adopted the day before the test as follows:

1st cycle	Pressurize to 66.3 MPa (9.61 ksi), and depressurize to observe the behavior of the Section XI weld repair.
2nd cycle	Pressurize to 124 MPa (18 ksi), and depressurize to as low a pressure as is practicable. Note crack growth, if any.
Subsequent cycles	Repressurize to 3.4 MPa (0.5 ksi) above previous high pressure level, and note crack growth, if any. If none, continue pressurization until crack growth is observed. Determine whether pressure cycling with slightly increasing peak pressure causes the crack to grow and, if it does, continue the recycling without increasing peak pressure until the vessel fails.

Consideration of the possibility and consequences of a failure of the test vessel head to reseal, if the vessel were completely depressurized after being at high pressure, led to a decision to avoid complete depressurization. Seal replacement would require special equipment and several days' time at the Dahlgren site, where the usual supporting shops and personnel were not available. Furthermore, some or all of the internal instrumentation connections would have to be cut. During the planning of the test, it was also recognized that one pneumatic pressurization cycle required a few hours; but the time needed to depressurize, although not measured, would become long if complete depressurization were desired.

4.6.2 Heatup phase

Heatup of the vessel was started at 1448 on June 14, 1976, and a satisfactory temperature distribution was attained by the time the first pressure cycle was scheduled on June 15.

4.6.3 Pressurization phase

The complete pressurization schedule, starting at 0930 on June 15, is shown in Fig. 4.17; details of the schedule are given in Table 4.2. The temperature history of the vessel is shown in Fig. 4.18.

The planned pressure cycling program was carried out through the first two pressure cycles, reaching 66.1 MPa (9.58 ksi) in the first and 126.0 MPa (18.28 ksi) in the second. The pressure was dropped to 13.9 MPa (2.02 ksi) and 38.5 MPa (5.58 ksi) at the ends of the first and second cycles, respectively. The third cycle, which was to go (at least initially) to the previous peak pressure of 126.0 MPa (18.28 ksi), was started at 1300 on June 16. It was hoped that this cycle could be completed during that day. However, failure of seals in one of the Haskel high-pressure pumps interrupted the test at 76.7 MPa (11.12 ksi).

Both Haskel pumps working in parallel had produced pressurization rates of 0.2 to 0.5 MPa/min (30 to 70 psi/min), depending upon the pressure level. With this capacity cut in half, it appeared imprudent to resume the test until the following morning, June 17. Parts were ordered from the pump manufacturer so that repairs could be made early on June 17.

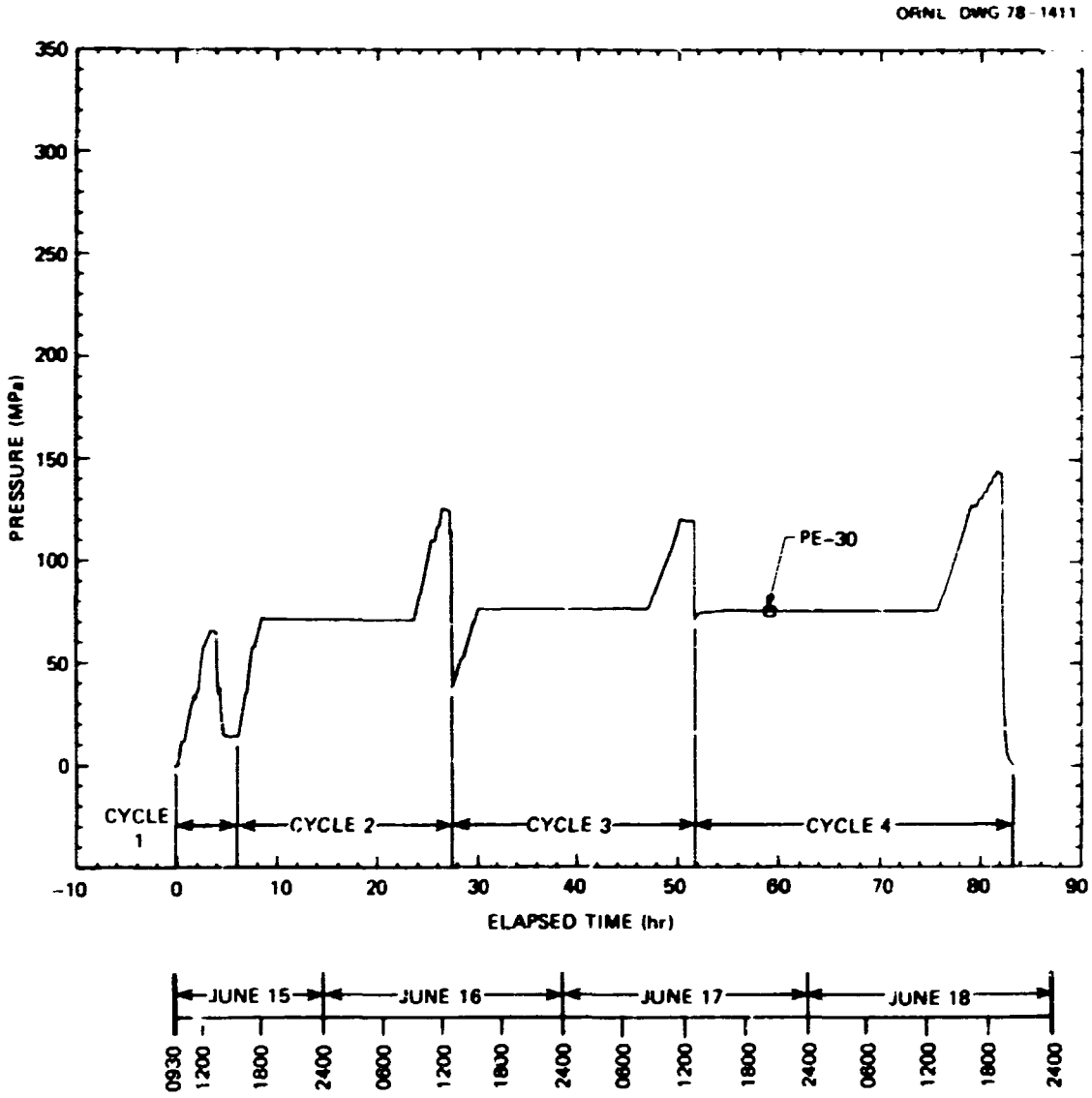

Fig. 4.17. Pressurization history of intermediate vessel test V-7A, June 15–18, 1976 (1 MPa = 145.04 psi).

The pressurization in the third cycle was resumed with one Haskel pump at 0828 on June 17, and at 1132 pressurization was interrupted by the failure of the second Haskel pump. The peak pressure in cycle 3 was 121.0 MPa (17.55 ksi), slightly below the maximum pressure attained in the second cycle.

The parts needed for repairing the pumps did not arrive until mid-morning June 18, by which time both pumps had been disassembled and it

Table 4.2. Pressure cycle data for the V-7A test (June 1976)

Cycle	Activity	Time at start (d:hr:min:sec)	Pressure (MPa)[a]	
			Start	End
1	Pump	15:09:33:29	0	66.1
	Hold	:12:48:48	66.1	65.3
	Vent	:13:25:15	65.3	14.4
	Hold	:14:11:29	14.4	13.9
2	Pump	:15:28:36	13.9	72.4
	Hold	:17:58:36	72.4	70.9
	Pump	16:09:01:05	70.9	109.8
	Hold	:10:39:01	109.8	109.1
	Pump	:10:59:01	109.1	116.9
	Hold	:11:19:01	116.9	116.4
	Pump	:11:29:01	116.4	126.0
	Hold	:11:49:01	126.0	125.0
	Vent	:12:36:09	125.0	38.5
3	Hold	:13:00:09	38.5	42.8
	Pump	:13:15:08[b]	42.8	76.7
	Hold	:15:25:47	76.7	76.4
	Pump	17:08:28:14	76.4	121.0
	Hold	:11:31:39[c]	121.0	119.7
	Vent	:13:00:16	119.7	68.8
4	Hold	:13:08:16	68.8	75.7
	Pump	18:13:03:11	75.7	127.6
	Hold	:16:28:52	127.6	126.3
	Pump	:16:52:52	126.3	130.9
	Hold	:17:16:46	130.9	130.6
	Pump	:17:28:53	130.6	134.4
	Hold	:17:44:53	134.4	133.9
	Pump	:17:57:10	133.9	137.9
	Hold	:18:13:45	137.9	137.4
	Pump	:18:23:23	137.4	141.5
	Hold	:18:40:50	141.5	141.0
	Pump	:18:48:11[d]	141.0	144.3
	Hold	:19:02:26[e]	144.3	142.7
	Vent	:19:33:12	142.7	0.3
	End	:20:45:22	0.3	

[a] 1 MPa = 145.04 psi.

[b] Pump failure at 16:15:07:00.

[c] Second pump failed at this time.

[d] Power to heaters turned off at 18:18:51:00.

[e] Nominal time of rupture.

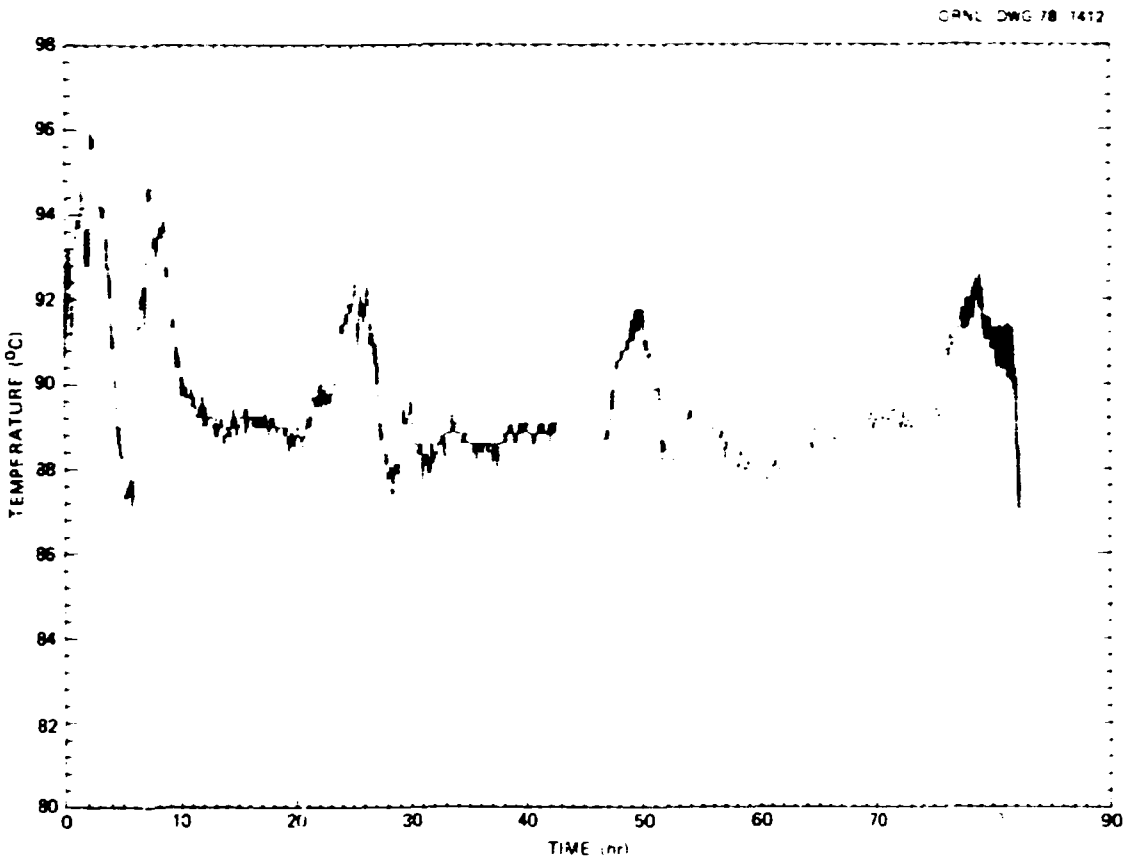

Fig. 4.18. Temperature history of intermediate vessel test V-7A, June 15–18, 1976, as measured by thermocouple TE 21 on inside surface near end of notch.

had been determined that overheating had led to failure. After considering various means of cooling the pumps, arrangements were made with the NSWC to pump river water to cool the air receiver of the compressor which provides air for driving and cooling the Haskel pumps. One pump was repaired quickly, and the fourth pressurization cycle was started at 1303 on June 18. The second pump was repaired but not used. The new cooling arrangement was effective in preventing a recurrence of overheating.

In consideration of the merits of attaining the principal goal of testing the vessel to the point of rupture without further failures and delay, which would have become costly, it was decided to pressurize the vessel in the fourth cycle until rupture occurred. This point was reached at 1902 on June 18 at a pressure of 144.3 MPa (20.92 ksi).

4.6.4 Rupture phase

The rupture was first observed on the video monitor. The strip chart record of the PPS pressure was marked by hand when the rupture was seen on the video monitor, about 20 to 25 sec prior to a recorded rapid drop in PPS pressure. The CCDAS data, which were plotted later, give a more precise record of the rupture and confirm the strip chart record. Figure 4.19 shows the pressures plotted from the CCDAS record for the vessel and the patch-pressurization system at about the time of rupture. It also shows that the temperature in the notch dropped abruptly as the escaping gas cooled that region. (The location of the thermocouple in the notch is shown in Fig. 4.7.) This drop in temperature marks the time that has been nominally defined as the time of rupture.

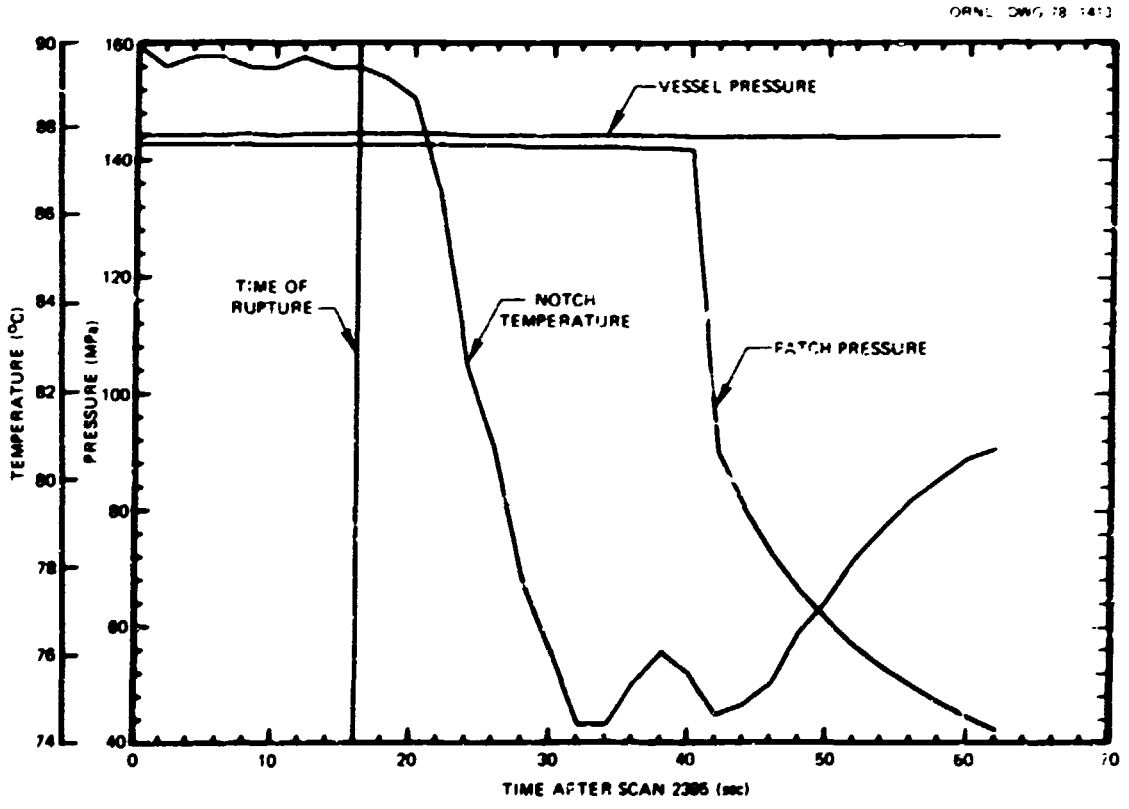

Fig. 4.19. Data defining the nominal time of rupture in V-7A test as 19:02:26, June 18, 1976 (1 MPa = 145.04 psi).

A posttest review of the video record revealed that the blowdown of the patch volume was visible for a period of about 30 sec. Figures 4.20 and 4.21 show a sequence of video frames from this period. Features of the video camera view are defined in Fig. 4.20. The easily visible material being expelled from the notch is oil that was put in the notch for coupling the ultrasonic transducers to the vessel. When viewed at normal speed, the video record shows evidence of a small leak about 1 sec before the first globule of oil became visible (frame 1, Fig. 4.21). The intensity of the flow appeared to be at a maximum in the period between 10 and 33 sec after frame 1. The leak was not visible on video after frame 5.

Although the exact sequence of events at ligament rupture cannot be stated with certainty, the video and CCDAS data are consistent with the following supposition. Prior to rupture, the patch was slightly displaced from the vessel wall so that it enclosed a substantial volume of gas. When the first material was ejected from the notch, the rupture was still small. The rupture developed to full size in about 10 sec, during which time PPS pressure was maintained at vessel pressure by virtue of the diaphragm action of the patch. Rapid patch volume depressurization commenced when the patch volume reached a minimum, the patch then being firmly pressed against the vessel wall. This may have occurred at about the time frame 8, shown in Fig. 4.21, was recorded, about 33 sec after the first visible appearance of a leak on video.

4.6.5 Data-acquisition system performance

Several data sources were used during the pressurization phase of the test for evaluating the status of the vessel and test equipment so that appropriate decisions could be made on the conduct of the test. Since test preparations represented most of the expenditure of manpower and funds, it was essential that checks be made as the test proceeded to ensure that succeeding phases would be carried out properly with the maximum recovery of data.

It was particularly important, for test control, to know the actual crack depth in the flaw ligament and the extent of crack growth in the axial direction. Cycling decisions depended upon the behavior of the crack in the ligament, while the axial extent of the crack was related

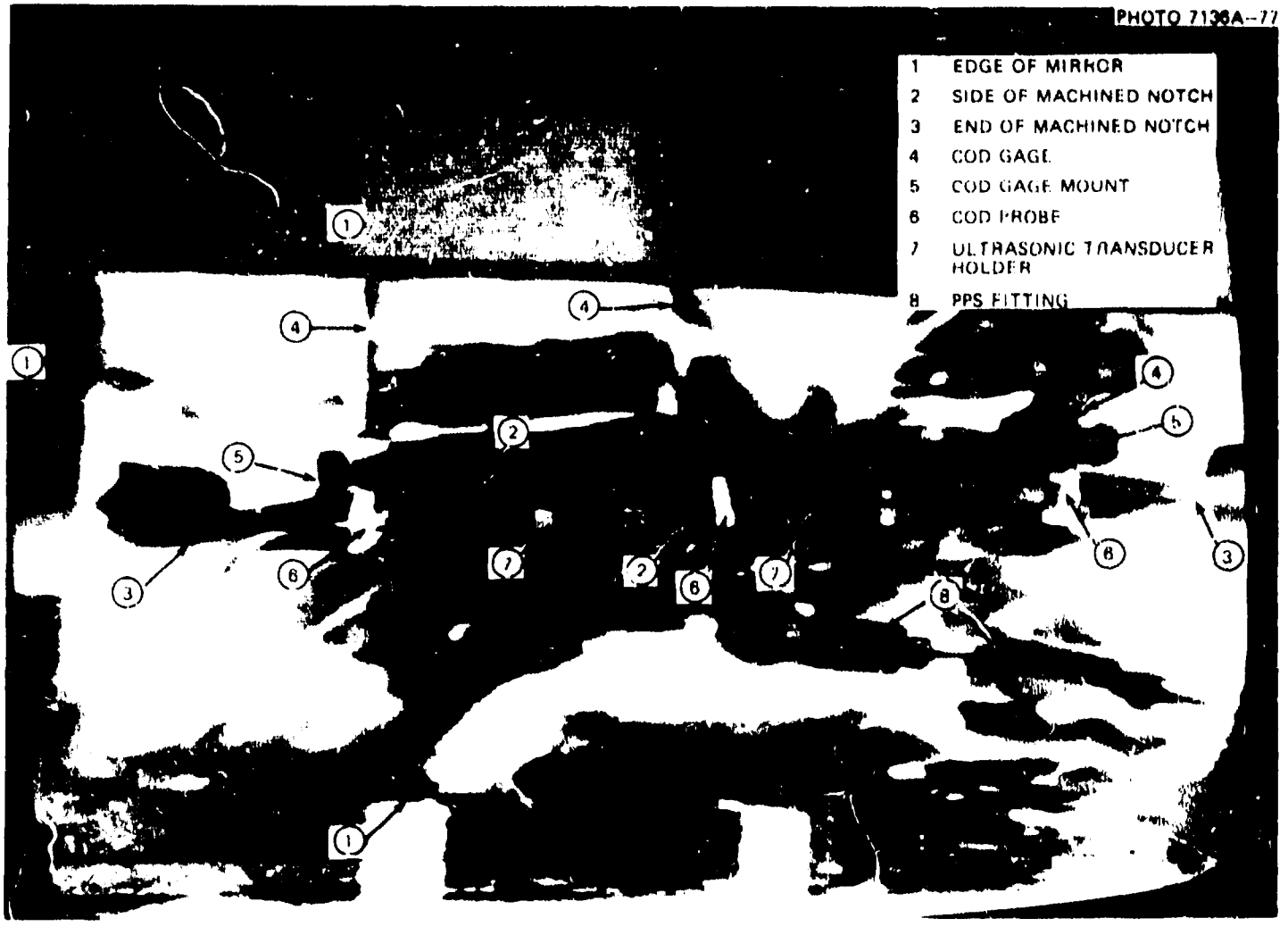

Fig. 4.20. Video view of notch in vessel V-7A a few seconds before rupture.

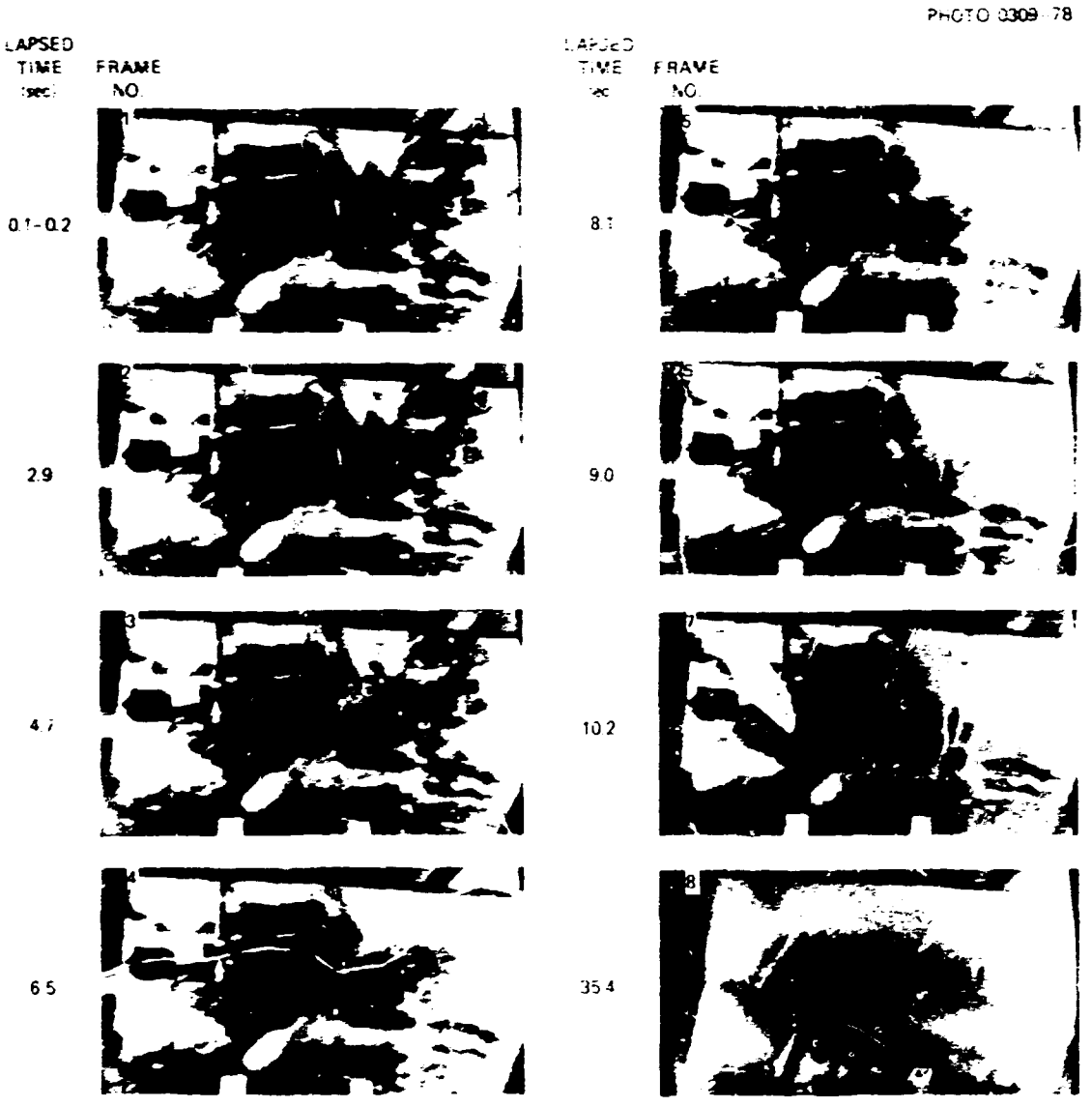

Fig. 3.21. Video sequence of notch during rupture. Lapsed time is measured from the first appearance of a droplet.

to the margin to burst. Because ultrasonic reflection from the crack tip had to compete with interferences not present in the V-7 test, observations made during the test were interpreted only tentatively.

Strain and COD measurements were inherently more precise than ultrasonic measurements, although the immediate implications of strain and COD with regard to crack size were imprecise. Comparisons of V-7A with V-7 measurements at corresponding pressures provided reassurance during the test that the vessel and the flaw were behaving as expected.

Except for the difficulties with the high-pressure pumps, the electrical and mechanical test equipment performed as desired. The CCDAS and most of the associated sensors performed satisfactorily. The test was started with only 1 out of 87 strain gages defective. All other sensor channels were functioning properly. During the test, 4 additional strain gages became defective; both crack propagation gages broke on the first application of pressure to about 27 MPa (4 ksi). One ultrasonic transducer failed when the vessel was heated. Defective sensors are noted in Appendix D.

All other data channels remained active throughout the test, but some instrumentation was not as effective as had been expected, namely: (1) ultrasonic sensing of the location of the crack tip; (2) COD measurement outside the notch with Transteck linear displacement transducers; and (3) COD measurement at mid-depth of the notch with "divider" gages.

The ultrasonic observations in the V-7A test were inherently more difficult than those in V-7, since both the transducer signal and the reflection from the crack tip had to be reflected from the inside surface of the V-7A test vessel. Ultrasonic energy scattered from the nearer crack surfaces provided additional disturbances. Furthermore, during the first pressurization cycle, the coupling fluid was a source of fluctuating reflections. During the low-pressure hold at the end of the first cycle, the transducer installation was inspected, and it was found that a great number of dead insects had accumulated in the fluid in the notch. The insects had been attracted by lights illuminating the vessel shelter and the notch and were killed by the exposed hot metal in the vicinity of the notch. The notch was cleaned and refilled with clean fluid; however, installed instrumentation and heat precluded the removal of all debris. Subsequently, lights at the vessel were turned off before nightfall and left off at night as much as practicable. The cleaning improved the performance of the ultrasonic system substantially.

The two types of COD gages exhibited anomalies peculiar to each type. The outside gages (ZT 127, 128, and 129) consistently indicated displacements free of noise, but their response at times suggested that the end of

the COD probe might not have followed the stop against which it was supposed to be held by spring compression. Figure 4.22 illustrates this behavior at a time when the loading changed from increasing to decreasing. This shows a tendency for the COD at one point to stay constant for some time after the load reversal while other associated measurements indicate it should be changing. Table 4.3 summarizes the performance of the COD gages. Subsequent test work with a redesigned stop shows that these COD gages should have been responsive during the early stages of pressurization. Figure 4.23 shows the COD calculated by an elastic-plastic finite-element method for the type of flaw in V-7 and V-7A. (See Appendix G for details of the calculation.) It is now believed that the COD threshold exhibite in the first cycle of the V-7A test, as well as in V-7, is an artifact

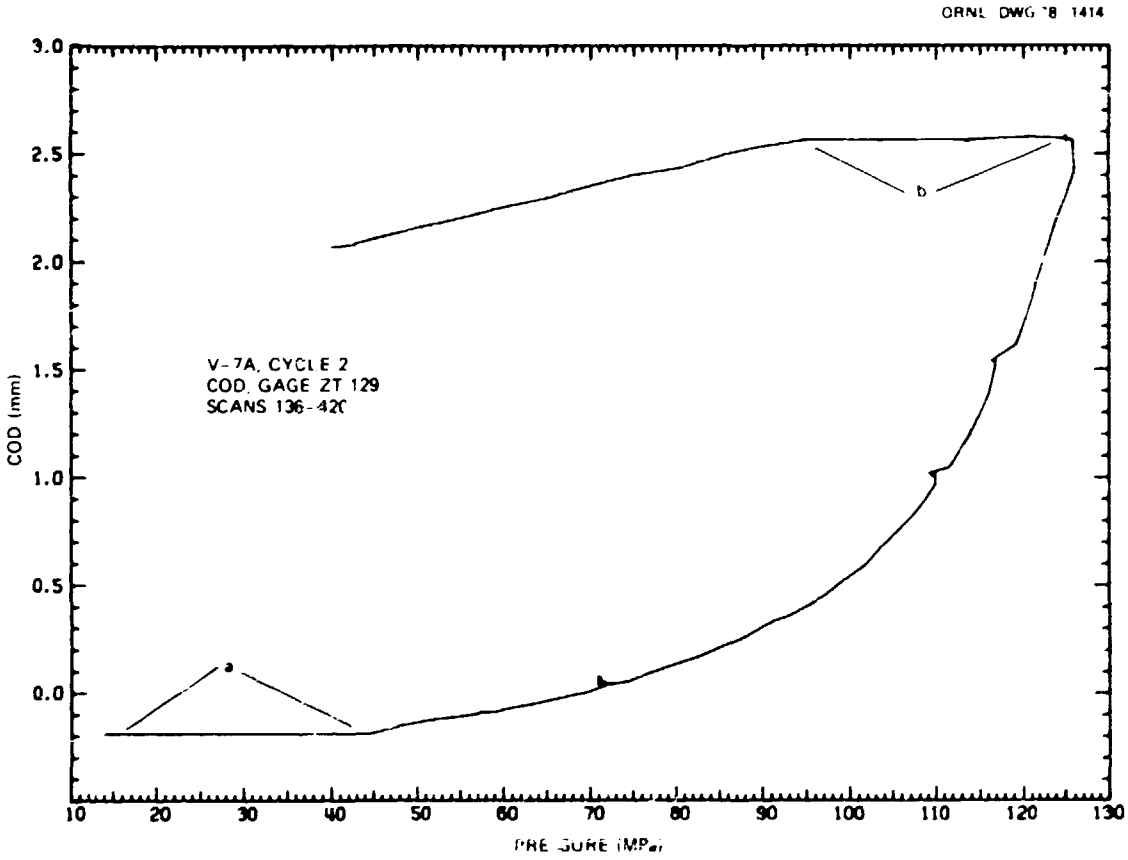

Fig. 4.22. Examples of anomalous behavior of outside COD gages indicating possible slippage during (a) increasing load and (b) decreasing load (1 MPa = 145.04 psi; 1 mm = 0.0394 in.).

Table 4.3. Summary of COD gage performance during test of vessel V-7A[a]

COD gage No.	Cycle No. 1	2	3	4
ZT 127	No response	No response below 100 MPa; proper response only on rising load between 112 MPa and 126 MPa; hang up on unloading	Negligible response	No response below 134 MPa; normal response during balance of cycle, both loading and unloading
ZT 128	Negligible response	No response on increasing load; normal response on rapidly decreasing load	Normal response over entire cycle	Normal response on rising load; hang up on decreasing load until 55 MPa was reached; normal thereafter
ZT 129	Small erratic response	No change in output in first 30 MPa of loading and unloading; otherwise normal	No change in output on first 30 MPa of loading and 25 MPa of unloading; otherwise normal except for a spurious point at scan No. 609	No change in output in first 30 MPa of loading and during entire unloading portion; otherwise normal response
ZT 130	Normal response except for spurious point at scan No. 87	Normal response except for small drift during the 2 hr prior to loading above 71 MPa	Normal response except for drift during 17-hr period at ~76 MPa	Normal except for anomalous drop in COD for ~3.5 hr during hold and initial loading above 110 MPa
ZT 131	Normal response except for spurious point at scan No. 26	Normal response	Normal response	Normal response
ZT 132	Erratic response	Erratic response	Erratic response	Large drift during hold period; normal response during loading and unloading

[a]1 MPa = 145.04 psi.

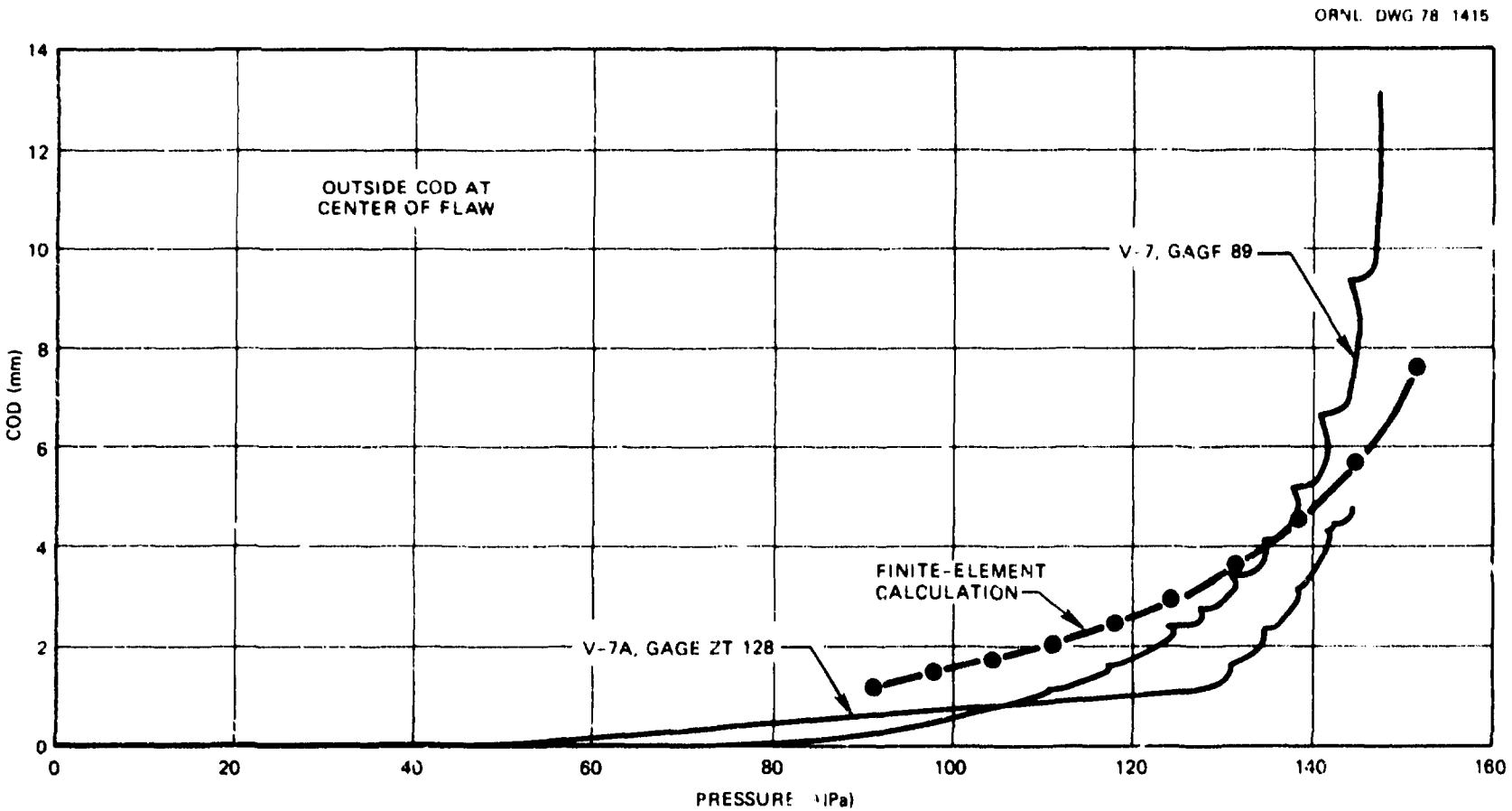

Fig. 4.23. COD measured by outside DCDT-type gages in V-7 and V-7A compared with calculated values (1 MPa = 145.04 psi; 1 mm = 0.0394 in.).

associated with the way the gages were mounted. However, when the gages indicate a change in COD, the response of the gages to loading in one direction appears to give reasonable differential values.

The type of COD gage used at the mid-depth of the notch (ZT 130, 131, and 132) is a divider with strain gages attached to the surfaces of the clip spring. Details of this device and its calibration are given in Appendix F. The inherent problem with this gage is its low level of output, about 0.05 mV/mm of displacement with 5-V excitation. The output during the V-7A test was noisy, as shown in Fig. 4.24, and drifted with time, as shown in Fig. 4.25. As a consequence of this behavior, recalibrations were

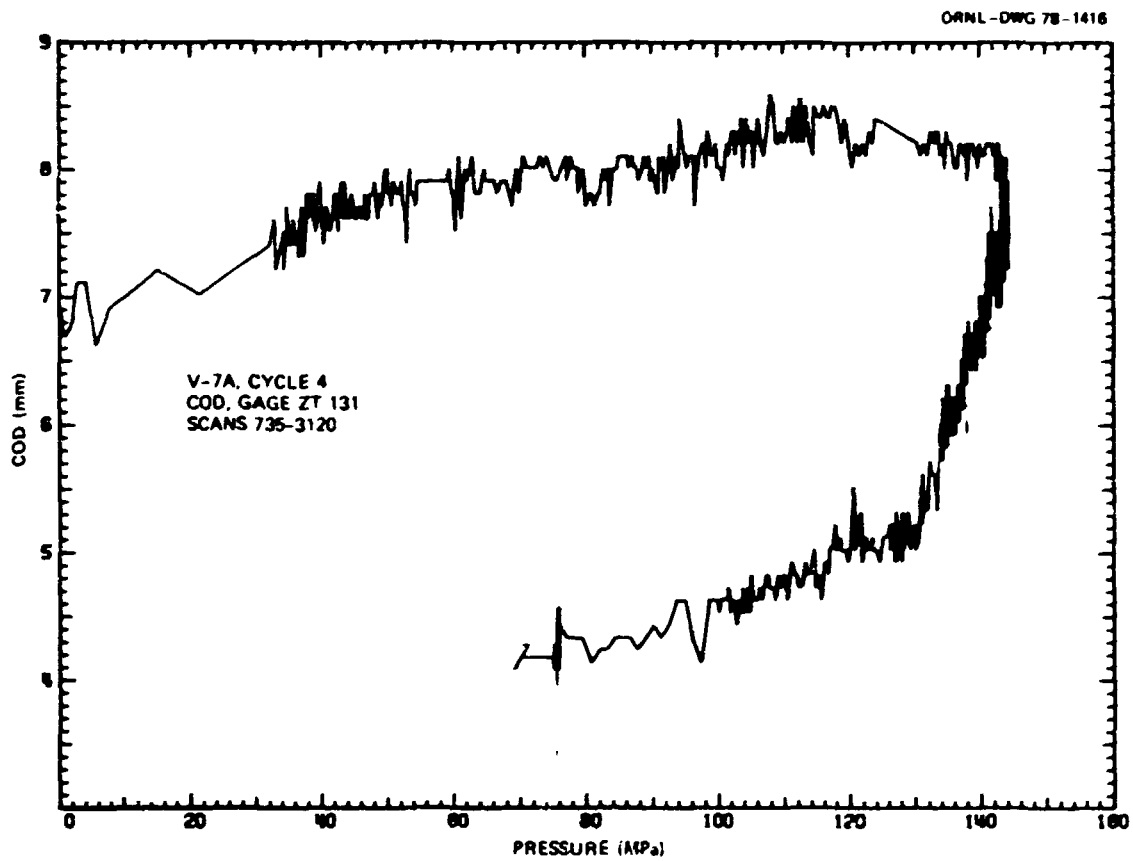

Fig. 4.24. Noisy response typical of COD gages ZT 130, 131, and 132. COD (ZT 131) vs pressure in 4th cycle (1 MPa = 145.04 psi; 1 mm = 0.0394 in.).

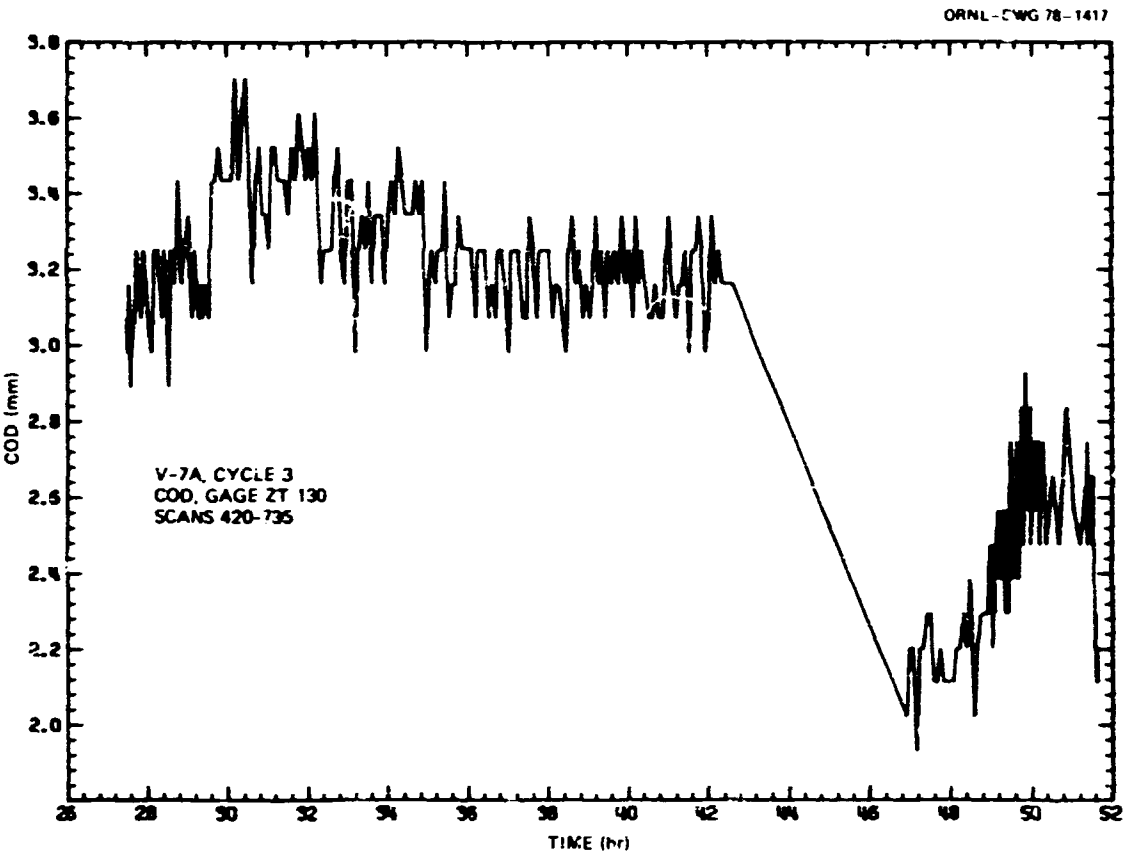

Fig. 4.25. Drift in COD (ZT 130) during hold period in 3rd cycle (1 mm = 0.0394 in.).

made after the test, and the sensitivity of the output to temperature changes was investigated. This work confirmed the original calibration. With curve-fitting analysis of these COD data, results are obtained that are believed to be valid. An illustration of this treatment of the data is given in Fig. 4.26. In the case illustrated, a correct interpretation of the data immediately after the time of rupture is not possible because of the disturbance the escaping fluid caused, but it would be reasonable to suppose that values of COD could be interpolated between the two sections of the fitted curve as indicated by the dashed line.

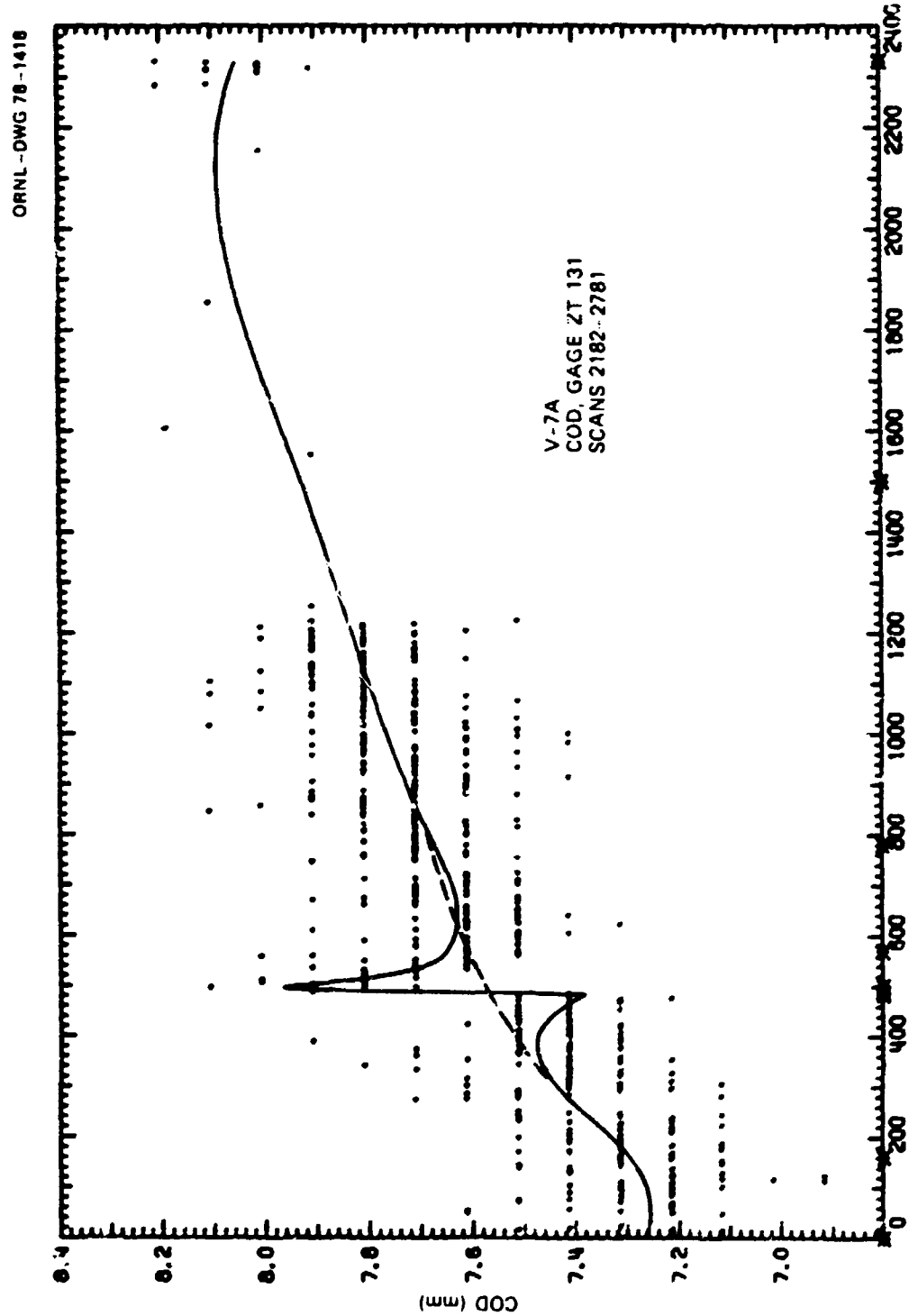

Fig. 4.26. Piecewise cubic spline fit of COD data from ZT 131; nominal time of rupture is at 484 sec on this plot (1 mm = 0.0394 in.).

References

1. C. L. Segaser, *System Design Description of the Intermediate Vessel Tests for the Heavy-Section Steel Technology Program*, ORNL/TM-2849 (June 1970), revised July 1973.

2. R. W. Derby et al., *Test of 6-Inch-Thick Pressure Vessels, Series 1: Intermediate Test Vessels V-1 and V-2*, ORNL-4895, Appendix A (February 1974).

5. TEST RESULTS

This chapter presents data and observations that generally characterize the behavior of vessel V-7A in terms of its response to pressure changes and its continued deformation during periods of constant load. A complete record of test data is included in this report on microfiche, as described in Appendix B. The behavior of the flaw during pressurization of the vessel is characterized by COD changes, nearby strains, location of the crack tip, and acoustic-emission activity. After the test, the flawed region was cut from the vessel and sectioned to determine the nature and extent of the final crack.

A complete report by M. P. Kelly and R. J. Schlamp of Dunegan/Endevco on acoustic-emission monitoring is included as Appendix C of this report.

5.1 General Response of Vessel to Pressure Changes

The overall response of the test section to increasing pressure is represented by circumferential strains measured around the vessel at the circumferential midplane of the flaw. The locations of strain gages that measured this response are defined in Fig. 5.1.

To give a simple illustration of the effect of cycling on strain behavior Figs. 5.2 and 5.3 show strain vs pressure over all four cycles for two inside locations, 180° and 270° from the flaw, respectively. These plots show that there was little hysteresis during the first three cycles at locations far from the flaw.

The inside and outside circumferential strains at 45° intervals from the flaw are shown in Fig. 5.4 through 5.10. The points plotted are a composite of the increasing load data from cycles 1, 2, and 4, which cover the full range of all test pressures.

The behavior of the region of the flaw over all cycles is summarized in the plots of one COD (ZT 129) and one outside strain near the end of the flaw (XE 104). Locations of sensors in the flaw region are shown in Fig. 5.11; the COD and strain plots are Figs. 5.12 and 5.13, respectively. Since deformations are high, there is substantial residual deformation upon unloading. However, one may notice that, in a subsequent reloading of the

vessel, the strain or COD tends to retrace the previous unloading line until the previous high pressure is reached again.

It has been noted in Chapter 4 that the long segments of constant outside COD while pressure is changing are probably artifacts and not true representations of vessel behavior. This applies to COD gages ZT 127, 128, and 129. See Table 4.3 for a summary of COD gage anomalies.

The COD data for the composite of cycles 1, 2, and 4 are presented in Figs. 5.14 and 5.15. Similarly, composite data for outside and inside strain gages near the flaw are given in Figs. 5.16 through 5.19.

5.2 General Response of Vessel to Sustained Load

When subjected to pneumatic loading, vessel V-7A exhibited a creeping deformation for some time after pumping stopped. This phenomenon had been noted in X-Y plots of strain and COD in previous (hydraulic) tests of intermediate vessels. The data system for V-7A, unlike that of earlier tests, was equipped to record the changes with time at nearly constant load. This behavior during sustained load is shown in Figs. 5.20 and 5.21 for strains far from the flaw and in Figs. 5.22 and 5.23 for nearby strains. A plot of pressure vs time for the time interval of these plots is shown in Fig. 5.24.

5.3 Sustained-Load Behavior of Flaw

The sustained-load behavior of the flaw is characterized by the changes in COD of the flaw and strains nearby. At several levels below maximum (rupture) pressure, the pressurization of V-7A was interrupted so that, even if the vessel had eventually burst, sustained load behavior would have been recorded near maximum load. The sustained-load period of greatest interest, since the vessel did not burst, is that following rupture. Plots of the CODs vs time for a period of about 30 min after rupture are shown in Figs. 5.25 and 5.26. The plots start at a time when the pressure is still rising, as shown in Fig. 5.24. These data indicate that the vessel was stable at the time of ligament rupture.

5.4 Response of Weld-Repair Zone to Pressure Changes

The observation of the behavior of the Section XI weld-repair zone was a secondary objective of the V-7A test. Accordingly, strain gages were placed in the repair zone 225° from the flaw, as shown in Fig. 5.27. Outside and inside strains at the center of the repair and in base metal at symmetrical locations with respect to the flaw centerline are presented in Figs. 5.28 through 5.31.

5.5 Ultrasonic Observation of Crack Tip

The ultrasonic monitoring of the crack growth in vessel V-7A was accomplished by K. K. Klindt by the arrangement shown in Fig. 5.32. This arrangement is different from that used in vessel V-7, in which the transducers were placed on the inside surface of the vessel for direct transmission to the crack tip.[1] In the arrangement for the V-7A test, the inside surface was used as a reflector from which to "bounce" the sound into the crack and the reflected sound back to the transducer. This less desirable arrangement was necessary because of the pressure-retaining membrane on the inside surface of V-7A in the region of the crack.

The V-7A method resulted in loss of signal strength and a confusing mixture of signals from irrelevant reflectors at about the same time as the signal from the crack. Interpretation was difficult; however, with close observation throughout the test, the relevant signal was separated from the others with a fair degree of assurance. By calibration of the system with an external block 25.4 mm (1 in.) thick, it was inferred that the machined ligament in the vessel was only 23 mm (0.91 in.) thick, while it was supposed to be 25.4 mm. This ultrasonic measurement was confirmed in the posttest examination of the vessel.

Crack depth vs vessel pressure for transducer 2 (XE 141) is plotted in Fig. 5.33. The ultrasonically measured crack depth is reckoned from the machined surface at the bottom of the notch. The first pressure cycle to 66.1 MPa (9.6 ksi) did not open the EB weld crack sufficiently to make it detectable in the V-7A test. [With the V-7 arrangement of transducers, the EB weld crack was detected at less than 35 MPa (5 ksi).] On the second

cycle, the crack became visible at 115 MPa (16.7 ksi), and its depth increased with pressure to 11 mm (0.45 in.) at the peak pressure in the cycle, 126 MPa (18.3 ksi). During the third cycle, the crack indication was visible at the same depth from a pressure of 43 MPa (6.2 ksi) near the beginning of the cycle until 83 MPa (12 ksi), after which the point from which a reflection was received progressed to a depth of 14 mm (0.55 in.) at the peak pressure in the cycle, 121 MPa (17.5 ksi). The ultrasonic indication during the fourth cycle followed the path of the third except for an unexplained excursion at 90 to 97 MPa (13 to 14 ksi). When the pressure reached the previous maximum pressure [126 MPa (18.3 ksi)], the signal began to indicate a more rapid rate of crack growth. After 134 MPa (19.5 ksi) was reached, the crack grew uniformly with increasing pressure until just before vessel failure when the confusion of signals made interpretation impossible.

Transducer 3 (XE 140) ceased to function properly after the vessel test temperature was reached.

Transducers 1 (XE 143) and 4 (XE 142) failed to detect any crack at the end of the notch until near the end of cycle 4. At 134 MPa (19.5 ksi), transducer 1 showed the crack to be at a depth of 15 mm (0.6 in.) from the sloping machined surface of the notch. Transducer 4 gave no definite indication of any crack extension beyond the EB weld depth.

5.6 Posttest Characterization of Flaw

After the test, the flawed region of vessel V-7A was examined, local deformations and gross dimensions were measured, and the cracked region was cut out and examined.

Figure 5.34 shows the creased inside surface of the vessel beneath the machined notch. A plaster cast of the creased region was made and sectioned for measurement of the local deformations. In the central 100 mm (4 in.), the crease is sharp and about 3 mm (0.1 in.) deep relative to the cylindrical surface in this locality. This area was inspected visually with the aid of dye penetrant and Zyglow. No evidence of the crack could be found by this means.

When the flawed region was flame cut from the vessel, the fracture along the crease opened so that a crack over 100 mm long (4 in.) was clearly visible, as shown in Fig. 5.35. The cutting operation removed the posttest residual compressive load, allowed the crack to open, and possibly allowed some additional tearing along the inside surface. The surface of the unruptured patch is shown in Fig. 5.36. As seen in this photograph, the patch deformed smoothly and bridged the opening of the vessel without being marked by the edges of the crack. In Figs. 5.34 to 5.36, the linear markings transverse to the crease are vestiges of the patch spacer wires on the vessel surface and indentations made by the wires on the patch.

The posttest appearance of the crack from outside the vessel is shown in Fig. 5.37. The residual crack opening at the base of the machined notch was 3.5 to 4.0 mm wide (0.14 to 0.16 in.). Photographs of the crack opening in Figs. 5.38 and 5.39, which were taken after the flaw was cut from the vessel, show the fibrous appearance of the crack beyond the smooth EB weld crack.

The block removed from the vessel (Fig. 5.40) was chilled in liquid nitrogen and broken open along the plane of the crack to expose the fracture surfaces (Fig. 5.41). A detailed fractographic examination of the fracture was performed by D. A. Canonico and R. S. Crouse, whose report is found in Appendix I. The principle features shown in the photograph of Fig. 5.41 are identified schematically in Fig. 5.42.

The EB weld crack was found to be nonuniform in depth along the sloping ends of the flaw and to be deeper than expected along the ligament, namely, about 13 mm (0.51 in.) rather than 8 mm (0.31 in.). The machined ligament (before EB weld cracking and necking) was found to be 23 mm thick (0.91 in.) rather than the nominal 25.4 mm (1 in.) planned. This discrepancy was discovered during the test by the ultrasonic instrumentation.

The crack extensions axially were variable up to about 13 mm (0.51 in.), confirming the measurement made ultrasonically during the test by transducer XE 143. Crack extensions in all regions were by a dimple fracture mode, which is indicative of ductile tearing. Canonico concluded, from the fractographic examination, that the crack breached the inside surface of the vessel over a distance of 73 mm (2.9 in.).

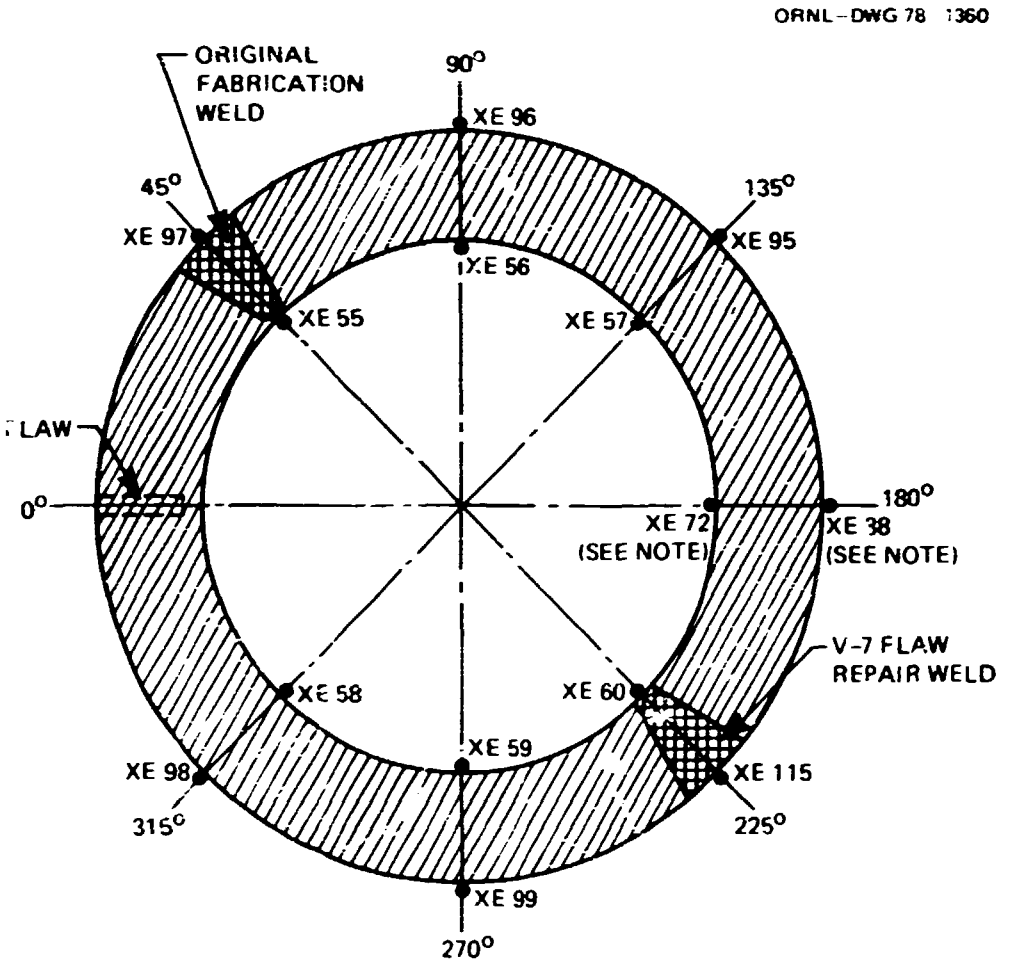

NOTE: XE 72 AND XE 88 ARE 51 mm (2 in.) FROM THE CIRCUMFERENTIAL MIDPLANE OF THE FLAW IN V-7A. THESE ARE PLOTTED BECAUSE ONE MIDPLANE GAGE WAS DEFECTIVE AND THE OTHER WAS ON THE VISHAY SYSTEM, WHICH RECORDED FEWER DATA.

Fig. 5.1. Locations of strain gages in circumferential midplane of V-7A flaw.

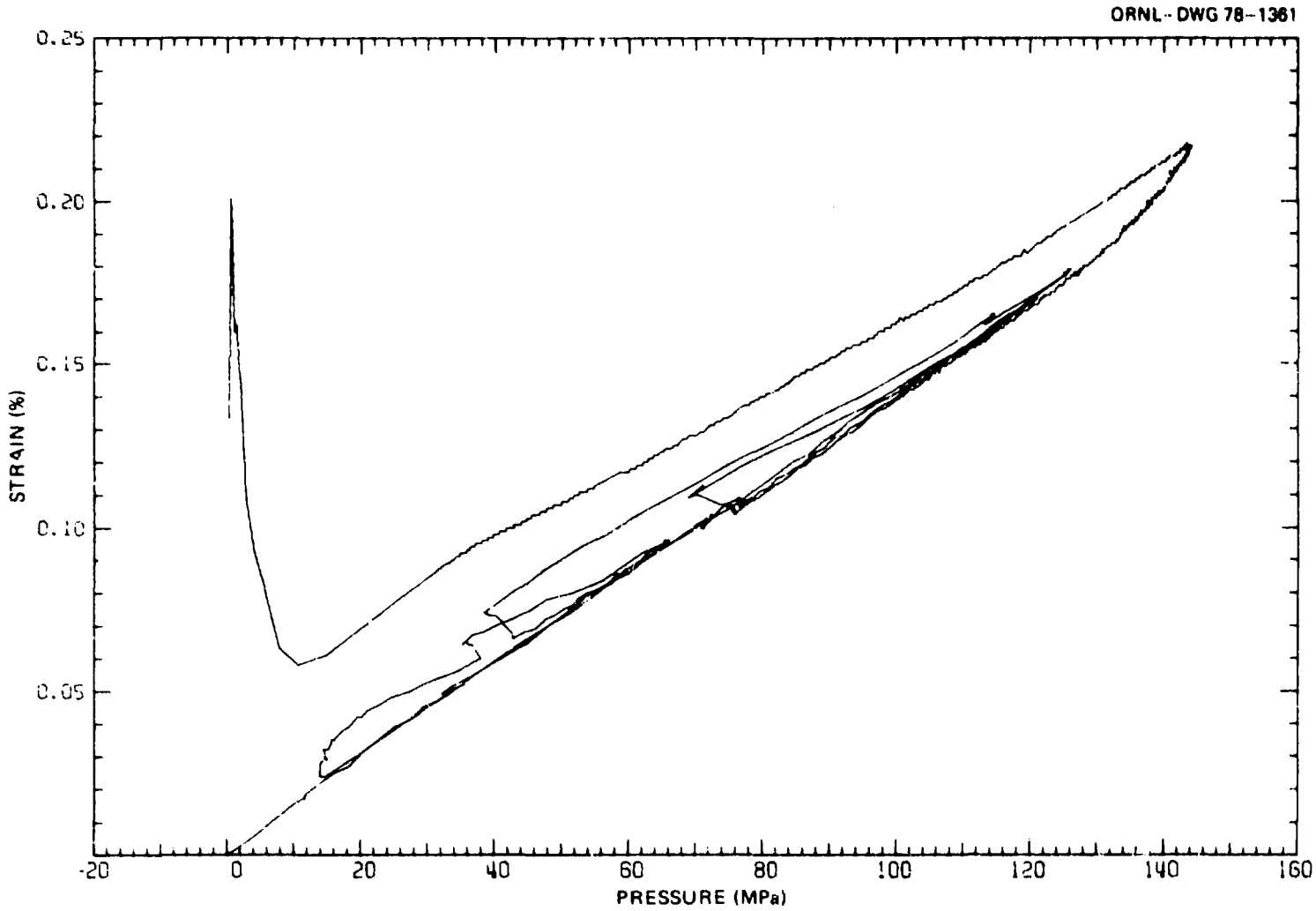

Fig. 5.2. Inside circumferential strain (XE 72) 180° from flaw vs pressure during four cycles in V-7A test.

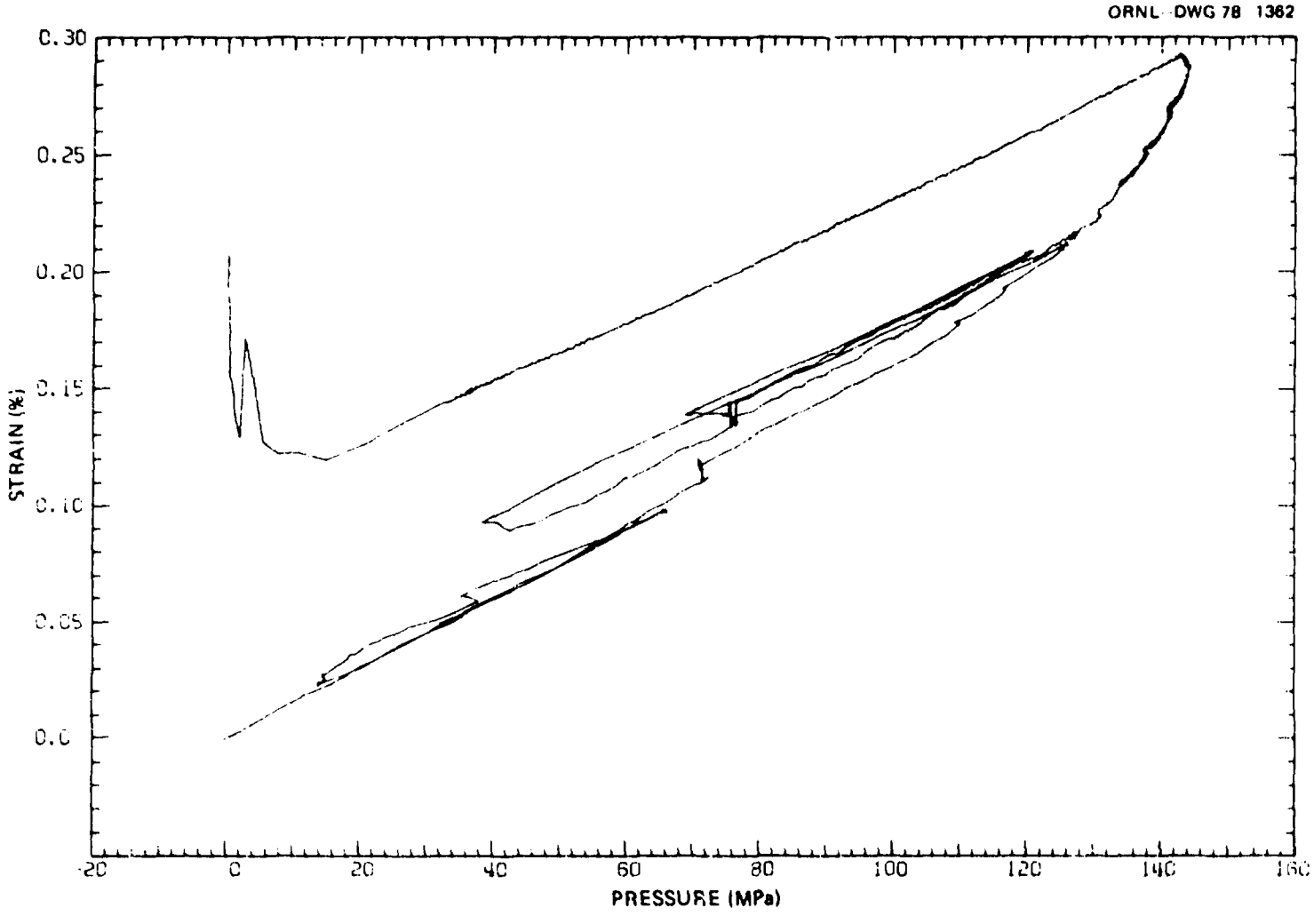

Fig. 5.3. Inside circumferential strain (XE 59) 270° from flaw vs pressure during four cycles in V-7A test.

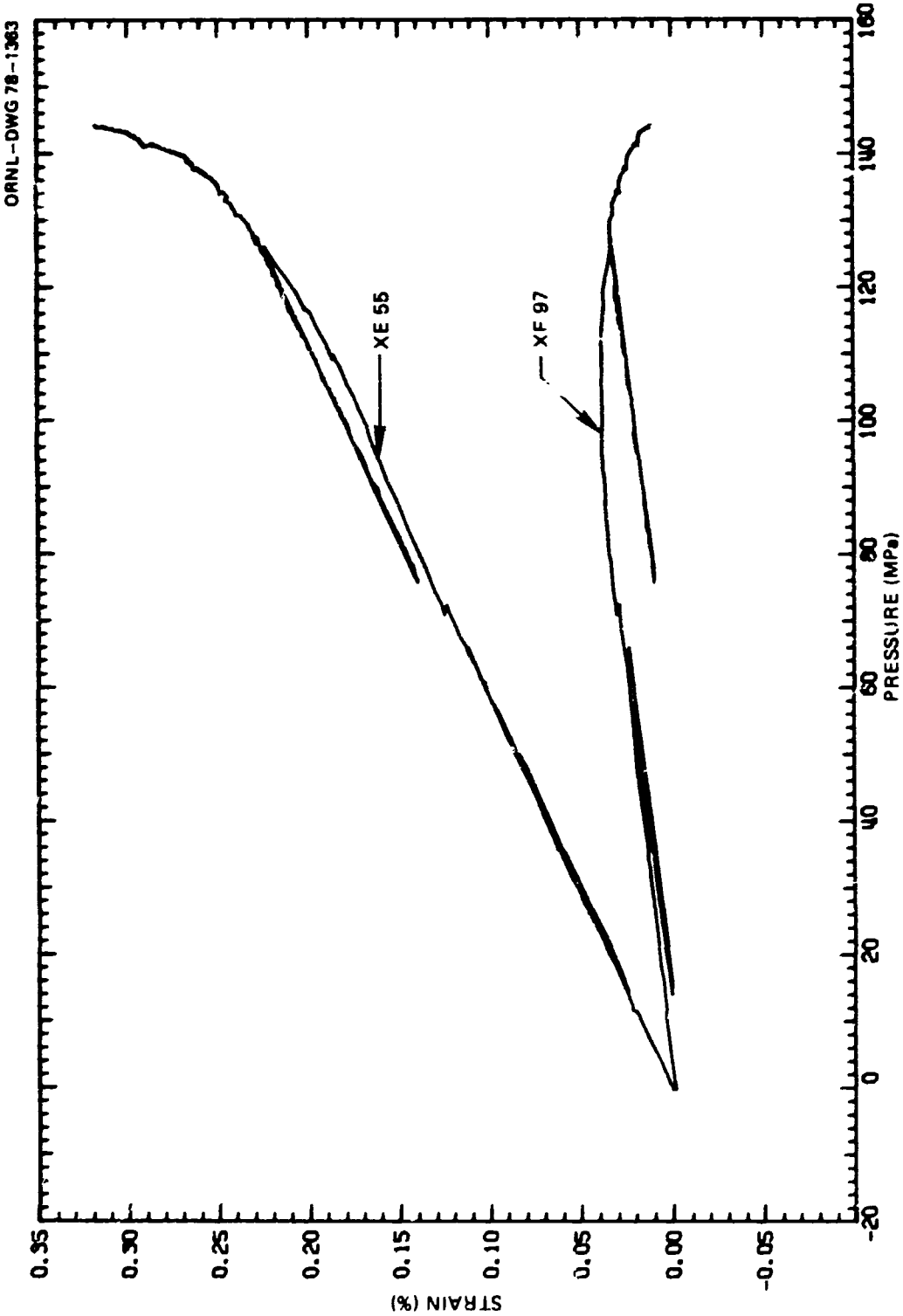

Fig. 5.4. Inside (XE 55) and outside (XF 97) circumferential strain 45° from flaw vs pressure. Data for rising pressure only plotted for cycles 1, 2, and 4.

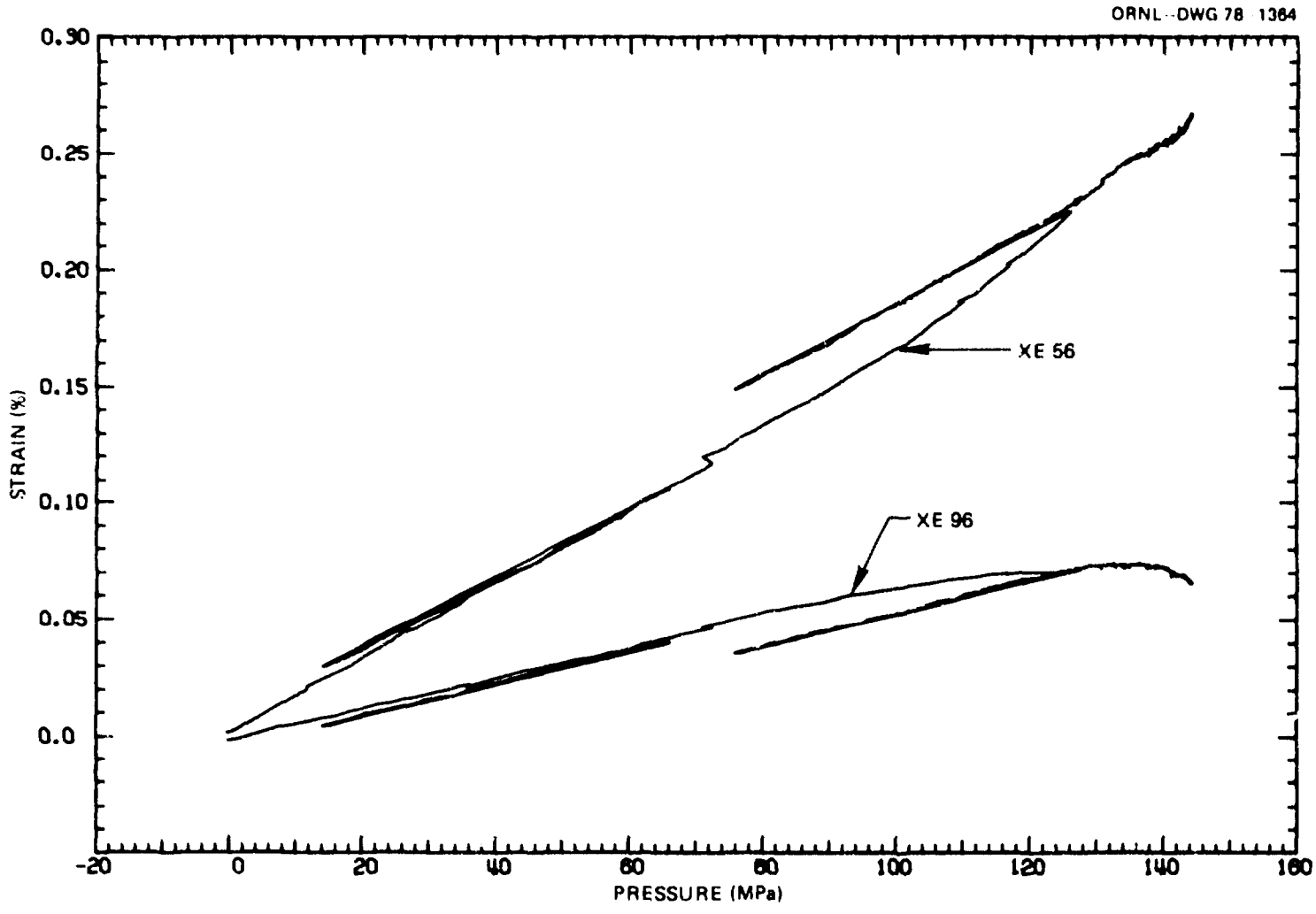

Fig. 5.5. Inside (XE 56) and outside (XE 96) circumferential strain 90° from flaw vs pressure. Data for rising pressure only plotted for cycles 1, 2, and 4.

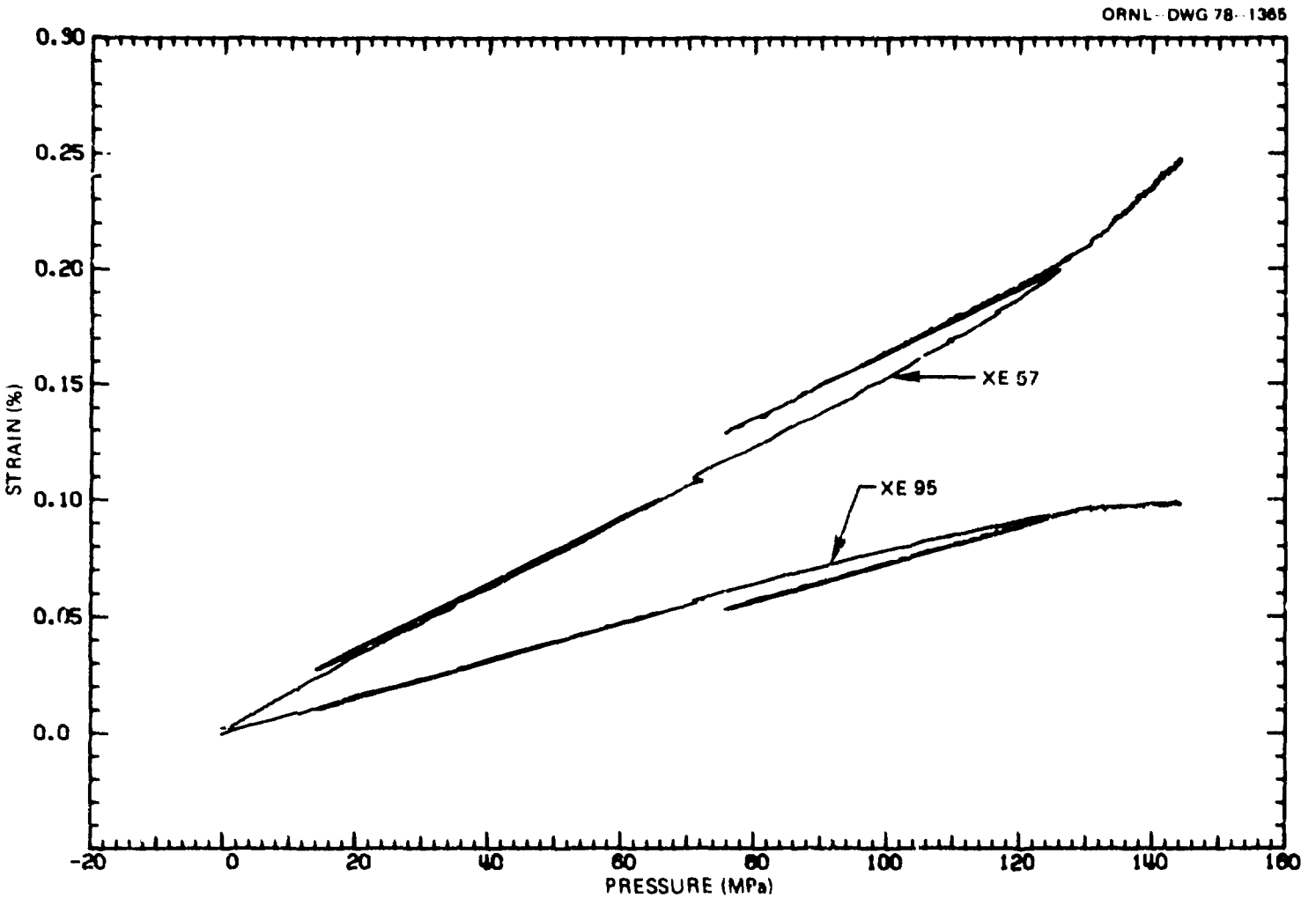

Fig. 5.6. Inside (XE 57) and outside (XE 95) circumferential strain 135° from flaw vs pressure. Data for rising pressure only plotted for cycles 1, 2, and 4.

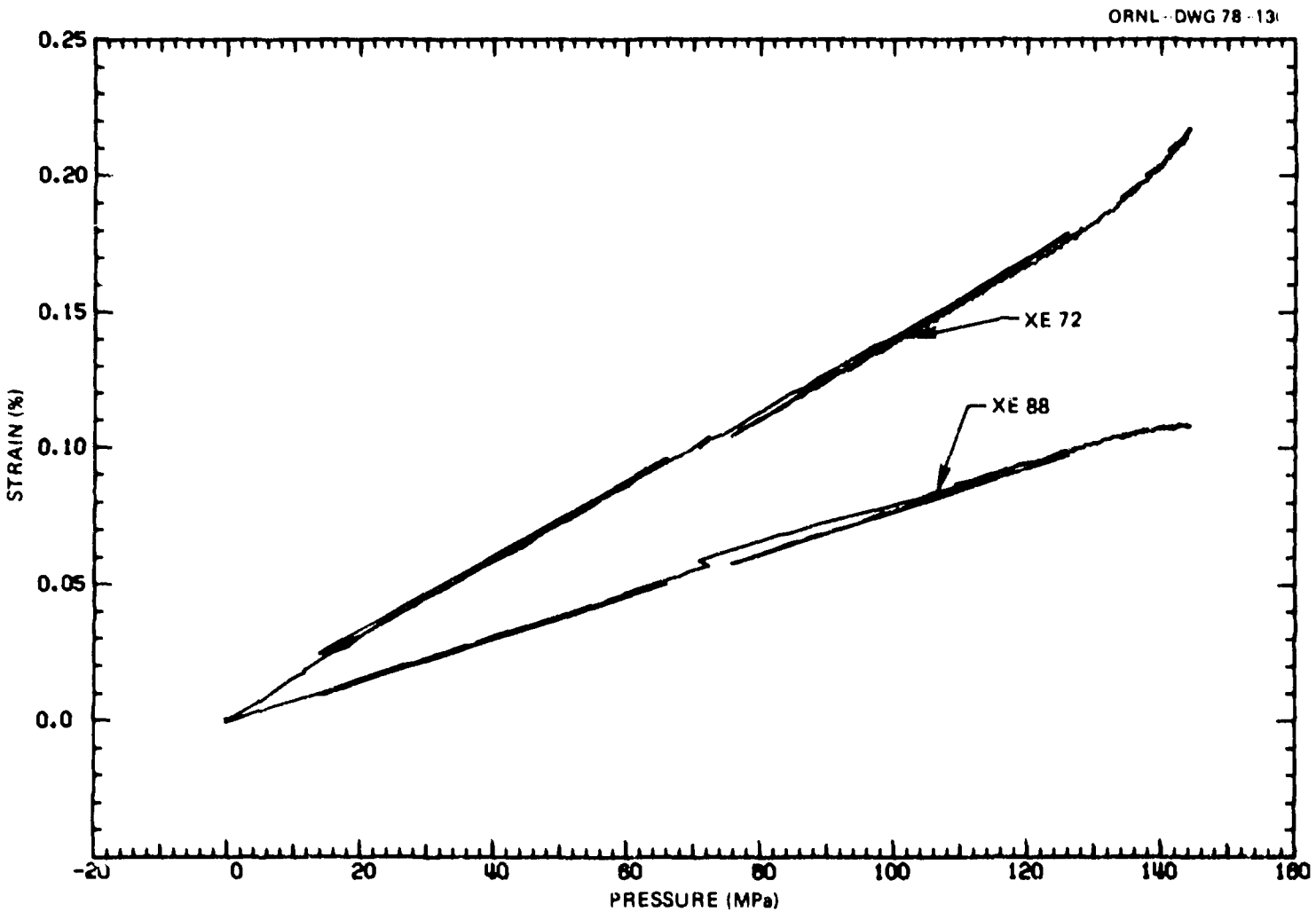

Fig. 5.7. Inside (XE 72) and outside (XE 88) circumferential strain 180° from flaw vs pressure. Data for rising pressure only plotted for cycles 1, 2, and 4.

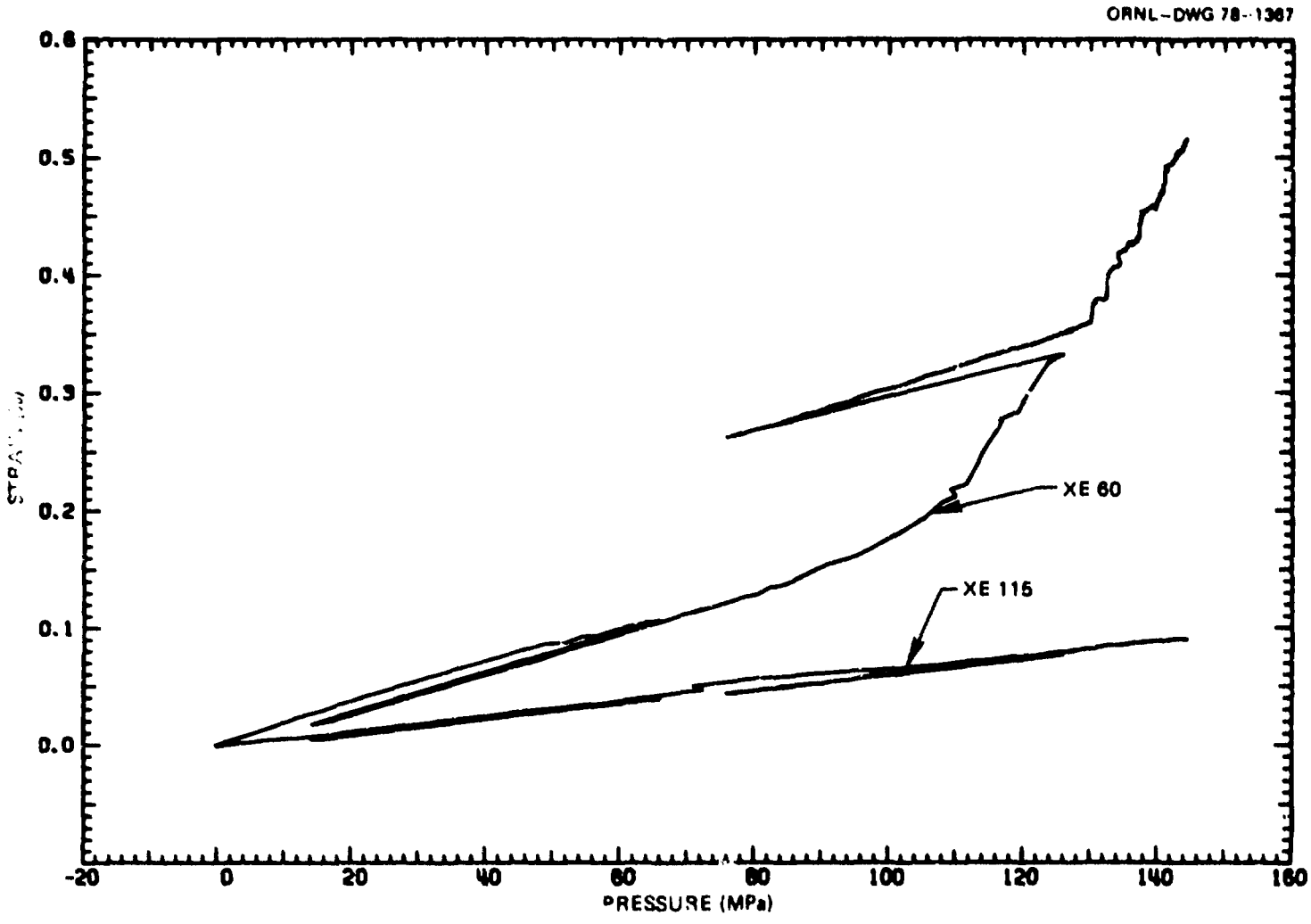

Fig. 5.8. Inside (XE 60) and outside (XE 115) circumferential strain 225° from flaw vs pressure. Data for rising pressure only plotted for cycles 1, 2, and 4.

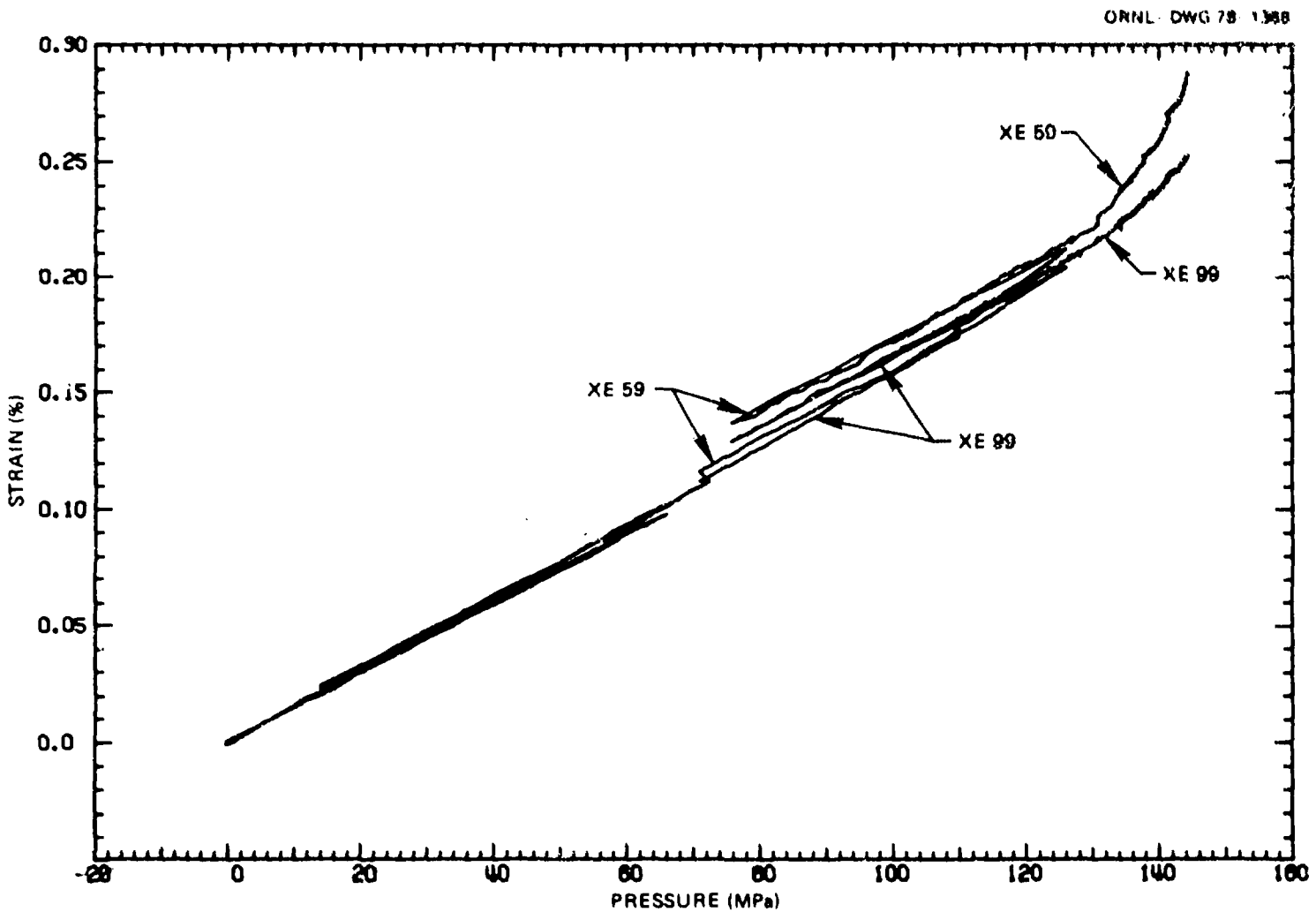

Fig. 5.9. Inside (XE 59) and outside (XE 99) circumferential strain 270° from flaw vs pressure. Data for rising pressure only plotted for cycles 1, 2, and 4.

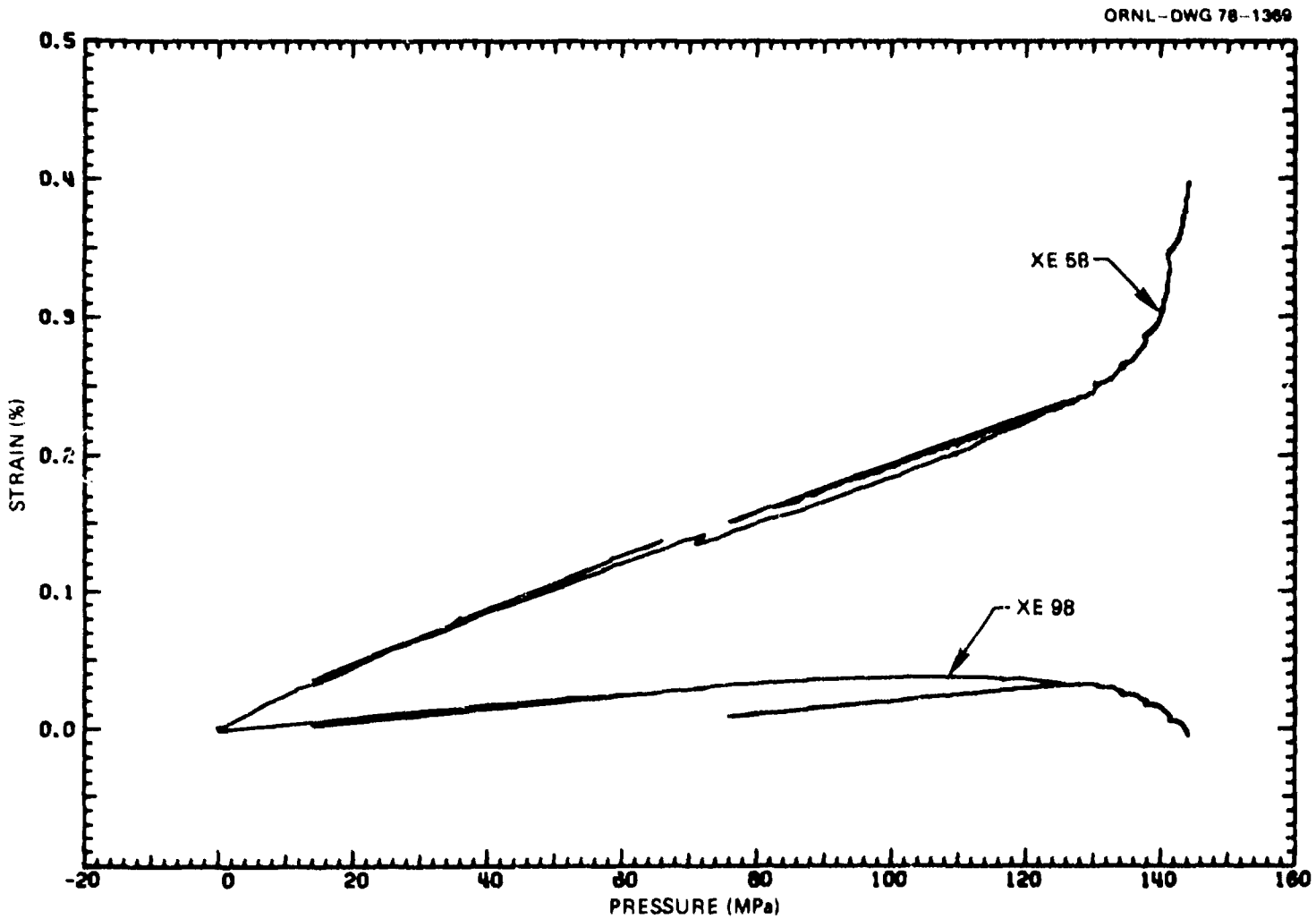

Fig. 5.10. Inside (XE 58) and outside (XE 98) circumferential strain 315° from flaw vs pressure. Data for rising pressure only plotted for cycles 1, 2, and 4.

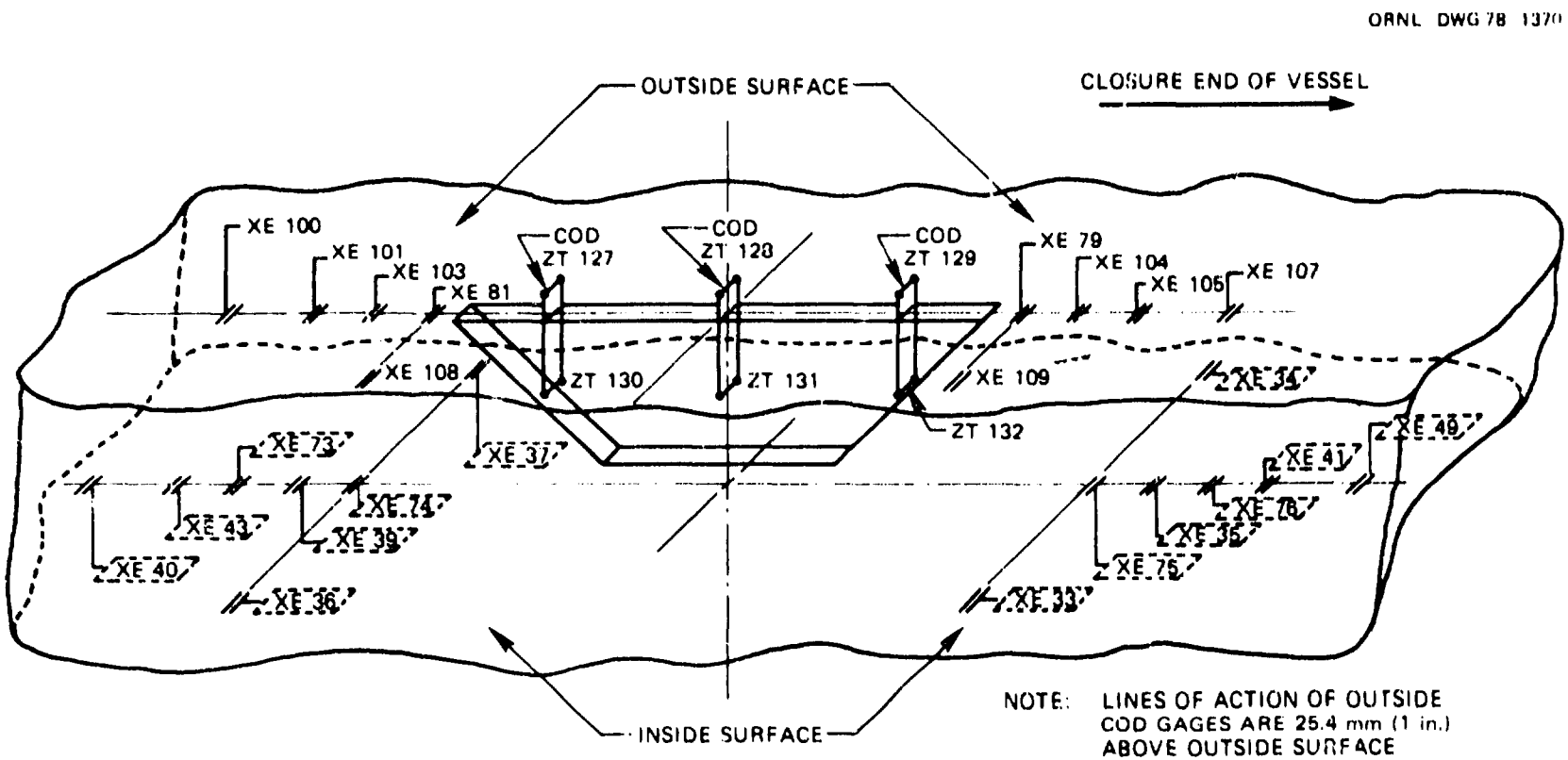

Fig. 5.11. Locations of sensors near the flaw in V-7A.

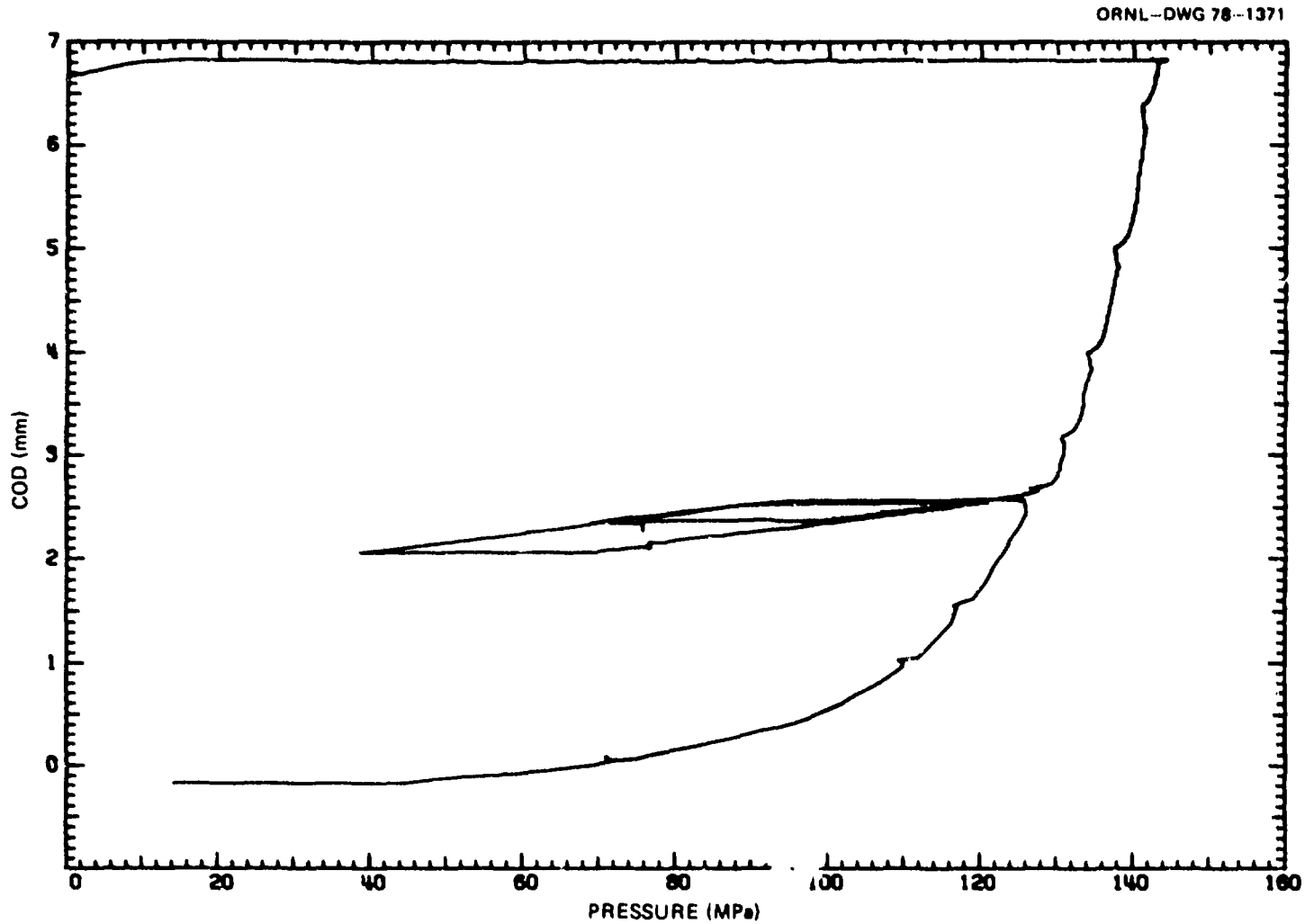

Fig. 5.12. Outside COD (ZT 129) vs pressure during cycles 2, 3, and 4.

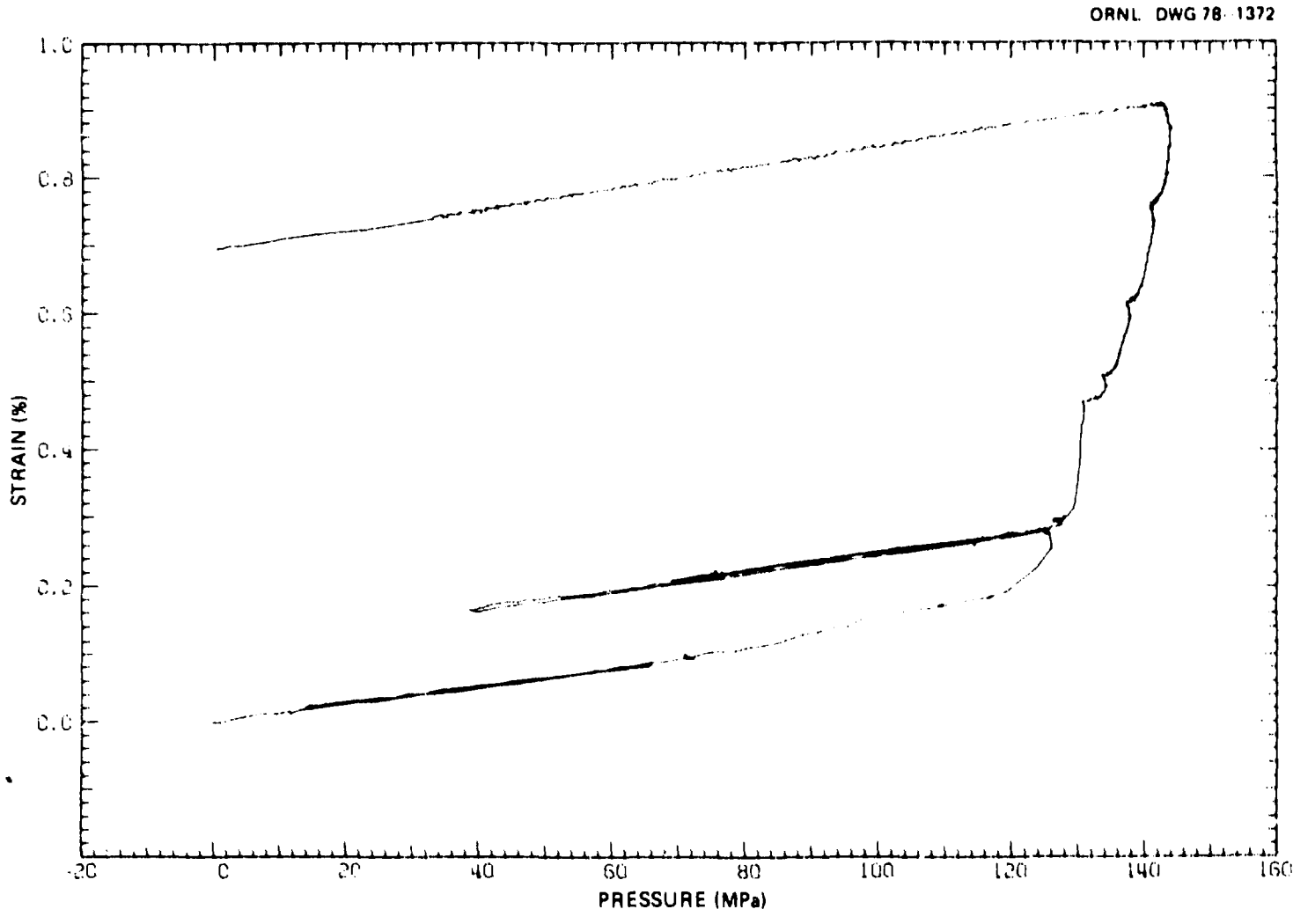

Fig. 5.13. Outside circumferential strain (XE 104) in the axial plane of the flaw 76 mm (3 in.) from the end of the machined notch vs pressure during all four cycles.

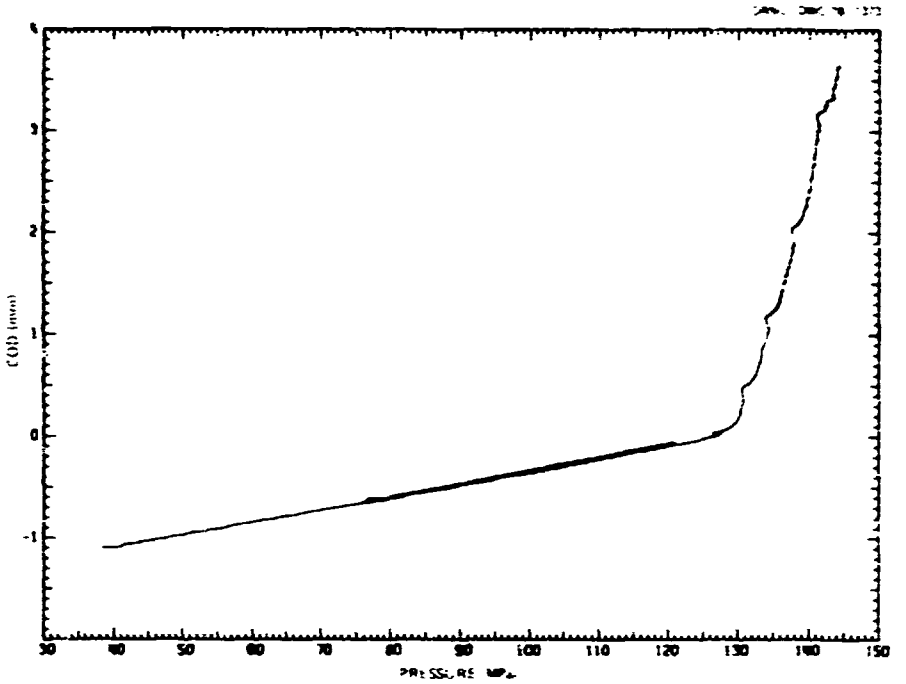

Fig. 5.14. Outside COD (ZT 128) vs pressure. Data for rising pressure only plotted for cycles 3 and 4.

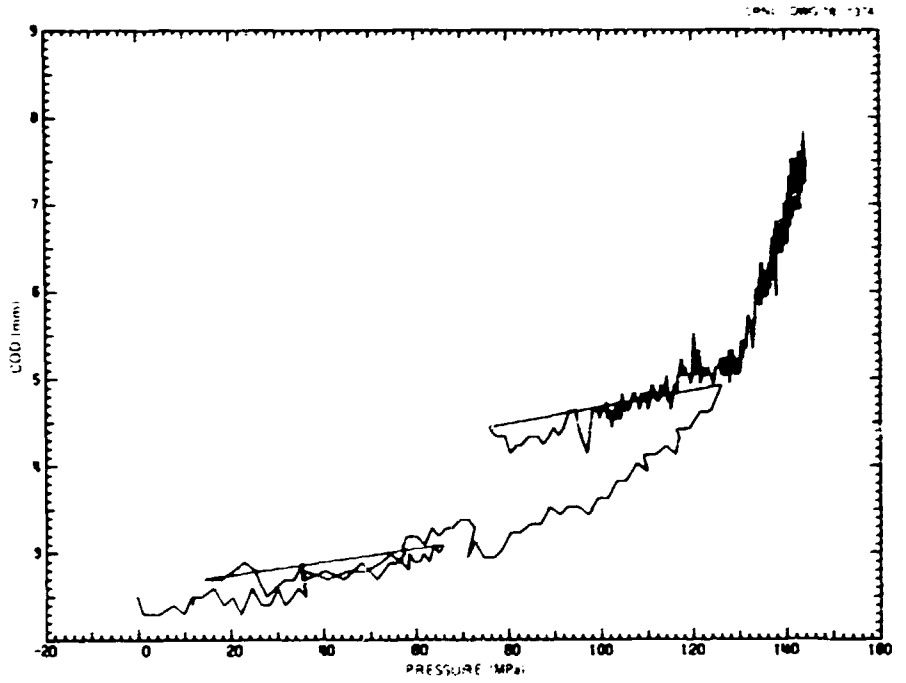

Fig. 5.15. Mid-depth COD (ZT 131) vs pressure. Data for rising pressure only plotted for cycles 1, 2, and 4.

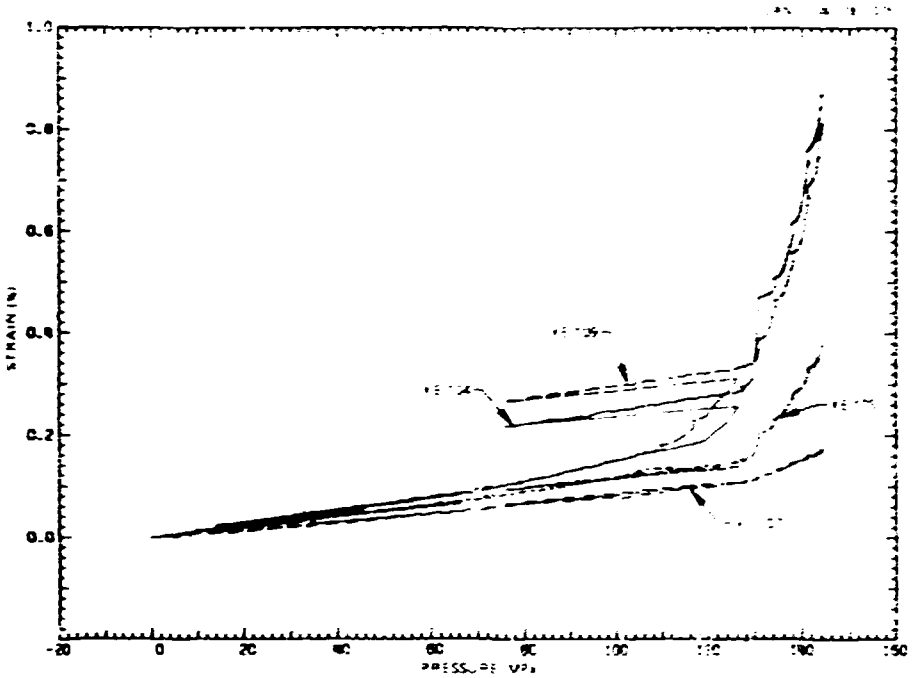

Fig. 5.16. Outside circumferential strains near the flaw at closure end vs pressure. Data for rising pressure only plotted for cycles 1, 2, and 4.

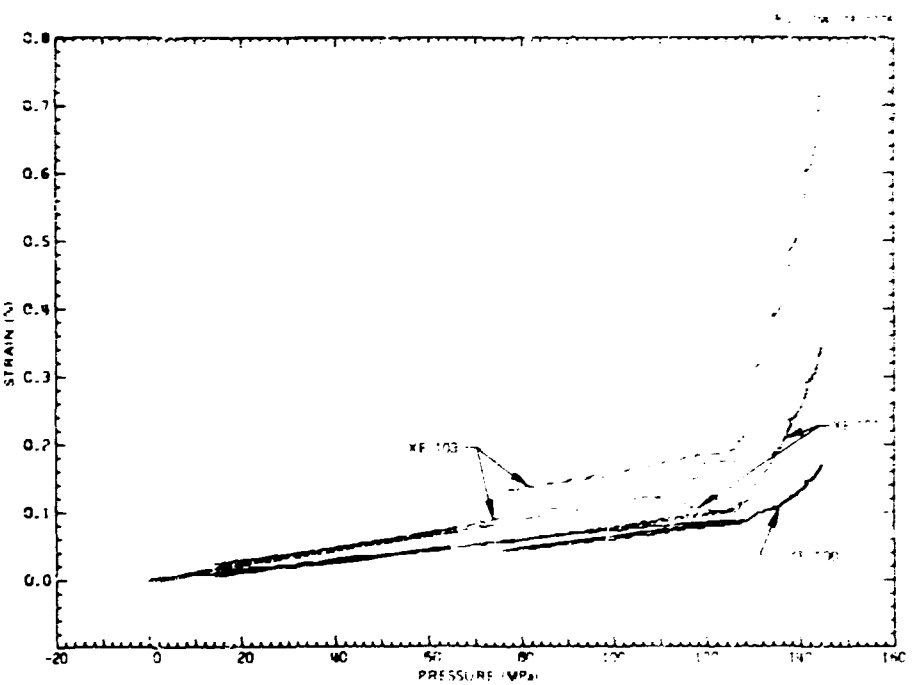

Fig. 5.17. Outside circumferential strains near the flaw at hemispherical end vs pressure. Data for rising pressure only plotted for cycles 1, 2, and 4.

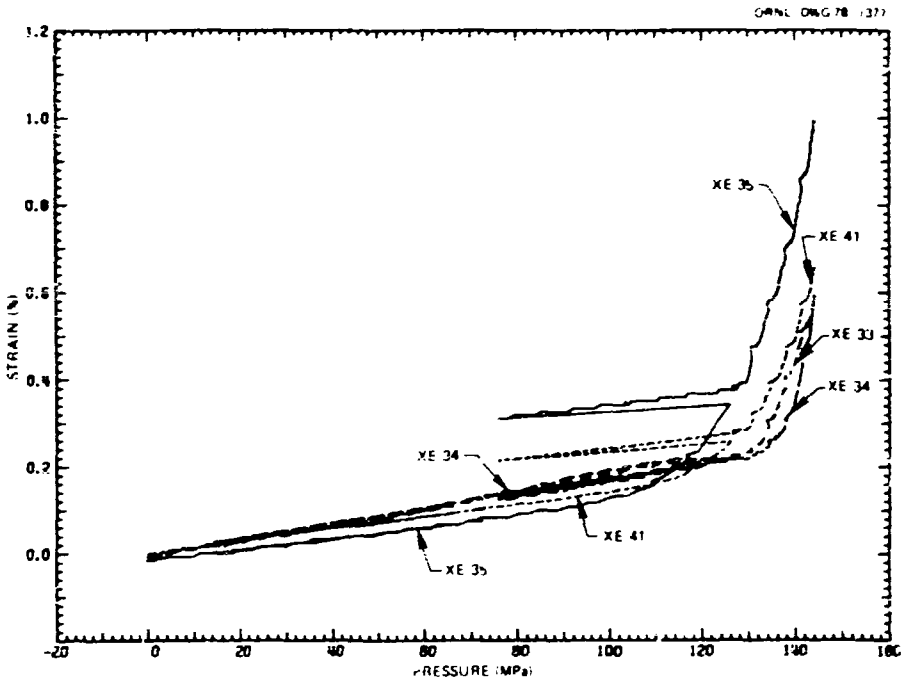

Fig. 5.18. Inside circumferential strains near the flaw at closure end vs pressure. Data for rising pressure only plotted for cycles 1, 2, and 4.

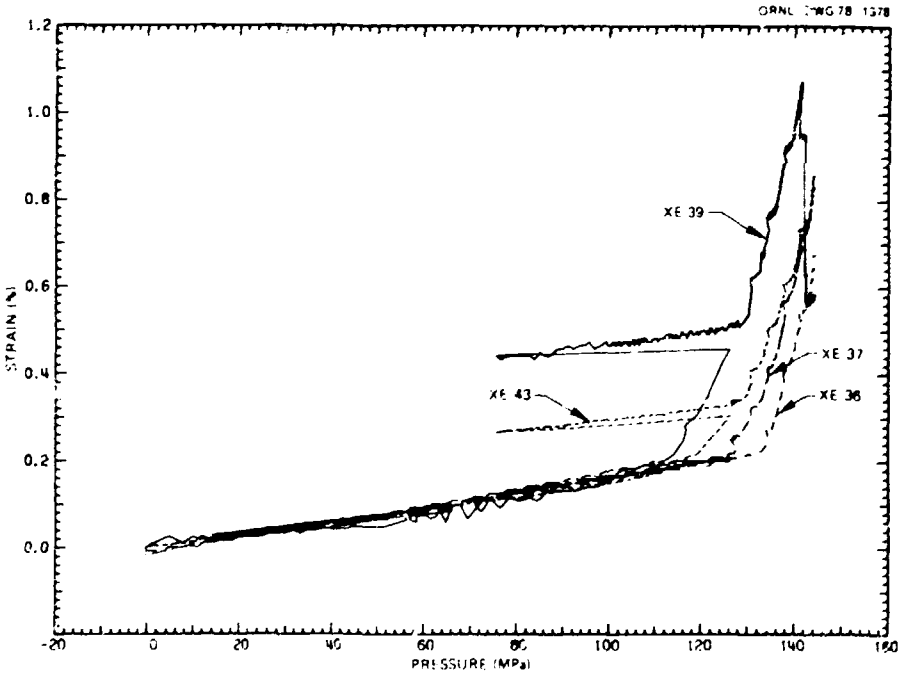

Fig. 5.19. Inside circumferential strains near the flaw at hemispherical end vs pressure. Data for rising pressure only plotted for cycles 1, 2, and 4.

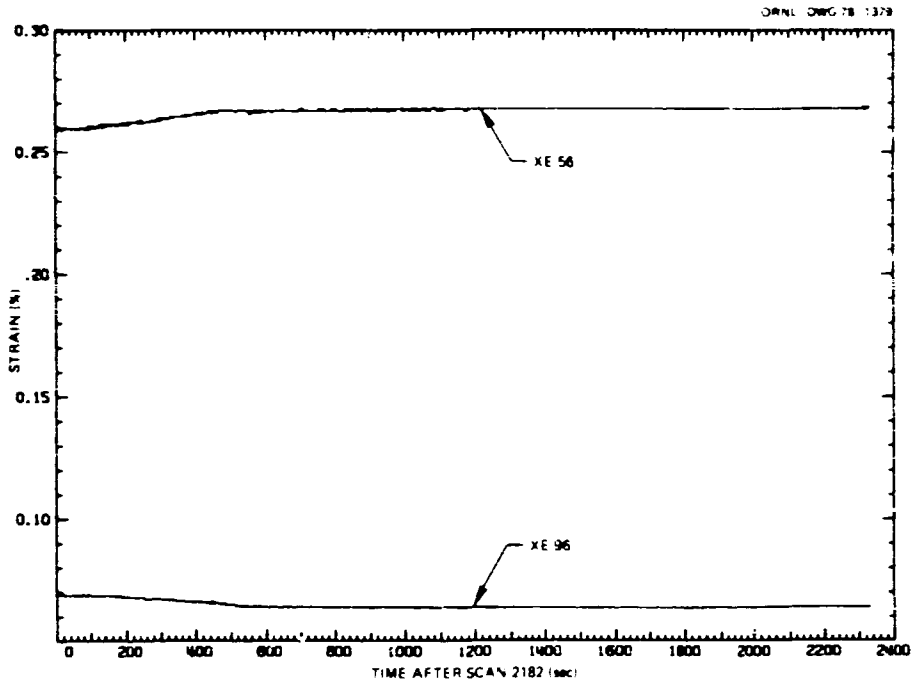

Fig. 5.20. Inside (XE 56) and outside (XE 96) circumferential strain 90° from flaw vs time during postrupture sustained load.

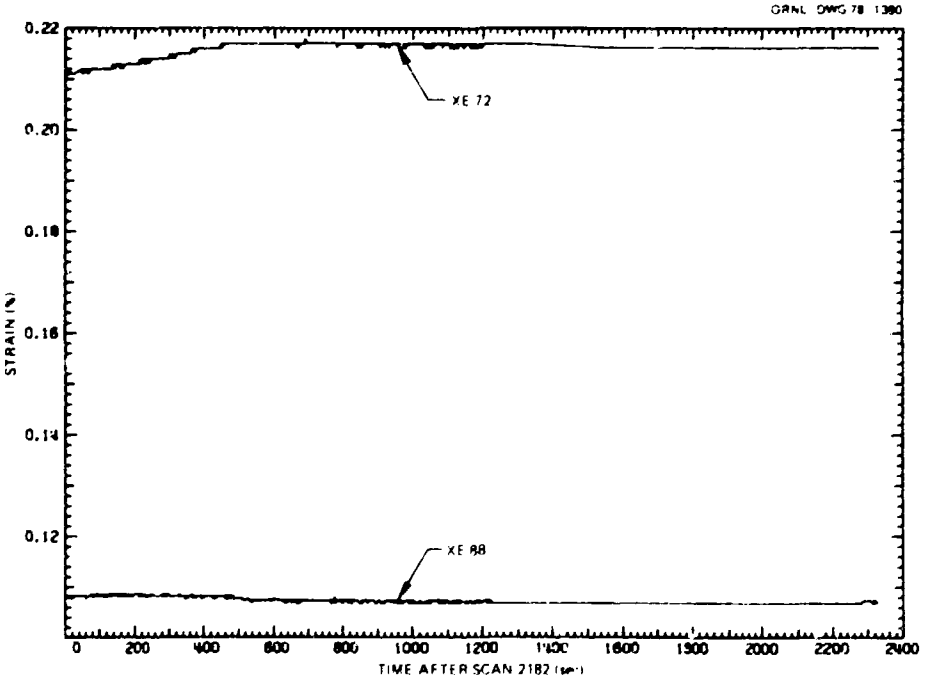

Fig. 5.21. Inside (XE 72) and outside (XE 88) circumferential strain 180° from flaw vs time during postrupture sustained load.

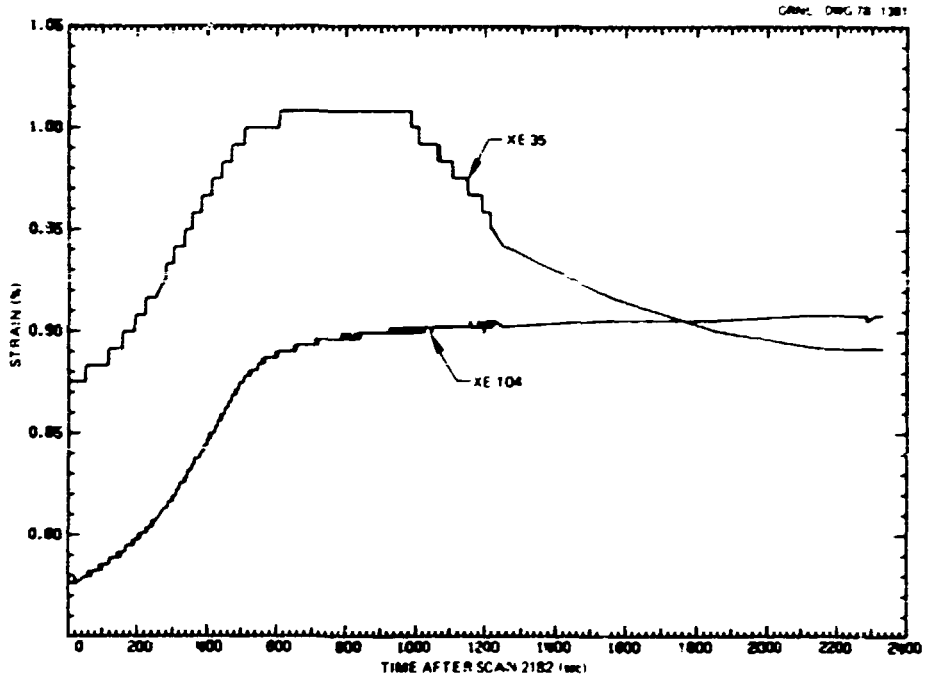

Fig. 5.22. Inside (XE 35) and outside (XE 104) circumferential strain near flaw at closure end vs time during postrupture sustained load.

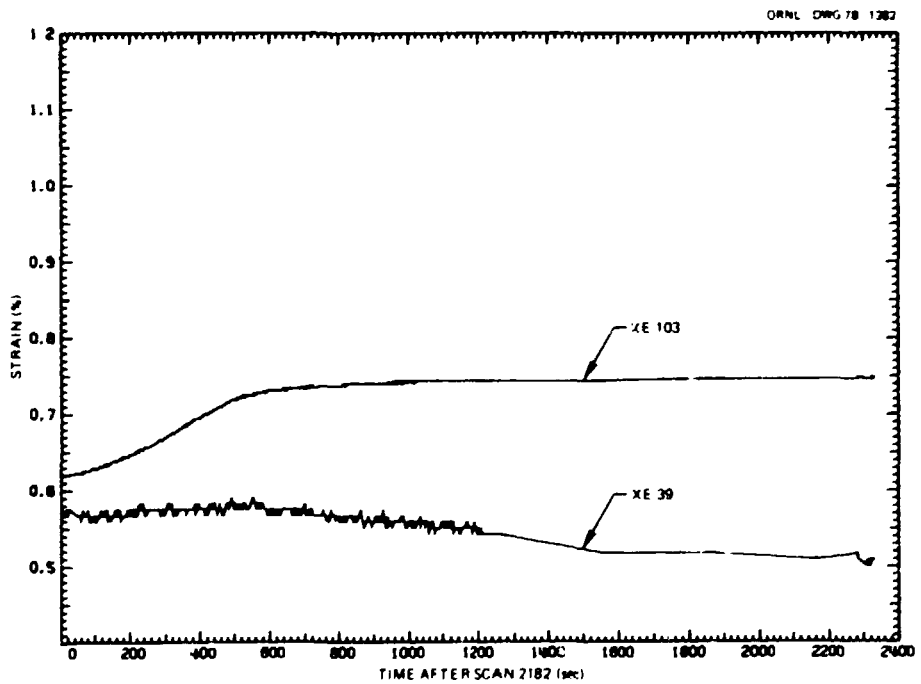

Fig. 5.23. Inside (XE 39) and outside (XE 103) circumferential strain near flaw at hemispherical end vs time during postrupture sustained load.

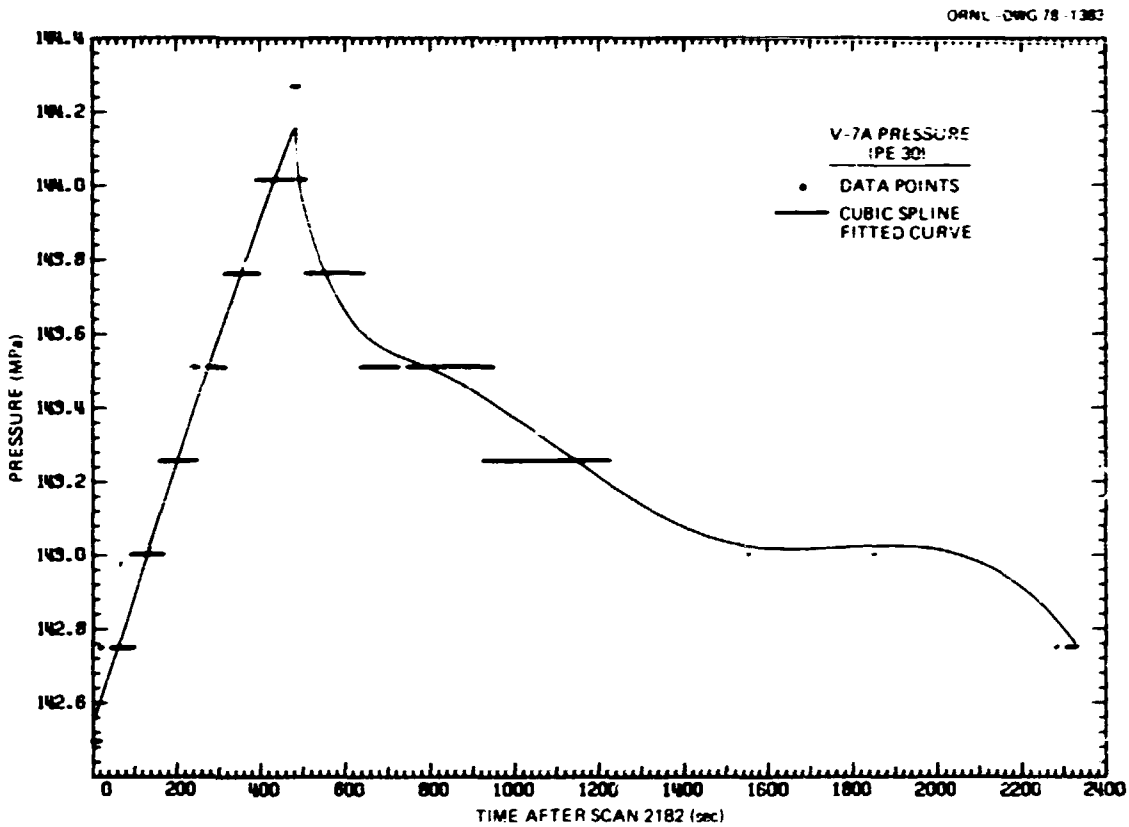

Fig. 5.24. Vessel pressure vs time during postrupture sustained load.

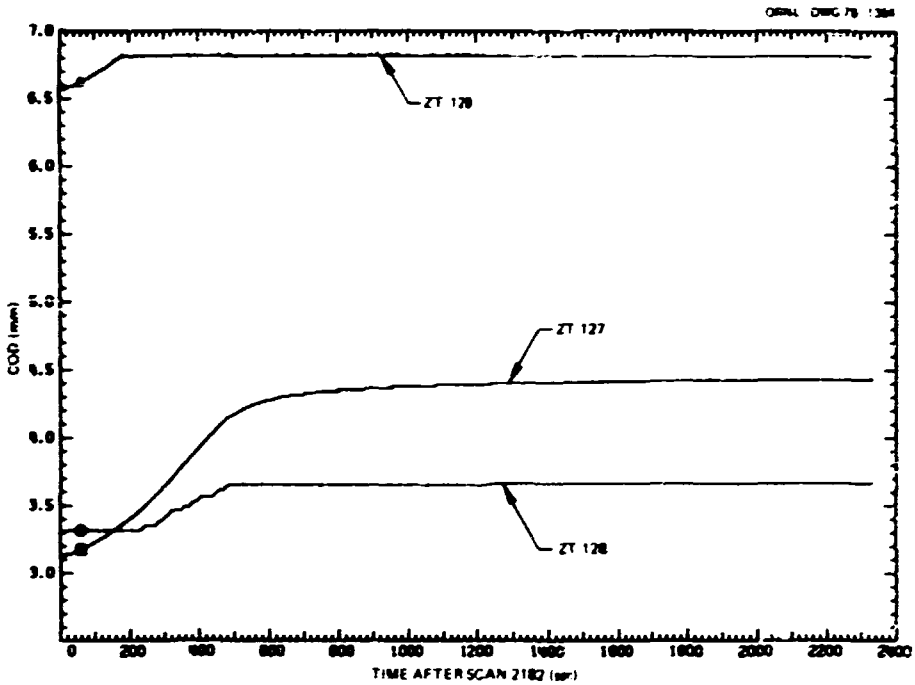

Fig. 5.25. Outside COD vs time during postrupture sustained load. The completely constant responses of gages ZT 128 and ZT 129 may be artifacts and not real.

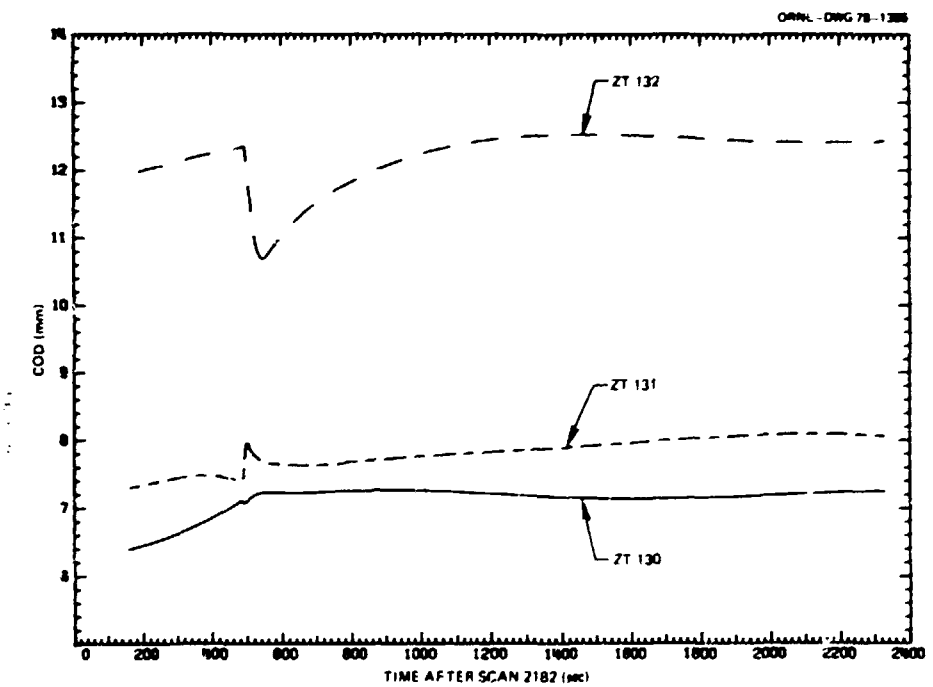

Fig. 5.26. Mid-depth COD vs time during postrupture sustained load. Data fitted by piecewise cubic splines.

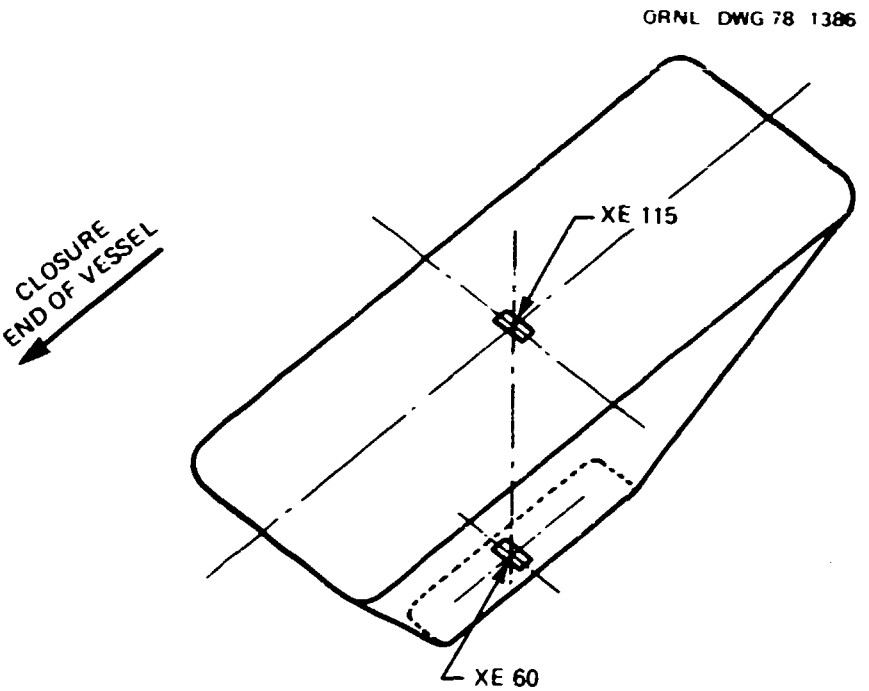

Fig. 5.27. Layout of strain gages in weld-repair zone.

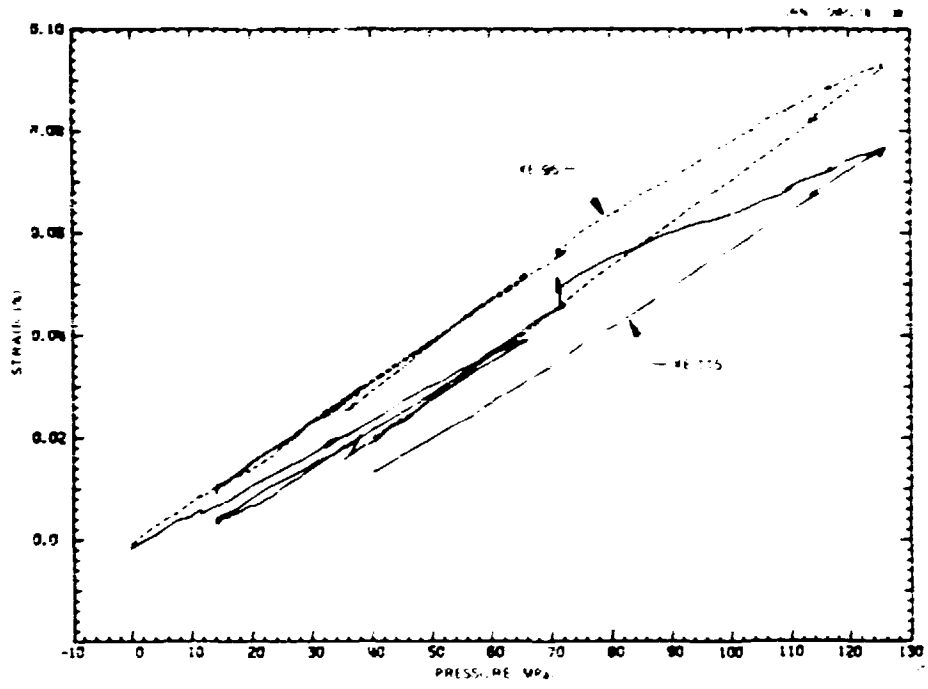

Fig. 5.28. Outside circumferential strains at center of repair zone (XE 115) and at symmetrical location (XE 95) vs pressure during cycles 1 and 2.

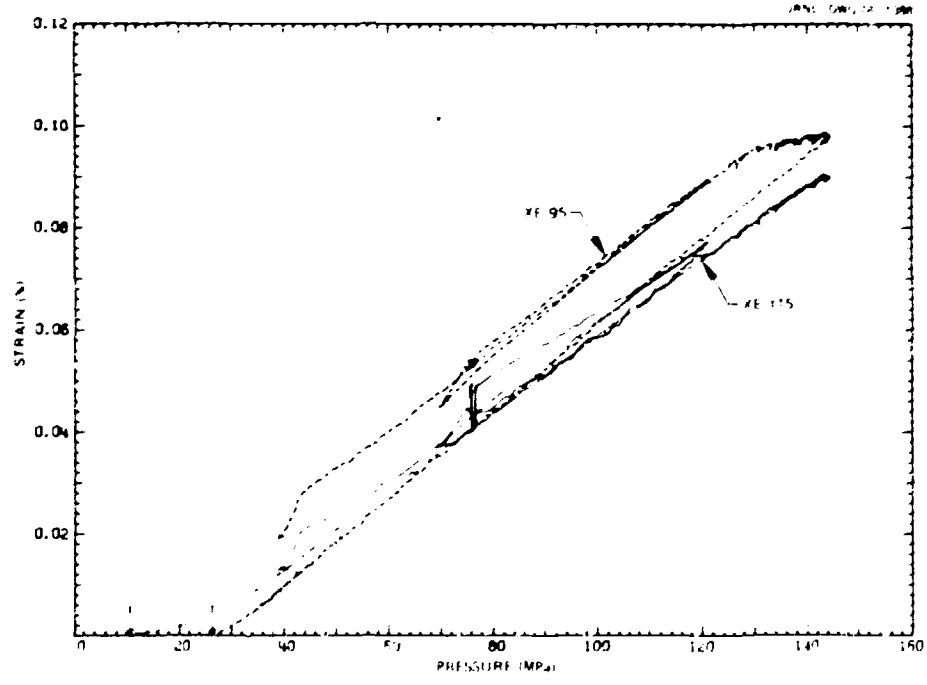

Fig. 5.29. Outside circumferential strains at center of repair zone (XE 115) and at symmetrical location (XE 95) vs pressure during cycles 3 and 4.

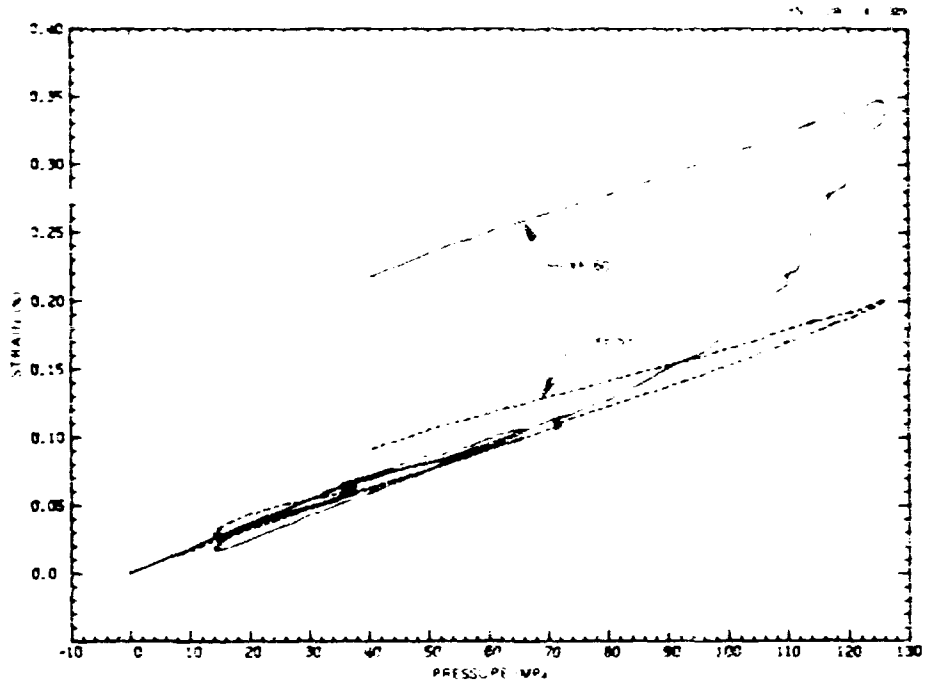

Fig. 5.30. Inside circumferential strains at center of repair zone (XE 60) and at symmetrical location (XE 57) vs pressure during cycles 1 and 2.

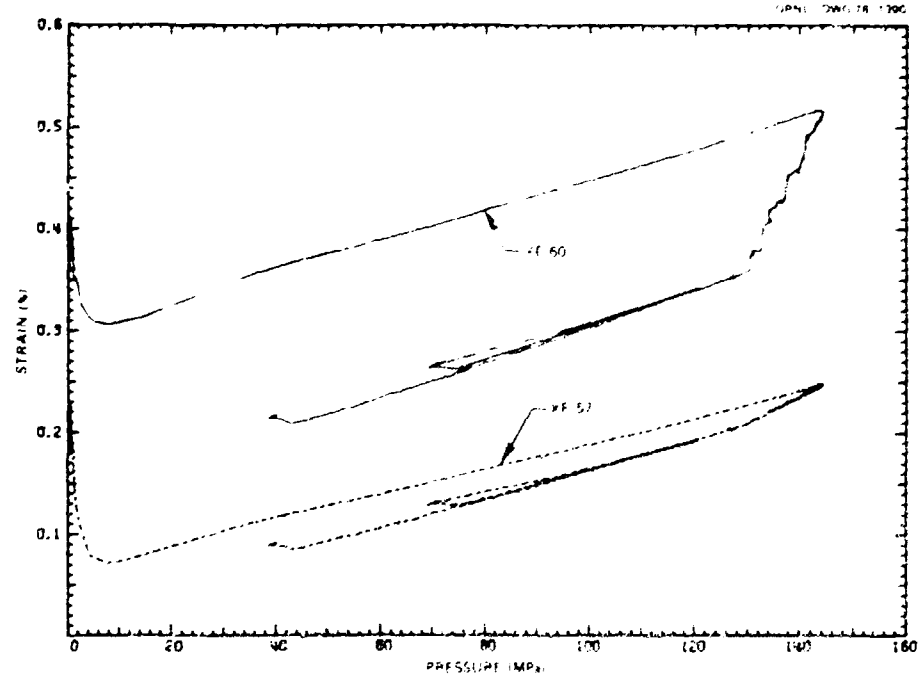

Fig. 5.31. Inside circumferential strains at center of repair zone (XE 60) and at symmetrical location (XE 57) vs pressure during cycles 3 and 4.

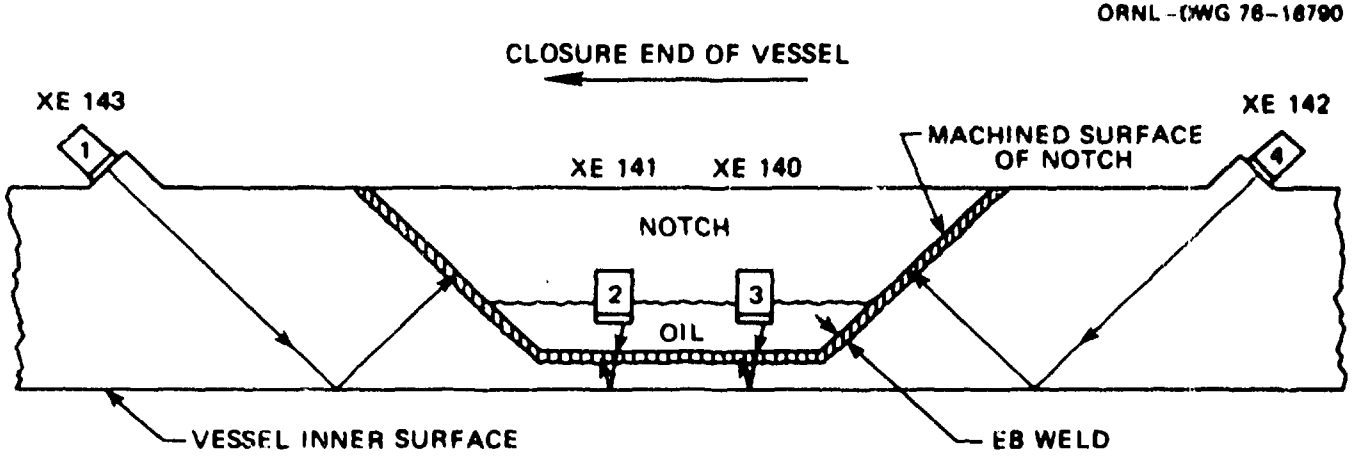

Fig. 5.32. Ultrasonic transducer arrangement for test vessel V-7A.

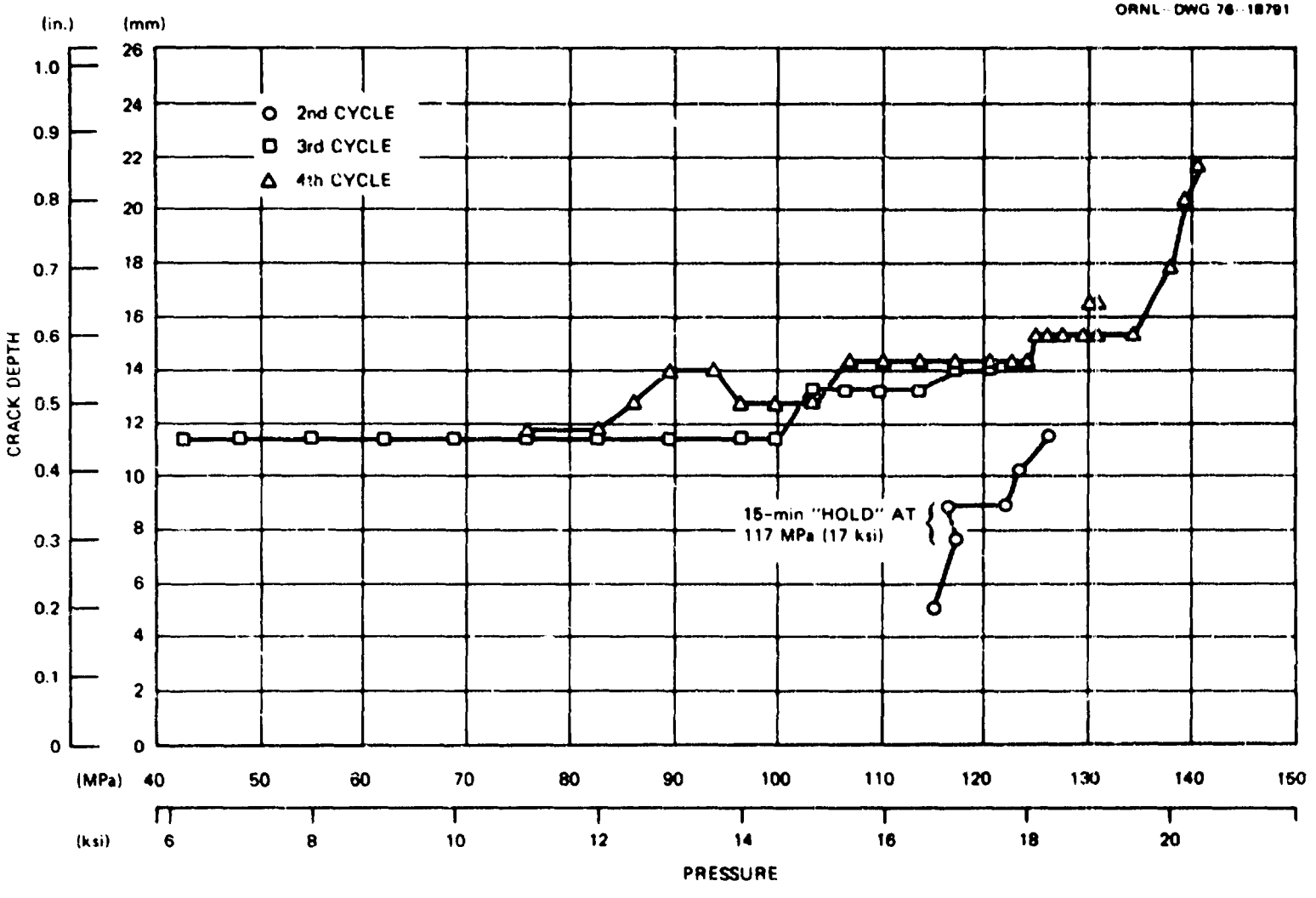

Fig. 5.33. Ligament crack depth as measured ultrasonically from machined bottom surface of the notch in vessel V-7A.

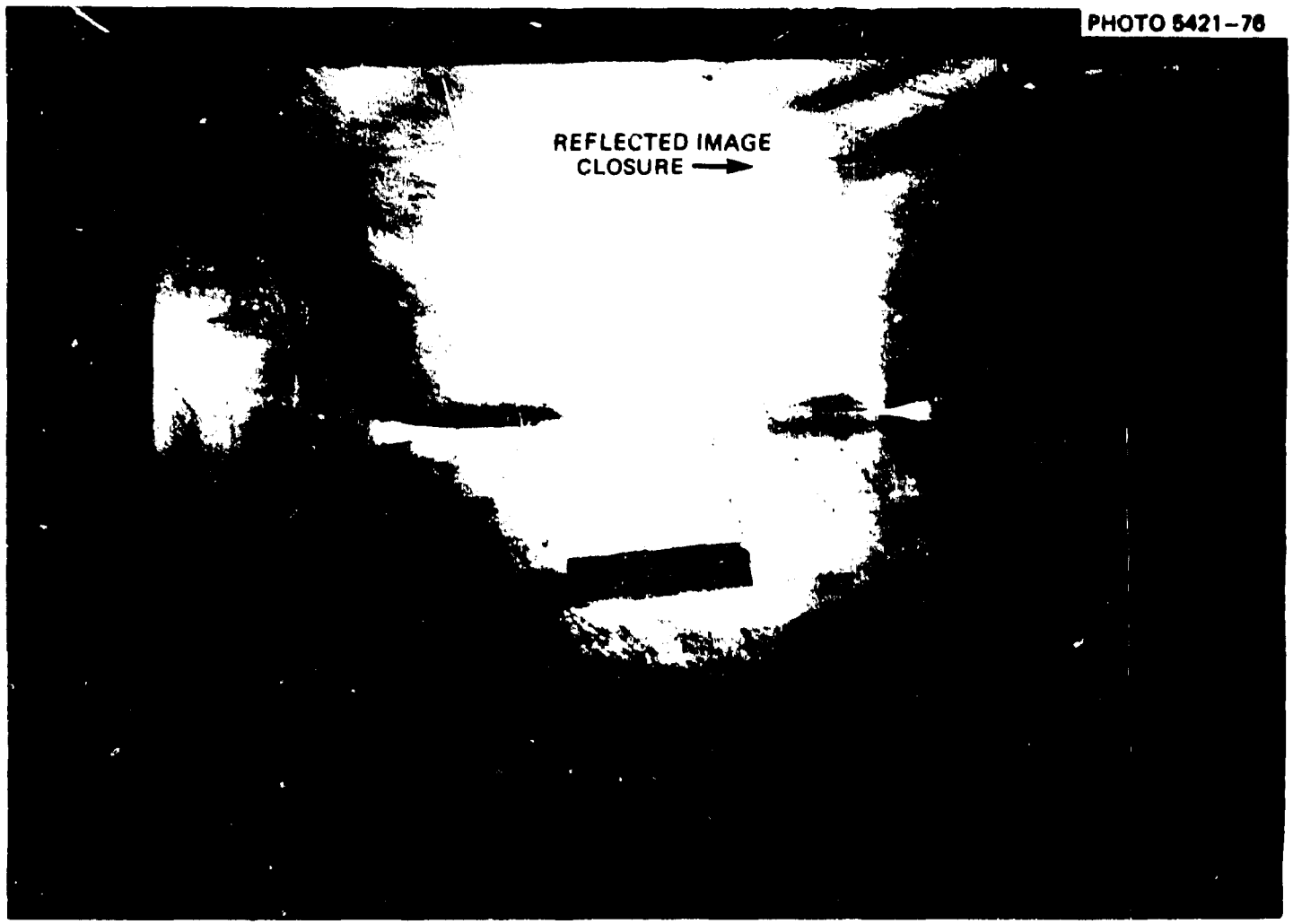

Fig. 5.34. Mirror image of inside surface of vessel V-7A beneath the notch after rupture.

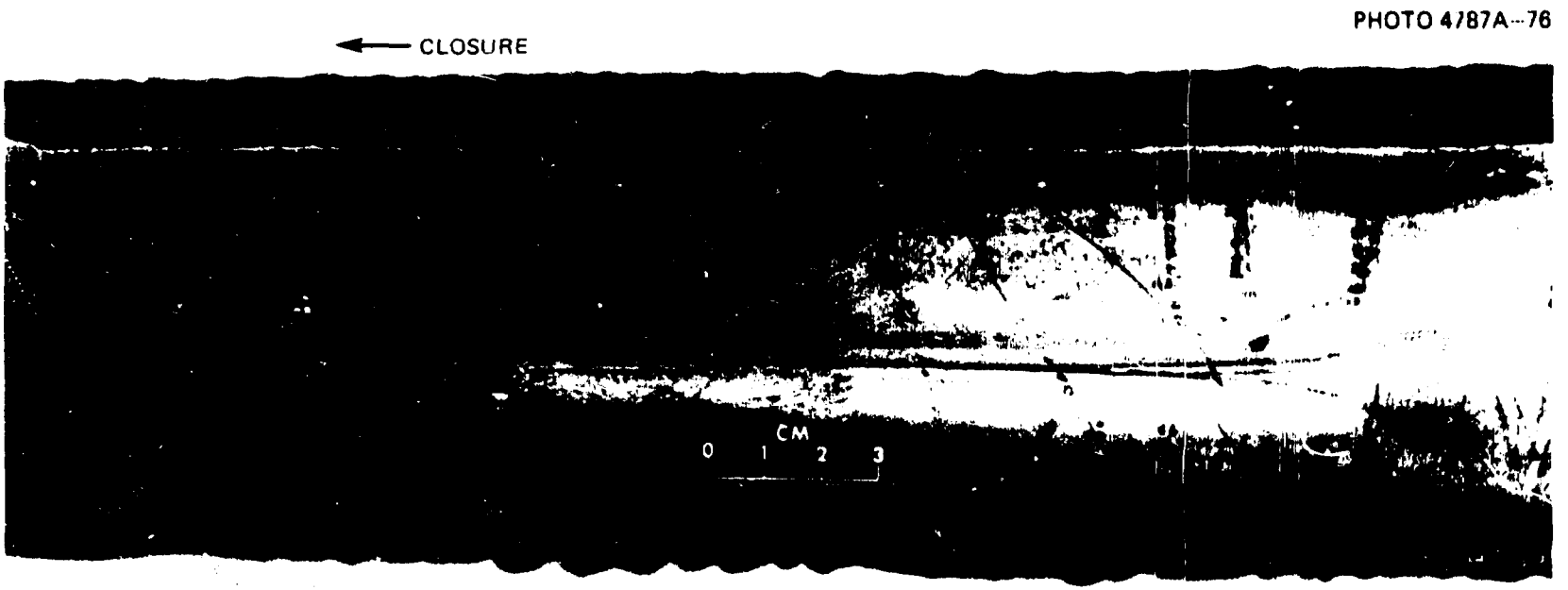

Fig. 5.35. Appearance of crack at inside surface of V-7A after the fracture zone was cut from vessel (1 cm = 0.394 in.).

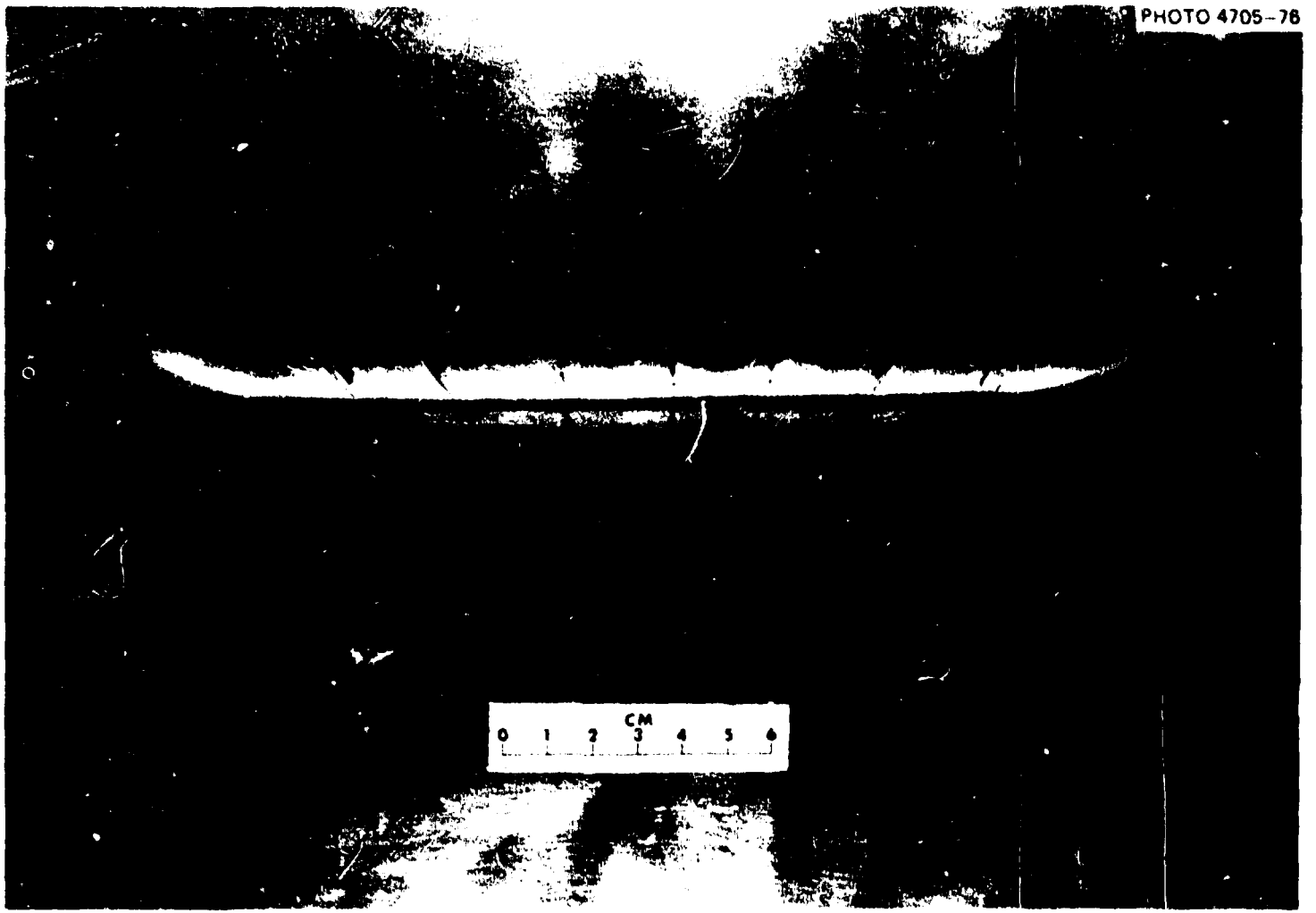

Fig. 5.36. Posttest appearance of the surface of the patch that had been pressed against the vessel (1 cm = 0.394 in.).

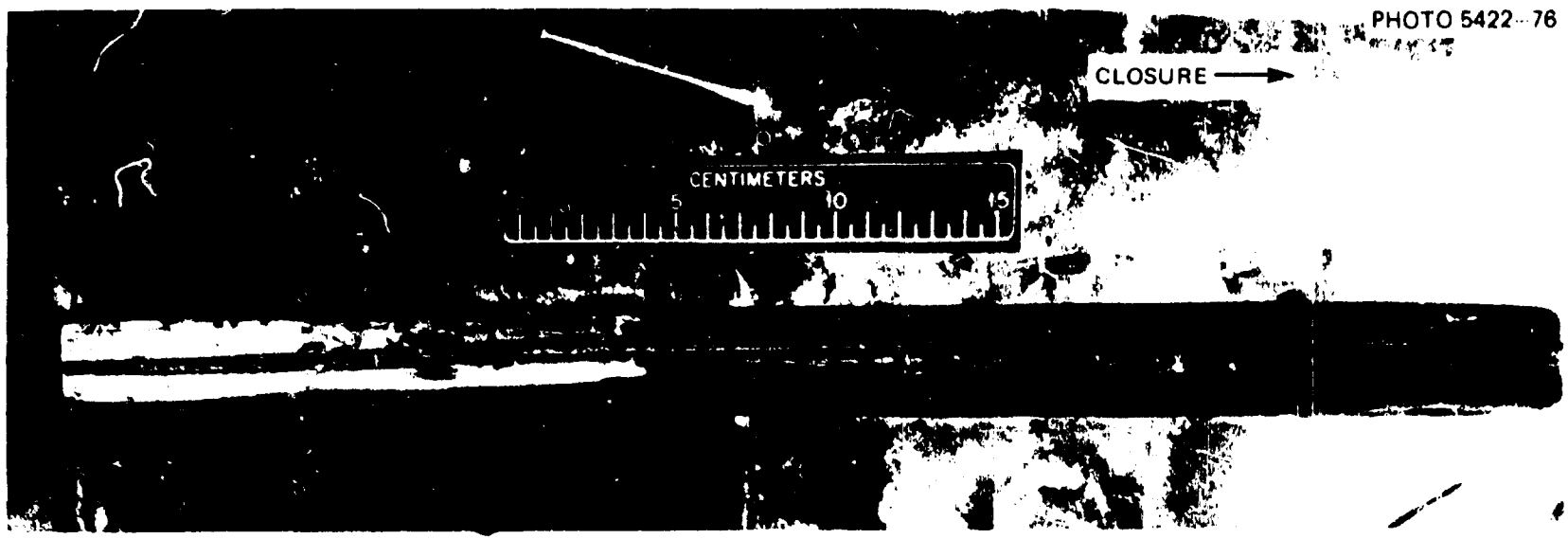

Fig. 5.37. External appearance of V-7A flaw after rupture before removal from vessel (1 cm = 0.394 in.).

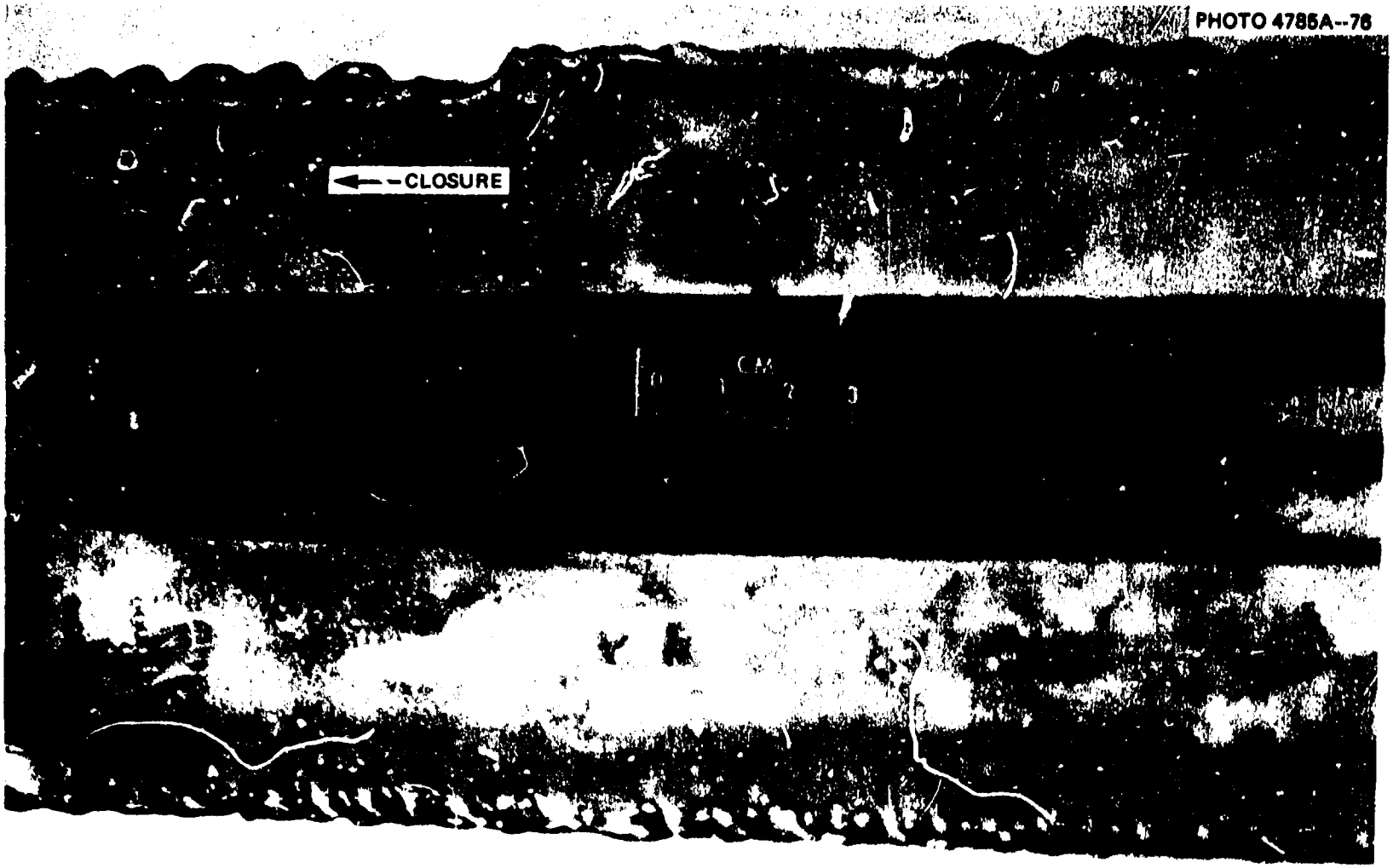

Fig. 5.38. External appearance of closure end of V-7A flaw after removal of fracture zone from vessel (1 cm = 0.394 in.).

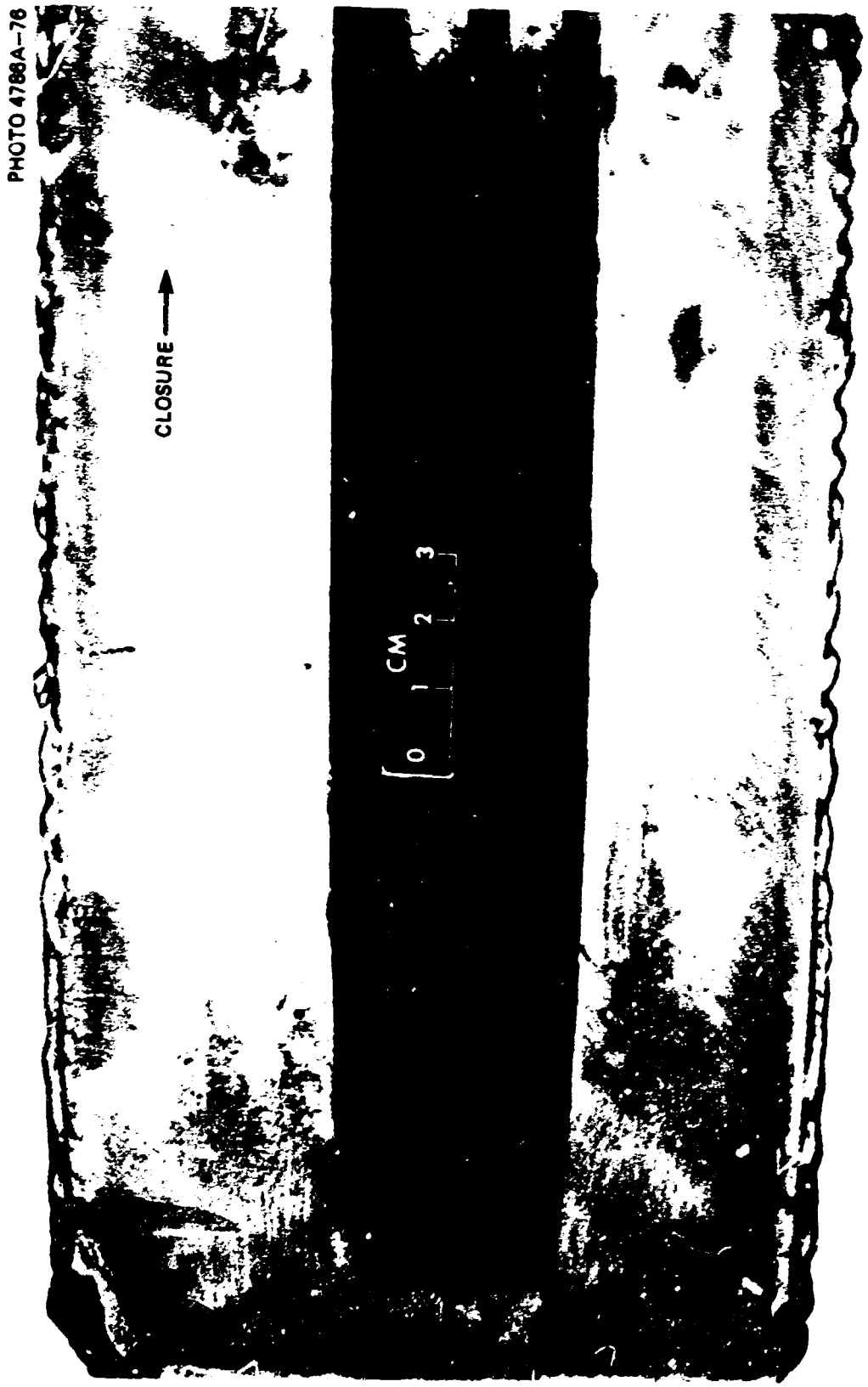

Fig. 5.39. External appearance of end of V-7A flaw toward hemispherical head after removal of fracture zone from vessel (1 cm = 0.394 in.).

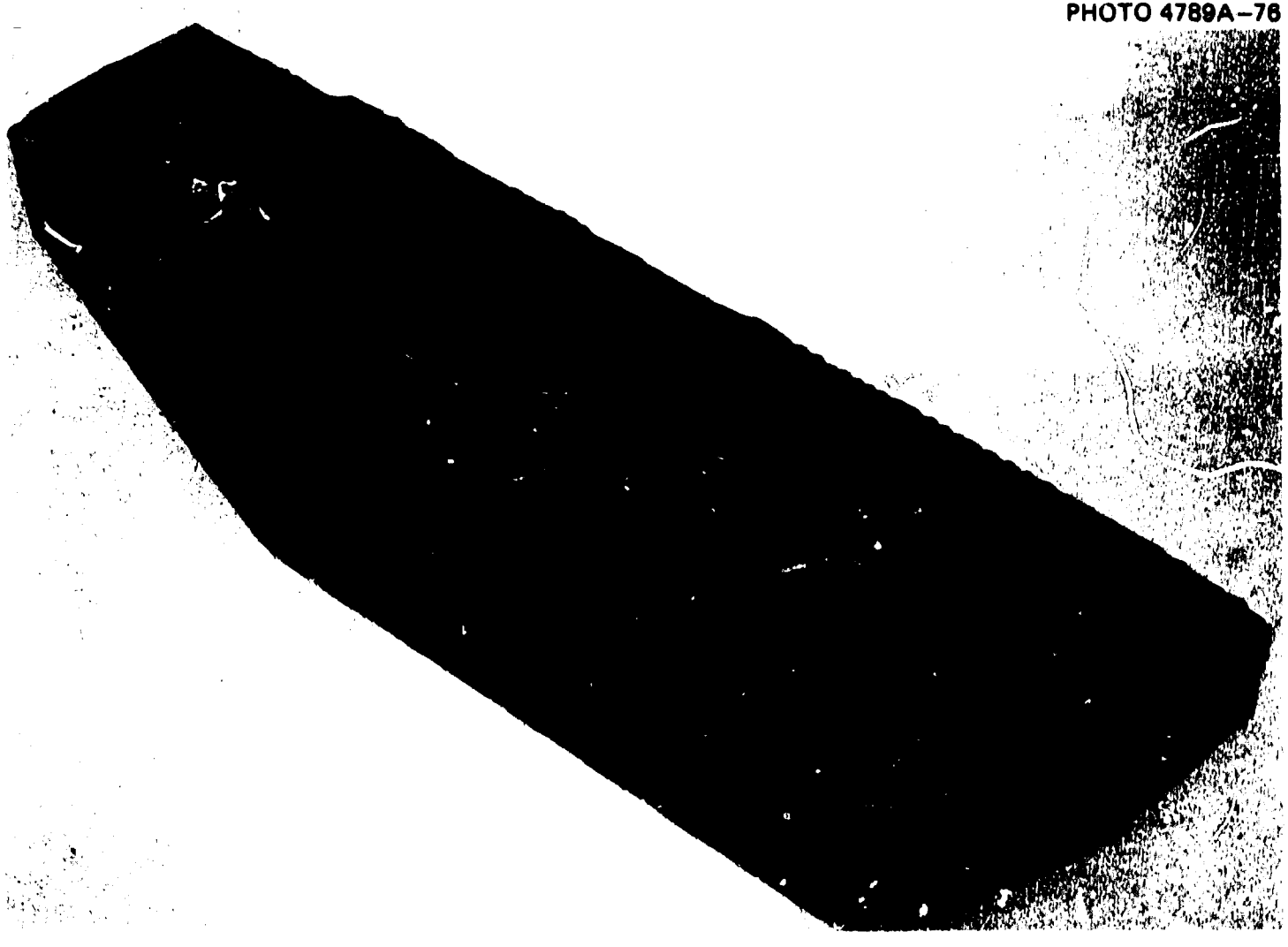

Fig. 5.40. Fracture zone flame cut from vessel V-7A (1 cm = 0.394 in.).

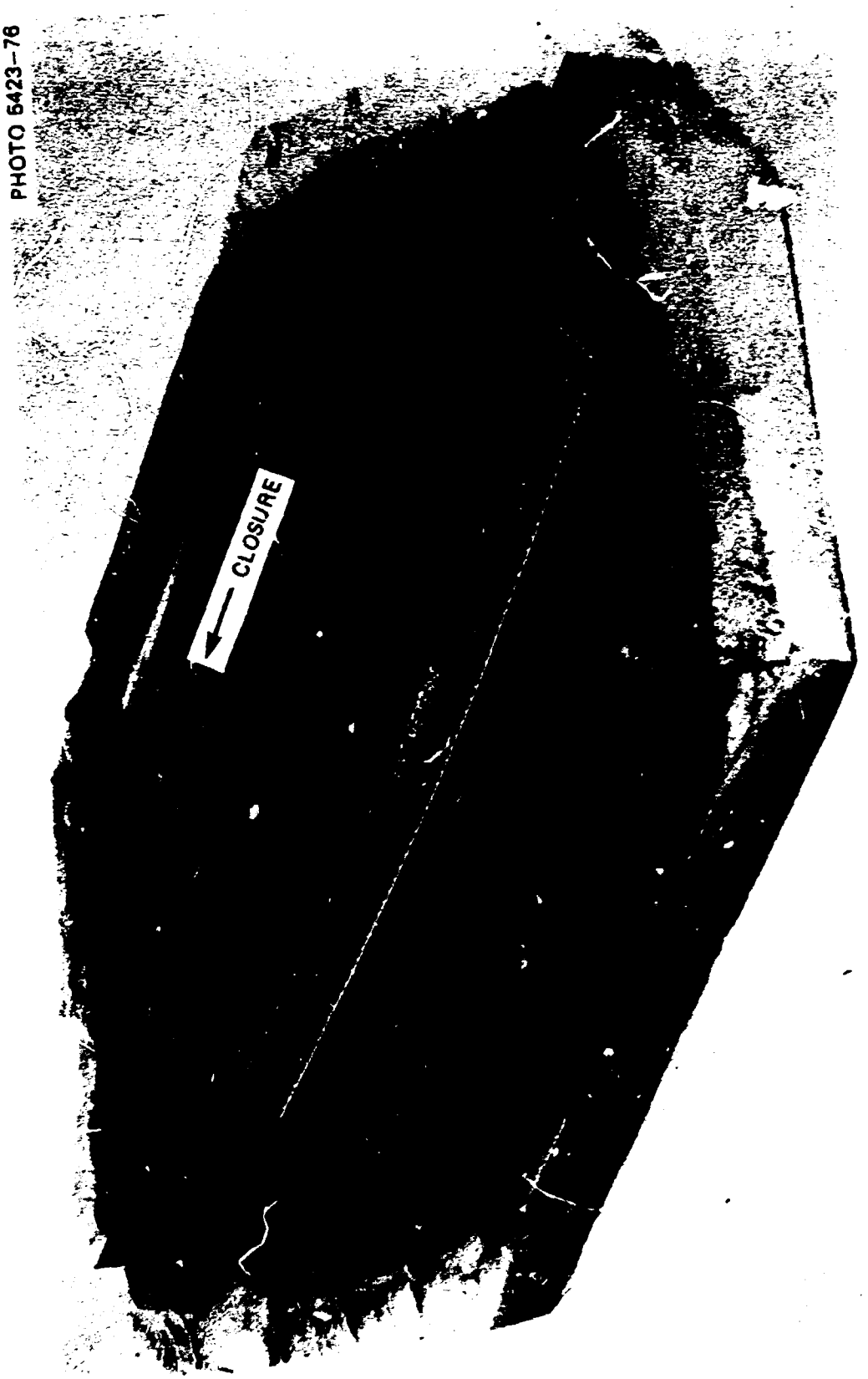

Fig. 5.41. Fracture surfaces of V-7A flaw (1 cm = 0.394 in.).

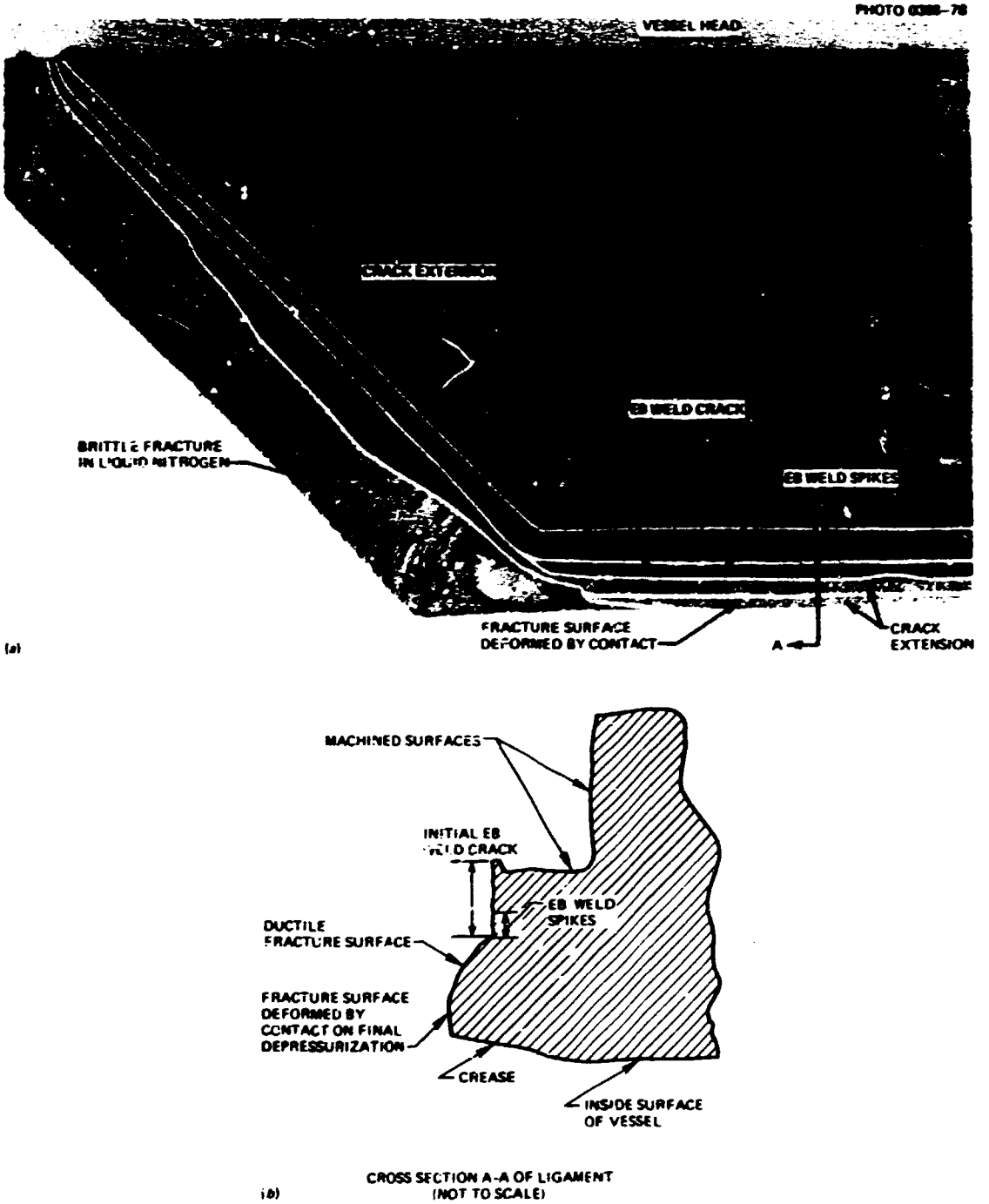

Fig. 5.42. Schematic of V-7A fracture surface.

Reference

1. J. G. Merkle et al., *Test of 6-in.-Thick Pressure Vessels. Series 3: Intermediate Test Vessel V-7*, ORNL/NUREG-1 (August 1976).

6. CONCLUSIONS

The V-7A test was initially conceived as an attempt to replicate, except for the pressurizing fluid, the conditions imposed on the vessel in the original V-7 test and thus to determine whether the sustained-load tendency of the gas in comparison with a liquid would accelerate crack tearing and possibly precipitate a burst. In our pretest studies of this question, we concluded that the influence, if any, of the more compliant fluid on slow crack growth and on burst strength could not be discerned either analytically or experimentally for flaws and test conditions of the intermediate test vessel type. As this conclusion gained acceptance, the primary objective shifted to the determination of the influence, if any, of sustaining the load after rupture on the propensity of the vessel to burst. With this objective, it became less important to replicate some details of the V-7 test, particularly the single pressurization cycle. Nevertheless, the conditions imposed on the vessels for the two tests were very nearly the same insofar as palpable effects on fracture are concerned. The pressurization schedules of the two tests are shown in Fig 6.1, and COD measurements are compared in Fig. 6.2. From comparisons of these data and the ultrasonic and acoustic-emission observations, we have found no evidence that the pneumatic loading, the cycling, or the protracted pressurization schedule affected the stable crack growth.

The principal objective of studying the effect of sustained loading after rupture was accomplished. The pressure was maintained within ±1% of maximum pressure for 30 min after rupture. Vessel deformations continued during sustained loading after rupture generally as they had before rupture, as indicated in Figs. 5.20 through 5.23. The stability of the flaw after rupture was demonstrated by its rapid approach to a static condition, as shown in Figs. 5.25 and 5.26.

The test subjected the Section XI weld repair to an overload condition of about 2.2 times the design pressure and demonstrated the integrity of the repair zone. The repair zone withstood high strains, imposed partly as a result of the residual deformation from the earlier test. The region was remarkably free of acoustic-emission activity.

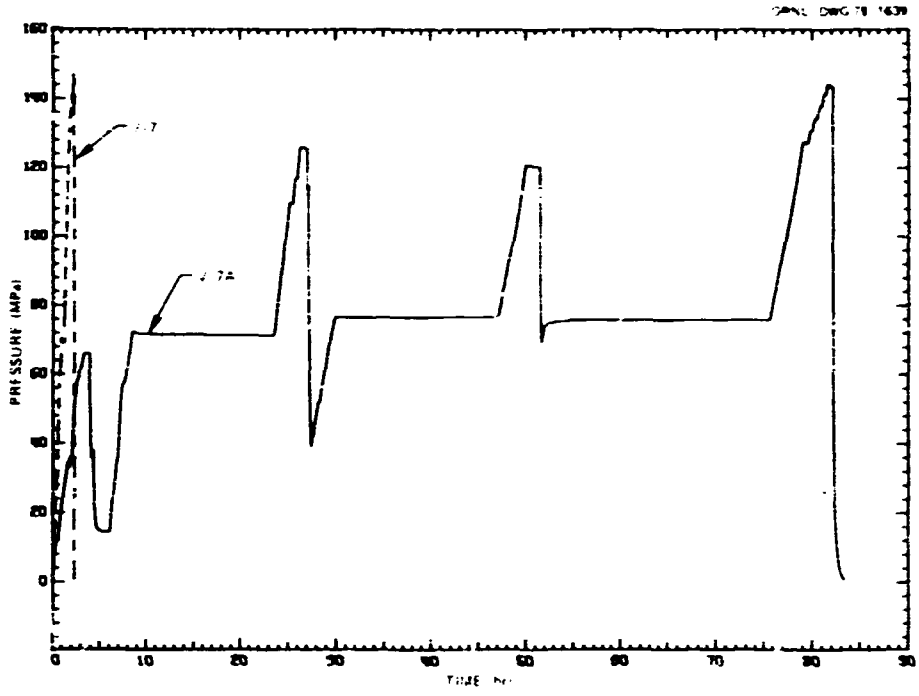

Fig. 6.1. Pressurization histories for intermediate vessel tests V-7 and V-7A (1 MPa = 145.04 psi).

The flaw ligament ruptured (without the vessel bursting) as had been predicted. Neither the V-7 nor the V-7A test provides any basis for confirming the estimated margin to burst. The ligament rupture pressure of V-7A was very close to that of V-7. Crack extension as a function of pressure can be compared only approximately, but there appears to be little difference.

The initial flaw in V-7A was deeper than had been estimated from EB weld crack studies before the V-7 test. The uncracked ligament in V-7A was actually 10 mm (0.39 in.), while the pretest estimate was 17.5 mm (0.688 in.). Comparable posttest measurements were not made on vessel V-7. If the ligament size was different in vessel V-7, it did not affect the rupture pressure, presumably because the crack in the ligament extended stably prior to rupture in both tests.

Posttest metallographic examination of the fracture surfaces in vessel V-7A confirm that the original flaw was sharpened around the entire periphery, and that crack extension was by a dimpled mode of fracture typical of stable crack extension on the upper shelf.

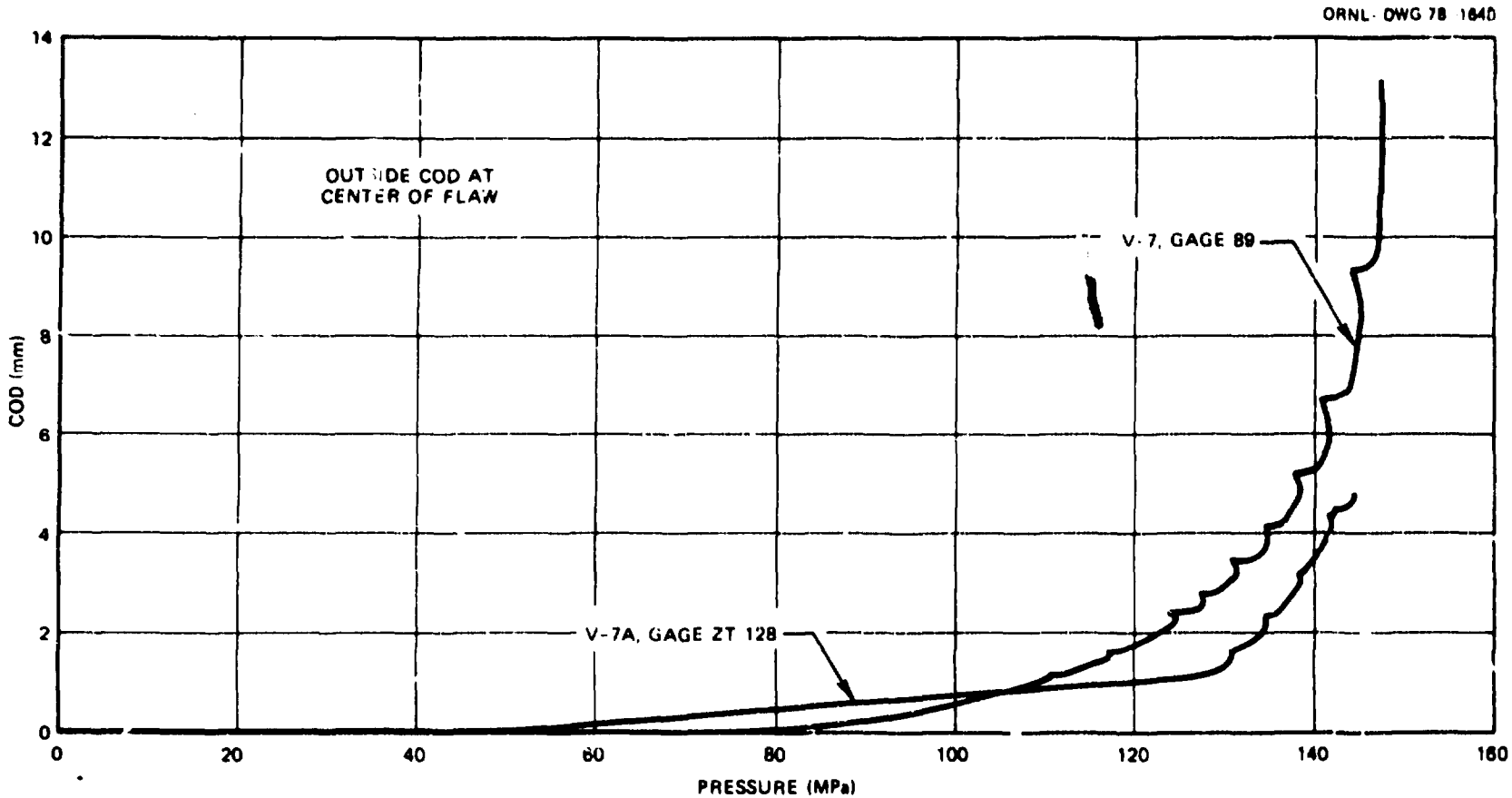

Fig. 6.2. Comparison of COD measurements in tests V-7 and V-7A (1 MPa = 145.04 psi; 1 mm = 0.0394 in.).

APPENDICES

Appendix A

WELDING SPECIFICATION NO. W-HB 100*†

Low Hydrogen Electrode Manual Shielded Metal-Arc Welding for "Half-Bead" Repair Welding

Scope

This specification covers the Welding Procedure (Part I) and Welder Performance Qualification and Procedure Qualification Tests (Part II) for manual shielded metal-arc repair welding on 6-in.-thick low-alloy steel materials using low-alloy (middle 70 ksi as-welded yield strength), low hydrogen steel electrodes. This weld procedure is specifically applicable for vessel weld repairs from the exterior using the "half-bead" technique, whereby the entire cavity of the preheated vessel is "buttered" using 3/32-in.-diam electrodes. The "buttered" deposit thickness is then half removed by grinding. Subsequently, the remainder of the cavity is then filled using first 1/8-in., then 5/32-in.-diam electrodes. Removal of half of the initial weld layer (buttering) permits the heat from the next weld to pass to reheat, for tempering purposes, the base metal heat-affected zone. Preheat is to be maintained throughout the entire welding operations.

The machined notch and the adjacent cracked and yielded zone of the vessel shown in Fig. A.1 will be repaired by this welding procedure. This procedure may require the preparation and welding of two types of test pieces, as follows:

Test Piece A: 3-in. (minimum thickness) plate, ASTM A533, grade B, class 1, or equal to dimensions of Fig. A.2, plus steel plates to simulate the physical obstruction of a 6-in.-deep cavity.

---

*Reference: *ASME Boiler and Pressure Vessel Code*, Section XI (In-Service Inspection), Subsubarticle IWB-4420 (Repair Procedure No. 4). References to portions of the Code are to the 1974 edition with the Summer 1974 and Winter 1974 addenda and are to Section XI unless stated otherwise.

†In this Welding Specification "fabricator" is used to mean the subcontractor in whose shop the welding is performed, and "UCC-ND" is used to mean the Union Carbide Corporation—Nuclear Division.

BLANK PAGE

ORNL-DWG 78-1204

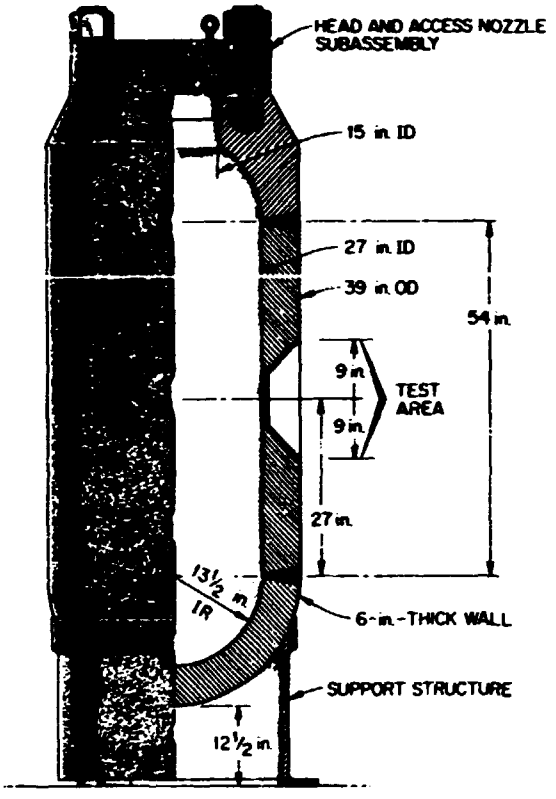

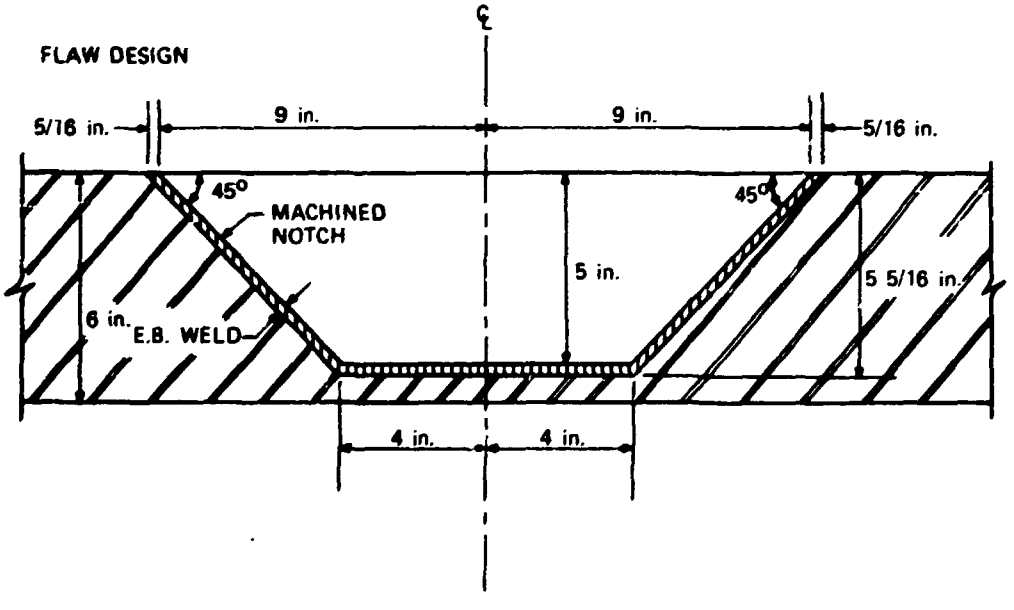

Fig. A.1. HSST intermediate vessel V-7.

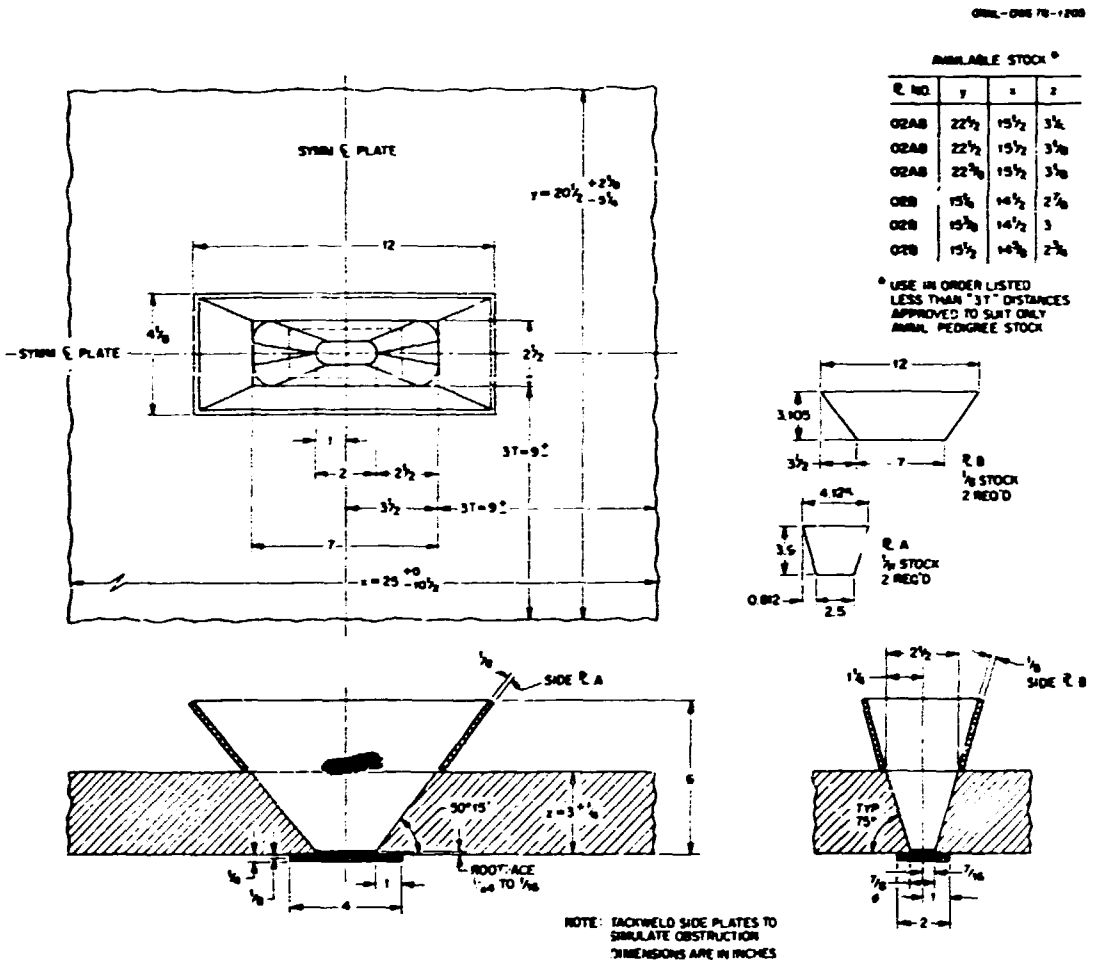

Fig. A.2. Preparations for 3-in. qualification plate weld. Welding position — 1G, fixed flat.

Test Piece B: 6-in.-thick, ASTM A533, grade B, class 1, or equal plate as shown in Fig. A.3; or a prolongation from a vessel as shown in Fig. A.4, along with a bracing arrangement for the backing plates and end restraints for the cylinder ends.

Individual welders must be qualified under Section IX of the Code for a procedure having the same essential variables for welding performance qualification as the procedure of Part I, or they must weld Test Piece A to demonstrate qualification under these procedures. Test Piece B is used to demonstrate the qualification of the procedures used by the welders for repair of the vessel.

Numbered footnotes in this specification are for information only.

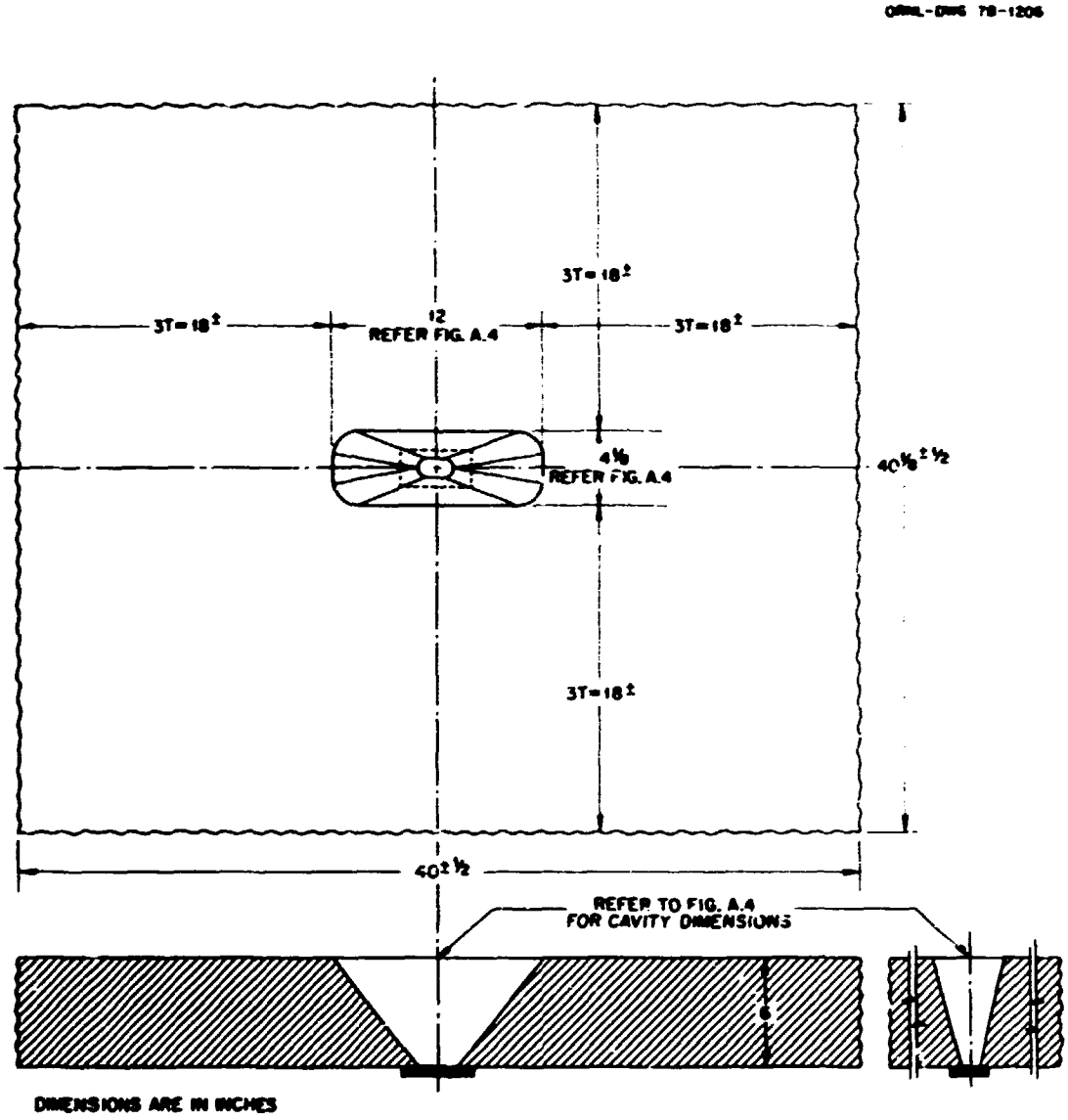

Fig. A.3. Preparations for 6-in. qualification plate weld. Welding position — 1G, fixed flat.

Participation of UCC-ND

The UCC-ND's representatives and inspectors shall have access to the fabricator's facilities to witness all work and to make strain measurements.

Surface strain measurements may be made by the UCC-ND on Test Piece B. The UCC-ND shall furnish materials, labor, and equipment for this work; the fabricator shall provide utilities to support the work. This work consists of the application of weldable strain gages to the piece after the backing

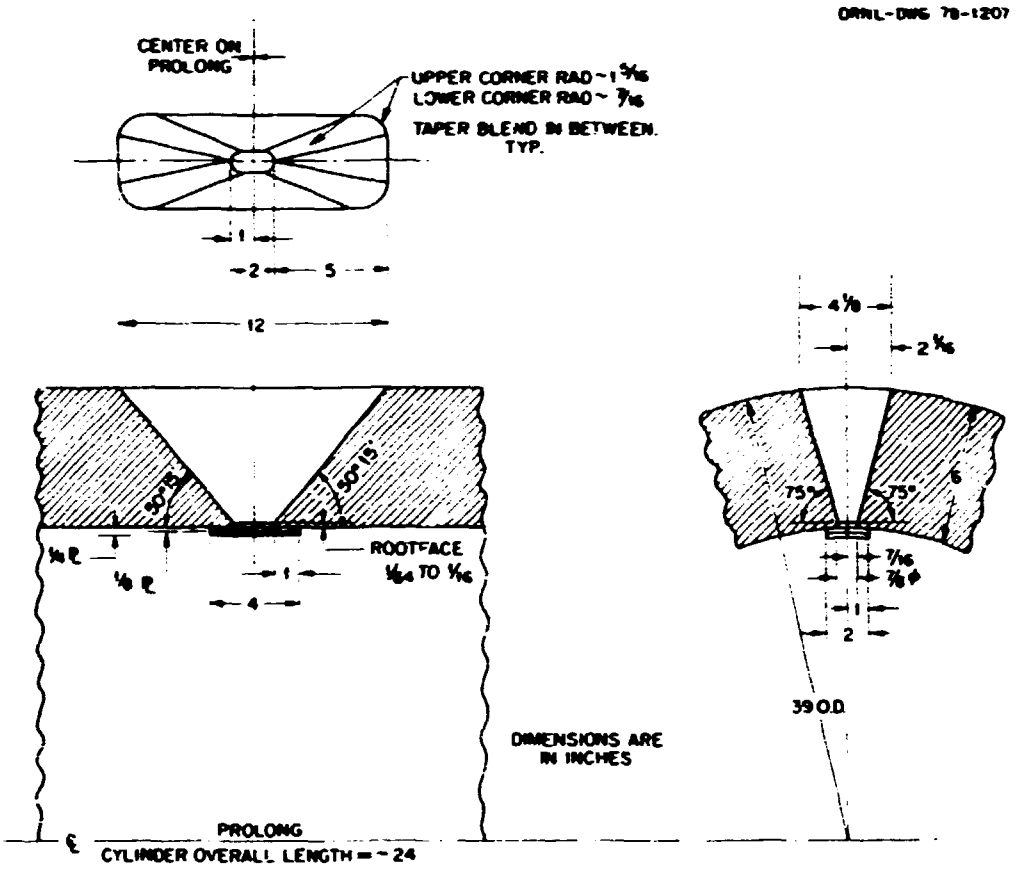

Fig. A.4. Weld repair preparations for intermediate test vessel V-7 prolongation. Welding position — 1G fixed flat. (Not shown: a center brace arrangement for the 1/8-in. backing plates and end restraints for the cylinder ends.

plate and suitable internal brace restraints have been installed but prior to preheating. Strain gage measurements will be recorded as follows:

1. prior to the application of preheat;
2. after the vessel reaches the specified preheat range but before welding commences;
3. after all welding is completed but prior to the post-weld heat treatment;
4. after the post-weld heat treatment is completed but before cooling;
5. after the temperature has been at ambient temperature for a minimum of 2 hours but before removal of bracing and restraints;
6. after removal of bracing and restraints.

Acceptance of work

The fabricator shall furnish test coupons made in accordance with NB-2431.1 of Section III of the Code for each lot of electrodes. The coupon for each lot shall be of sufficient width and thickness such that tensile and impact specimens can be removed and shall be no less than 56 in. in total length.

Prior to the start of welding on the cavity of the vessel the fabricator shall furnish the UCC-ND a report of the welding material properties determined in accordance with Section 3 of Part I of this specification. Welding on the cavity in Test Piece B and the vessel shall not commence without the buyer's consent of UCC-ND if tensile and impact properties of welding material do not conform to the specification SFA-5.5, AWS Classification E8018-C3 of Section II of the Code. The UCC-ND may, under terms agreed upon with the fabricator, require the preparation of a revised welding procedure and the repetition of Test B of this specification in accordance with the revised procedure.

All test pieces and the repaired vessel shall be accepted by the UCC-ND upon acceptance of the vessel in accordance with Section 13 of Part I of this specification.

Records and documentation

Appropriate records as follows shall be kept by the fabricator for transmittal to the UCC-ND within 30 days after acceptance of the test piece and vessel:

1. documentation on welding electrodes and their care;
2. welder certification papers;
3. procedure for air-arc gouging and grinding for cavity preparation;
4. sketches showing as-fabricated cavity preparations in the vessel and Test Piece B;
5. procedures for grinding and thickness control of the "buttering layer";
6. material certification papers for all backing plate materials;
7. a summary report of the evaluation made pursuant to Section 13 of Part I of this specification;

8. charts, or copies thereof, from temperature recording instruments and sketches showing locations of thermocouples related to the charts for the vessel and Test Piece E;

9. sketches showing size, location, and orientation of both repaired and allowable flaw indications found during post-weld nondestructive inspections.

Part I — Welding Procedure

1. Welding qualification

All welding in accordance with this procedure shall be done by welders qualified and currently certified under Part II below or under Section IX of the Code for a procedure having the same essential variables for welding performance qualification as this procedure. Welder certification papers shall be available at the job site at all times.

2. Base metal

The base metal will be low-alloy, high-strength carbon steel plate (ASTM A533, grade B, class 1, or equal), P number 3, Group 3, (Table QW 422, Section IX of the Code).

3. Filler metal

The filler metal shall be covered low-alloy steel electrodes and shall conform to the requirements of specification SFA-5.5, AWS Classification E8018-C3 of Section II of the Code or, if the fabricator so elects, shall conform to such other specifications as may be approved, in writing, by the UCC-ND. Electrodes shall be clean and dry, and the flux shall not be cracked or spalled. (See Care of Welding Electrodes, Section 8 of Part I of this specification.) Tests of welding materials shall conform to Subarticle NB-2400 of Section III.

4. Electrical characteristics

Direct current at 20 to 26 volts connected for reverse polarity (DCRP), with the base metal on the negative side of the line shall be used with

amperages, based upon electrode diameter, as follows:

Electrode diameter (in.)	Amperages
3/32	85-100
1/8	110-140
5/32	130-185

5. Repair zone

For preheating purposes the repair zone of a test piece shall consist of the entire piece, and the repair zone of the vessel shall consist of the cavity plus a region around the cavity lying beneath the area circumscribed by a line on the outside surface a minimum distance of 3T* from the boundary of the cavity. For inspection purposes the repair zone of the vessel and test pieces shall consist of the regions specified above for the vessel, except the distance there specified shall be 1T.[1]

6. Instrumentation

Thermocouples and recording instruments shall be used to monitor the preheat, gouging, grinding, welding, and final post-weld heat treatment operations. Thermocouples may be attached by welding where practicable.

7. Cavity preparation and cleaning

The cavities for the vessel repair and Test Piece B shall be formed by air-arc gouging to rough dimensions and grinding to finished dimensions. Finished dimensions are shown in Fig. A.5 for the vessel and in Figs. A.3 and A.4 for Test Piece B. The repair zone shall be preheated and maintained at temperatures in the range of 350°F to 400°F until air-arc gouging and grinding are finished.[2] After air-arc gouging is completed

*nT means n times the wall thickness.

[1]This is a deviation from the Code, which requires an examination of a 3T band.

[2]This is a deviation from the Code, which does not allow flame (thermal) cutting. (With agreement of the Advisory Task Group on Weld Repair for Pressure Vessels. PVRC, Atlanta meeting 6-6-75)

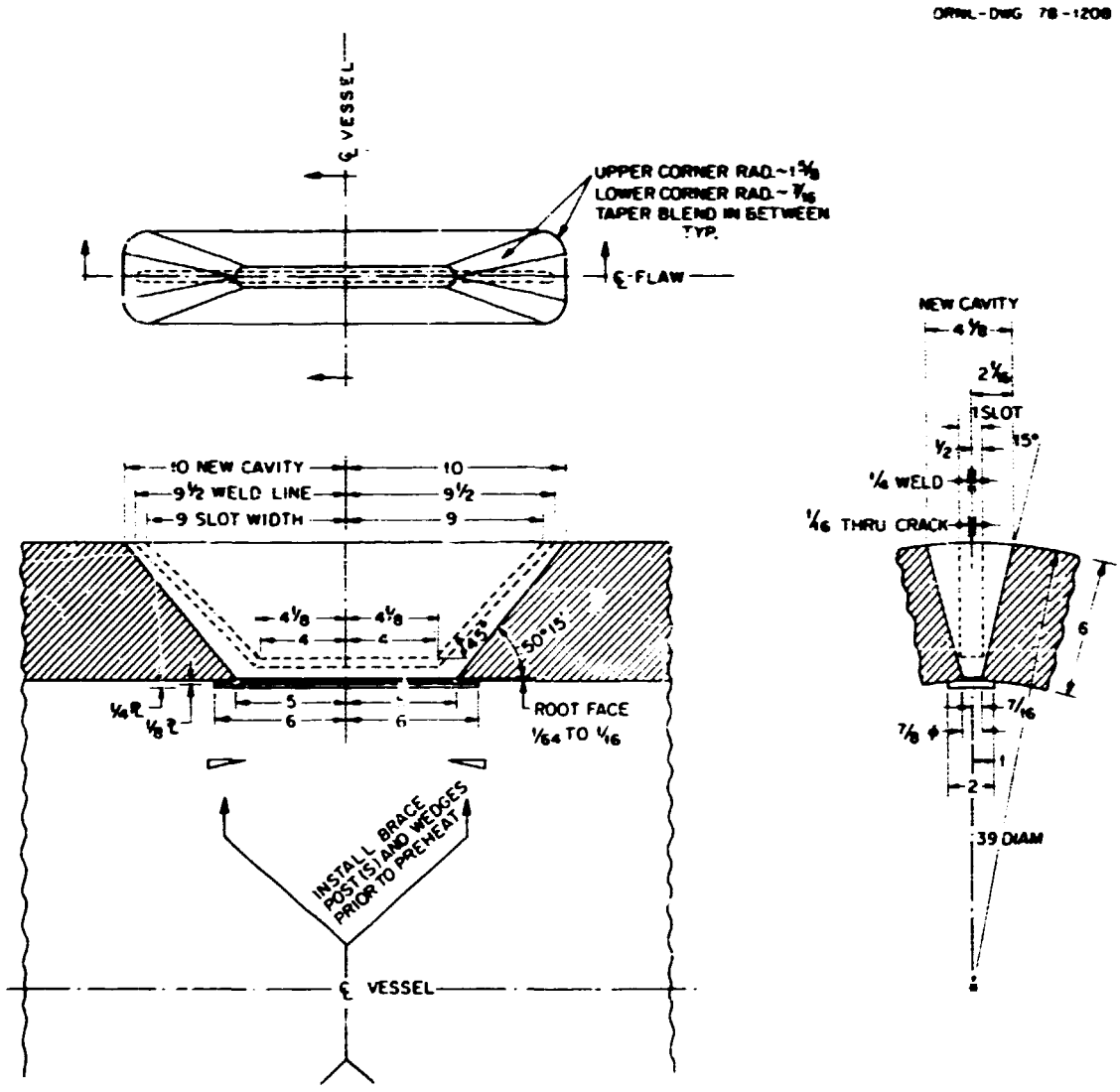

Fig. A.5. Weld repair preparation for intermediate test vessel V-7. Welding position — 1G, fixed flat.

a layer of metal under the gouged area a minimum of 1/4 in. in depth shall be removed by grinding.

Detailed procedures for cavity preparation and cleaning shall be prepared and kept at the job site.

Care shall be exercised in cavity corners to retain minimum radii as shown in Figs. A.4 and A.5.

In final preparation for welding, the cavity shall be ground smooth and clean with beveled sides and edges slightly rounded to provide suitable accessibility for welding. The surfaces within 1T distance of the

joint shall be cleaned of all dirt, oil, grease, paint and excessive amounts of scale and rust. The cavities of the vessel and test pieces shall be examined by magnetic particle inspection in accordance with the requirements of IWA-2221 prior to welding. Additional grinding shall be performed with preheat as necessary to remove indications of flaws. Actual dimensions and location of the cavity shall be documented.

8. Care of welding electrodes

Prior to welding Test Piece B or the vessel the fabricator shall submit to the UCC-ND his detailed procedures for care of electrodes.

The moisture content in the protective coating of the low hydrogen electrodes shall not exceed 0.4% by weight. The following steps shall be taken to prevent moisture pickup provided that, with prior written approval of UCC-ND, minor deviations may be allowed.

All coated electrodes shall be baked before use at temperatures of 800°F ± 25°F for 30 minutes to one hour. The temperature of the oven shall be at 300°F or lower when the electrodes are placed in the oven for baking. During the baking cycle, the temperature shall not be raised more than 300°F per hour when oven temperatures are above 500°F, and the total time above 500°F shall not exceed five hours. After baking, and before the electrodes are allowed to cool below 150°F, they shall be transferred to holding ovens operating in temperature ranges of 225°F to 300°F. Electrodes shall not be rebaked more than once.

During the repair, the electrodes shall be kept in portable heated ovens which shall be at the work station. These ovens shall be at 225°F to 300°F. Electrodes shall not be out of an oven more than 20 minutes prior to use. Electrodes not used within 20 minutes after removal from the oven shall be returned to the holding oven and held at 225°F to 300°F for at least 8 hours before reissue. The fabricator shall initiate and maintain records to indicate conformance to the above electrode bakeout and rod issuance regulations.

9. Conditions for welding

The vessel shall be adequately braced to prevent warpage. Test pieces shall be restrained to avoid warpage and to simulate the restraint of the

vessel. Backing plates shall be installed before anchoring or bracing. Backing plates shall consist of two layers of 1/8-in.-thick by 2-in.-wide cold-rolled steel strip, ASTM A108, grade 1018 or 1020. Flat test pieces shall be anchored to heavy support plates or welding tables.

All subsequent repair work shall be performed with preheat applied to the base material. The preheat temperature in the repair zone shall be within the temperature range of 350 to 500°F. The temperature shall not be allowed to fall below 350°F until the completion of a post-weld heat treatment at 450 to 550°F for 4 hours. If electrical heat is used, standby torches shall be provided to maintain vessel temperature in case of prolonged power outages.

10. Position of welding

All welding shall be done in the 1G, fixed flat position.

11. Weld metal deposition

Welding shall be done in general accordance with the illustrations of Fig. A.6.

The cavity shall be buttered using 3/32-in. maximum diameter electrodes as shown in Step 1, Fig. A.6. Approximately one-half the thickness of this buttering layer shall be removed by grinding before depositing a second layer. Special procedures shall be established as needed to control the grinding of the buttering layer. Such procedures may employ the use of workmanship specimens, dimensional measurements, or other means to demonstrate compliance. The maximum interpass temperature shall be held to 500°F. See Step 2. The second layer and the initial 1/4-in. deposit (as a minimum) shall be welded with a 1/8-in. maximum diameter electrode. Subsequent passes shall be deposited with either 1/8-in. or 5/32-in.-diam electrodes. The maximum bead width shall not exceed four times the electrode core diameter. Bead deposition shall be performed in a manner to temper the prior beads and their heat-affected zones as shown in Step 3. The completed weld shall have at least one layer of weld reinforcement (temper pass) deposited, and then this reinforcement shall be removed by grinding, making the finished surface of the repair substantially flush

ORNL-DWG 78-1209

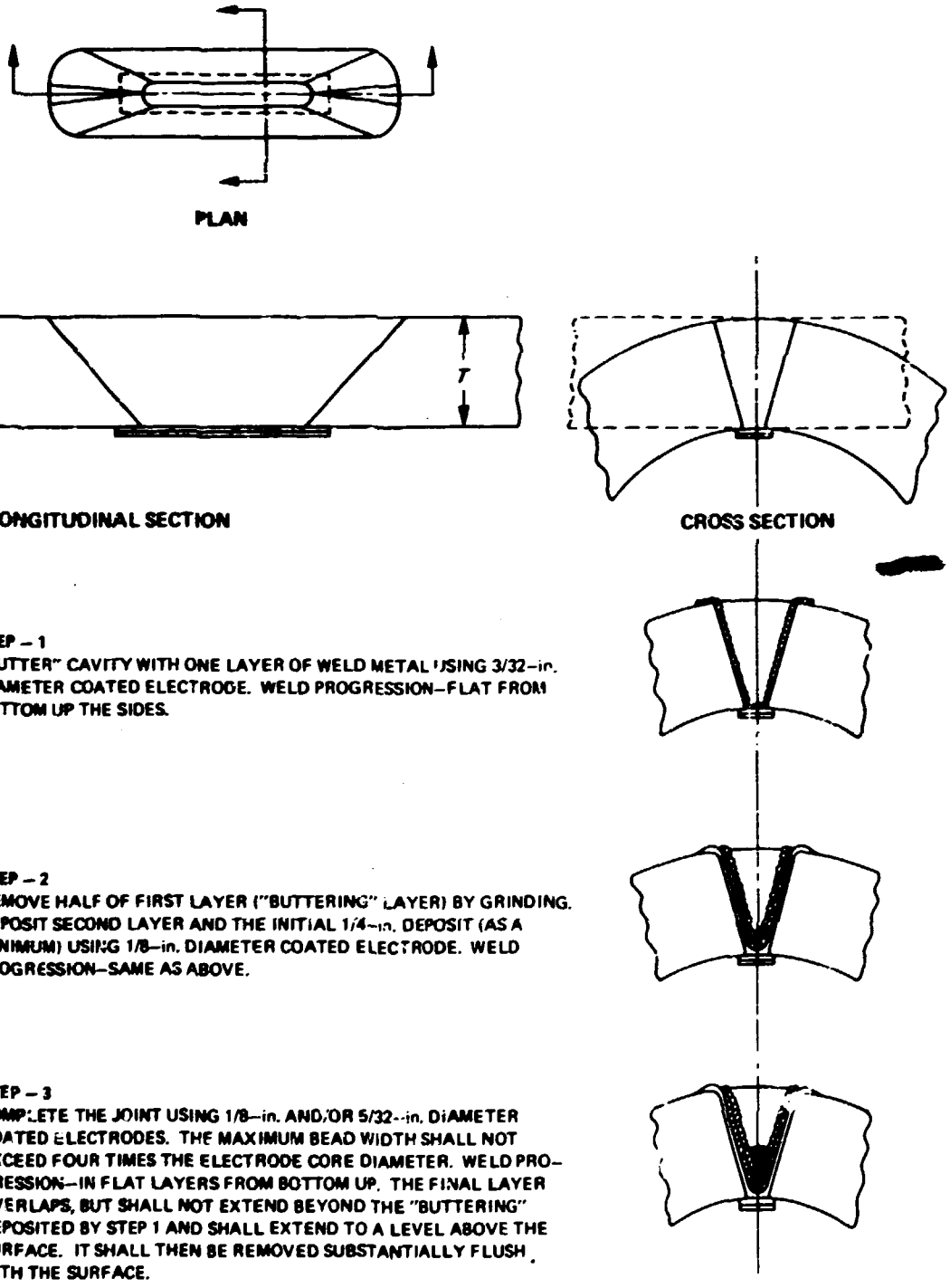

Fig. A.6. Half bead weld repair and weld temper bead reinforcement for heavy wall vessels and/or thick plates. Welding position – 1G, fixed flat.

with the surface of the vessel surrounding the repair. Likewise, following all welding and the post-heat and cooldown, the backing plate shall be removed, and the interior repair surface shall be contoured evenly to conform to vessel inside diameter dimensions plus or minus 1/8 in. Peening shall not be employed for purposes of stress relief.

Detailed procedures for grinding and controlling the thickness of the buttering layer shall be kept at the job site during this part of the work.

12. Inspection during welding

A magnetic particle examination (MT) shall be performed on the ground "buttered" layer, the next 1/8-in. layer, and thereafter on alternate layers and the final ground outside surface.[3] The final MT shall be completed prior to the start of the four-hour post-weld heat treatment. Layers not inspected by MT shall be visually inspected. Where necessary weld defects shall be removed and the repaired zone reinspected. If defects occur within 3/16 in. of the base metal, such repairs shall be made using the "buttering" and half-bead grinding technique.

13. Post-weld nondestructive inspection

The repair zone as defined above under Repair Zone shall be nondestructively examined after the completed weld has been at ambient temperature for a period of not less than 48 hours. A volumetric examination of the repair zone shall be made by radiography in accordance with IWA-2231 and the ultrasonic examination in accordance with IWA-2232, except that calibration block material of the same specification as the base material shall be deemed to meet the requirement of paragraph I-3121. A magnetic particle examination in accordance with IWA-2221 shall be made of the surfaces of the repair zone and of areas representing locations of weld attachments. A visual examination shall be made in accordance with IWA-2210.

An evaluation shall be made of each flaw indication. If necessary, repairs of the repair zone of the vessel shall be made in accordance with

[3]This is a deviation from the Code, which calls for examining every layer (with agreement of the Advisory Task Group on Weld Repair for Pressure Vessels, PVRC, Atlanta meeting, 6-6-75).

the half-bead weld technique as described in the foregoing sections of Part I. Size of flaw indications not completely removed shall be part of the evaluation. Acceptance of the repaired vessel and Test Piece B shall be determined in accordance with IWB-3500 and Examination Category B-A.

Part II — Welder Performance Qualification and Procedure Qualification Tests

1. General

All welding shall be in accordance with the requirements of Part I. The welder performance and procedure qualification requirements will be satisfied upon the successful completion of the tests described below.

2. Test welds

Test A. Each welder to be qualified under this procedure shall be tested by completing the welding of a plate as specified for Test Piece A, which shall be tested in accordance with QW-302 and QW-304 of Section IX of the Code. Each test piece of this type shall be stenciled with the welder's stencil number on the upper surface where he originates the weld.

Test B. Test B is a procedure qualification. Test Piece B shall be prepared and welded in accordance with the procedure of Part I. Only welders who have qualified under Test A or are qualified under Section IX of the Code for a procedure having the same essential variables for welding performance qualification as the procedure of Part I shall be permitted to weld in Test B.

3. Welder certification

A welder passing Test A and participating in the procedure qualification, Test B, shall be certified to weld in accordance with W-HB 100.

4. Retests

A welder who fails to meet the requirements as set forth in Test A may be retested after he has had further training or practice. A complete repetition of Test A shall be made. Retest specimens shall be tested and evaluated by the same procedure used for the first test.

5. Period of effectiveness

The qualification of a welder for this procedure shall be considered as indefinite but shall expire upon termination of a 90-day period in which the welder has not used this process. This qualification period may be extended to six months if the welder is continuously employed in shielded metal-arc welding. A welder's qualification may be withdrawn if the quality of his work is substandard to the requirements of this procedure. When a welder leaves the employment of that particular manufacturer or contractor for whom he worked at the time of his qualification, his qualification is automatically canceled.

Renewal of qualification

Renewal of qualification may be obtained by passing Test A.

Records

Certified records of the welder qualification tests shall be originated by the fabricator at the plant where the test was conducted. When a welder from an outside agency is qualified, a record of the test shall be submitted to and become the responsibility of that agency. A suggested form for the record is provided in Fig. A.7.

ORNL-DWG 78-1210

RECORD OF WELDER QUALIFICATION TEST

WELDER'S NAME	STENCIL NO.	BADGE NO.	DEPT. NO.
EMPLOYER	PROCEDURE NO.	DATE STARTED	DATE COMPLETED
MATERIAL (PLATE OR PIPE & SPEC. NO.)	THICKNESS AND DIAMETER	ROD OR ELECTRODE & SPEC. NO.	
WELD PROCESS (ARC, GAS, HELIARC, ETC.)	WELD TEST POSITION	FIRST TEST, DOUBLE, RETEST	

RECORD TEST RESULTS BELOW GIVING A BRIEF DESCRIPTION OF DEFECTS.
RECORD SILVER BRAZING TESTS ON BACK SIDE.

TEST METHOD	SPECIMEN NO.	PASSED	FAILED	NATURE, SIZE, AND LOCATION OF DEFECTS
X-RAY	1			
	2			
	3			
	4			
FACE BEND	1			
	2			
	3			
	4			
ROOT BEND	1			
	2			
	3			
	4			
OTHER (EXPLAIN)	1			
	2			
	3			
	4			

I CERTIFY THAT THE STATEMENTS IN THIS RECORD ARE CORRECT AND THAT THE TEST WELDS WERE PREPARED, WELDED, AND TESTED IN ACCORDANCE WITH THE REQUIREMENTS OF SECTION IX OF THE ASME CODE.

INSPECTOR	DATE
APPROVED	DATE

UCN-826A
(12 10-71)

Fig. A.7. Record of welder qualification test.

Appendix B

TEST DATA

A complete tabulation of data recorded during the testing of vessel V-7A has been produced on microfiche and attached inside the back cover of this report. The data recorded on the computer-controlled data acquisition system (CCDAS) consist of 3120 scans of temperature, pressure, crack-opening displacement (COD), and strain measurements recorded on magnetic tape. Ten additional channels of strain data were recorded on Vishay equipment; these data consist of 333 scans, the times of which were recorded by hand from the CCDAS clock.

The data on microfiche are divided into 11 tables: (1) temperature, (2) pressure and COD, (3–10) CCDAS strain, and (11) Vishay strain. Each line of a table presents a scan number, the lapsed time relative to CCDAS scan number 5, and a set of measured data in SI units. Conversions are given in Table B.1. The data tables occupy 3 fiche, each of which has 18 columns. An index to the data is given in Table B.2.

Data known to be erroneous but produced by sensors that were generally functioning properly are identified in Table B.3. Improperly functioning sensors are identified in Appendix D.

Table B.1. Conversions from SI to English units

Variable	SI unit	Multiplier of SI value to obtain English value	English unit
Pressure	MPa	0.14504	ksi
COD	mm	0.039370	in.
Strain	μm/m	1.0	μin./in.
Temperature (°F) = 9/5 [temperature (°C)] + 32			

Table B.2. Index to V-7A data on microfiche

Fiche No.	Column No.	Table No. and description
1	1–5	1 — Temperature
	6–10	2 — Pressure and CCS
	11–15	3 — CCDAS strain, XE33–42
	16–18	4 — CCDAS strain, XE43–49, XE51–53[a]
2	1–2	4 — continued
	3–7	5 — CCDAS strain, XE54–61, 64, 65
	8–12	6 — CCDAS strain, XE66–69, 72, 83–87
	13–17	7 — CCDAS strain, XE88–97
	18	Blank
3	1–5	8 — CCDAS strain, XE98–107
	6–10	9 — CCDAS strain, XE108–115, 117, 118
	11–15	10 — CCDAS strain, XE119–124
	16	11 — Vishey strain, XE73–82
	17–18	Blank

[a]Table 4 is continued on fiche No. 2.

Table B.3. Erroneous data from good sensors

Sensor	Scan No.
PE30	344
XE41, 48–61	137
ZT129	609
ZT130	87
ZT131	26
XE93–124	345
TE21–29	345
XE37, 49–72	346
XE83–124	346
TE21–29	346

Appendix C

ACOUSTIC-EMISSION MONITORING OF HSST INTERMEDIATE TEST VESSEL V-7A*

Introduction

Acoustic emission (AE) is the term applied to the spontaneously generated elastic waves produced within a material under stress. Plastic deformation and the nucleation and growth of cracks are the primary source of AE in metals. Unlike most other nondestructive test (NDT) methods, the energy comes from the material itself. As a result, AE is more sensitive to growing defects and potentially less reliant on operator interpretation than conventional NDT techniques. Acoustic emission offers a further advantage in the inspection of complex structures containing inaccessible areas. Normally, just a few stationary transducers can detect, locate, and qualify defects over a very large area, including regions inaccessible by alternate methods.

Acoustic-emission techniques have been successfully applied to the evaluation of structural integrity in bridges, nuclear and petrochemical pressure vessels, pipeline, wind tunnels, rocket motor cases, composite materials, and aircraft.[1-11] Acoustic emission has already been incorporated into production line testing in one Nuclear Regulatory Commission (NRC) facility.[9]

Although AE has not specifically been incorporated into the American Society of Mechanical Engineers (ASME) Boiler and Pressure Vessel Codes, there is a proposed ASME standard[12] covering the application of the technique. Several acoustic-emission examinations have already been performed in accordance with this document.[13-14]

The Nuclear Regulatory Commission (NRC), in conjunction with Oak Ridge National Laboratory, is conducting a continuing test program on heavy-section steel pressure vessels. The purpose of this program is to gather experimental data concerning the failure modes of thick-walled pressure vessels with vary large flaws. A secondary purpose is to demonstrate and

---

*This appendix is a report to ORNL by M. P. Kelly and R. J. Schlamp, Dunegan/Endevco, whose work was performed under UCC-ND Purchase Order 11Y-7328V.

evaluate various methods of nondestructive testing techniques in detecting and analyzing flaws and thus preventing catastrophic in-service failure. Dunegan/Endevco (D/E) has participated in the acoustic-emission monitoring of a number of these test vessels. This report covers the monitoring of intermediate test vessel V-7A during the first pneumatic test of an intermediate test vessel in the HSST program. The D/E source location system utilized in this test is described in the next section.

Instrumentation

The D/E model 1032 Source Location System is a portable system which provides a real-time display of acoustically active sources and their relative severity. The 1032 accepts input from up to 32 transducers, measures relative arrival times, calculates source coordinates, and displays source information in real time on a storage display scope (CRT). In addition, pertinent event information, including source coordinates, event size, and parametric input, are printed by a high-speed teleprinter and recorded on cassette for future use.

The 1032 utilizes a unique monitoring configuration of four transducers called the "quad" array. The array consists of three transducers forming an equilateral triangle with the fourth transducer directly in the center. The array monitors AE activity both inside and outside the triangle boundary. Multiple arrays can be positioned arbitrarily on a structure as each array has its own monitoring area and wave speed calibration routine. Each array is totally independent of all other arrays, allowing validity checking in hardware and rejection of erroneous data before it gets to the computer. If structural acoustics allow, valid data can be accepted at a rate of 3000 events per second for short periods of time. Data processing occurs at approximately 100 events per second, depending on the incoming data rate.

The 1032 also provides linear location capability for piping and pipeline testing. In this configuration, two transducers can be attached to a test piece in lieu of four channel arrays. Lines and arrays can be intermixed, allowing maximum coverage of difficult geometries. A block diagram of the system is presented in Fig. C.1.

The 1032 CRT provides an instantaneous display of the location of each source in relation to the position of the sensors (array) involved. In addition, a histogram (or bar graph) showing the number of events for each array is constantly updated and displayed on the CRT along with the currently displayed array. The histogram keeps the operator aware of total system activity, thus allowing alternate viewing of any active array. All CRT source coordinates are stored in computer memory, allowing alternate viewing of active arrays or lines without loss of data. Figure C.2 represents a typical CRT display, including the array sensors, active sources, events per array histogram, and appropriate histogram scaling factors.

Experimental Procedure

HSST vessel V-7, fabricated from ASTM A533 grade B, class 1 steel plate, was instrumented with a machined flaw and hydrostatically pressure tested on June 19, 1974. After this initial test, the flawed area was repaired in accordance with the ASME Boiler and Pressure Vessel Code, Section XI, weld repair procedure without postweld stress relief and the vessel was redesignated V-7A. A new flaw, identical to the original one, was machined in the vessel outside surface along the longitudinal axis 135° away from the original defect. A dimensional diagram of the flaw is shown in Fig. C.3; its location is shown in Fig. C.4. Vessel V-7A was monitored for acoustic-emission during a pneumatic pressure test conducted June 15 to 18, 1976. Test and calibration procedures were in accordance with the ASME Proposed Standard for Acoustic-Emission Examination During Application of Pressure.[12]

The cylindrical section of vessel V-7A was instrumented with two arrays of 4 transducers each (8 channels). Transducers were attached to the structure with magnetic hold-downs. A thin layer of GE-G-623 silicone grease was used as a coupling agent between the surface and each transducer. Figures C.4 and C.5 show the locations of the transducers.

The amplified output of an ORNL pressure transducer was connected to the parametric input of the 1032 in order to monitor the pressure throughout the test. The scaling factor required to convert parametric counts to pressure is shown under system specifications.

The pneumatic test consisted of four pressure cycles as shown in Fig. C.6. Monitoring of vessel V-7A for AE was initiated at the start of the first pressure cycle and continued for the pressurization period of the four cycles. No monitoring for AE was done during the overnight hold periods at pressure (refer to Fig. C.6 for these hold periods). The vessel temperature was maintained between 88 and 93°C (190 and 200°F) throughout the test period.

The 1032 system specifications during the conduct of the pneumatic test were as follows:

Transducers: S140B, 140 kHz resonant frequency, single ended
Filters: 120 to 240 kHz
Preamplifier gain: 40 dB
Signal conditioner gain: 40 dB
Total system gain: 80 dB
Arrival time resolution: 0.1 μsec
Parametric input: PARAM COUNTS X 14.67 = psi

Test Results

Each array was calibrated and operation verified through the use of pulser transducers. These transducers, of the same resonant frequency as the monitoring transducers, were attached to the structure within the monitoring area of each array. The 1032 pulse generator provided repeatable electrical signals to each pulser transducer; the resulting mechanical surface waves were detected and located by the neighboring monitoring transducers. The actual source coordinates of the pulser transducer were then compared with the resulting calculated coordinates to determine the locational accuracy of the various arrays. The locational accuracy for each of the arrays is listed in Table C.1. The accuracy was within ±5% of transducer spacing for both arrays as specified in the ASME Proposed Standard for Acoustic-Emission Examination during Application of Pressure.[12] A 1032 printout of the initial operator/computer communication is shown in Fig. C.7. Printouts of the acoustically active sources for the four test cycles are shown in Figs. C.8 through C.11.

Table C.1. Intermediate test vessel V-7A simulated source locational accuracy

Array No.	Accuracy [mm (in.)]
0	±25 (±1.0)
1	±13 (±0.5)

The column headings in Figs. C.8 through C.11 are defined as follows:

EVENT	Sequence number of events evaluated for validity
ARY	Array number
DT0, ..., DT3	Differential times (0.1 μsec) of arrival at transducer locations
X, Y	Coordinates of event (inches); see Fig. C.5 for coordinate system
COUNTS	Number of peaks in signal exceeding selected threshold
TIME	Internal clock time of event (0.01 hr)
PARAM	Pressure signal from CCDAS system PE30 (atm)

A diamond in the PARAM column means the location of the source is outside the area of the CRT display.

Figures C.12 through C.19 represent hard copy reproductions of the actual CRT test data from each array for the four pressure cycles. Figures C.20 and C.21 give the data from each array for all four pressure cycles. The flaw location and length (18 in.) are indicated by a dashed line in Figs. C.12 through C.21. As can be seen from these data, the located sources do not agree with the actual flaw coordinates. This has been a typical pattern for HSST vessels monitored with AE. As discussed in the initial V-7 report,[15] the reasons for this disparity are vessel geometry, transducer spacing and placement, and the presence of multiple sound paths. Both of the arrays were equidistant from the flaw; and in each case, the bulk of the defect emission was pulled inside the boundaries of the array. In an ideal test situation, transducers would be

separated by at least five times the vessel thickness in order to reduce the effect of bulk wave velocity transmission paths. The V-7A heating coils prevented transducer spacings of this magnitude. The system accuracy for a single type of wave velocity (surface wave) is demonstrated by the pulser locational accuracy shown in Table C.1.

Several of the events recorded during the first cycle originated in the electron-beam (EB) weld at the base of the flaw. Events attributed to crack propagation through the base metal commenced at about 83 MPa (12,000 psi) and continued until rupture occurred at 144 MPa (20,920 psi). No emission was detected from the weld repair zone, but minor emissions originating in the longitudinal weld were recorded. Some of the scattered emissions outside the general flaw area might be attributed to frictional noise generated by rubbing of the heater coils against the vessel surface.

The Dunegan/Endevco Test Analysis Program was utilized to generate a summation of counts-vs-pressure CRT graphs for each array (Figs. C.22 and C.23). Figure C.24 is a summation of counts from both arrays vs pressure. As can be seen from these graphs, the approaching failure was clearly indicated by the rapidly changing slope of the counts-vs-pressure graph between 128 and 144 MPa (18,500 and 20,920 psi).

Conclusions

The following conclusions can be drawn from the test results:

1. The counts-vs-pressure curve could have been utilized to halt pressurization prior to failure had this been desirable. A substantial change in slope was detected between 128 and 144 MPa (18,500 and 20,920 psi).

2. The bulk of the recorded emission appears to have originated in the flaw zone. The error in location is due to geometry constraints. A larger vessel, and significantly larger arrays, would reduce scatter and improve locational accuracy.

3. The repaired flaw did not generate acoustic emission under the imposed stress conditions.

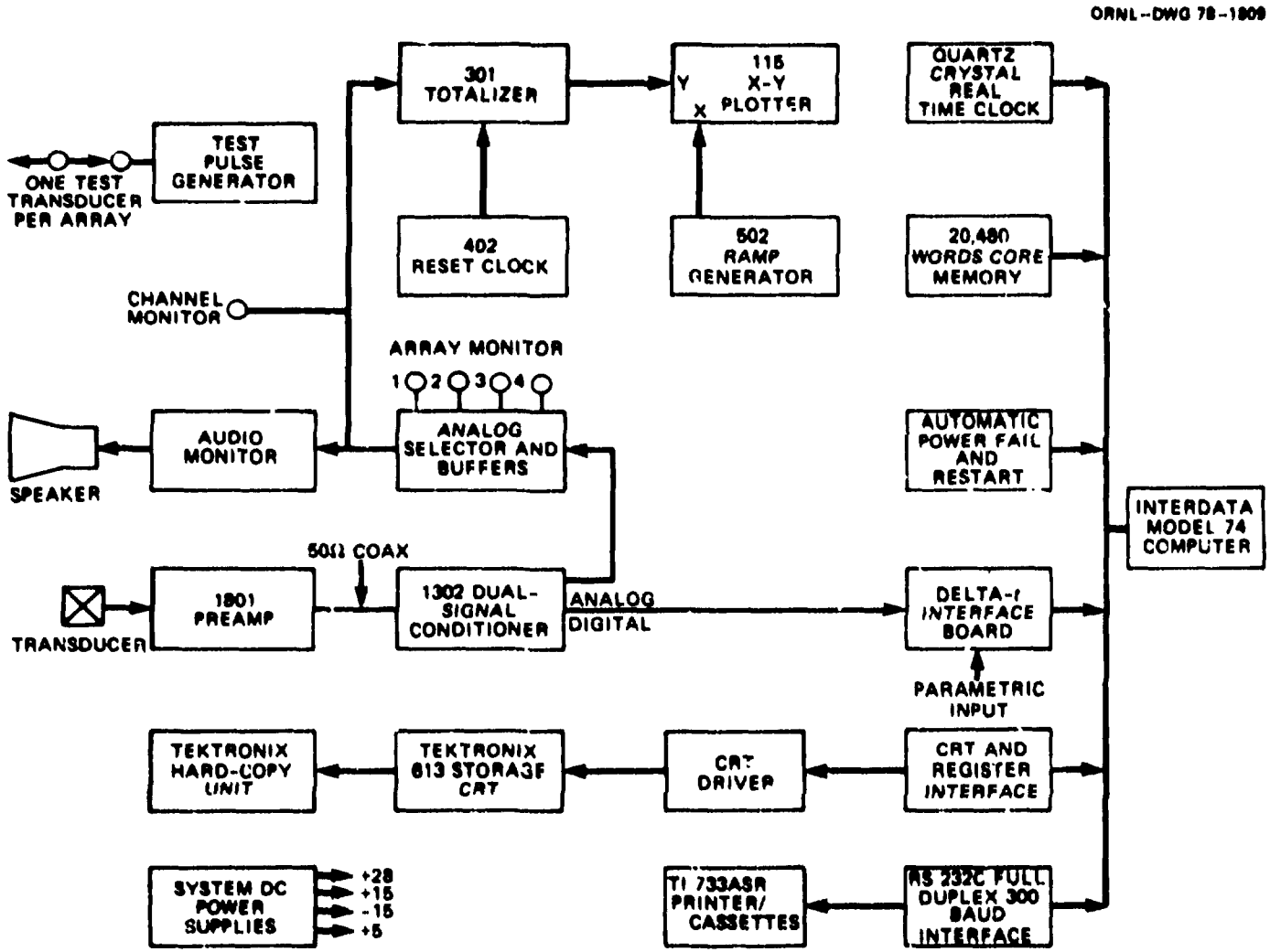

Fig. C.1. D/E model 1032 block diagram.

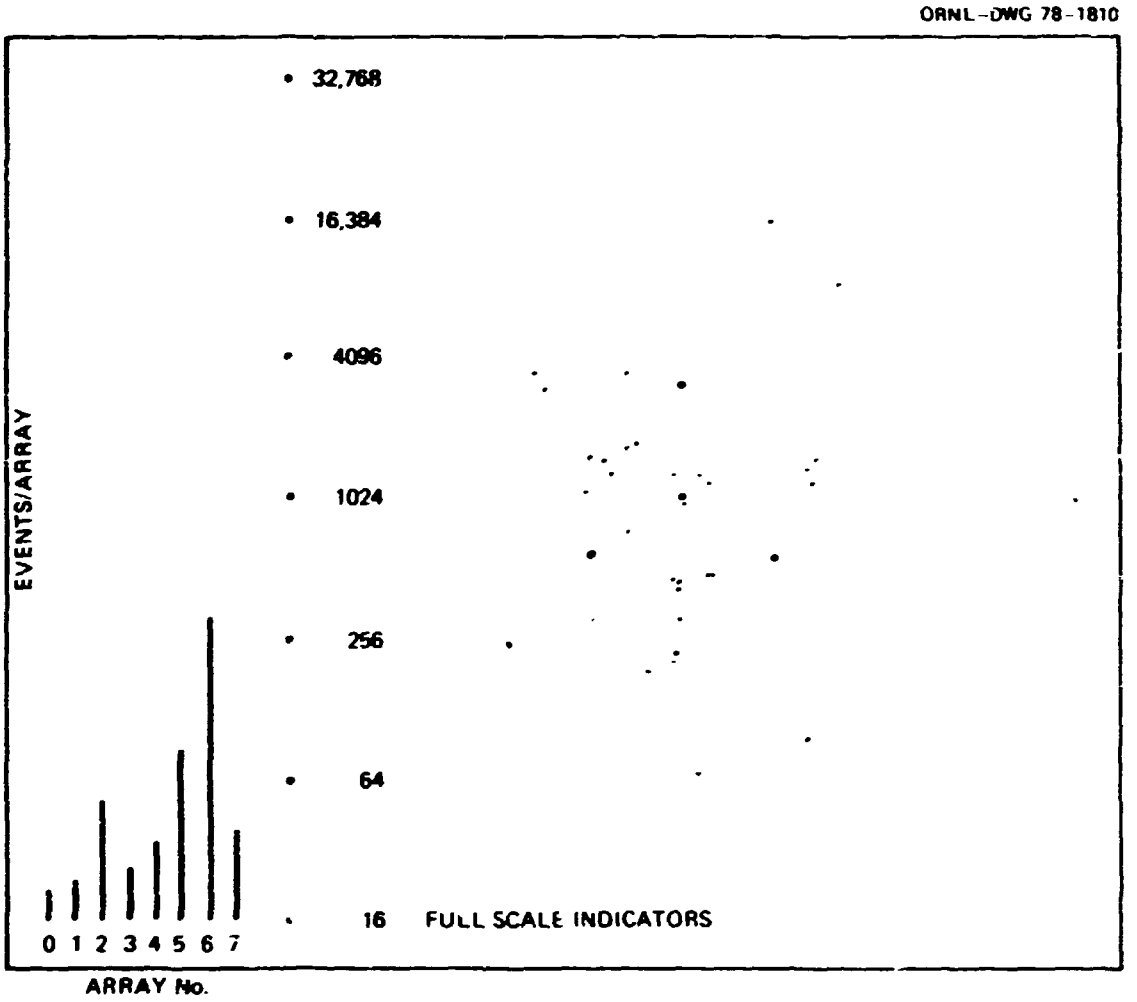

Fig. C.2. CRT array presentation. The histogram bars are linear with the full-scale value (top of graph) indicated by the number of dots displayed (N) as full-scale indicators. Full scale = $4^N + 1$.

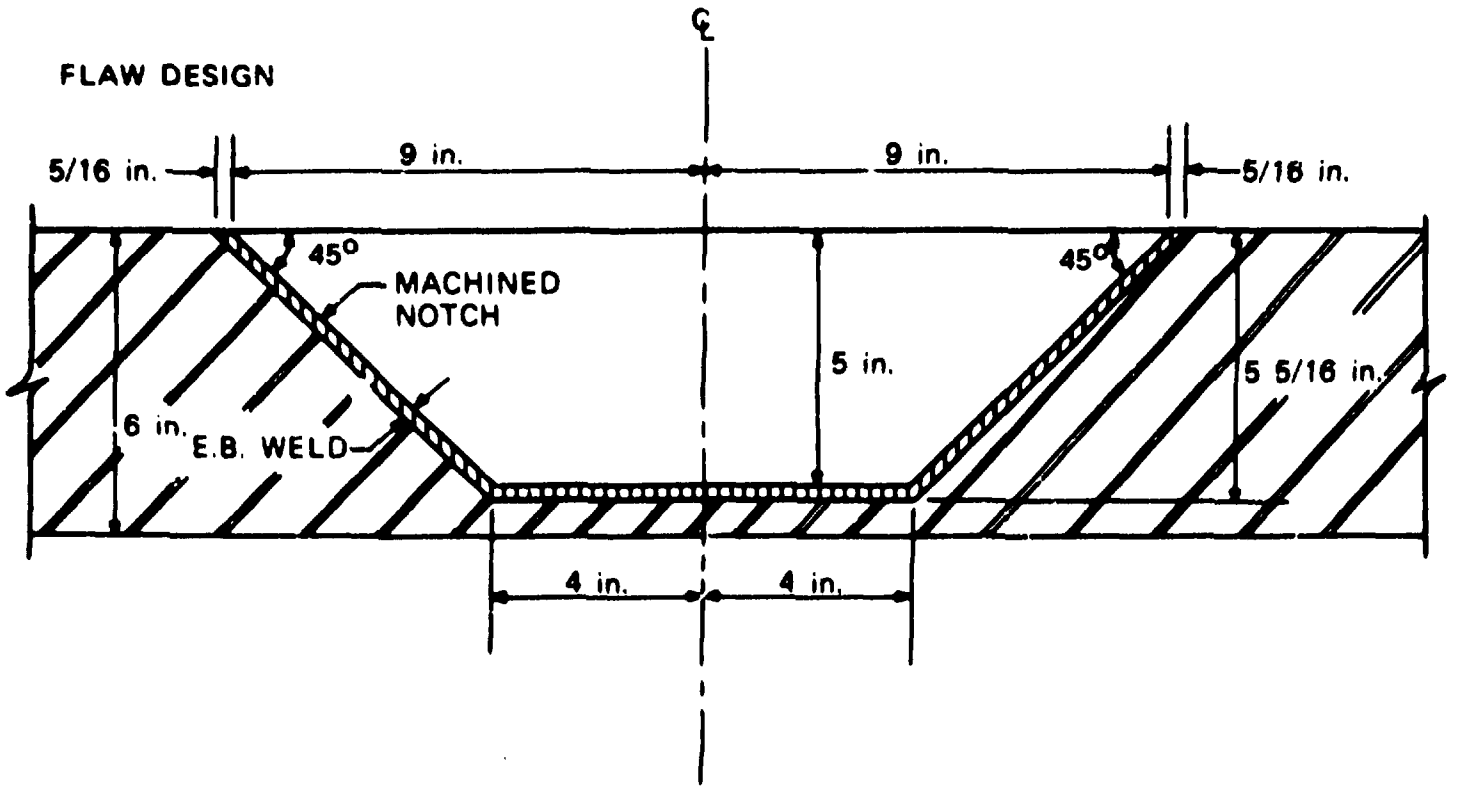

Fig. C.3. Flaw design for V-7A (1 in. = 25.4 mm).

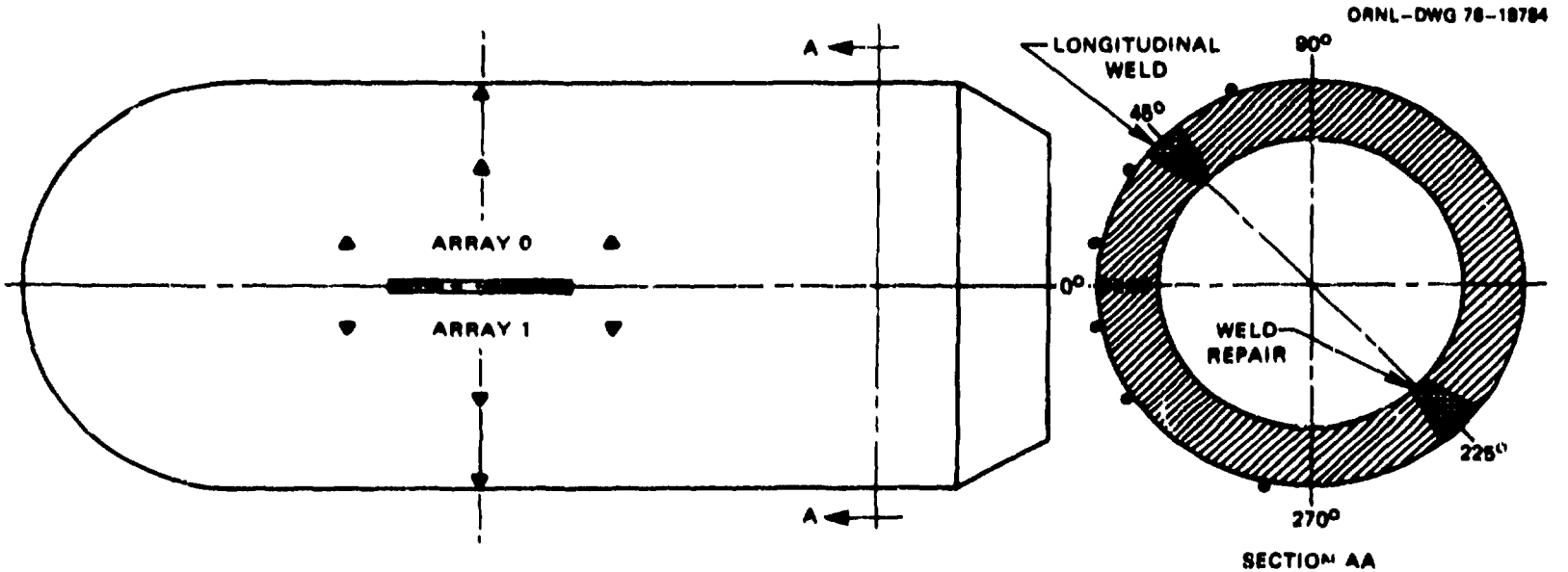

Fig. C.4. V-7A transducer location diagram.

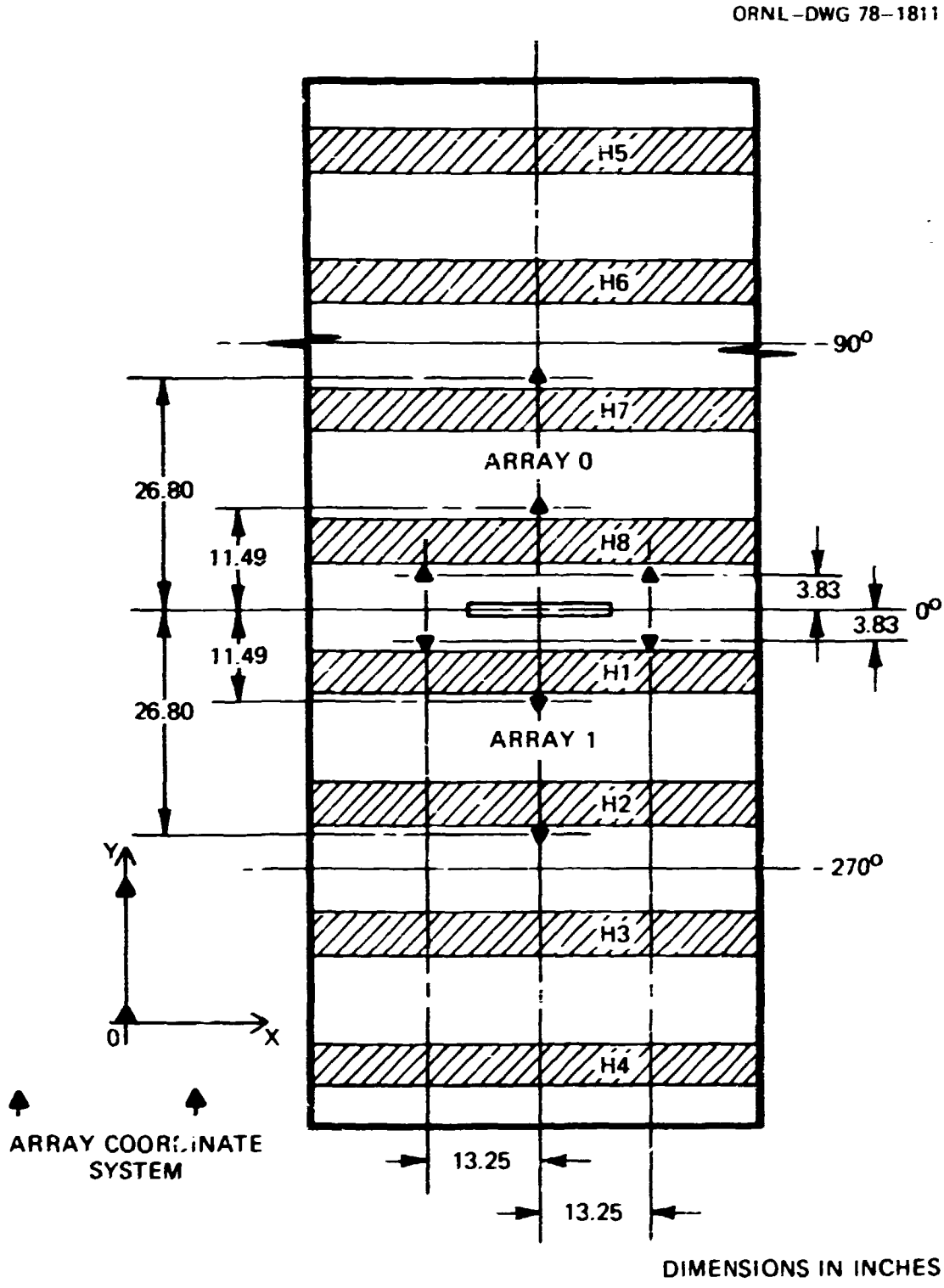

Fig. C.5. Plan view of V-7A transducer locations (1 in. = 25.4 mm).

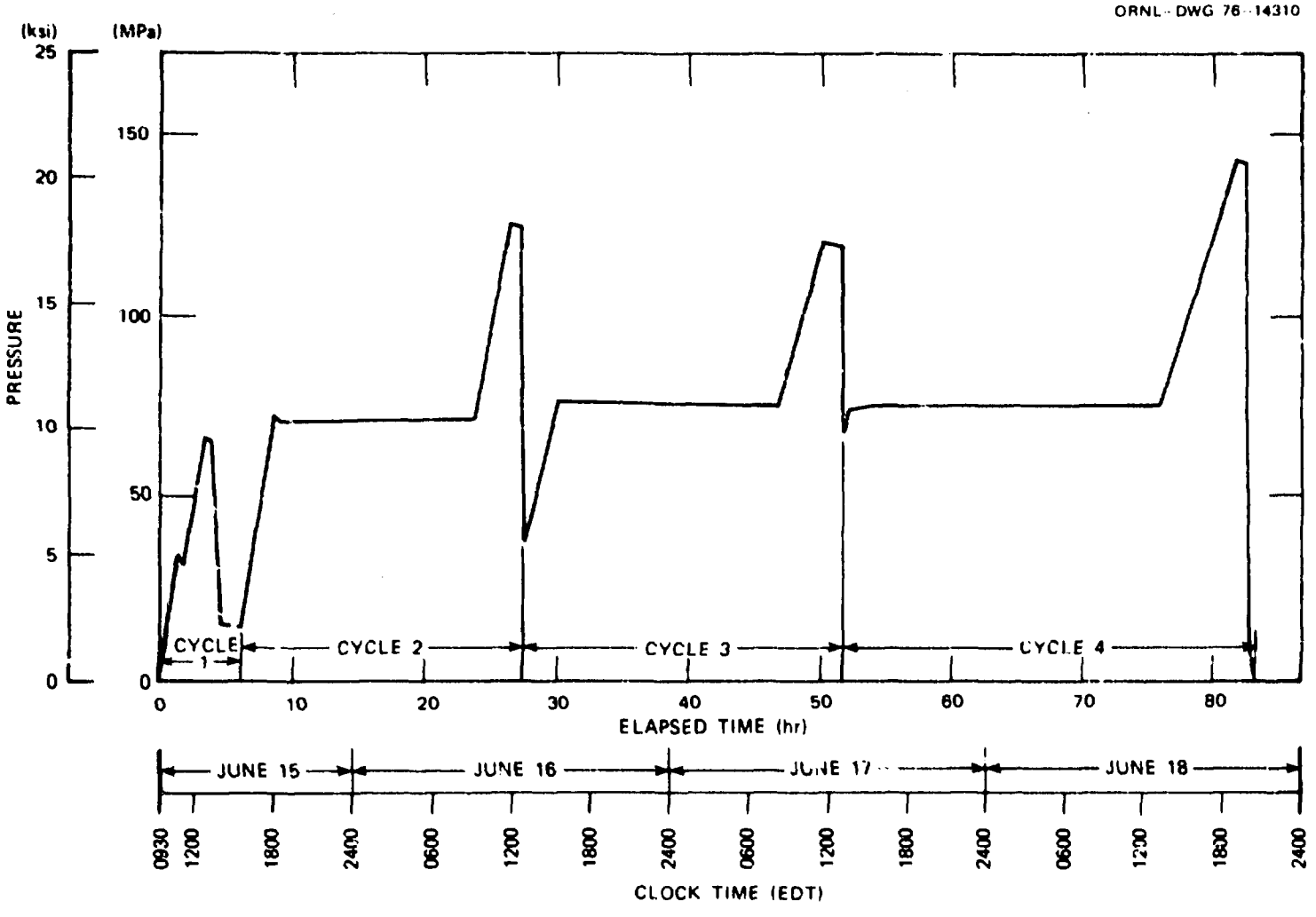

Fig. C.6. Approximate pressurization schedule for intermediate test vessel V-7A.

```
DUNEGAN/ENDEVCO VESSEL TESTING PROGRAM - VERSION 3     COPYRIGHT 1974

ARRAY  0

  LINE,ARA,OFF A
  EDGE=26
  CAL VALUE=2250
  MAX DT=2600

ARRAY  1

  LINE,ARA,OFF A
  EDGE=26
  CAL VALUE=2250
  MAX DT=2600

HARD. MAX DT= 2600
```

Fig. C.7. Initial operator/computer communication prior to testing.

ORNL-DWG 78-1813

DATA RUN 1

EVENT	APY	DT0	DT1	DT2	DT3	X	Y	COUNTS	TIME	PARAM
POWER FAIL AT TIME=				0						
CAS ON										
111	0	807	2224	0	734	29.0	8.9	18	32	0123
148	0	205	654	0	750	10.0	-7.7	568	46	0165
152	0	1290	2481	2188	0	2.7	8.5	12	49	0172
181	1	44	0	418	591	-6.0	-6.6	1106	57	0195
183	1	0	330	1064	1726	-3.1	-7.8	20	59	0200
185	0	1	0	4	1	-26.0	7.5	1	61	9356
193	0	0	898	124	1027	5.1	-4.3	43	67	0220
197	1	0	1194	0	1769	4.2	-7.8	48	70	9573
204	0	698	240	2286	0	-28.4	18.6	35	78	0246
223	0	0	724	367	1414	1.2	-10.9	8	85	9654
233	0	601	1578	0	1670	8.8	-6.1	29	95	9594
237	1	0	565	865	1809	-1.3	-8.8	16	97	9703
249	1	0	358	640	1475	-1.4	-8.4	10	114	0322
254	1	0	1071	486	1740	2.6	-7.5	18	120	0330
269	0	75	0	1410	1692	-5.4	-5.8	75	128	0340
291	1	539	0	1182	787	-76.3	-13.7	1895	146	0345*
294	1	741	1126	1827	0	-10.5	19.4	748	147	0354
313	0	927	0	1617	1868	-15.8	-13.3	9	173	0389
315	0	60	0	971	1067	-6.4	-4.8	79	174	0385
325	0	759	34	1974	0	43.6	-26.2	46	177	0403
328	0	0	147	878	1113	-4.6	-5.0	33	177	0406
333	1	357	0	1602	1652	-6.9	-4.5	34	178	0411
335	1	503	1882	0	405	22.7	9.1	6	178	0412
336	0	0	689	200	1366	2.6	-8.0	9	178	0413
345	1	297	0	1465	837	-12.1	0.6	49	181	0425
350	0	419	1142	0	302	69.1	19.6	3577	181	0428*
356	1	0	623	351	1436	1.4	-8.3	9	182	0435
358	0	767	1375	0	1432	25.0	-15.9	3	184	0441
360	1	393	0	1194	875	-15.1	-3.2	62	184	0443
369	0	855	2167	0	1054	24.3	3.9	8	186	0453
375	0	554	0	1298	1515	-10.1	-8.8	5	187	0458
378	0	26	1013	0	1043	6.5	-4.1	47	188	0459
379	0	912	2167	0	1056	32.0	3.9	13	188	0460
386	0	813	2134	0	914	26.6	5.5	9	190	0470
398	0	702	0	1461	1975	-6.9	-9.8	9	194	0488
407	1	977	0	2199	1389	-22.4	-0.1	25	198	0502
410	0	913	2168	0	1057	32.1	3.9	16	199	0504
413	0	911	2219	0	1058	28.4	4.4	9	201	0512
414	0	857	2166	0	1056	24.5	3.8	8	201	0513
416	0	850	2101	0	951	31.9	5.0	41	202	0514
429	1	0	91	1387	1665	-5.3	-5.7	25	208	0534
432	1	469	1709	0	4	47.7	27.4	48	210	0539
435	0	0	1056	483	1741	2.6	-7.6	17	211	0542
442	1	793	1534	0	1888	9.9	-10.4	12	217	0559
457	1	337	0	1189	1766	-5.0	-8.7	42	220	0567
519	0	435	0	1623	1677	-7.2	-4.7	37	223	0573
589	0	857	2167	0	1056	24.5	3.8	9	244	0591
594	1	741	1126	1825	0	-10.5	19.5	572	247	0595
597	1	1526	0	1944	1915	28.2	12.6	24	257	0606
601	1	447	0	1840	1663	-7.4	-4.5	35	260	0610
606	0	781	1434	0	1960	8.8	-11.8	5	263	0615
607	0	857	2167	0	1055	24.5	3.8	10	265	0617
613	0	794	1495	0	1696	14.5	-11.6	10	267	0620
619	1	534	287	2283	0	-16.5	10.3	34	278	0634
621	1	77	448	0	1079	3.8	-10.4	169	280	0636
622	0	909	2217	0	1056	28.4	4.4	10	281	0638
CAS OFF										

Fig. C.8. Terminal printout of information associated with each valid event of cycle 1.

ORNL-DWG 78-1814

DATA RUN 2

EVENT	ARY	DT0	DT1	DT2	DT3	X	Y	COUNTS	TIME	PARAM
ARY 1										
CAS ON										
49	1	497	0	1301	1061	-15.8	-5.0	109	125	0532
55	1	743	1129	1827	0	-10.5	19.5	359	127	0537
65	0	0	989	394	1016	4.0	-2.5	15	128	0540
525	1	630	298	2348	0	-18.5	11.7	11	135	0560
827	0	751	0	1671	1690	-11.5	-6.9	29	228	0690
861	0	224	111	0	111	-3.3	1.9	8	255	0712
CAS OFF										
CAS ON										
29	0	535	1434	0	740	26.7	1.8	28	11	0733
60	1	0	10	333	990	-2.8	-10.0	109	42	0807
61	0	577	0	1417	1732	-7.9	-8.2	37	42	0807
62	1	0	428	424	1675	0.0	-10.6	54	44	0811
64	0	722	1556	0	1800	9.5	-8.5	16	46	0816
82	1	553	0	1995	1594	-8.8	-1.1	25	70	0875
85	1	480	0	1366	1676	-7.2	-7.5	16	74	0886
86	1	826	0	1743	1831	-10.7	-7.3	28	75	0886
87	1	857	0	2199	2049	-6.5	-2.3	2	75	0886
99	0	421	1197	0	403	40.2	8.5	4096	83	0905
100	1	416	0	1277	904	-15.2	-2.7	103	85	0904
103	0	1721	1842	0	1765	-13.9	7.8	10	88	0908
106	1	0	526	1246	1092	-4.6	-1.3	9	90	0914
115	0	1545	2338	0	1997	-41.4	18.9	17	95	0926
120	0	130	1308	0	1447	6.2	-5.0	28	105	0951
130	0	691	2285	0	1358	11.3	2.5	39	115	0976
136	0	356	1468	0	1540	7.3	-5.0	58	124	0998
141	0	493	0	1338	1849	-5.8	-8.7	23	126	1004
142	1	671	2025	0	796	21.3	5.5	4	126	1004
144	0	463	1283	0	1637	7.2	-8.2	24	129	1011
154	1	424	0	1446	1630	-7.1	-6.1	14	140	1037
157	1	126	1366	0	1249	7.4	-3.1	55	141	1040
161	0	0	903	23	1325	4.6	-6.8	30	143	1044
165	0	126	0	1550	1737	-5.7	-5.1	20	148	1058
167	0	771	0	1336	1968	-8.7	-13.5	4	150	1064
168	1	0	511	697	1505	-0.9	-7.6	30	151	1064
184	1	618	0	2545	1930	-6.7	1.5	73	199	1097
189	0	269	0	1046	1480	-5.9	-8.2	7	204	1112
191	0	0	906	764	1800	0.7	-7.9	22	206	1117
193	1	18	1164	1633	0	-3.8	7.5	25	208	1123
195	1	0	879	60	1338	4.3	-7.0	47	212	1136
198	0	0	1016	412	1751	2.6	-8.1	18	215	1142
205	1	607	0	1551	1658	-9.1	-6.5	18	221	1161
214	1	525	0	1464	1565	-8.9	-6.3	17	249	1173
215	0	0	574	369	376	2.3	1.2	110	249	1174
220	1	875	1807	0	1863	11.2	-7.1	47	254	1187
230	1	492	0	1430	1540	-8.6	-6.2	15	259	1202
246	0	0	550	730	1809	-0.7	-9.5	32	267	1222
249	1	53	1035	0	1242	5.8	-5.5	75	268	1225
250	1	0	130	738	1073	-4.0	-5.9	71	268	1226
264	0	391	0	1121	1359	-8.6	-8.0	78	278	1254
270	0	955	1782	0	1974	8.9	-7.3	4	280	1253
271	1	248	8	1470	0	-21.3	12.4	84	283	1251
10249	0	471	2206	0	911	12.6	4.8	79	380	0652
CAS OFF										

Fig. C.9. Terminal printout of information associated with each valid event of cycle 2.

ORNL-DWG 78-1815

DATA RUN 3

EVENT CAS	ARY ON	DT0	DT1	DT2	DT3	X	Y	COUNTS	TIME	PARAM
4	0	1582	0	599	263	3.9	-0.0	1	110	0596
6	1	1073	0	2000	2217	-8.2	-7.2	31	114	0603
5	0	479	2108	0	413	17.1	8.1	7	19	0779
20	1	558	603	1400	0	-26.9	36.6	792	30	1795
40	0	613	1615	0	1486	11.2	-4.9	133	151	0963
73	1	1083	0	2113	1334	-75.5	-8.4	12	231	1079◆
77	0	0	1059	590	1305	2.8	-3.8	73	290	1183

Fig. C.10. Terminal printout of information associated with each valid event of cycle 3.

BLANK PAGE

DATA RUN 4

EVENT	ADV	DT0	DT1	DT2	DT3	X	Y	COUNTS	TIME	PHDAM
CNT	CH									
31	0	696	495	1602	0	-11.9	10.6	16	304	1186
35	1	1012	0	1816	2172	-9.1	-9.6	24	321	1214
39	1	490	0	1629	527	-24.2	6.7	111	321	1216
44	1	1535	0	1561	2497	19.1	17.3	128	324	1221
58	0	0	6	3	0	-13.0	7.5	1	280	1256
60	1	1522	0	1563	2262	17.8	14.2	149	414	1279
61	1	561	0	1177	671	-80.0	-5.5	353	414	1279
66	1	729	0	1756	21	38.0	-19.5	12	419	1285
68	1	95	1160	0	1144	7.0	-3.9	41	424	1291
70	0	1360	2165	2227	0	-0.9	20.7	66	424	1291
73	1	118	1433	0	1707	5.5	-5.7	31	425	1293
74	0	0	163	976	1303	-3.9	-6.5	21	426	1294
78	1	545	2579	0	568	11.4	6.3	40	430	1296
79	0	0	584	1728	1116	-7.2	1.3	71	434	1296
84	0	279	0	1046	1490	-5.9	-6.3	6	446	1294
85	0	692	0	1860	1728	-8.9	-3.7	56	451	1297
88	1	490	0	1986	2030	-5.6	-3.6	25	455	1303
89	1	349	0	1622	1558	-6.6	-7.4	12	455	1303
91	0	58	0	1019	1055	-6.7	-4.2	111	455	1303
93	1	1269	2322	0	1906	26.2	-7.3	1	456	1305
94	0	0	872	56	1220	4.7	-6.2	30	457	1306
99	1	48	0	1505	1733	-5.6	-5.4	19	462	1313
102	0	208	0	1454	1377	-7.4	-3.5	48	463	1314
103	1	715	0	1447	1856	-5.8	-10.2	17	463	1315
120	0	0	313	376	962	-0.5	-6.9	387	466	1319
133	1	0	1287	553	1049	4.8	-9.6	100	468	1321
134	0	371	0	1924	90	-19.2	10.5	18	468	1322
141	0	847	0	2459	1396	-11.8	3.5	131	469	1323
144	1	1466	0	2325	2393	-21.4	-10.6	11	470	1324
146	1	200	0	1412	1551	-6.3	-5.0	29	471	1325
152	1	0	866	117	1299	4.1	-6.6	80	473	1328
164	1	147	1502	661	0	7.7	8.5	29	476	1331
168	0	666	0	1360	1648	-11.1	-10.5	5	477	1331
179	1	159	1047	1444	0	-3.5	8.3	17	486	1328
181	0	619	1765	0	1679	6.8	-4.2	110	491	1326
183	0	396	1460	0	1548	7.5	-5.3	27	493	1326
185	0	228	0	1368	1367	-7.3	-4.2	51	501	1336
188	0	319		1541	1303	-8.8	-2.6	62	502	1337
190	0	605	1410	0	1560	10.6	-8.1	17	504	1340
196	0	851	0	1531	1728	-16.6	-13.1	12	506	1343
200	0	0	358	1986	1491	-8.5	-0.3	54	508	1347
207	0	0	576	983	1029	-2.7	-2.0	71	511	1350
214	0	0	180	1047	515	-7.4	1.5	430	512	1351
218	0	364	0	1525	1426	-8.3	-3.7	30	512	1351
221	1	0	1030	160	1333	4.9	-5.2	80	513	1353
225	0	0	831	548	1358	1.6	-5.6	166	514	1354
227	1	0	2067	819	177	9.3	7.3	250	514	1354
229	1	1316	2313	0	1989	24.7	-10.4	11	514	1354
230	1	0	1284	599	1131	4.3	-1.1	36	514	1355
242	1	236	0	1586	1595	-7.0	-4.0	41	516	1357
244	0	911	0	1796	1825	-12.0	-8.1	6	517	1358
245	1	497	1772	0	1321	10.7	-1.3	54	517	1358
250	1	479	2015	0	1201	11.1	1.7	24	519	1360
272	1	520	0	1542	1558	-8.9	-5.1	26	524	1366
275	1	0	933	35	1021	5.9	-4.3	52	525	1366
282	1	0	1362	612	1120	4.8	-0.6	93	528	1365
284	1	466	1766	1642	0					
300	0	965	1972	0	1952					
307	0	540	1673	0	1546					
309	1	630	0	1431	1513					
310	1	1275	2206	0	2164					
314	1	571	1598	0	975					
318	1	658	0	2309	1357					
319	1	863	0	2131	1117					
321	1	1063	2021	0	1909					
323	0	95	945	0	1331					
324	1	766	0	1709	1828					
325	1	959	0	2188	1361					
328	0	306	0	1622	794					
329	1	924	1944	0	1775					
331	1	876	1893	0	1892					
335	1	966	1830	0	972					
340	1	865	1787	0	1726					
341	0	652	1399	0	1849					
362	1	421	1616	0	925					
364	1	759	1763	0	1791					
369	0	365	0	1450	757					
379	1	498	2137	0	795					
389	1	862	1764	0	1617					
390	1	134	0	555	724					
391	1	844	2013	0	1089					
394	1	422	1786	0	661					
398	1	462	1607	0	796					
399	1	481	0	1405	1471					
407	1	968	1874	0	1881					
413	1	903	0	1642	1773					
416	0	849	0	1483	2111					
419	1	414	0	1399	1422					
423	0	1369	2258	0	2290					
429	1	358	2247	0	610					
430	0	435	1292	2097	0					
441	0	186	0	1070	1052					
445	1	301	1319	0	799					
448	1	619	1297	0	1688					
449	1	455	1431	0	1457					
450	1	617	1874	0	1879					
456	1	917	1964	0	2073					
457	1	785	1709	0	1598					
461	0	470	1678	0	1189					
468	0	1162	2245	0	1993					
486	0	855	1763	0	1975					
491	1	913	1866	0	1913					
504	1	1266	2322	0	1905					
514	0	279	0	1046	1489					
517	1	926	1872	0	1782					
529	1	1204	1345	0	1668					
550	0	1169	2375	0	1936					
571	0	330	0	1590	820					
572	1	522	1346	0	1663					
579	1	298	1793	0	530					
581	1	361	1855	0	591					
588	0	977	0	1844	2230					
606	0	243	1361	0	1555					
624	0	0	330	176	719					
626	0	525	0	2235	346					
635	0	845	1583	2005	0					

Fig. C.11. Terminal printout of information

BLANK PAGE

1.1	8.4	50	529	1354
10.6	-6.0	31	549	1376
9.2	-3.9	162	553	1383
-11.9	-8.1	7	553	1383
13.1	-5.7	10	554	1384
18.7	-0.6	119	554	1384
-14.2	2.4	68	554	1384
-24.2	2.7	129	554	1384
12.7	-5.9	16	554	1385
5.2	-7.0	72	555	1385
-9.5	-6.9	99	556	1386
-16.0	1.1	118	556	1387
-12.5	2.1	266	557	1387
13.4	-5.5	58	557	1387
10.1	-5.8	34	557	1387
20.9	1.7	76	558	1389
13.9	-7.2	35	559	1389
7.7	-9.8	24	558	1389
13.6	0.8	115	560	1392
9.7	-5.9	33	560	1392
-14.7	1.2	126	561	1392
14.0	5.2	16	561	1393
18.3	-8.1	109	562	1394
-7.8	-7.6	1242	562	1394
28.2	1.6	79	562	1394
15.8	4.6	44	562	1394
16.9	2.1	88	562	1395
-9.1	-6.1	62	562	1394
10.2	-6.0	30	563	1395
-16.9	-12.0	29	563	1396
-7.7	-12.2	3	563	1396
-8.7	-5.3	21	564	1396
17.6	-10.7	7	564	1396
13.0	6.4	20	564	1396
-6.6	7.9	39	564	1396
-8.1	-4.4	410	565	1397
12.7	-0.3	238	565	1398
9.3	-10.5	147	565	1397
8.9	-4.9	38	565	1396
9.1	-5.3	34	565	1398
8.2	-7.1	31	565	1398
14.1	-6.6	57	565	1398
11.7	-1.1	69	566	1399
13.7	-4.7	9	566	1399
8.3	-7.3	7	567	1400
10.9	-6.9	48	567	1401
25.7	-7.1	2	568	1401
-6.0	-8.3	6	568	1402
10.7	-5.0	36	568	1401
-23.1	13.2	2	569	1401
12.9	-2.1	107	570	1401
-12.8	1.6	75	573	1400
7.8	-9.2	5	573	1400
14.2	5.3	50	574	1400
14.6	5.3	47	574	1400
-6.9	-8.2	44	574	1399
6.9	-6.0	3	579	1398
1.6	-6.3	1454	586	1406
-17.6	6.9	91	587	1406
-4.6	13.1	25	588	1402

637	1	266	1511	0	1496	7.2	-4.6	96	590	1409
641	0	1397	0	1817	1712	24.5	13.1	6	591	1412
643	0	42	1557	2044	0	-4.0	7.4	23	591	1413
652	1	0	1062	77	1077	6.1	-3.5	59	593	1415
668	0	629	0	1597	1633	-9.7	-6.0	10	594	1417
673	0	291	0	1276	776	-12.6	-0.4	109	595	1417
707	1	0	1063	86	613	7.9	0.3	318	596	1419
717	1	1077	2268	0	1616	19.5	-1.4	4	597	1420
724	0	806	1722	0	1883	9.5	-7.4	5	597	1419
737	0	815	0	1750	1719	-12.4	-6.8	12	597	1420
738	1	503	0	1502	2489	-1.7	-4.6	14	597	1420
755	1	721	1956	0	1207	16.5	0.4	363	598	1421
756	1	729	0	1633	1677	-11.2	-7.1	52	598	1421
773	1	230	0	1343	1068	-9.2	-2.3	53	598	1421
775	1	550	1890	0	975	15.6	2.4	30	598	1421
781	1	355	0	1855	1296	-9.6	-0.0	76	598	1421
786	0	484	1498	0	1593	8.2	-5.6	18	598	1422
788	1	273	1239	0	1050	9.7	-3.3	122	598	1421
798	1	1015	1969	0	1996	11.6	-7.0	57	599	1422
799	0	299	0	1134	776	-13.2	-2.0	313	599	1422
810	0	435	1448	0	1498	5.3	-5.4	15	599	1422
813	0	630	0	1734	1521	-10.8	-3.7	24	599	1422
816	1	0	609	190	1397	2.2	-8.6	10	599	1422
832	1	861	1544	0	1719	17.5	-13.3	127	599	1423
833	0	404	0	1266	903	-14.8	-2.7	996	599	1423
836	1	608	0	1593	1615	-9.6	-5.8	100	600	1423
860	1	272	1448	0	758	12.4	1.2	661	600	1423
870	0	548	1638	0	1576	9.0	-4.5	7	600	1424
871	1	328	1561	0	1635	6.8	-4.6	27	600	1424
872	1	221	1364	0	1459	6.8	-4.9	41	600	1424
882	0	237	0	1543	1382	-7.8	-2.9	42	600	1424
883	1	884	1575	0	1486	33.2	-15.6	1	600	1424
884	0	240	0	1216	728	-12.0	-0.3	101	600	1424
886	0	501	0	1693	896	-14.6	3.1	157	600	1424
894	0	498	1516	0	1605	8.1	-5.7	10	601	1424
927	1	121	1394	0	125	14.9	7.4	105	601	1425
939	1	788	0	1460	1879	-10.3	-11.7	26	602	1425
963	0	504	1389	0	1626	7.9	-7.3	54	603	1427
968	1	919	2046	0	1652	11.4	-2.1	89	603	1427
975	0	764	1832	2062	0	-2.0	3.4	23	603	1427
1028	0	497	0	1855	893	-14.8	2.9	259	604	1428
1031	1	134	1227	0	1745	4.6	-7.5	26	604	1428
1032	1	313	0	1563	1664	-6.5	-4.8	50	604	1428
1056	1	0	1065	1312	28	-2.1	7.4	45	604	1428
1065	1	1059	1935	0	2007	13.9	-9.0	18	605	1428
1066	1	666	0	1672	1729	-8.9	-5.9	11	605	1428
1073	1	152	0	921	980	-7.6	-5.1	153	605	1429
1363	0	96	1329	0	1372	6.6	-4.2	18	606	1429
1486	1	727	0	1656	1784	-9.5	-7.0	7	606	1429
1515	0	0	333	1275	991	-6.1	-0.8	56	607	1429
1516	0	0	368	1254	1031	-5.7	-1.2	119	607	1429
1523	0	387	1371	0	1194	10.4	-3.8	51	607	1429
1524	1	449	1552	0	1546	8.2	-4.6	102	607	1429
1526	1	700	0	1418	1795	-9.4	-10.3	12	607	1429
1614	0	543	1567	0	1686	7.9	-5.9	6	608	1429
1615	1	895	0	1493	1941	-13.2	-14.8	6	608	1429
1625	0	0	1094	52	1182	6.0	-4.4	5	610	1424
1639	0	1254	2356	0	1706	40.9	-7.3	2	625	1420
1649	0	634	1674	0	1710	3.9	-5.5	3	631	1419
1652	1	336	1240	0	669	16.0	0.4	558	636	1418

CAL OFF

associated with each valid event of cycle 4.

BLANK PAGE

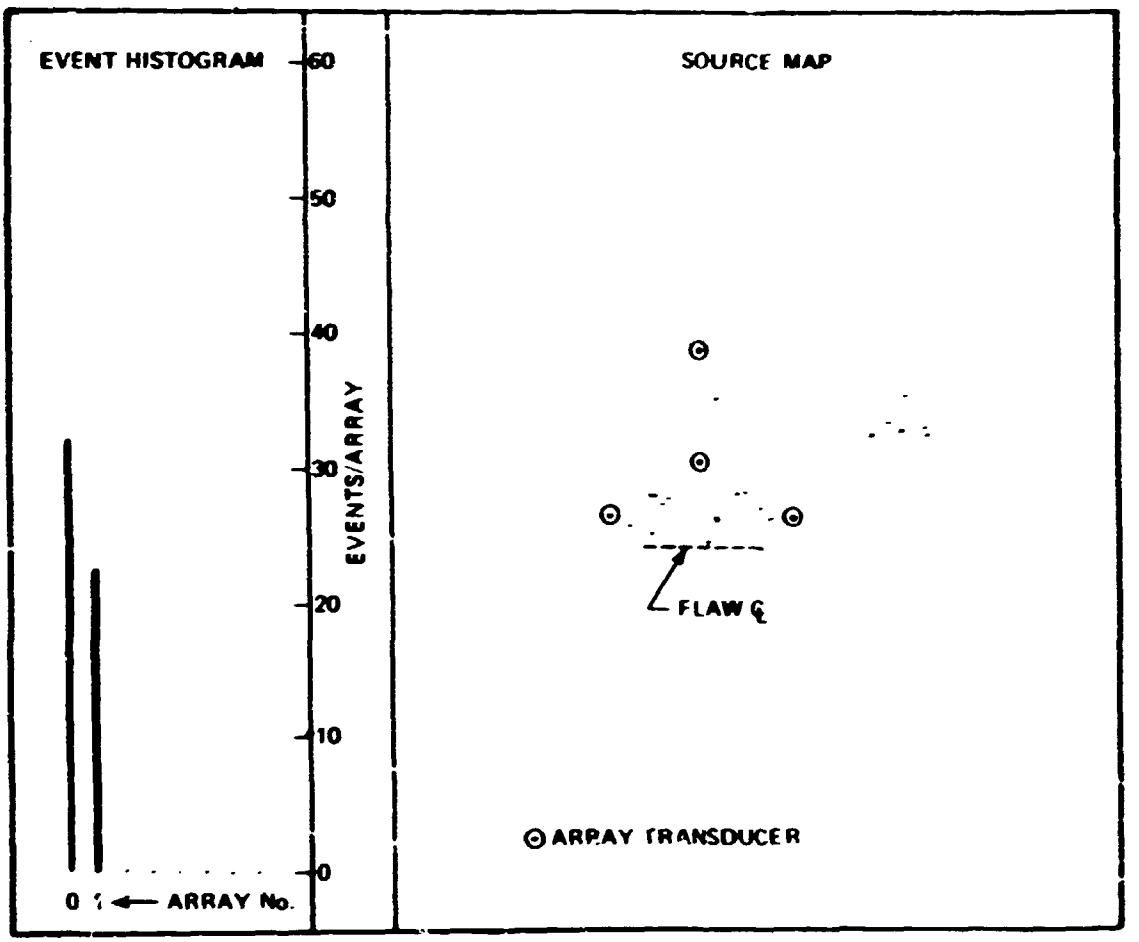

Fig. C.12. Array 0 sources in cycle 1.

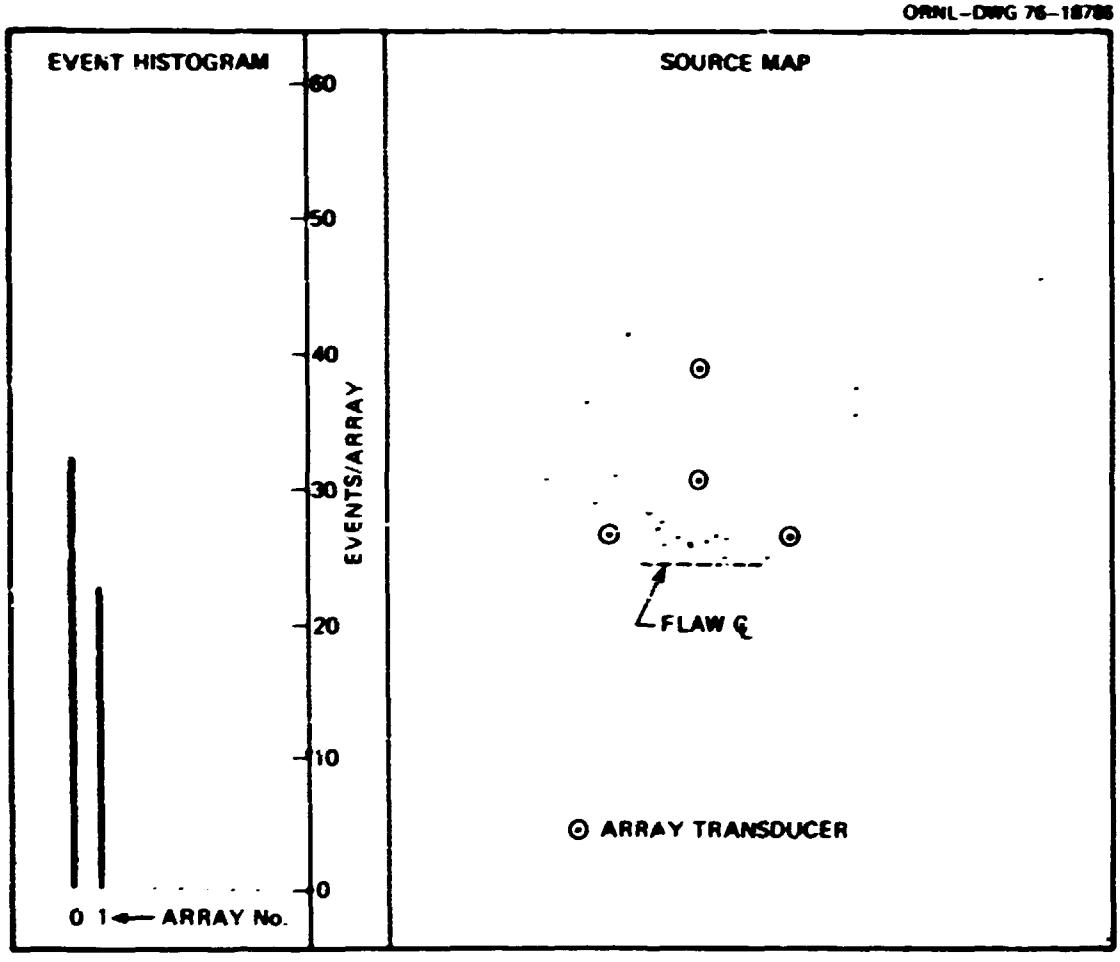

Fig. C.13. Array 1 sources in cycle 1.

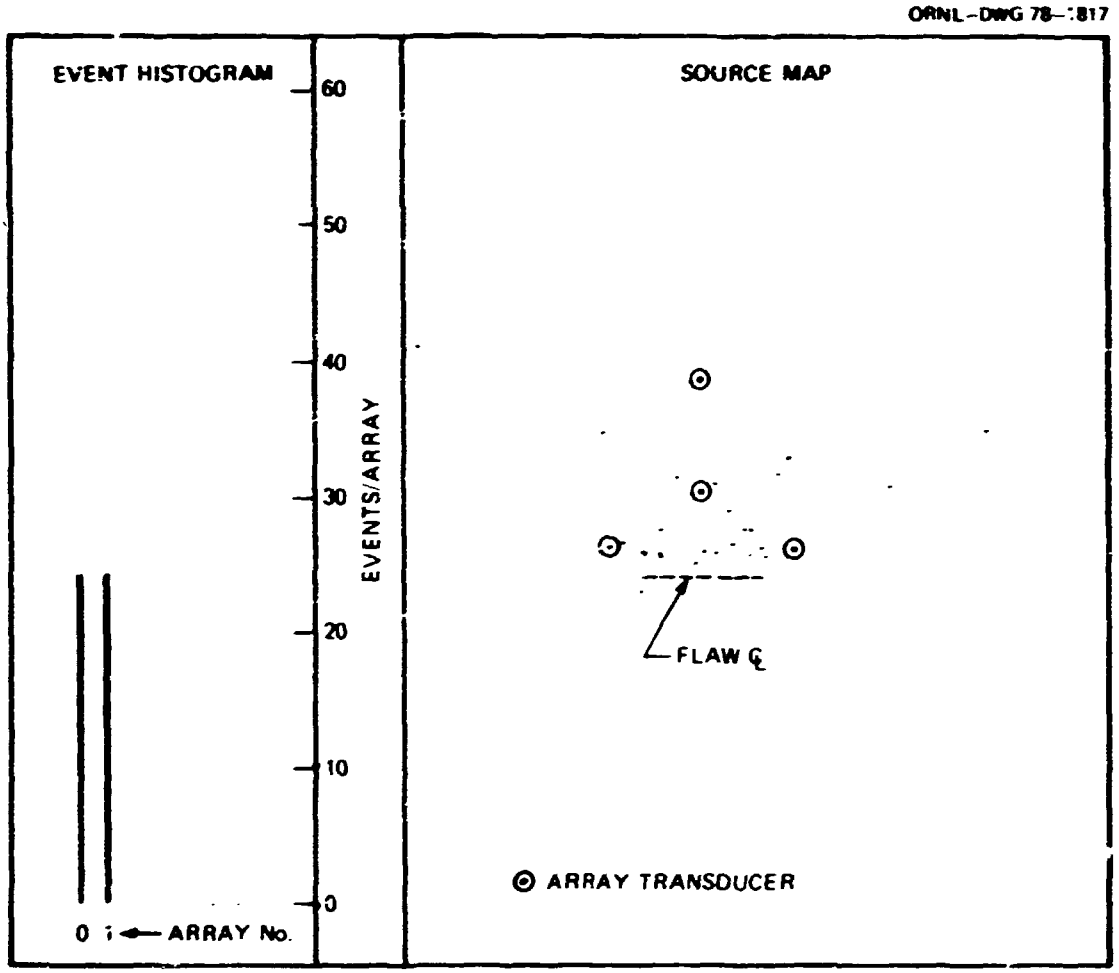

Fig. C.14. Array 0 sources in cycle 2.

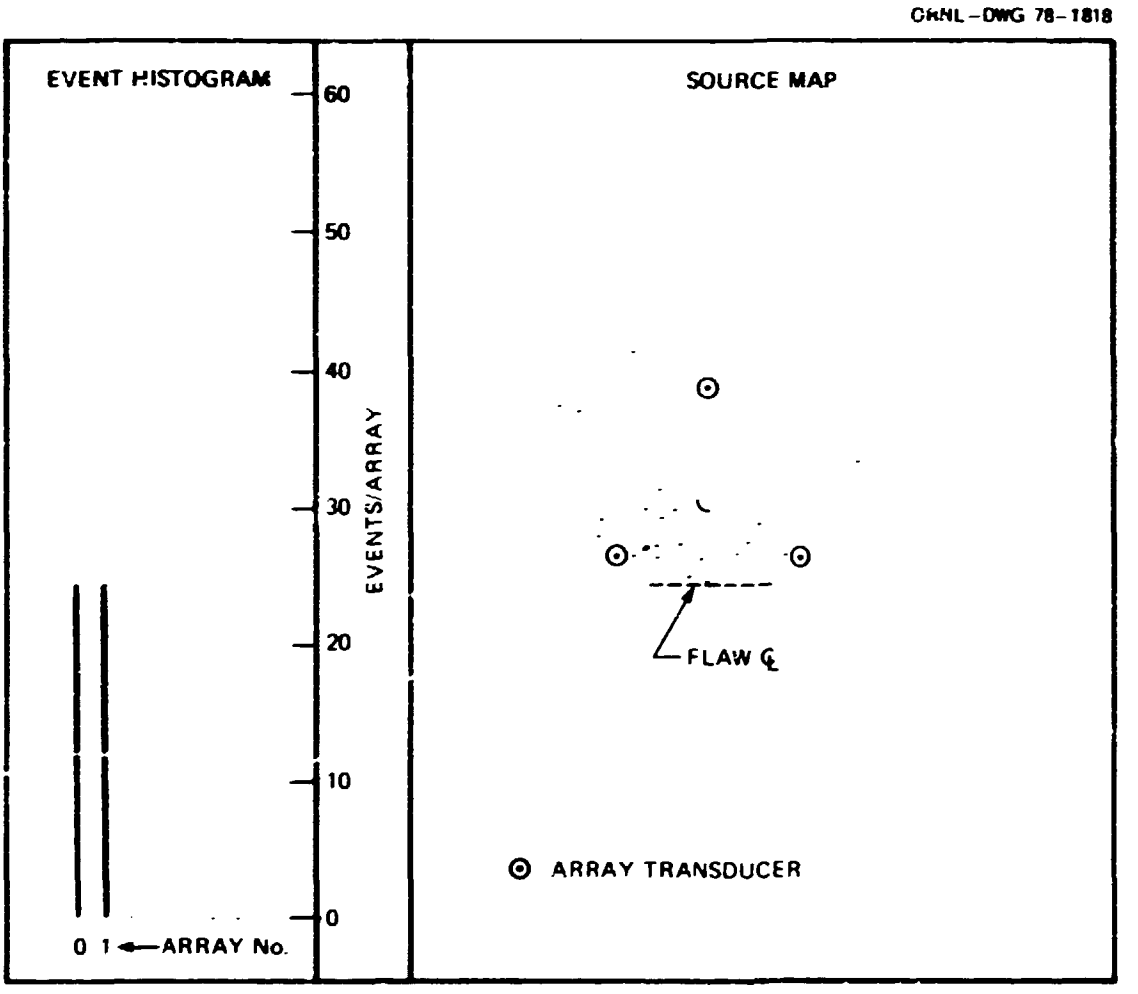

Fig. C.15. Array 1 sources in cycle 2.

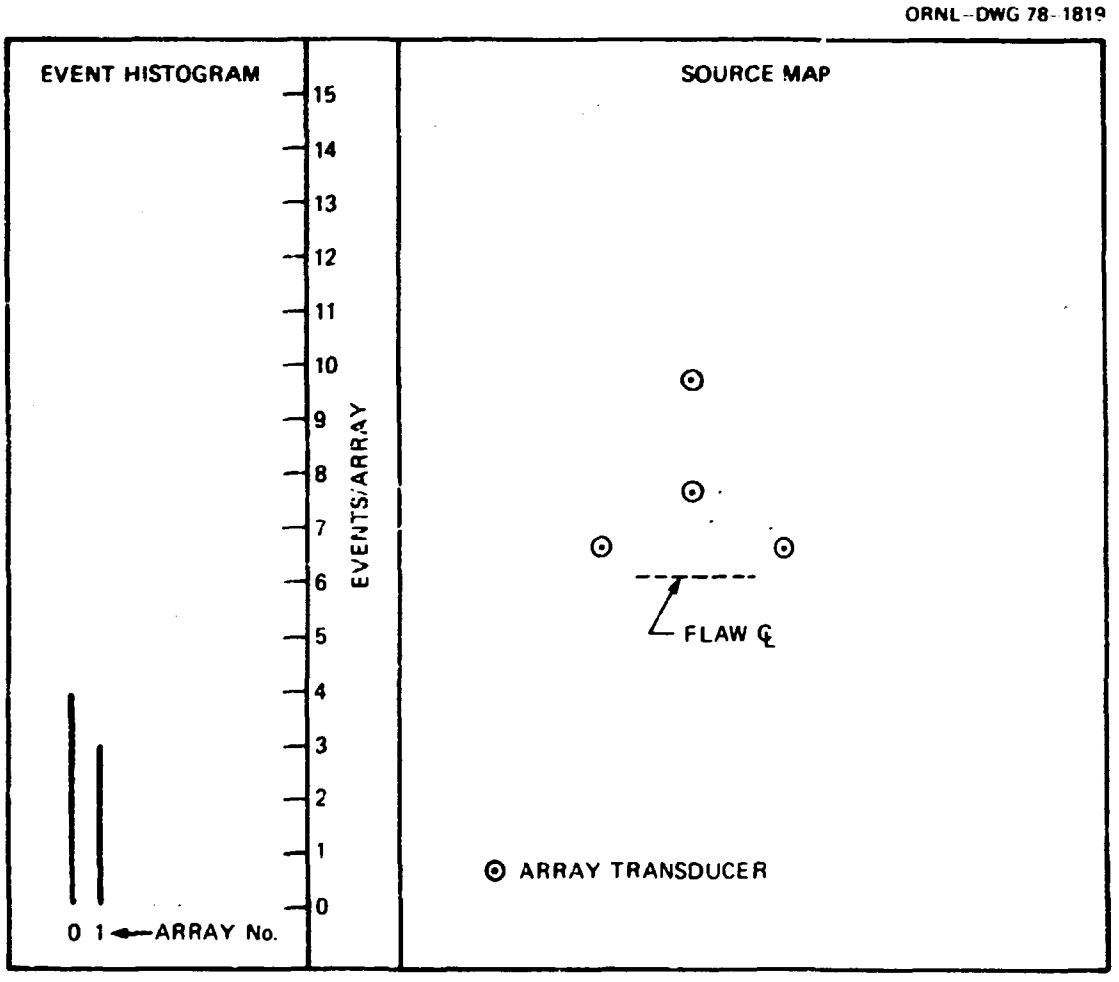

Fig. C.16. Array 0 sources in cycle 3.

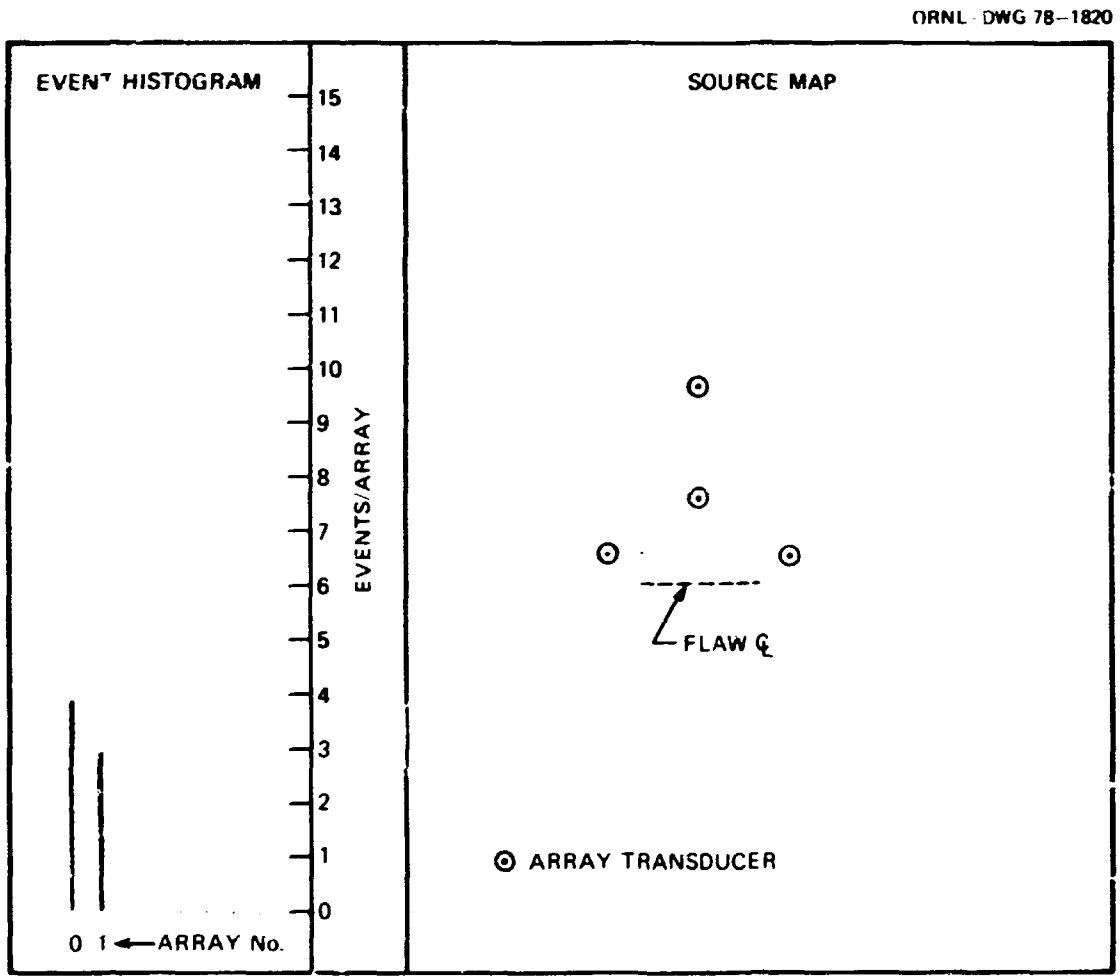

Fig. C.17. Array 1 sources in cycle 3.

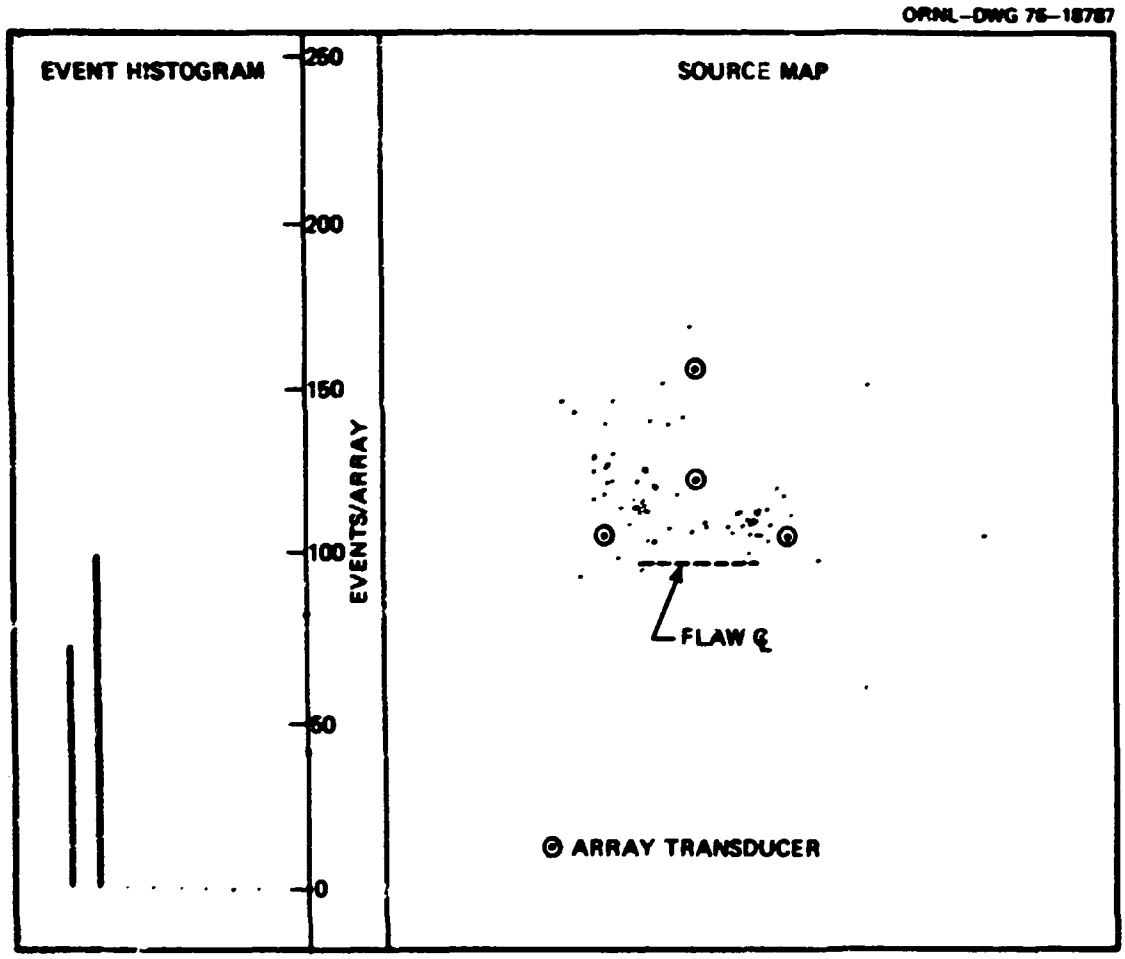

Fig. C.18. Array 0 sources in cycle 4.

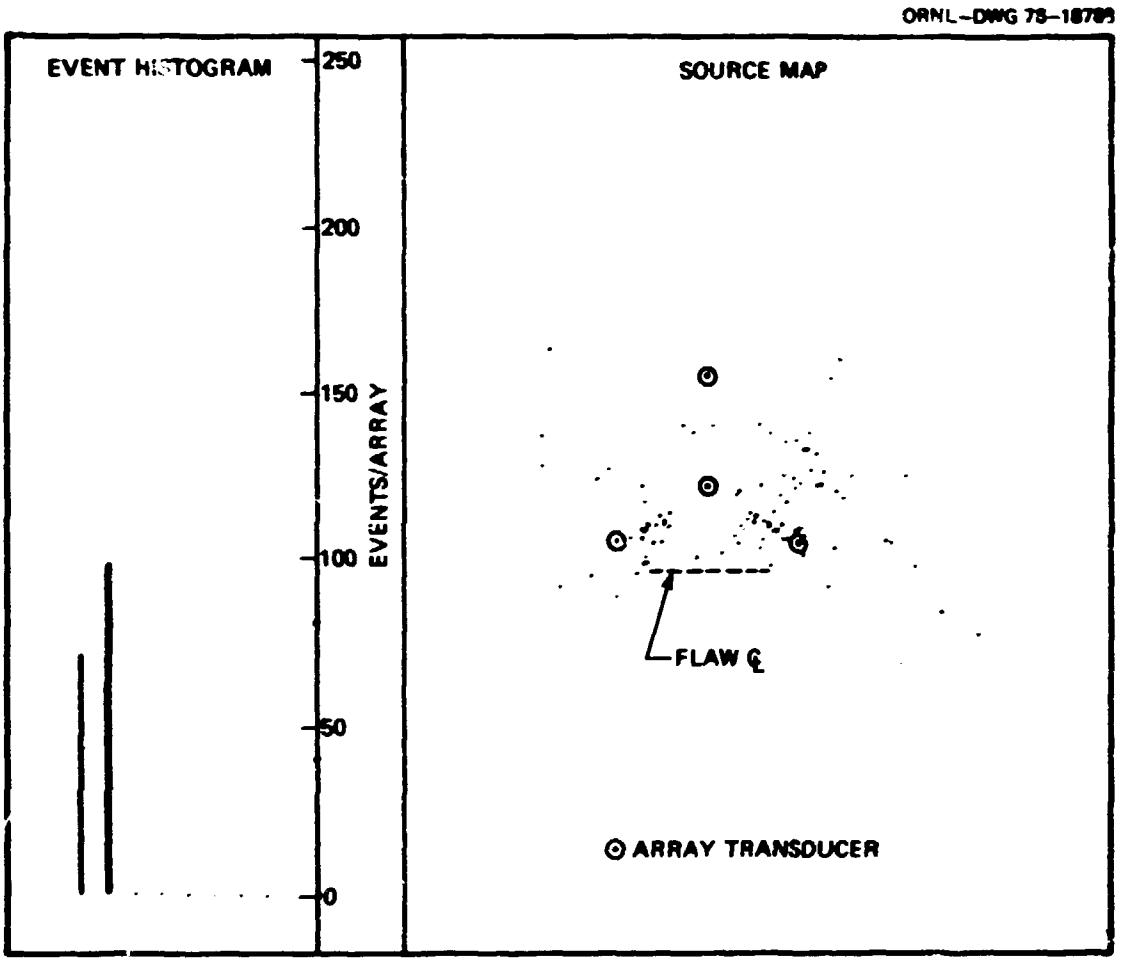

Fig. C.19. Array 1 sources in cycle 4.

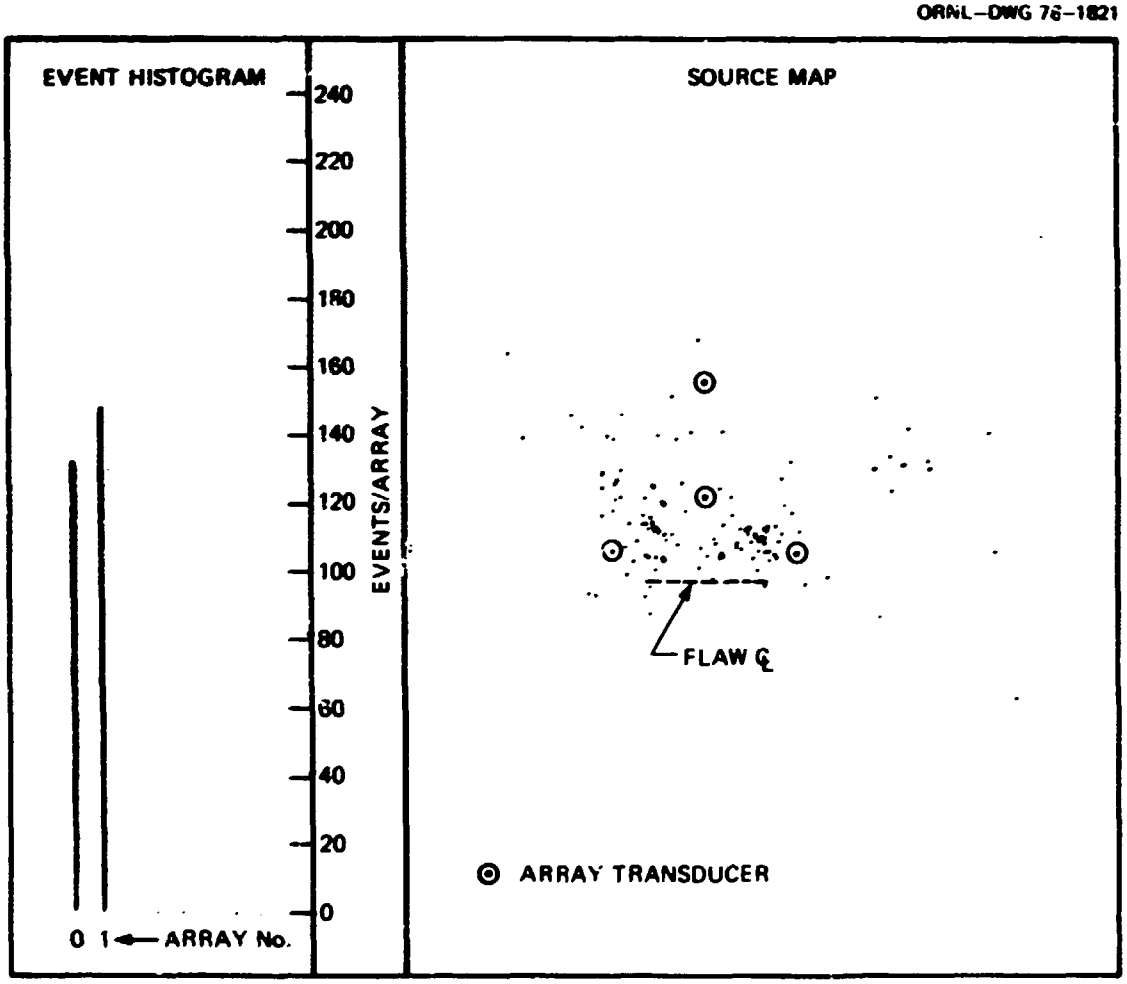

Fig. C.20. Array 0 sources — summation of all cycles.

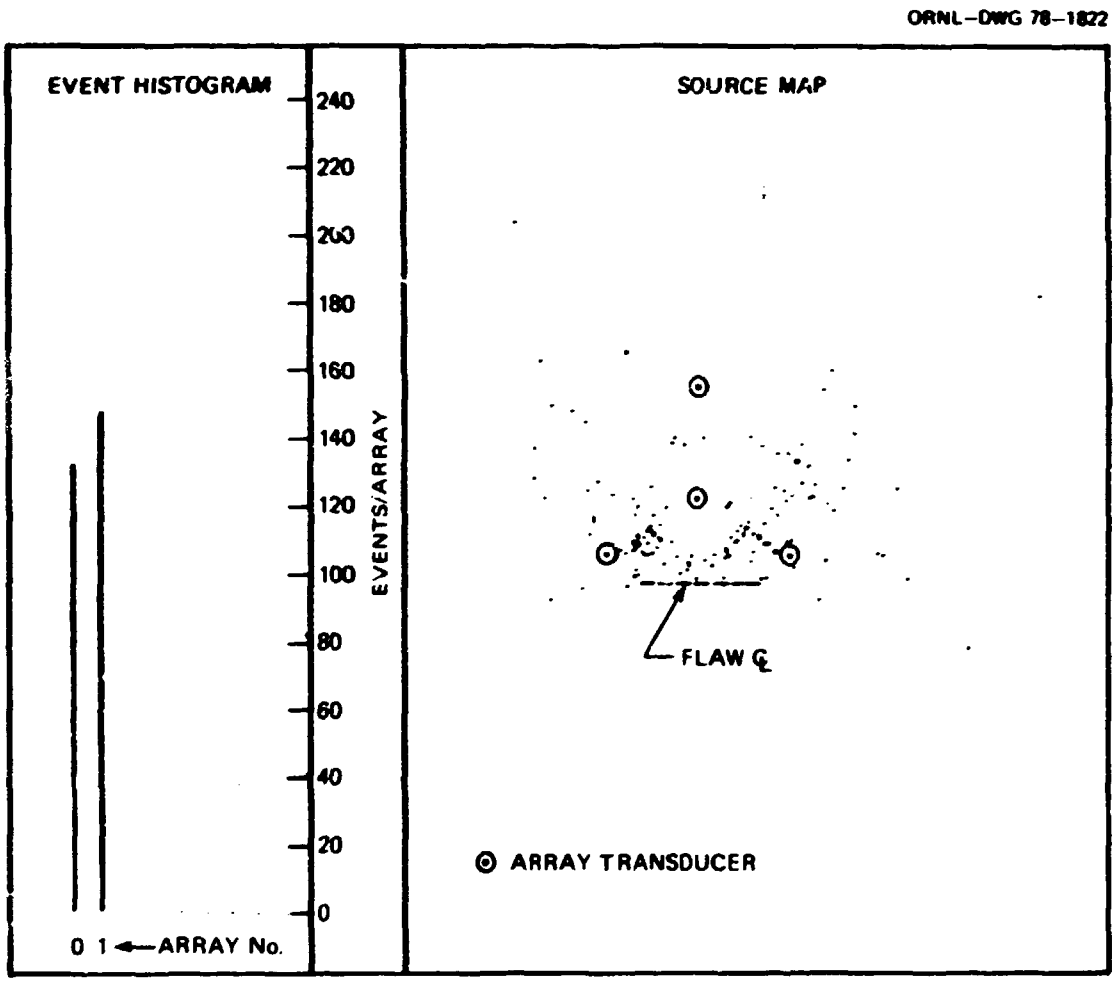

Fig. C.21. Array 1 sources – summation of all cycles.

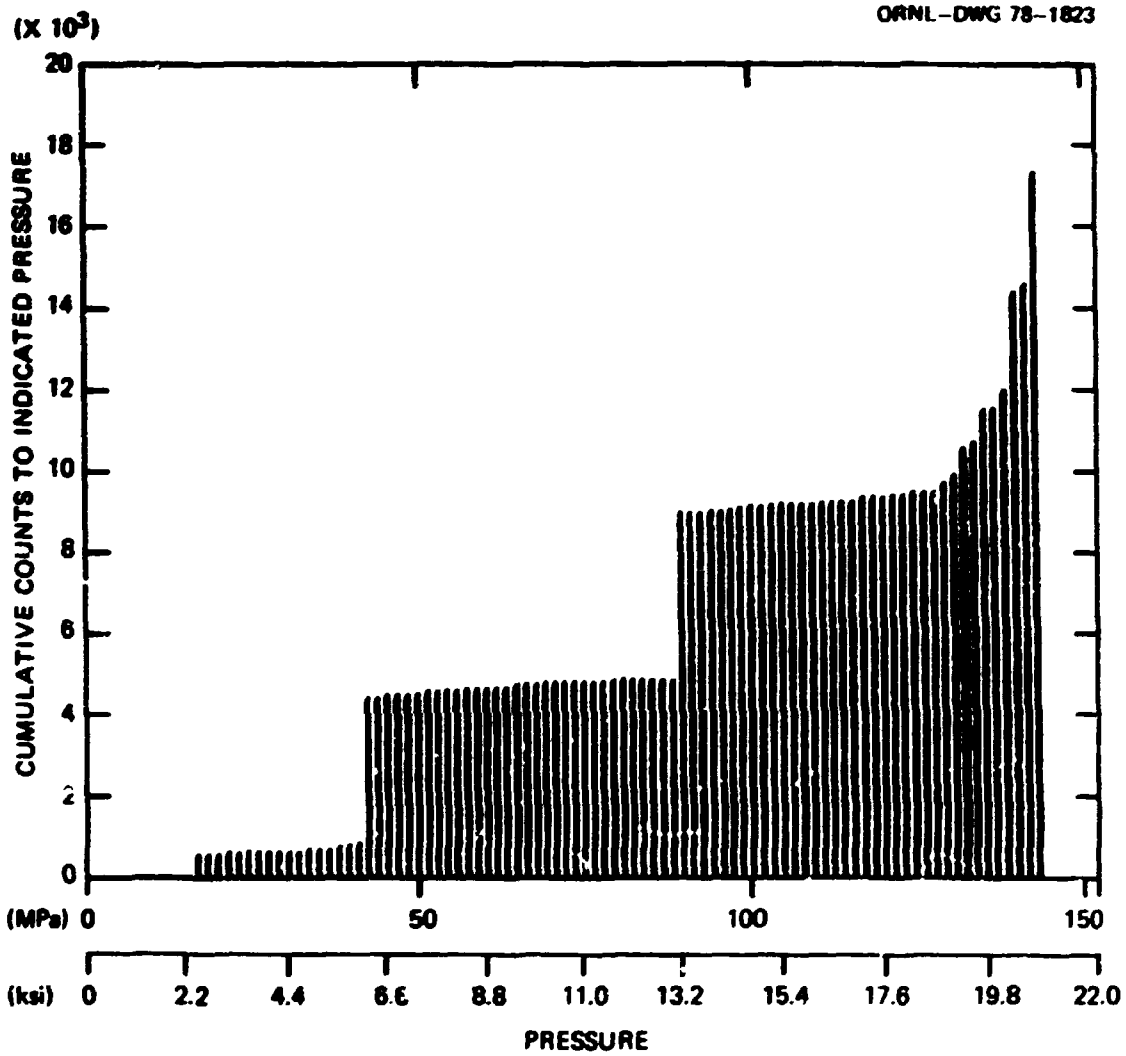

Fig. C.22. Summation of counts vs pressure for all cycles for array 0.

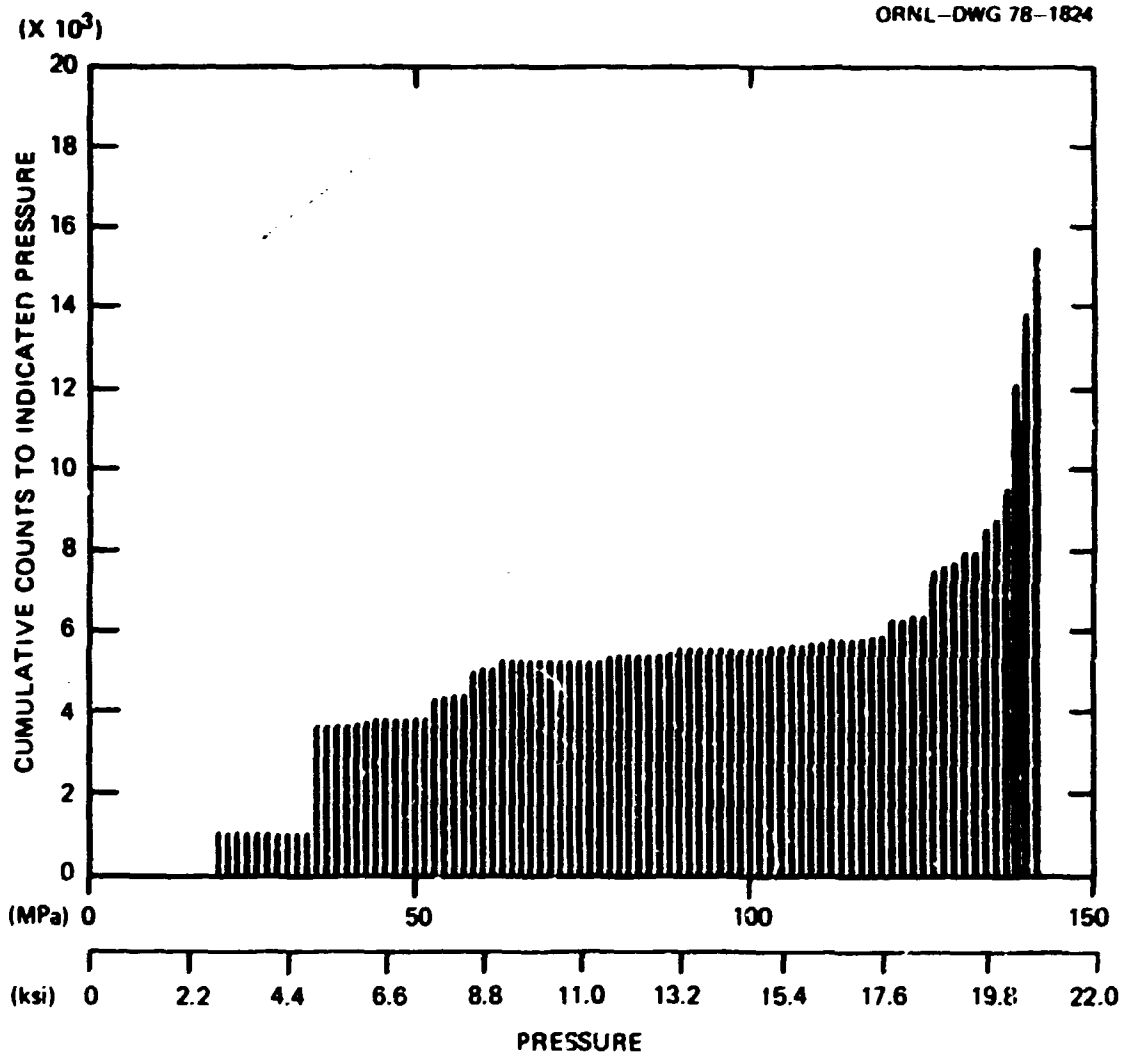

Fig. C.23. Summation of counts vs pressure for all cycles for array 1.

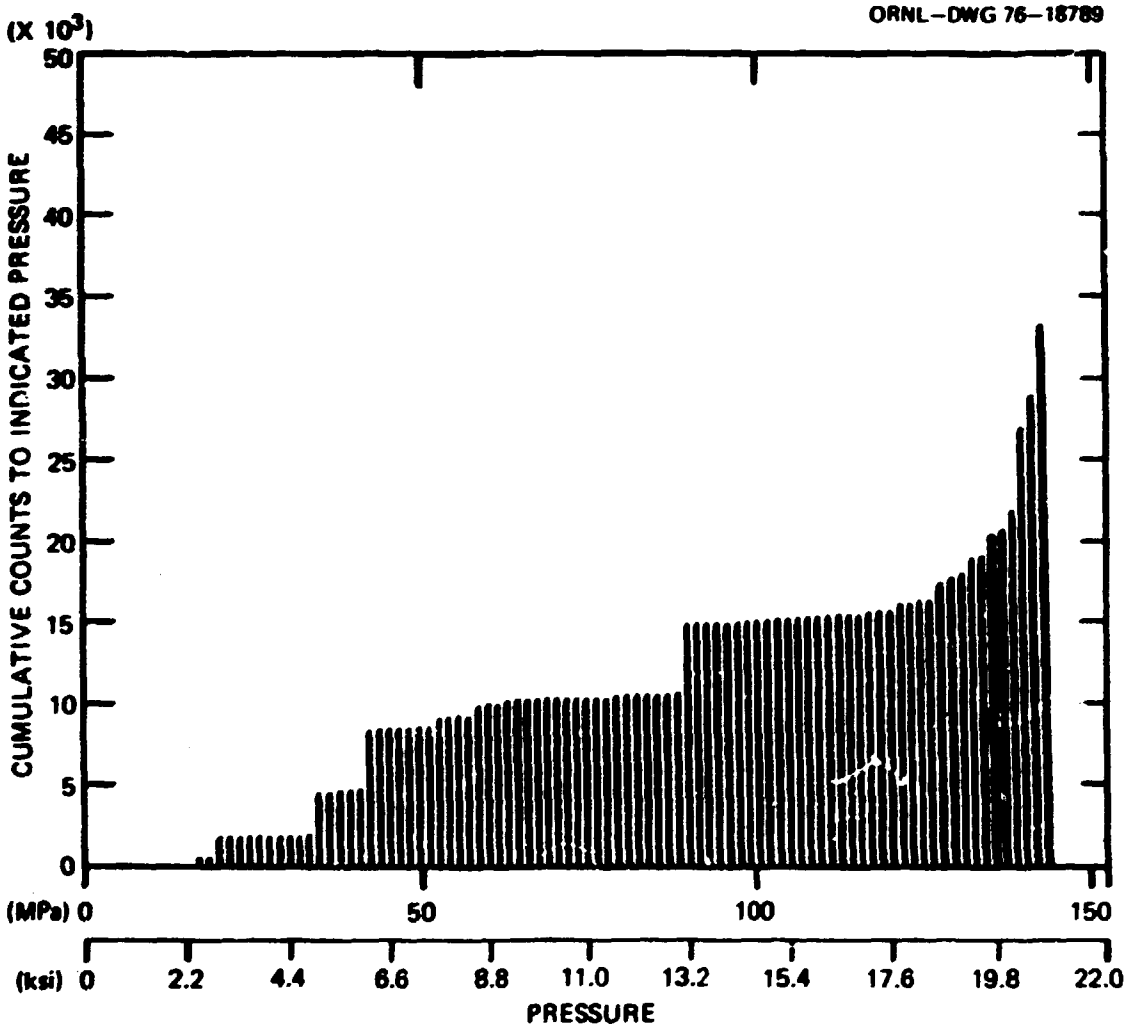

Fig. C.24. Summation of counts vs pressure for all cycles for both arrays.

References

1. D. O. Harris and H. L. Dunegan, "Verification of Structural Integrity of Pressure Vessels by Acoustic Emission and Periodic Proof Testing," *Testing for Prediction of Material Performance in Structures and Components*, STP-515, pp. 158–70, American Society for Testing and Materials, 1972.

2. A. T. Green and H. L. Dunegan, "Acoustic Emission Analysis of Crack Propagation and Fracture in Pressure Vessels and Pressure Vessel Materials," presented at the First International Conference on Structural Mechanics in Reactor Technology, Berlin, Germany, September 1971.

3. N. O. Cross, L. L. Loushin, and J. L. Thompson, "Acoustic Emission Testing of Pressure Vessels for Petroleum Refineries and Chemical Plants," *Acoustic Emission*, STP-505, pp. 270–96, American Society for Testing and Materials, 1972.

4. A. A. Pollock and B. Smith, "Stress-wave Emission Monitoring of a Military Bridge," *Non-Destructive Testing*, pp. 348–53, December 1972.

5. M. P. Kelly and R. L. Bell, "Detection and Location of Flaw Growth in the EBOR Nuclear Reactor Vessel," DE-73-4, Dunegan/Endevco, San Juan Capistrano, Calif.

6. K. Gopal, "Westinghouse Acoustic Emission Studies at EBOR," Final EEI-TVA Rp 79 Meeting, San Antonio, Tex., Dec. 11, 1972.

7. D. L. Parry, "Acoustic Emission Analysis in Oil and Chemical Industry," Exxon Nuclear Company, Richland, Wash., April 1972.

8. M. P. Kelly, D. O. Harris, and A. A. Pollock, "Detection and Location of Flaw Growth in Metallic and Composite Structures," *Monitoring Structural Integrity by Acoustic Emission*, STP-571, pp. 221–40, American Society for Testing and Materials, 1975.

9. T. F. Drouillard, R. G. Liptai, and C. A. Tatro, "Industrial Use of Acoustic Emission for Nondestructive Testing," *Monitoring Structural Integrity by Acoustic Emission*, STP-571, pp. 122–49, American Society for Testing and Materials, 1975.

10. R. R. Corle, "The Use of Acoustic Emission to Improve Rocket Motor Case Structural Reliability," presented at AIAA/SAE 9th Propulsion Conference, Las Vegas, Nev., November 1973, AIAA Paper 73-1258.

11. C. D. Bailey and W. M. Pless, "Acoustic Emission Used to Nondestructively Determine Crack Locations in Aircraft Structure Fatigue Specimens," *9th Symposium on Nondestructive Testing*, San Antonio, Tex., April 1973.

12. "Proposed Standard for Acoustic Emission Examination during Application of Pressure," available from the American Society of Mechanical Engineers, United Engineering Center, 345 East 47th Street, New York, N.Y. 10017.

13. M. P. Kelly, "Acoustic Emission Monitoring of a Reactor Vessel during Hydrostatic Testing," Dunegan/Endevco, San Juan Capistrano, Calif. September 1975.

14. R. J. Schlamp and M. P. Kelly, "Acoustic Emission Monitoring of Two Gulf Hydrotreaters during Hydrostatic Testing," Dunegan/Endevco, San Juan Capistrano, Calif., April 1976.

15. J. G. Merkle et al., *Test of 6-in.-thick Pressure Vessels. Series 3: Intermediate Test Vessel V-?*, ORNL/NUREG-1 (August 1976).

Appendix D

DATA-ACQUISITION SYSTEM AND INSTRUMENTATION

All data from the test of vessel V-7A, except the acoustic-emission (AE) information, were processed, displayed, and recorded by the data acquisition system (DAS) planned and integrated by ORNL. This appendix provides details on the relationships of each of the output devices, identified in Table D.1, to the measurement devices (sensors) listed in Table D.2. Sensors in Table D.2 are listed in number order for each of the following categories: heater control thermocouples, vessel temperature data thermocouples, pressure transducers and gages, inside strain gages, outside strain gages, crack propagation gages, COD gages, and ultrasonic transducers.

Table D.1. Output devices for the V-7A test

Symbol used in Table D.2	Description
A	Computer-controlled data-acquisition system (CCDAS) with magnetic tape data storage, line printer, and digital display Datum System 70
B	Vishay with paper tape printer, typewriter, and magnetic cassette recorder
C	Ampex model FR-1300 tape recorder
D	ERDAC digital memory
E-1	X-YY′ plotter No. 1
E-2	X-YY′ plotter No. 2
F-1	Strip-chart recorder No. 1
F-2	Strip-chart recorder No. 2
F-3	Strip-chart recorder No. 3
G	Brown recorder
H	Ultrasonic system with CRT display and magnetic tape recorder
I	Video with TV monitor and tape recorder

Table D.2. Sensors on vessel V-7A

Sensor No.	V-7 sensor in same location	Description[a]	Output device[b]	Recordable range[c]	Condition[d]
Heater control thermocouples			G		
TE 1					
TE 2					
TE 3					
TE 4					
TE 5					
TE 6					
TE 7					
TE 8					
TE 9					
TE 10					
TE 11					
TE 12					
TE 13					
TE 14					
TE 15					
TE 16					
Vessel temperature data thermocouples			A	−18 to 260°C (0 to 500°F)	
TE 21					
TE 22					
TE 23					
TE 24					
TE 25					
TE 26					
TE 27					
TE 28					
TE 29					
Inside strain gages					
XE 33		F350	A, C	5%	
XE 34		F350	A, C	5%	
XE 35	27[e]	F350	A, C	5%	

Table D.2 (continued)

Sensor No.	V-7 sensor in same location	Description[a]	Output device[b]	Recordable range[c]	Condition[d]
Inside strain gages (continued)					
XE 36		F350	A, C	5%	
XE 37		F350	A, C	5%	
XE 38	40	F350	A, C		Erratic and unresponsive
XE 39	9[e]	F350	A, C	5%	
XE 40		W	A	5%	
XE 41		W	A	5%	
XE 42	28[e]	W	A	5%	
XE 43		W	A	5%	
XE 44	10[e]	W	A	5%	
XE 45		W	A	5%	
XE 46		W	A	5%	
XE 47		F120	A	5%	
XE 48		F120	A	5%	
XE 49		W	A	5%	
XE 50		F120	A	5%	Shorted gage
XE 51		F120	A		
XE 52		W	A		
XE 53		W	A		
XE 54		F120	A	2%	
XE 55	30	F120	A	2%	
XE 56	31	F120	A		
XE 57	32	F120	A		
XE 58	35	F120	A	2%	
XE 59	34	F120	A		
XE 60	33	F120	A		
XE 61		F120	A		
XE 64	39	W	A		
XE 65	41	W	A		
XE 66	36	F120	A		
XE 67	37	W	A		
XE 68	43	F120	A		Anomalous discontinuities in cycles 1 and 4; unreasonably high output most of time
XE 69	44	W	A		Erratic after cycle 1
XE 72	42	F350	A, E-1, F-3		

Table D.2 (continued)

Sensor No.	V-7 sensor in same location	Description[a]	Output device[b]	Recordable range[c]	Condition[d]
Inside strain gages (continued)					
XE 73	8[e]	F350	B		
XE 74	11[e]	F350	B		
XE 75	26[e]	F350	B		
XE 76	29[e]	F350	B		
XE 77		F350	B		
XE 78	38	F350	B		
Outside strain gages					
XE 79	61	F350	B		
XE 80		F350	B		
XE 81	60	F350	B		
XE 82	80	F350	B		
XE 83	74	F120	A		
XE 84	75	F120	A		
XE 85	76	F120	A		
XE 86	77	F120	A		
XE 87	91	W	A		
XE 88	82	W	A		
XE 89	83	F120	A		
XE 90	85	W	A		
XE 91	84	W	A		
XE 92	86	F120	A		
XE 93	79	F120	A		
XE 94	81	W	A		
XE 95	70	W	A		
XE 96	68	W	A		
XE 97	66	W	A		
XE 98	73	W	A		
XE 99	72	W	A		
XE 100	56	W	A	5%	
XE 101	57	F120	A	5%	
XE 102	58	W	A	5%	
XE 103	59	F120	A	5%	
XE 104	62	F120	A	5%	

Table D.2 (continued)

Sensor No.	V-7 sensor in same location	Description[a]	Output device[b]	Recordable range[c]	Condition[d]
Outside strain gages (continued)					
XE 105	63	F120	A	5%	
XE 106	64	W	A	2%	
XE 107	65	W	A	5%	
XE 108		F120	A	5%	Output out of range and erratic
XE 109		F120	A	5%	
XE 110		F120	A		
XE 111		W	A		
XE 112		F120	A		
XE 113		W	A		
XE 114		F120	A		
XE 115	71	W	A		
XE 117		F120	A		
XE 118		W	A		
XE 119		F120	A		
XE 120		W	A		
XE 121		W	A		
XE 122		F120	A		
XE 123		F120	A		
XE 124		F120	A		
Pressure sensors					
PE 30		Vessel pressure, type DHF high-frequency pressure transducer, 0–30,000 psi, BLH Electronics, Inc.	A, E-1, E-2, F-1	0-30 ksi	
PE 31		Patch pressure; same type as PE 30	A, F-1	0–30 ksi	
PI 32		Vessel pressure, Bourdon gage	Visual		
PE 133		Vessel pressure, bulk modulus gage, Harwood Engineering Co.	A	0–30 ksi	Output was consistently lower than but approximately proportional to, that of PE 30 except for drift in 4th cycle

Table D.2 (continued)

Sensor No.	V-7 sensor in same location	Description[a]	Output device[b]	Recordable range[c]	Condition[d]
Crack propagation gages (CPG)			A, D Trigger		
XE 125		Each gage consisted of two electrically parallel strings of foil gages; each string consisted of 8 to 12 strain gages connected in series; strain gage types were 120 Ω, 2 and 4 in. long; Micromeasurement EA-06			Failed at about 3.5 MPa (500 psi)
XE 126					Failed at about 27 MPa (4 ksi)
Trigger		Trigger detects first break of CPG and generates a constant signal used as a time mark	A, C, E-1, E-2		
Outside COD gages					
ZT 127	87	Transtek linear displacement transducers, model 354-000, with self-oscillating and demodulating direct-current differential transformers (DCDT)	A, E-2, F-2	0–25.4 mm (0–1 in.)	See Table 4.3
ZT 128	89		A, E-1, F-3	Same	See Table 4.3
ZT 129	90		A, E-2, F-2	Same	See Table 4.3
Mid-depth COD gages					
ZT 130		Divider gage fabricated at ORNL; see Appendix F	A	0–12.7 mm (0–0.5 in.)	See Table 4.3
ZT 131			A	Same	See Table 4.3
ZT 132			A	Same	See Table 4.3

Table D.2 (continued)

Sensor No.	V-7 sensor in same location	Description[a]	Output device[b]	Recordable range	Condition[c]
Crack location sensors					
XE 140	A	Ultrasonic transducer in fluid in notch	H		Defective during all cycles
XE 141	C	Same	H		
XE 142		Ultrasonic transducer on 45° weld boss on vessel OD	H		
XE 143		Same	H		

[a]Strain gage types are F120 = 120-Ω foil gage, Micromeasurements EP-08-250BG-120; F350 = 350-Ω foil gage, Micromeasurements EP-08-250BF-350; and W = 120-Ω weldable gage, Ailtech 125.

[b]See Table D.1 for key.

[c]Unless noted otherwise, strain gage range is 1%.

[d]Unless noted otherwise, the output of the sensor was generally normal.

[e]Sensor location only approximately equivalent.

Appendix E

DEVELOPMENT OF TEE PATCH AND PATCH-PRESSURIZATION SYSTEM FOR INTERMEDIATE TEST VESSEL V-7A

Patch and Patch-Pressurization Nipple

Type 304L stainless steel was chosen for the patch material to be welded into vessel V-7A. Verification tests demonstrated the adequacy of the fabrication procedures and competency of the welders.

The design details of the patch and nipple installation are shown in Fig. E.1. Preparations included the following steps:

1. drilling the pressurization passageway through the wall of the vessel;
2. preparing and testing weld coupons;
3. preparing the patch;
4. cleaning and preheating the surfaces to be welded;
5. welding patch and nipple;
6. leak testing the installed patch.

To aid in the precise location and alignment of the drilled passageway, a drill guide assembly was fabricated and tack-welded to the vessel. The assembly was keyed into the notch in the vessel so that the hole would be aligned radially and intersect the inside surface of the vessel 51 mm (2 in.) from the centerline of the notch. The diameter of the hole varied with depth, as shown in Fig. A.1, to facilitate drilling. The diameter at the inside surface was 1.59 mm (1/16 in.) countersunk to 2.38 mm (3/32 in.), a diameter that had been demonstrated in mockup tests (described below) to allow satisfactory communication of pressurizing fluid between the external portion of the system and the internal patch volume.

The patch and nipple were welded into the vessel with 1.59-mm-diam (1/16-in.) INCO 82 filler in accordance with UCN Weld Specifications W501 for gas tungsten arc welding. Six weld test coupons consisting of samples of the patch material welded by the selected specifications to 6.35-mm-thick (1/4-in.) carbon steel bars were made. The bars were attached during welding to a 152-mm-thick (6-in.) plate to provide proper restraint and heat sink. The coupons were tested by bending in various orientations,

BLANK PAGE

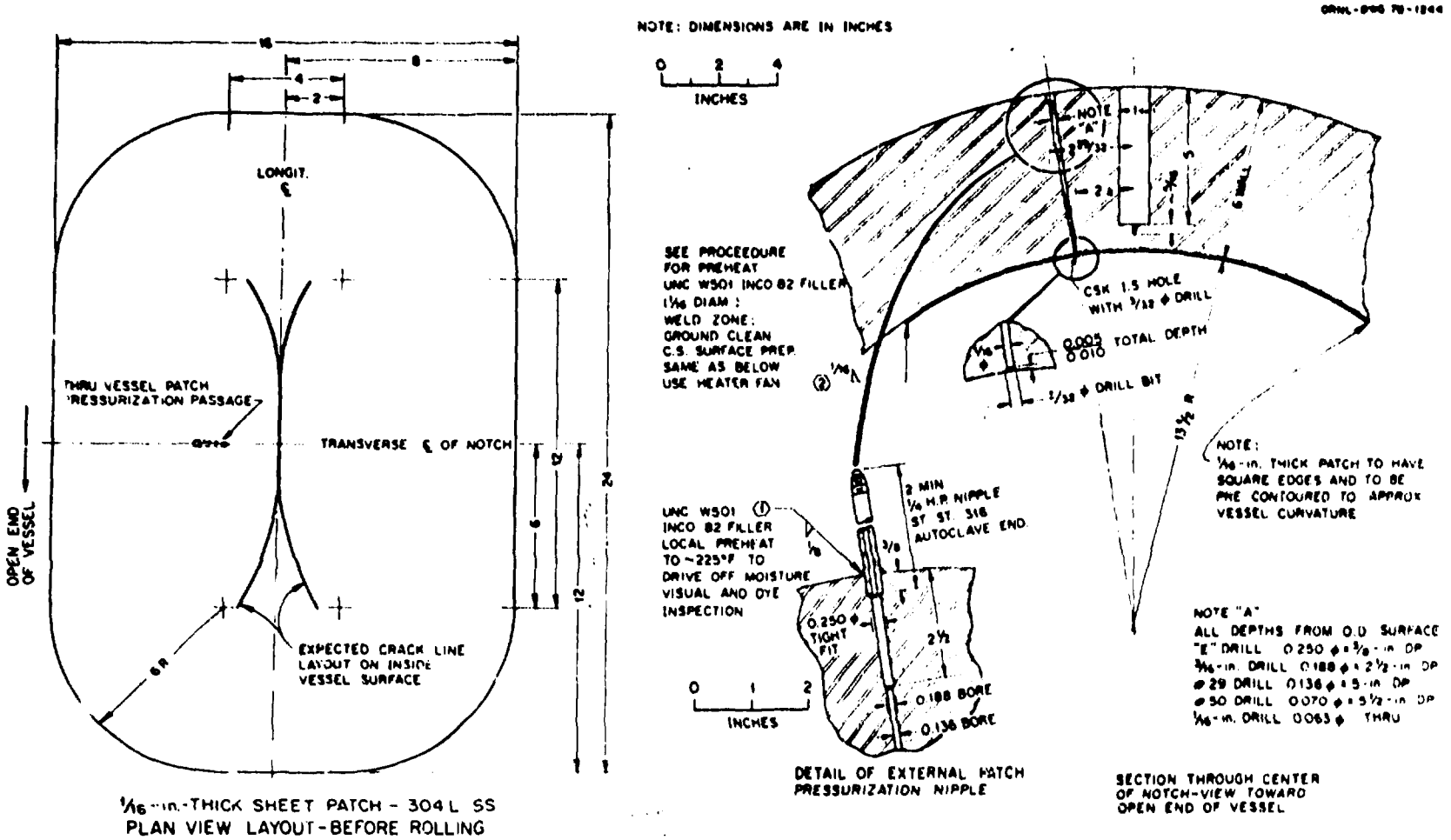

Fig. E.1. Design details of the patch and the patch pressurization nipple in vessel V-7A (1 in. = 25.4 mm).

as shown in Fig. E.2. The four narrow coupons (C, D, E, and F) were tested in a guided-bend test jig specified in Section IX of the ASME Boiler and Pressure Vessel Code. Coupons A and B were bent to a total deflection of about 20° and coupons C to F were bent to about 180°. Dye-penetrant inspections were made at various stages of bending. All test welds sustained extreme deformation without indication of flaws.

The vessel surface beneath the patch was left rough, except for a 25-mm-wide (1-in.) zone at the perimeter of the patch. This zone was cleaned and ground approximately to a No. 32 finish in preparation for welding the patch. The rough surface beneath the patch was desirable to provide passages for flow between the patch pressurization port and the region of rupture while the patch is pressed against the vessel by a large pressure differential. To ensure that adequate passages would exist at high differential pressure, 0.30-mm-diam (0.012-in.) stainless steel wires were spot-welded to the vessel as shown in Fig. E.3.

The vessel areas to be welded for the nipple and the patch were preheated overnight to provide temperatures of at least 93°C (200°F) and 66°C

Fig. E.2. Patch weld test coupons for vessel V-7A.

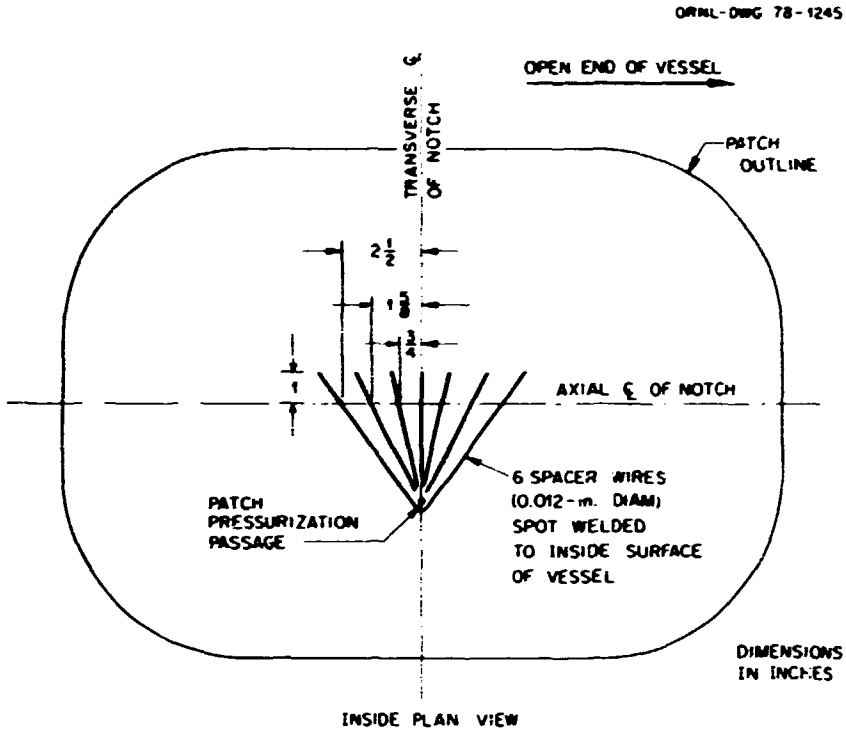

Fig. E.3. Location of spacer wires between the patch and the vessel V-7 inside surface (1 in. = 25.4 mm).

(150°F) in the two areas, respectively. Temperatures were maintained above those minima and below the maximum of 191°C (375°F) during welding. Dye-penetrant inspection indicated several places on the patch weld requiring minor repair; after the repair operation, vacuum and helium leak checks were made. Additional repairs were made, and the final test of the welds was made with a helium detector probe while the patch volume was slightly pressurized with helium.

Patch-Pressurization System

The patch-pressurization system was designed to give a highly reliable and accurate indication of the rupture time of the intermediate test vessel wall without permitting significant leakage. The thin stainless steel patch welded to the vessel wall at the location shown in Fig. E.1 was thought to have a reasonable chance of remaining gastight after vessel rupture in the V-7A test, inasmuch as the length, width, and thickness

were selected to tolerate the deformation found in the V-7 test. It was recognized, however, that the patch could not remain intact if a long rupture developed or if the crack opening at the inside surface became large. Hence, the patch pressurization system was designed principally to function properly as a rupture detector on the premise that the patch would remain leaklight; the system should also provide a means for determining, if necessary, whether the patch ruptured prematurely.

The general scheme of the system (described in Chapter 3 and Fig. 3.28) requires that two critical components of the system function properly in all phases of the test. First the flow-restricting element in the external system must freely allow sufficient flow for simultaneous pressurization (or depressurization) of the patch and vessel volumes; otherwise, a slight overpressurization of the patch volume would tear the patch from the vessel. Second, in the rupture situation, there must be low resistance to flow within the patch volume relative to that of the external flow restrictor in order for a significant pressure drop to be detected at the restrictor (see Fig. E.4).

With pressures equalized, the patch membrane would lie loosely against the wall of the vessel or be stretched across the chord of the vessel.

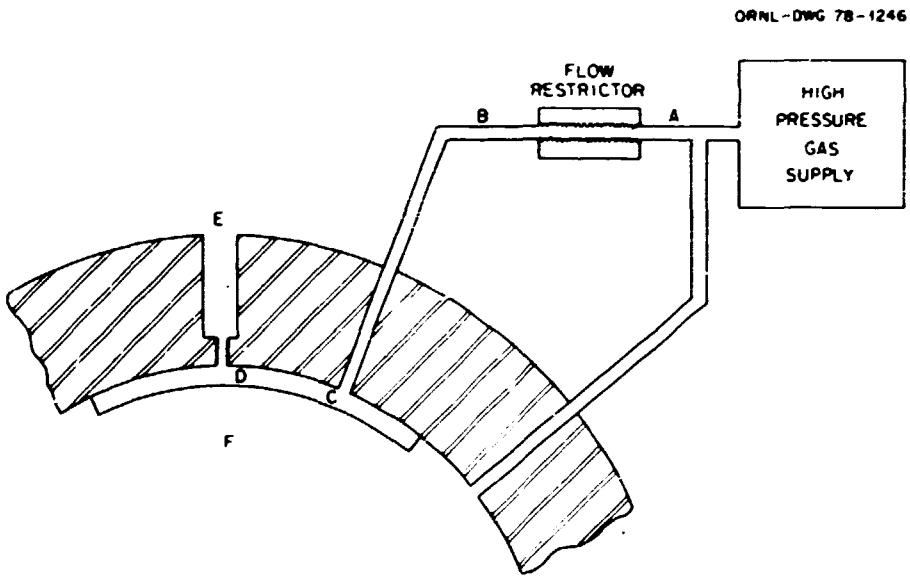

Fig. E.4. Schematic of patch pressurization system.

When rupture occurs, the pressure differential between the inside of the patch (the side toward the center of the vessel) and the outside (toward the vessel wall) would increase as dictated by the pressure gradient along the flow path from the gas supply through the rupture to the atmosphere (A to E in Fig. E.4). Increasing differential pressure forces the patch toward the wall of the vessel. When the resistance of the rupture pathway itself to flow is large relative to that of the flow restrictor, the pressures in the patch volume at points C and D would be almost as great as the vessel pressure (point F). However, as the rupture area increases, the resistance in the flow restrictor makes the pressures at C and D approach atmospheric pressure; this results in the patch being forced against the wall and tends to interrupt flow from B to D. If, as a result of patch deflection, the restriction anywhere between B and D should become large prematurely, it would prevent or retard the development of a measurable pressure drop between points A and B, where the crucial pressure measurements are made.

A series of tests in a small high-pressure loop (Figs. E.5 and E.6) was carried out to verify the performance of components and the system. The test loop was arranged so that the simulated patch pressurization system could be charged with gas, while the balance of the system would contain hydraulic pump oil. An existing oil pressurizing system was used for economy, and the high-pressure gas volume was minimized for safety. The vacuum pump allowed the "vessel" side of the patch mockup to be charged with nitrogen if desired.

The gas accumulator was sized so that, when charged with nitrogen at 7 to 10 MPa (1000 to 1500 psi), liquid would not enter the flow restrictor upon pressurization from the oil pump and subsequent venting of the system through valve V-1.

In the course of the mockup tests, the effect of vessel surface preparation beneath the patch was considered. A disk of stainless steel patch material was welded to a mockup flange, shown in Figs. E.7 and E.8 before and after installation of the patch, respectively. Figure E.7 shows the outlet port counterbored from a diameter of 0.794 mm (1/32 in.) to 6.35 mm (0.25 in.). Before this port was counterbored, several tests were run at pressures up to 155 MPa (22.5 ksi) to determine whether flow could be

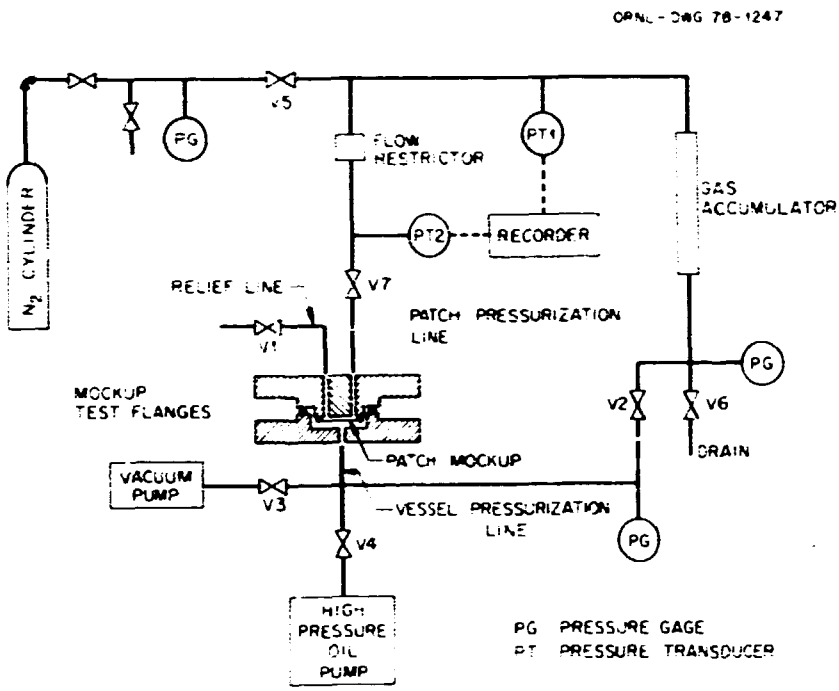

Fig. E.5. Schematic of patch pressurization system mockup test loop.

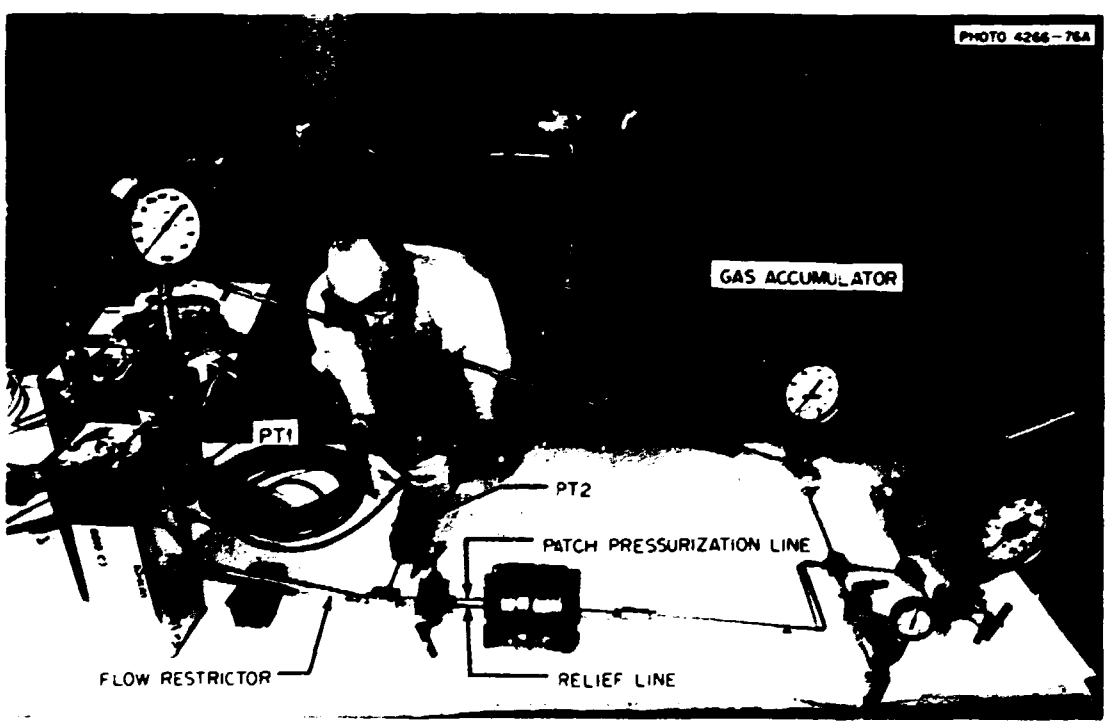

Fig. E.6. Patch pressurization system mockup test loop.

Fig. E.7. Patch volume simulation flange without patch installed.

established between the two ports while the opposite side of the patch was at high pressure. Adequate flow occurred with differential pressures across the patch membrane of 62 MPa (9 ksi) and greater. Thus, it appeared that little flow resistance would be expected over most of the pathway from the pressurization port to the rupture in a vessel (from C to D in Fig. E.4).

A patch mockup with the counterbored port was tested next to determine whether a wide rupture, one which would leave the patch unsupported over

PHOTO 4435-77

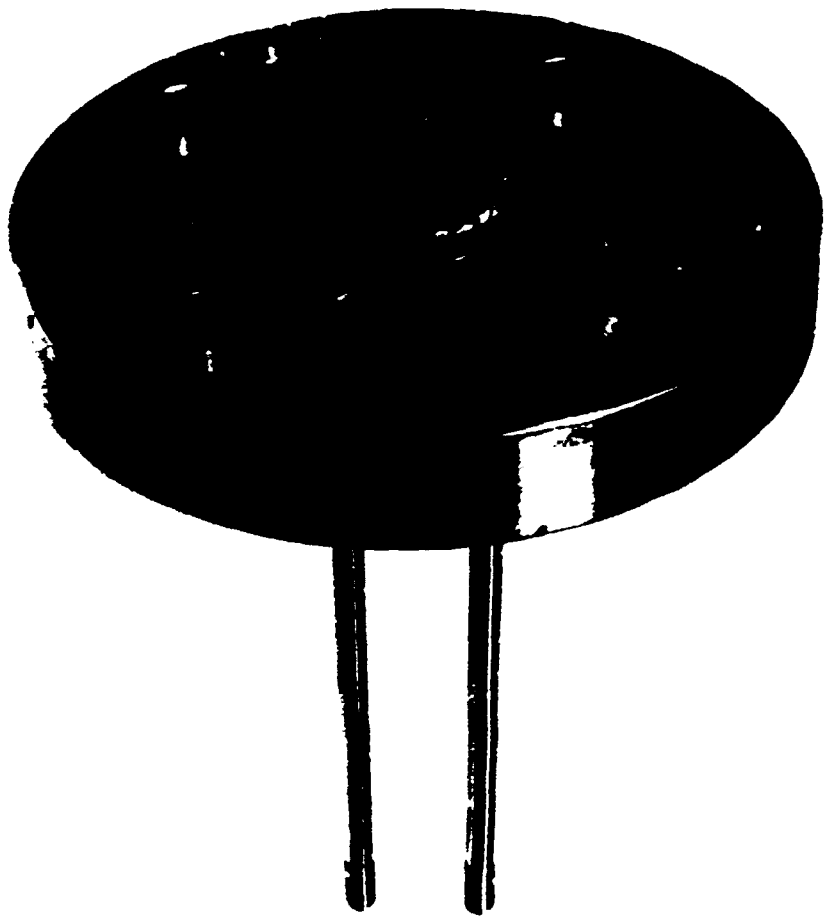

Fig. E.8. Patch volume simulation flange with patch welded in place.

a wide span, would be conducive to formation of a seal where the patch contacts the corners of the rupture in the vessel. This type of seal developed, but only after the patch had been exercised through several pressure cycles with pressures up to 172 MPa (25 ksi). Examination of the disk after disassembly showed that it had been deformed slightly to conform to the counterbored port. Subsequent tests were run successfully with a 0.305-mm-diam (0.012-in.) wire spacer between the mockup patch disk and flange. It was decided that spacers were probably not needed in the vessel but would be installed for additional assurance that a seal would not develop.

Seven types of flow restrictors were tested. Two long capillary tubes with 0.711 and 0.127 mm (0.028 and 0.005 in.) inside diameters were tried first. The larger tube did not restrict flow enough for the effect to be observed on the recorded pressure-time charts. The smaller one functioned well for a few tests but eventually plugged. Therefore, the long capillaries were abandoned because they were either too large or too susceptible to plugging. Quality control in reproducing a nominal capillary size was also a concern not resolved favorably.

The third device tested, an orifice 0.216 mm in diameter by 6.35 mm long (0.0085 × 0.25 in.), did not plug but gave poor resolution in the pressure drop tests.

A surge check valve (Autoclave Engineering type CK4402) was tested successfully in two different orientations, and two high-pressure gage snubbers (Chemiquip Company type 30-31-HF-6GS with element HP-50-HX or HP-50-G) were also tested. The performance of the surge check valve was excellent when it was mounted upside down. (In this orientation the ball check is always held in the check position by gravity.) Tests demonstrated however, that the patch volume could be pressurized consistently through the closed check valve at rates up to 10 MPa/s (1450 psi/sec), which is far beyond the potential capacity of the intermediate test vessel pneumatic pressurization system.

The performance of the two snubber elements in detecting rupture was fair to good in the mockup tests. Since the mockup tests were severe tests of rupture detectability, either snubber was considered adequate for the vessel test. Therefore, it was decided that the snubber with type HP-50-HX element, which was designed particularly for use with gases, would be included in the vessel test system in such a way it would be redundant to the surge check valve.

Appendix F

CALIBRATION AND EVALUATION OF CRACK-OPENING DISPLACEMENT GAGES USED AT MIDDEPTH OF NOTCH IN VESSEL V-7A

Each middepth crack-opening displacement (COD) gage was made by applying four Micromeasurements type EA-06-062TT-120 strain gages to the circular spring clip of a mechanical divider. A typical gage is shown in Fig. F.1. The outer and inner surfaces of the spring clip each had one axial and one circumferential gage. The four gages were connected as a full bridge as shown in Fig. F.2.

Each gage was calibrated at room temperature before the test by opening and closing the gage three times between the limits of 25.4 mm (1 in.) and 38.1 mm (1.5 in.) with the output being recorded at each 2.5-mm (0.1-in.) step. Typical behavior of this type of gage is shown in Fig. F.3, where the output is given as an indicated strain. Figure F.3 shows an apparent loss in linearity upon change of direction of motion. The calibration factors are given in Table F.1.

After the vessel test, recalibrations were made at room temperature, and the effects of temperature on the gages were investigated. The posttest calibration results are included in Table F.1. The latter calibrations deviated from the initial ones by 2, 6, and 11% for ZT 130, ZT 131, and ZT 132, respectively. The measured changes in indicated COD with temperature over a range from room temperature to about 75°C (170°F) are given in Table F.2. Measured drifts in output are given in Table F.2.

Table F.1. Calibration factors for COD gages

Gage No.	Calibration factor[a] (mm^{-1})	
	Pretest[b]	Posttest
ZT 130	0.01074	0.01093
ZT 131	0.009839	0.009235
ZT 132	0.01079	0.009683

[a] $\text{Factor} = \frac{\text{output voltage}}{\text{excitation voltage}} \times \frac{1}{\Delta\text{COD}}$.

[b] Pretest factors were used in reducing data presented in this report.

Table F.2. Effect of temperature on COD gages[a]

Gage No.	$\frac{\partial COD}{\partial T}$ (mm·K^{-1})	Drift in 9 hr (mm)
ZT 130	−0.02 to +0.02	0 (at 70°C) 1.5 (at 27°C)
ZT 131	−0.01 to −0.08	0 (at 70°C) 0.8 (at 27°C)
ZT 132	−0.05 to −0.14	2.9 (at 70°C) 0 (at 27°C)

[a] 1 mm·K^{-1} = 0.0229 in./°F; 1 mm = 0.0394 in.

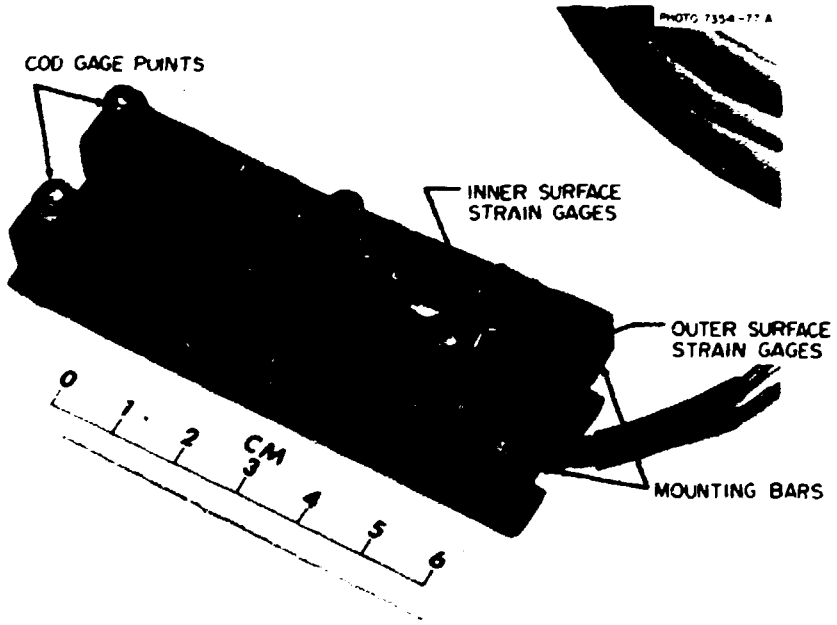

Fig. F.1. Mechanical-divider-type COD gage used at middepth of notch in vessel V-7A.

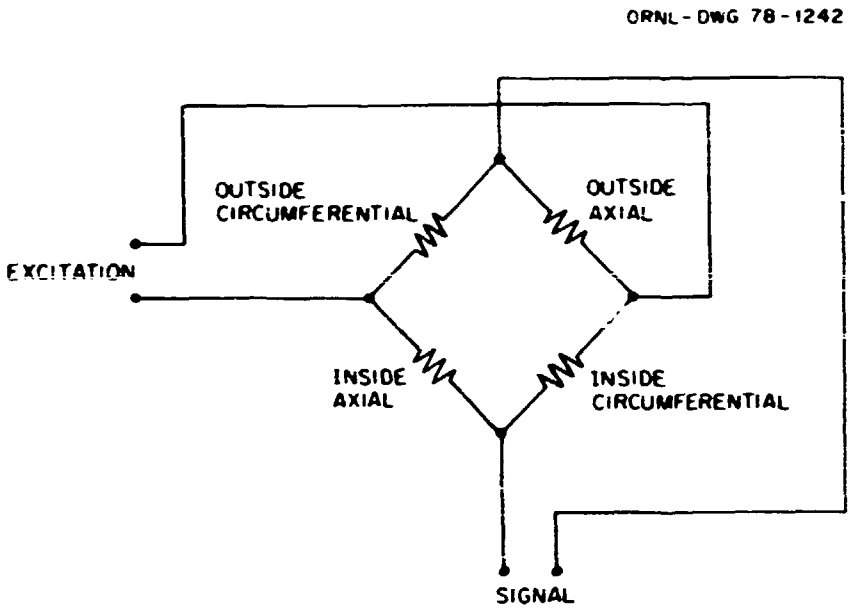

Fig. F.2. Schematic for connecting strain gages on spring clip of COD gage.

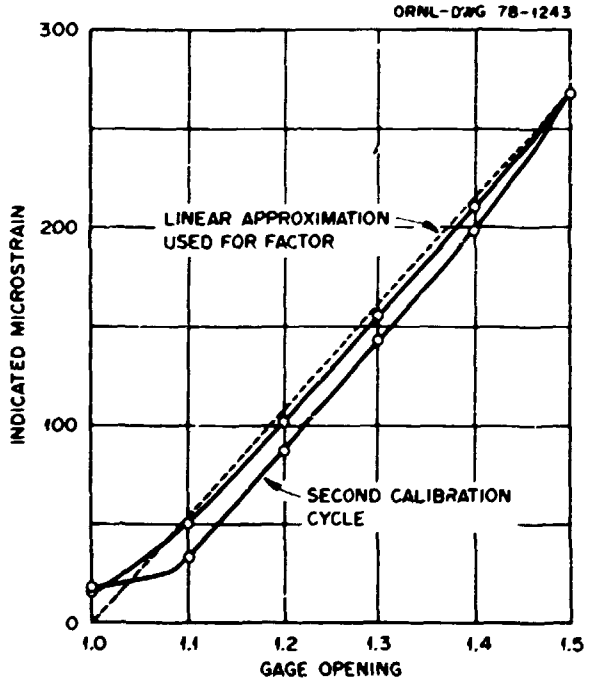

Fig. F.3. Calibration curves for pretest calibration of ZT 130 during one cycle; other cycles were almost identical (1 in. = 25.4 mm).

Appendix G

AN ELASTIC-PLASTIC FINITE-ELEMENT ANALYSIS OF INTERMEDIATE TEST VESSELS V-7 AND V-7A

An elastic-plastic finite-element analysis of intermediate test vessels V-7 and V-7A was performed during the preparations for the V-7A test using the code NEPSAP.[1,2] A partial schematic of the element arrangement (i.e., 192 sixteen-node thick-shell elements) is shown in Fig. G.1. The loading consisted of an initial 90 MPa (13 ksi) internal pressure that was subsequently increased in 17 equal increments of 6.9 MPa (1000 ksi) each. Selected results from the analysis and experimental data at comparable locations on V-7 are shown in Figs. G.2 to G.4.

Figure G.2 shows the circumferential strain at the outside surface, 76 mm (3 in.) from the flaw in the axial direction, as a function of pressure. Figure G.3 shows similar data for a location on the outside surface, 127 mm (5 in.) from the flaw. Figure G.4 is a record of the crack-opening displacements (COD) taken from test V-7. Superposed on that plot is the COD from the finite-element analysis at the point of maximum displacement, that is, the outside surface at the crack midpoint.

Although the model used for the finite-element analysis was quite coarse, the results from the analysis tend to agree with experimental measurements. A closer correlation would be expected with a finer mesh.

References

1. P. Sharifi and D. N. Yates, "Nonlinear Thermo-Elastic-Plastic and Creep Analysis by the Finite Element Method," AIAA/ASME/SAE 14th Structures, Structural Dynamics, and Materials Conference, Mar. 20–22, 1973, Paper 73-358.

2. P. Sharifi, "Nonlinear Buckling Analysis of Composite Shells," AIAA/ASME/SAE 15th Structures, Structural Dynamics, and Materials Conference, Apr. 17–19, 1974, Paper 74-411.

BLANK PAGE

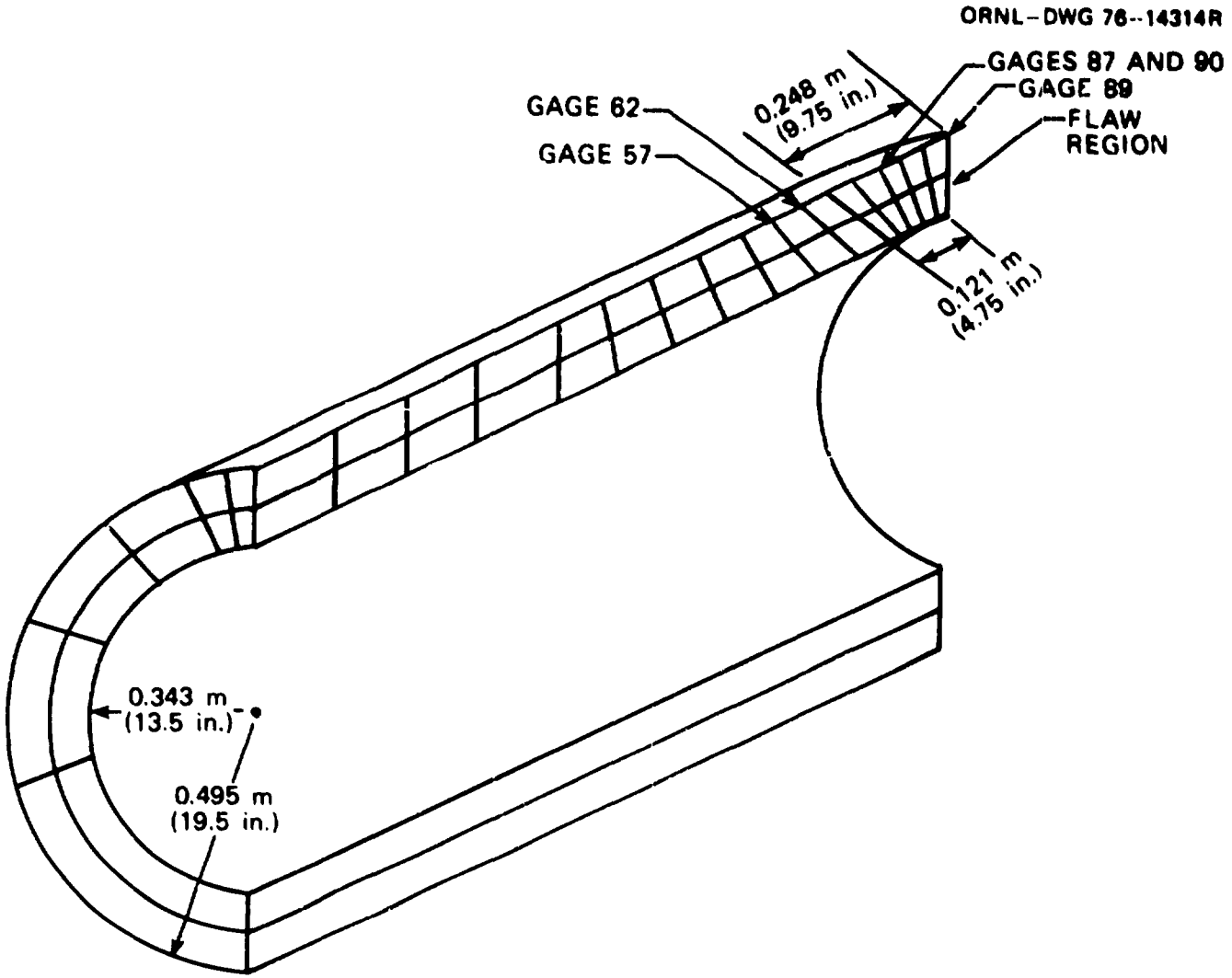

Fig. G.1. Schematic of the finite-element model of intermediate test vessels V-7 and V-7A.

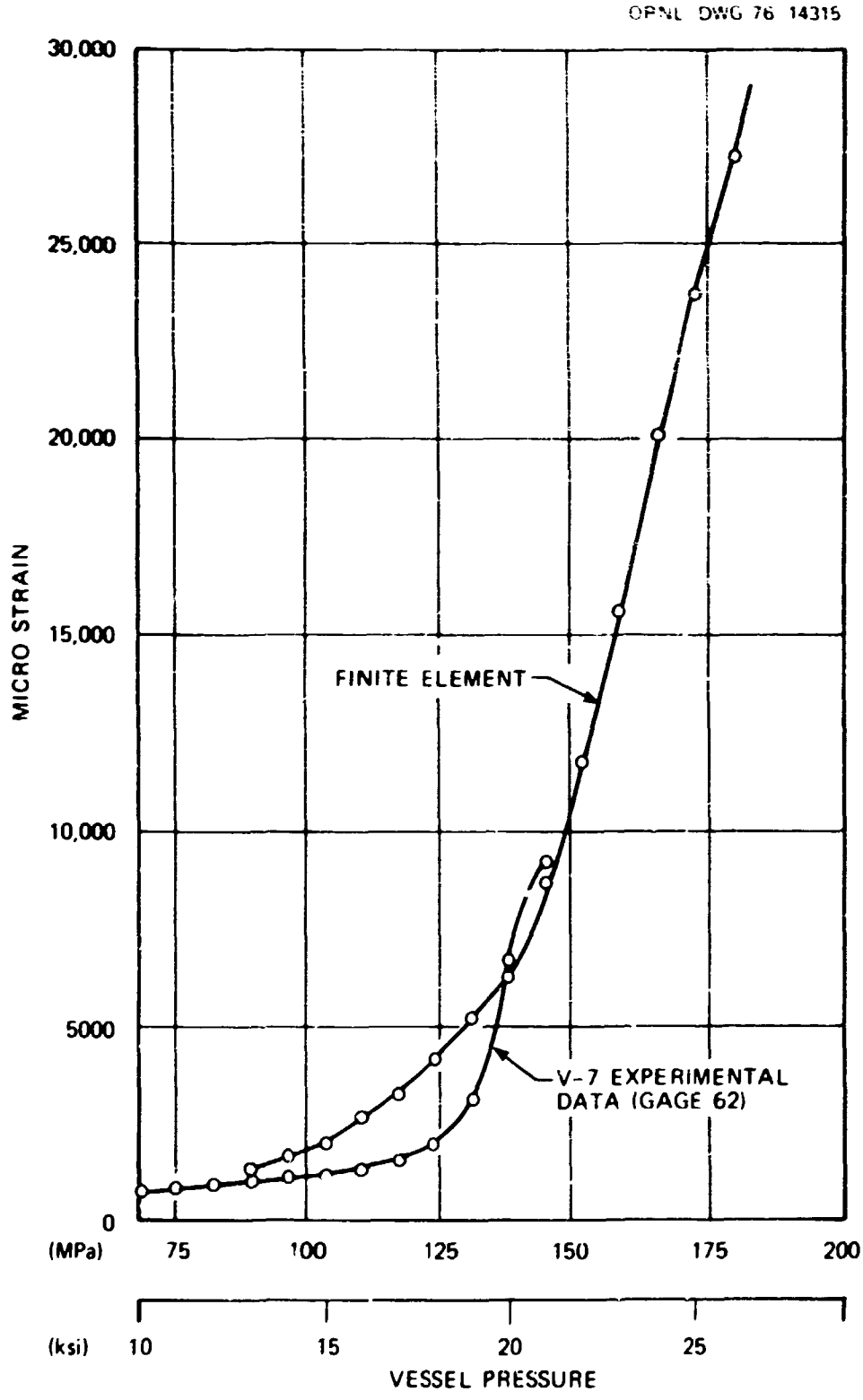

Fig. G.2. Strain vs pressure 76 mm (3 in.) from flaw on cylinder outside surface.

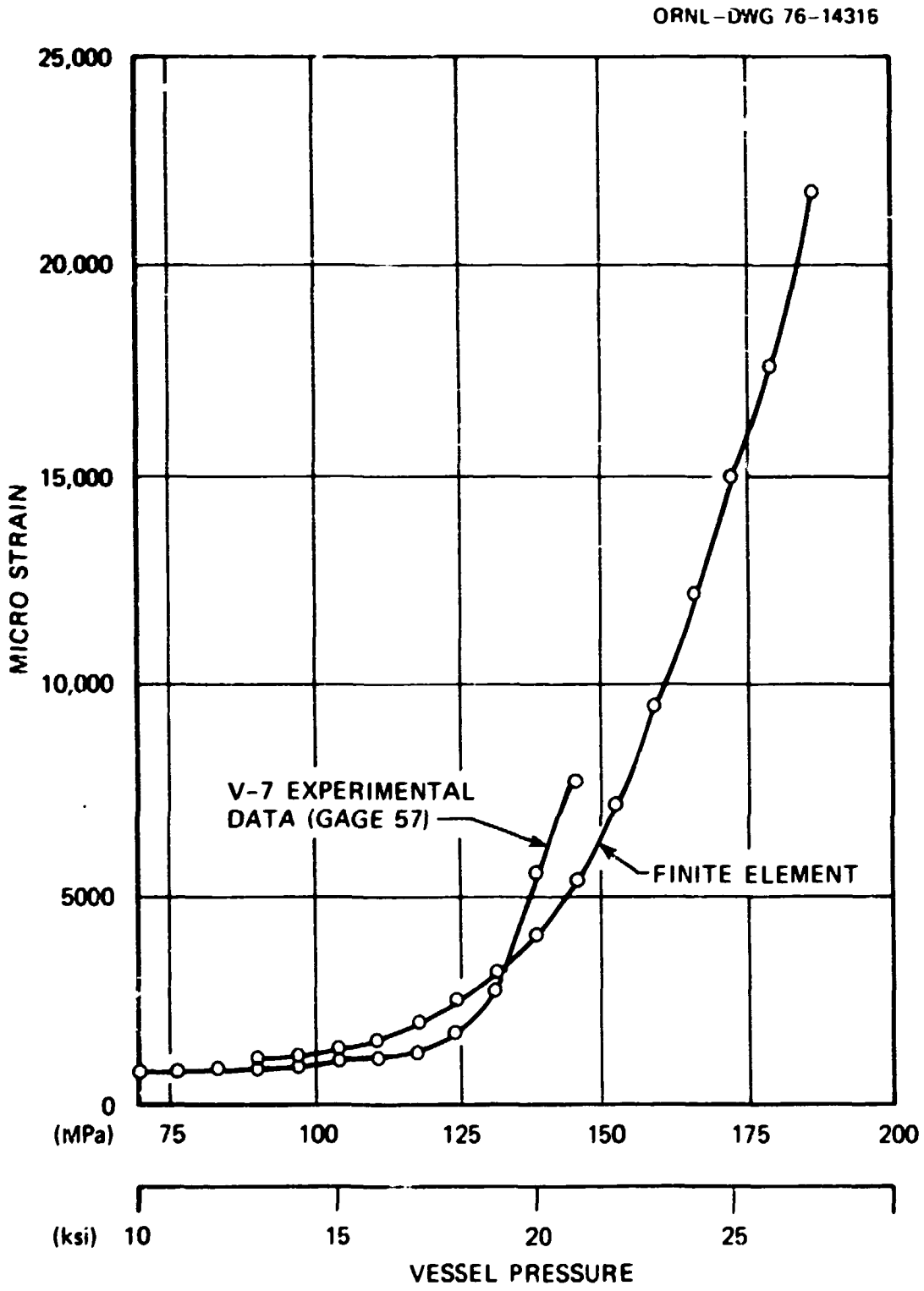

Fig. G.3. Strain vs pressure 127 mm (5 in.) from flaw on cylinder outside surface.

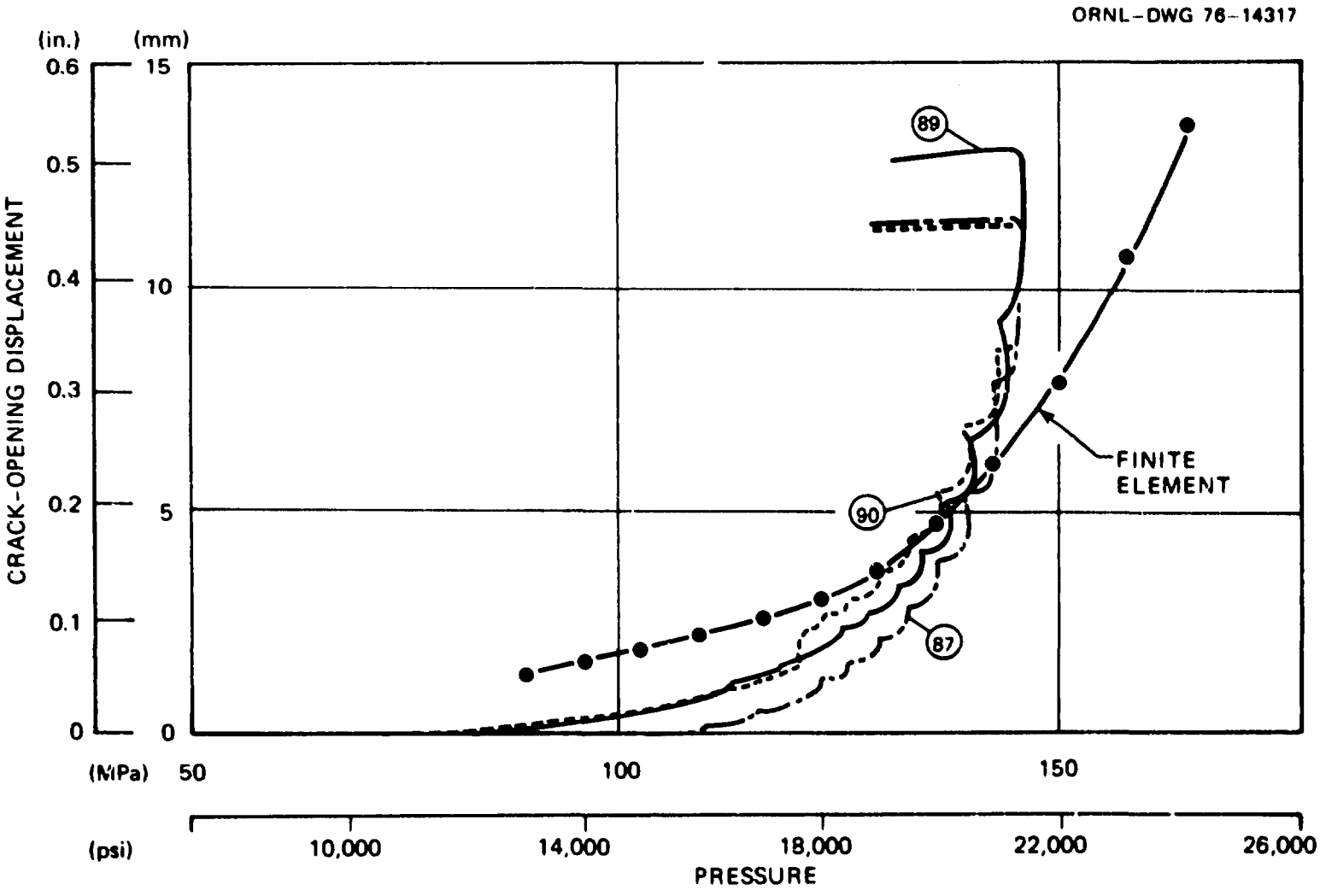

Fig. G.4. Crack-opening displacement vs pressure recorded by transducers 87, 89, and 90 in V-7 test compared with finite-element calculations.

Appendix H

NITROGEN PRESSURIZATION SYSTEM*

System Requirements

The nitrogen pressurization system, shown schematically in Fig. H.1, was designed to meet the following conditions:

1. Provide a relatively high volume and low pressure for the initial pressurization of the test vessel.
2. Provide a smaller volume, but higher pressure, system to be used in the final stages of the test vessel pressurization.
3. Provide appropriate valving so that any pump could be isolated from the remainder of the system in case of failure.
4. Provide a valving system for feeding the compressed nitrogen in the test vessel back into the supply trailer during the test vessel depressurization cycles. The valving also allowed the gas in the test vessel to be exhausted to the atmosphere.
5. Provide a means of prepressurizing the gas to the inputs of both high-pressure pumps should the trailer supply pressure drop below an acceptable level.
6. Maintain a cooling system to lower the temperature of the compressed gas at the output of the high-volume pump.
7. Provide pressure monitoring gages to indicate the pressure at the output of the pumping system (the input to the line feeding the test vessel) and at other points within the system.

The quantity of nitrogen in the test vessel, which has an internal volume of 0.696 m^3 (24.6 ft^3), is shown in Fig. H.2 as a function of pressure. The pressure-density curve of nitrogen is not straight because of real gas effects. As the pressure increases and the gas approaches a liquid, it becomes less compressible. As may be seen in Fig. H.2, to

---

*This description was prepared by J. F. Bampfield, White Oak Laboratory, Naval Surface Weapons Center, as part of the work performed for ORNL under the Interagency agreement.

BLANK PAGE

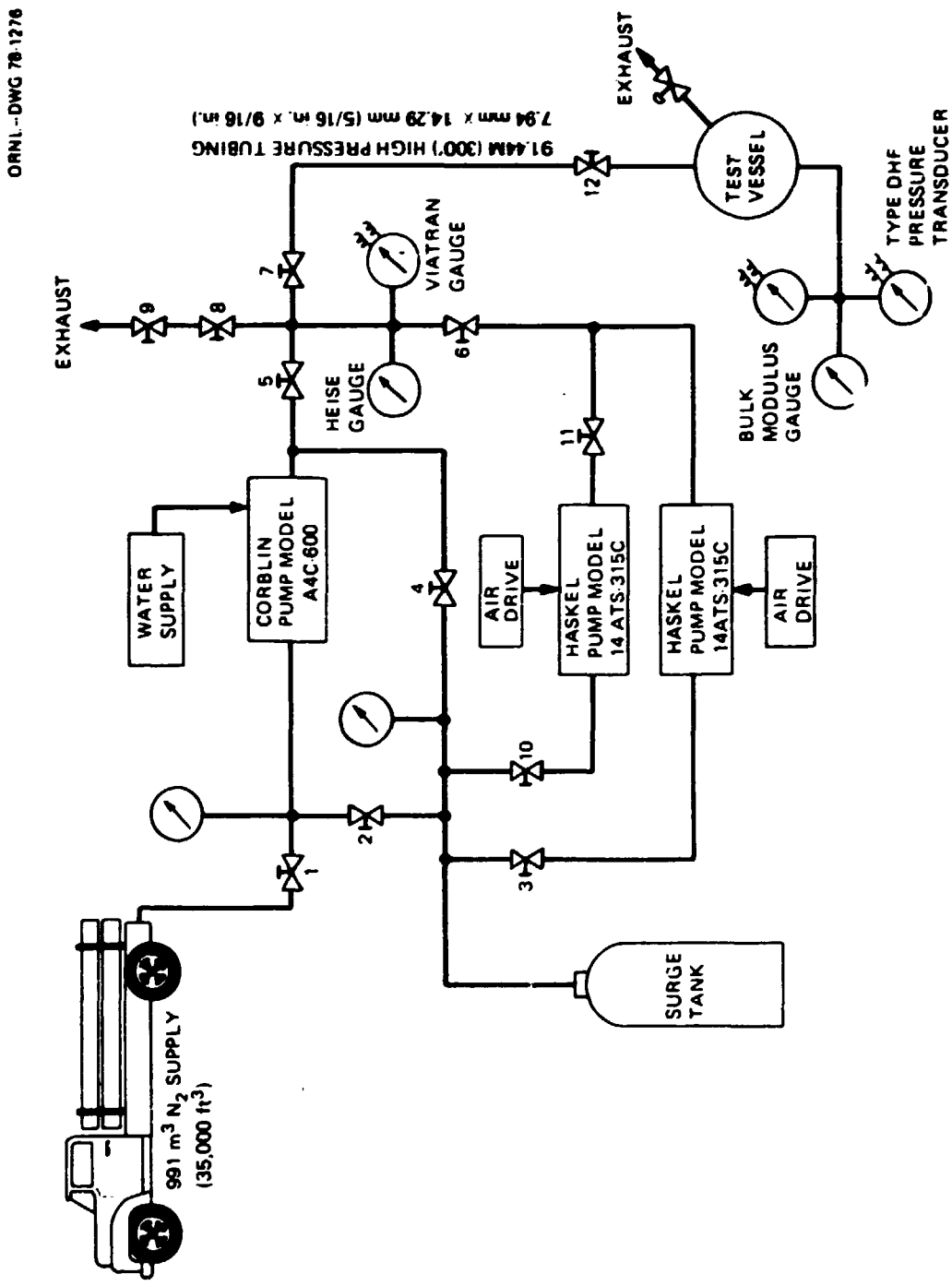

Fig. H.1. Nitrogen pressurization system.

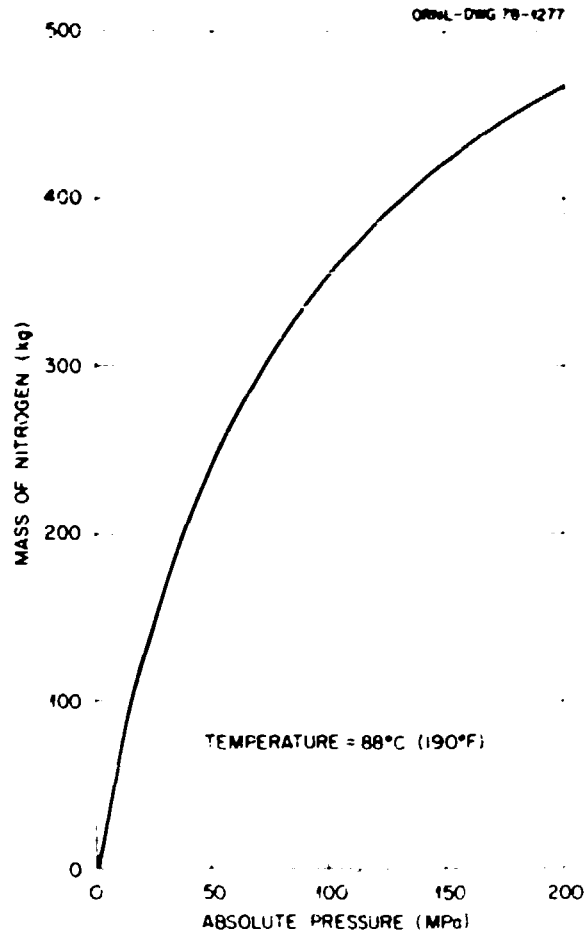

Fig. H.2. Quantity of nitrogen in test vessel V-7A vs pressure (1 MPa = 145.04 psi; 1 kg = 2.2046 lb_m).

produce a given pressure increase, less additional gas is needed at the higher pressures than the lower pressures.

Nitrogen Supply and Control Console

The nitrogen gas supply was contained in a compressed gas tank-trailer with a capcity of 991 scm (35,000 scf) at a pressure of 16.55 MPa (2400 psi) and a temperature of 21.1°C (70°F).* Each of the 22 tanks in the

*Standard conditions for the definition of 1 scf are 1 atm (14.696 psia) and 60°F; for nitrogen, 1 scf = 0.07380 lb_m = 0.03348 kg.

trailer were individually valved and fed into a common manifold which, in turn, was controlled by a master valve. The output of the trailer manifold was coupled to the input of the pump console via a 15.24-m (50-ft) length of flexible 6.4-mm-ID (1/4-in.) hose. The hose had a working pressure of 34.5 MPa (5000 psi) and a burst pressure of 138.9 MPa (20,000 psi).

A second tank-trailer was provided as a precautionary measure to ensure an adequate supply of nitrogen in case of large gas losses. Fortunately, additional nitrogen was not needed.

The control console, diagrammed in Fig. H.3, consisted of a group of valves interconnected with high-pressure nipples and arranged so that they

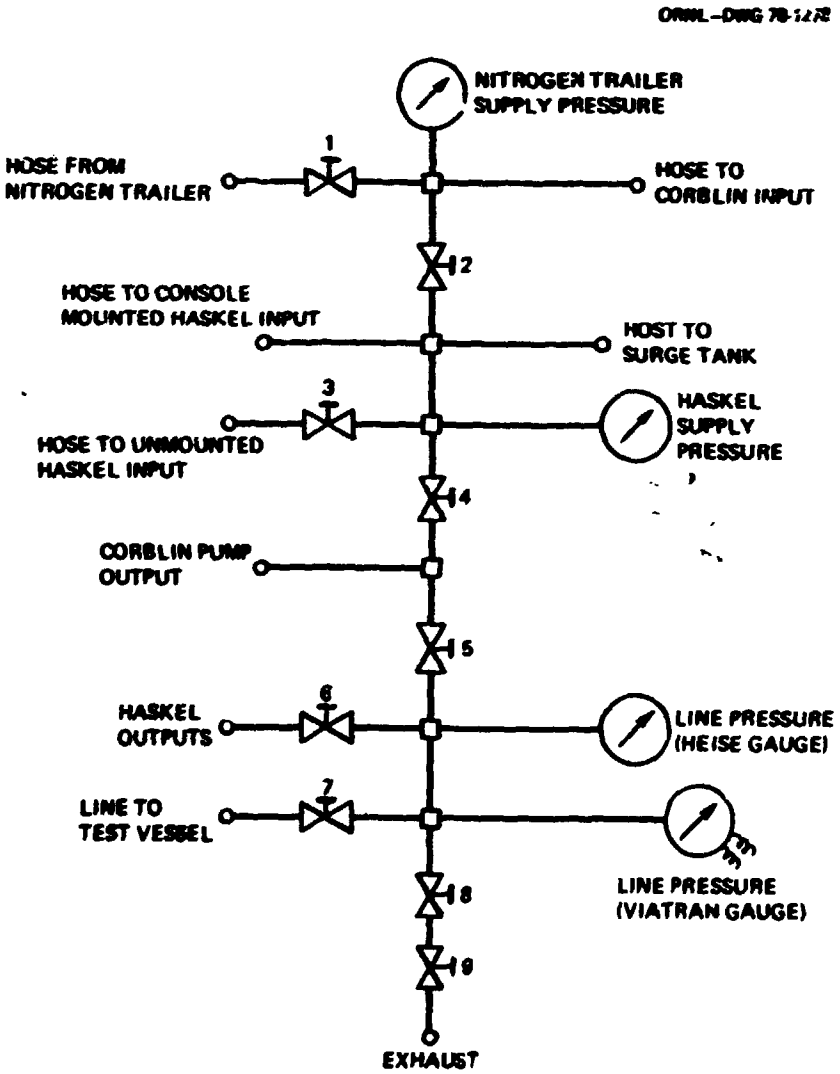

Fig. H.3. Nitrogen pressurization system control console.

could be reached conveniently from one spot. The valves were assigned numbers that corresponded to the valve positions shown in Fig. H.1. Valves 10 and 11 were physically located on a control panel associated with the Haskel pump, which was mounted in its own console. Valve 9 was added as a precaution against possible seat erosion of valve 8 during extended periods of venting to the atmosphere.

By opening or closing various valves, it was possible to route the gas flow to accommodate any requirement. Connections to the console were made with flexible rubber tubing where the pressure was not expected to ever exceed 20.7 MPa (3000 psi). This tubing, like that used to connect the tank-trailer, had a working pressure of 34.5 MPa (5000 psi) and a burst pressure of 137.9 MPa (20,000 psi). Other connections which involved the higher pressures were made with steel tubing having a minimum burst pressure of 547.7 MPa (80,000 psi).

The output of the pumping system was fed into about 90 m (300 ft) of type 304 stainless steel high-pressure tubing, coupled at 6.1-m (20-ft) intervals, and then to the test vessel. The tubing, 7.94 mm (5/16 in.) ID × 14.3 mm (9/16 in.) OD, had a burst pressure rating of 547.7 MPa (80,000 psi). The only constrictions in the line were at the couplings, two valves at the pump site (Nos. 6 and 7 located in the control console, see Fig. H.1) and one valve at the test vessel. The orifices at these points were 4.76 mm (3/16 in.). The coupling on the test tank had an ID of 3.17 mm (1/8 in.). The valve near the test vessel (No. 12 of Fig. H.1) proved useful when running leak and system operation tests prior to the actual pressurization of the test vessel.

The Low-Pressure System

The nitrogen pressurization system (Fig. H.1) consisted of two basic pumping systems interconnected with appropriate valving to provide the necessary operating flexibility. One was a relatively low-pressure, high-volume system capable of pumping 1.7 scm (60 scf) of gas at a maximum discharge pressure of about 62.1 MPa (9000 psi) when supplied with an input pressure of 13.8 MPa (2000 psi). The heart of this system was a model

A4C-600 Corblin diaphragm pump powered by a 20-hp, 220-V, 3Ø electric motor.

The Corblin pump was cooled by circulating water through a jacket surrounding the compression chamber, an oil reservoir, and then through a water jacket which surrounded the high-pressure output line. The temperature of the nitrogen gas delivered to the control console was about 48.9°C (120°F).

The water for cooling, from a 7451-liter (5000-gal) supply contained in a large [14,902-liter (10,000-gal)] tank adjacent to the pumps, was circulated from the storage tank through the Corblin pump and then back to the storage tank by a small electric pump. The volume of water which could be circulated could be varied from zero to a maximum of about 14.9 liters/min (10 gpm) by a valving arrangement on the output side of the water pump. However, a flow rate of about 4.5 liters/min (3 gpm) proved adequate.

A published curve showing the pumping characteristics of the Corblin pump is given in Fig. H.4.

At compression ratios* greater than 1, the volume of gas taken into the compression chamber is less than the piston displacement. This is due, in part, because some of the available space is filled by the reexpansion of the high-pressure gas remaining in the clearance volume at the end of the compression stroke. The ratio of the actual intake volume to the displacement volume, the volumetric efficiency, decreases linearly to zero at a compression ratio such that the reexpanded gas completely fills the available space and no fresh gas can be taken in. The volumetric efficiency of the Corblin pump is somewhat higher than that for a piston-type pump with a comparable pumping capacity because the diaphragm-type pump provides better cooling in the compression chamber.

When a gas is drawn into a hot compression chamber, it contacts the hot surfaces and immediately expands. For every 3.1 K (5.6°F) rise in the temperature of the gas in the compression chamber, the volumetric efficiency[1] will decrease by 1%. This holds true whether the gas is preheated in an inlet line or in the compression chamber during a compression

*The ratio, in absolute pressure units, of the delivery pressure to the supply pressure.

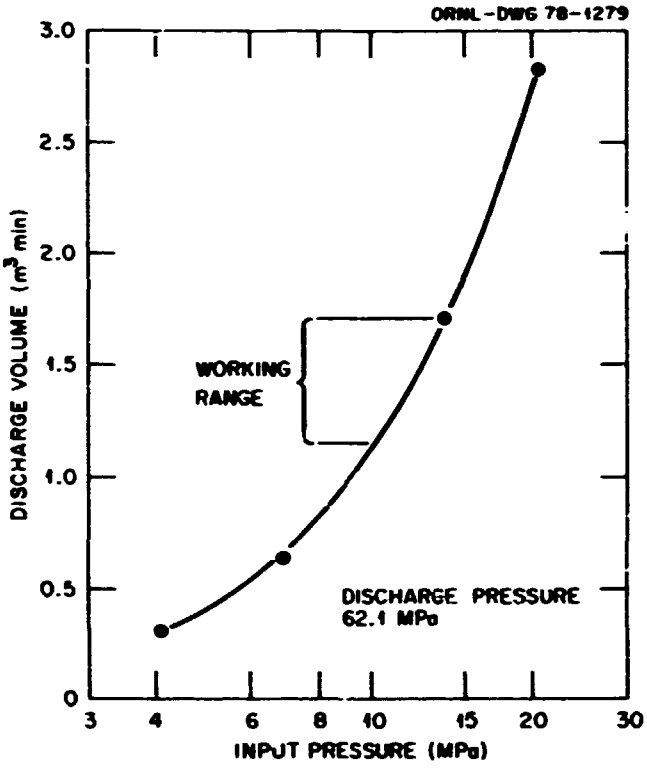

Fig. H.4. Discharge volume vs input pressure of Corblin pump.

stroke. A curve showing the volumetric efficiency of the model A4C-600 Corblin pump for various compression ratios is given in Fig. H.5.

Several measured pumping rates were made at average discharge pressures of 26.2 MPa (3800 psi) and 44.8 MPa (6500 psi) with an average supply pressure of 13.8 MPa (2000 psi). The results showed that the pumping capacity of the Corblin pump was a little lower than the curve of Fig. H.4 would indicate. The pumping rate at the average discharge pressure of 26.2 MPa (3800 psi) was found to be 1.56 scm/min (54.6 scfm), while at the discharge pressure of 44.8 MPa (6500 psi), the rate dropped to 1.42 scm/min (50 scfm). This loss of pumping efficiency can be partly explained by the volumetric efficiency curve of Fig. H.5.

At pressures above about 57.2 MPa (8300 psi), the pumping efficiency dropped very quickly because of the maximum pressure setting available on an oil bypass relief valve peculiar to this pump.

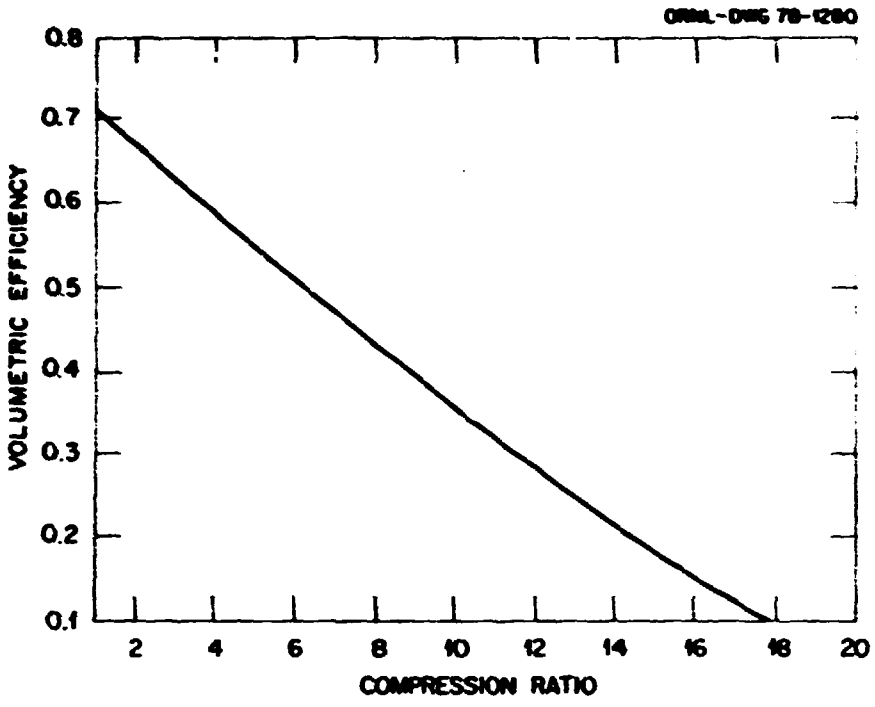

Fig. H.5. Volumetric efficiency of Corblin pump.

The High-Pressure System

When the output pressure of the system reached about 57.2 MPa (8300 psi), the pumping operation was transferred to two high-pressure pumps (Haskel model 14ATS-315C air-driven two-stage piston pumps). Both pumps were identical except for their method of mounting. One was just the basic unit (unenclosed), while the other was housed in a console. Since the Haskel pumps were air driven, power for them was supplied by two large diesel-driven air compressors, one with a capacity of 8.9 m^3/min (315 cfm) and the other 17.0 m^3/min (600 cfm). The air from the 8.9-m^3/min compressor was fed to the unenclosed unit via a 19-mm-ID (3/4-in.), 15.2-m-long (50-ft) air hose which was coupled to the pump with a standard 19-mm (3/4-in.) pipe nipple. The air pressure at the compressor was raised to its maximum of 0.76 MPa (110 psi) before a pressure-relief valve on the compressor opened. The pressure drop in the air hose was found to be 0.33 MPa (48 psi) when the Haskel pump was operating. Consequently, the Haskel

pump was operated on a maximum air drive pressure of only 0.43 MPa (62 psi). This slowed its normal cycling rate of about 50 strokes/min to around 30 strokes/min. Normal drive pressure for the pumps is about 0.68 MPa (100 psi); maximum drive pressure is 0.86 MPa (125 psi).

The Haskel pump which was housed in a console was supplied air from the 17.0-m^3/min (600-cfm) compressor. Maximum supply pressure at this compressor was 0.69 MPa (100 psi) with a 0.41-MPa (60-psi) drop in a similar air hose. Cycling rate of this pump was around 25 strokes/min.

Temperature of the drive air at the input to the pumps was about 65.6°C (140°F).

At an average exhaust pressure of 58.6 MPa (8500 psi) and an input pressure of 10.9 MPa (1580 psi), the two Haskel pumps operating together were able to pump 0.297 scm/min (10.5 scfm) of nitrogen. When the supply pressure was raised to an average of 15.5 MPa (2250 psi) and the output pressure was 89.6 MPa (13,000 psi), the pumping rate increased to 0.36 scm/min (12.8 scfm).

Both high-pressure pumps eventually failed because of excessively high temperatures at the second-stage cylinder walls. The Teflon seals in the pistons had deteriorated badly. It was then realized that the operating temperatures of the pumps had to be lowered. This was accomplished by (1) cascading large volumes of water over the receiver tank on the compressor unit, thus lowering the temperature of the drive air to the Haskel pump by about 22.2 K (40°F), that is, to 37.8°C (100°F) at the pump input; and (2) lowering the compression ratio of the gas pumped by the Haskel pumps. This was done by using the Corblin pump to prepressurize the nitrogen from 12.4 MPa (1800 psi) to 20.0 MPa (2900 psi) before it was fed to the Haskel pump.

The output of the Corblin pump contained high pressure peaks which were smoothed out before being fed to the Haskel pumps. This was accomplished by using a 5.2-scm (184-scf) (at 12.4 MPa and 21.1°C) nitrogen cylinder as a surge tank to absorb the pressure pulses from the Corblin pump (Fig. H.1).

After the failure of the Haskel pumps, both were repaired but only one (the unenclosed unit) was used to continue the test. The other was kept in reserve on a standby basis.

Pressure Measurements at the Pump Site

Dial gages having a range of 0 to 27.6 MPa (0 to 4000 psi) and an accuracy of 1% were placed in the system (see Fig. H.1) to monitor the pressure of the nitrogen gas supply and the input pressure to the Haskel pumps. The 1% accuracy was adequate at these stages.

A Heise model CM 216-mm-diam (8 1/2-in.), 344-MPa (50,000-psi) FS Bourdon dial gage with a calibration accuracy of 0.1% was located at the pump site to monitor the line pressure to the test vessel. Since the smallest graduation on the dial equaled 0.689 MPa (100 psi), it was comparatively easy to read to ±0.21 MPa (30 psi). It is felt that the overall accuracy with which the pressure in the test vessel could be measured from the pump site by the Heise gage was well within 0.20%.

A second gage, a Viatran model 221 with a full-scale range of 206.8 MPa (30,000 psi), was connected at the same point in the system as the Heise gage (Fig. H.1). It provided an output voltage which was proportional to the pressure. The voltage from the Viatran gage was recorded on a model 5211-2 Omni Scribe* X-Y recorder which provided a continuous history of the pressure at the pump site. The measurement error produced by these two units together (the Viatran gage and the X-Y recorder) along with the expected error of the gage excitation voltage resulted in an overall pressure measurement error of 1.0% at the pump site. The lower trace of Fig. H.6 through H.9 shows a reduced copy of the records produced by the Viatran gage.

When the pumps were operating, the pressure pulsations produced by the pumps as well as the static pressure drop in the line between the pump site and the test vessel would often produce a pressure reading of 6.89 MPa (1000 psi) higher than the actual pressure in the test vessel. The data for these traces were obtained at times when the pumps were stopped and after sufficient time had elapsed for the gas pressure in the test vessel to equalize with that in the feed line at the pump site. The pressure stabilization time was of the order of 30 sec.

---

*Manufactured by the Houston Instrument Co.

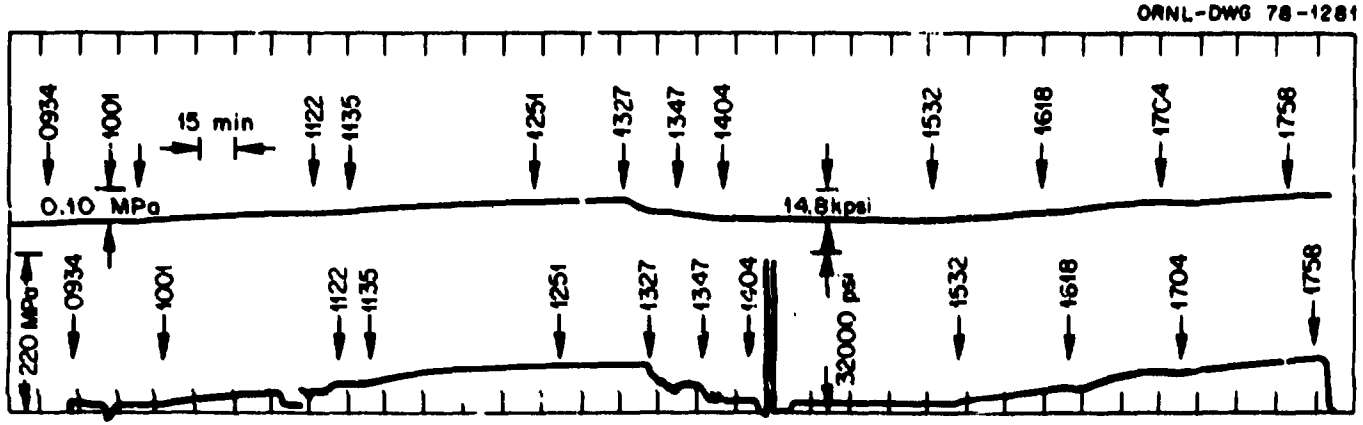

Fig. H.6. Pressure-time history at pump station, June 15, 1976.

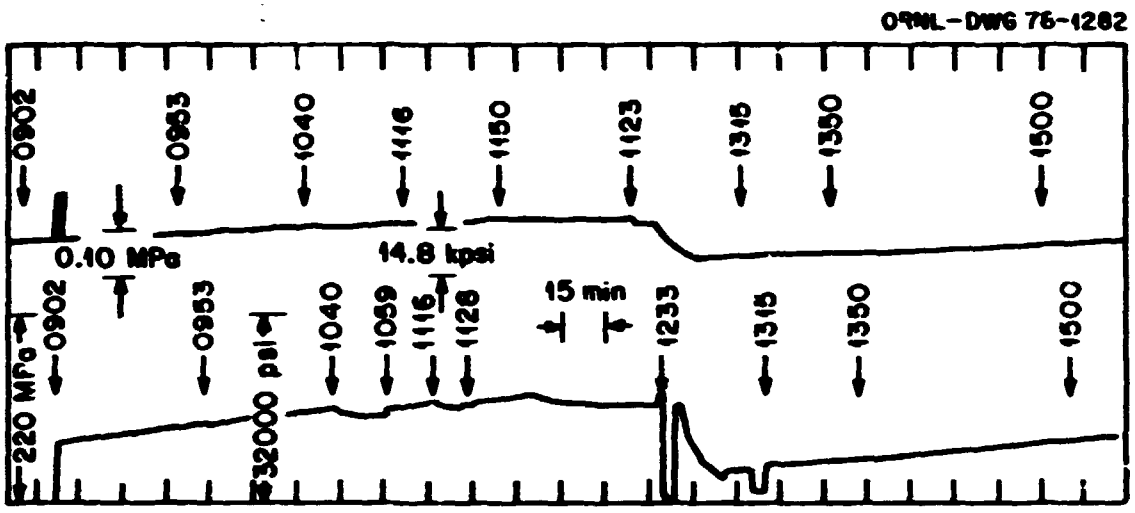

Fig. H.7. Pressure-time history at pump station, June 16, 1976.

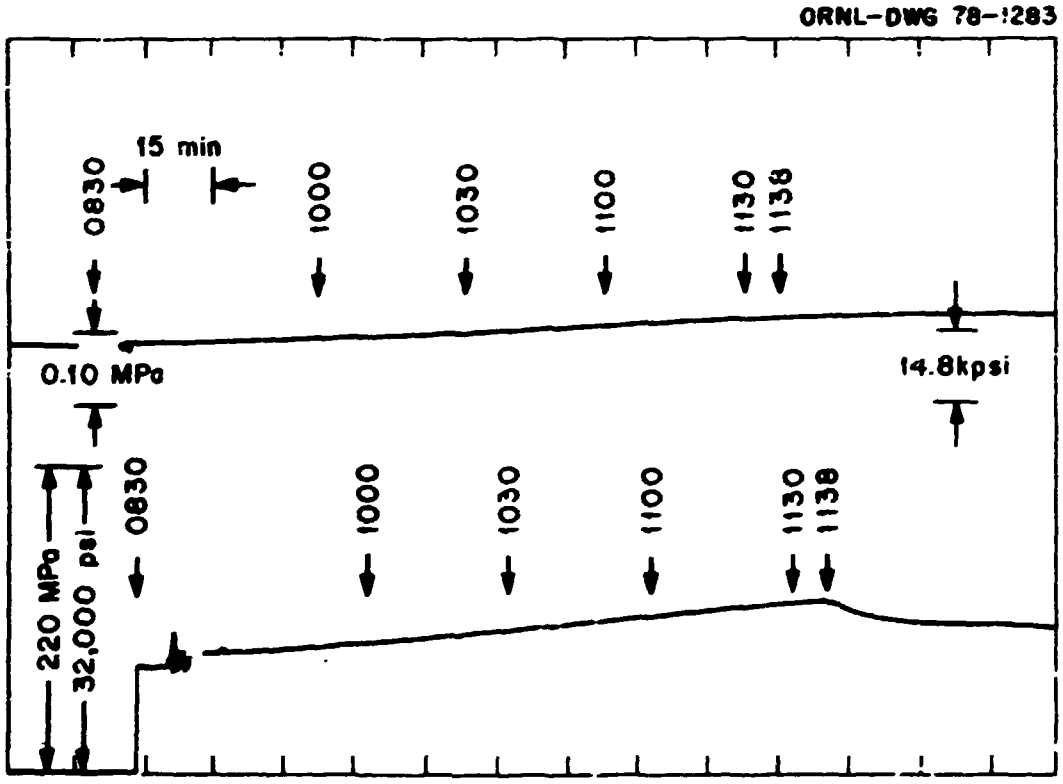

Fig. H.8. Pressure-time history at pump station, June 17, 1976.

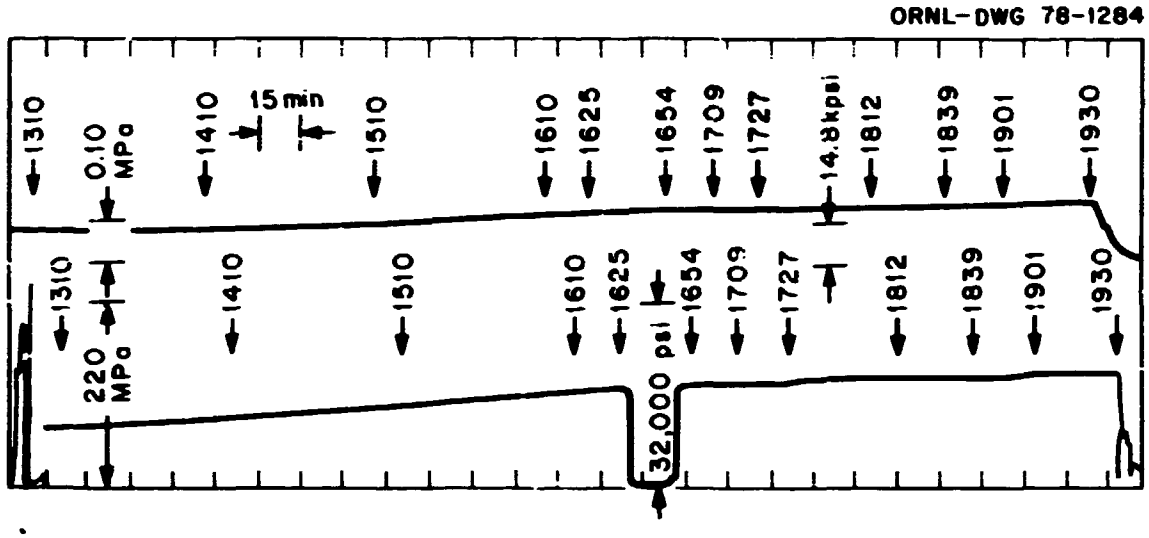

Fig. H.9. Pressure-time history at pump station, June 18, 1976.

Pressure Measurements at the Test Vessel

A 0- to 206.8-MPa (0- to 30,000-psi) type DHF pressure transducer* was placed in the line about 0.5 m from the test vessel (see Fig. H.1) and connected to a second channel of the Omni Scribe recorder. Unlike the Viatran gage located at the pump site, this gage responded only to the pressure in the test vessel and was independent of any pressure drops produced in the line between the pump site and the pressure vessel.

The transducer error (0.25% of full scale) plus an estimated measurement error of the excitation voltage (0.1%), that of the X-Y recorder (0.2%), and a reading error of perhaps 0.2% all combine to produce an overall error not exceeding 0.4%.

The traces showing the pressure-time histories produced by the DHF gage for each of the four days of pressure cycling are given in the upper trace of Figs. H.6 through H.9. Note that the timings between the upper and lower traces do not coincide; the writing pens on the X-Y recorder are mechanically off-set.

---

*Manufactured by BLH Electronics, Waltham, Mass. Identified as PE 30 on ORNL drawings.

A second gage to sense the test vessel pressure was mounted in parallel with the DHF pressure transducer (Fig. H.1). However, the output of this gage, a bulk modulus gage, was not monitored by the White Oak Laboratory. This gage was manufactured by Harwood Engineering Co., Walpole, Mass., and is identified as PE 133 on ORNL drawings.

Reference

1. *Handbook of Diaphragm Compressors and Pumps*, American Instrument Company, Inc., Silver Springs, Md.

Appendix I

FRACTOGRAPHIC EXAMINATION OF INTERMEDIATE TEST VESSEL V-7A

A fractographic examination employing both light microscopy and scanning electron microscopy (SEM) of the fracture surface from intermediate test vessel V-7A was made by D. A. Canonico and R. S. Crouse. Figure I.1 is an approximately half-size photograph of the fracture from V-7A. The goal of the fractographic examination was to determine the mode of fracture that occurred during testing. Of particular interest were the region in the main section of the vessel wall beneath the electron-beam (EB) crack starter (areas 1 and 5 in Fig. I.1) and the ligament region beneath the deepest part of the flaw, where rupture resulted in the termination of the test. The latter region is typified by areas 2, 3, and 4 in the figure.

The fractured zone was removed from the vessel, chilled, and separated. The bright portions of areas 1 and 5 are the areas that were fractured at low temperature in order to separate the two surfaces. Figure I.2 contains SEM photomicrographs of the bright fracture areas. The fractures in this area, as expected, are cleavage. Figure I.2 provides an example of a frangible fracture.

The region that leaked in V-7A, between areas 2 and 4 in Fig. I.1, was examined to determine the mode of cracking and to estimate the length of the ruptured surface. Previous estimates of the length of the crack were based on visual examination of the inside surface of the vessel before the fractured zone was chilled and separated. In the earlier examination, the inside surface rupture could not be seen until the zone was cut from the vessel. The relief of restraint during removal allowed the rupture to open and possibly allowed additional tearing. The fractographic examination of the ligament region between areas 2 and 4 shows a length of about 73 mm (2.9 in.) of plastically deformed fracture surface bounded at each end by a thin, pointed fracture area along the inside surface of the vessel. These thin areas have an appearance similar to that of the cleavage in areas 1 and 5, formed when the specimen was separated for examination. During the test the ligament must have ruptured to the inside surface over

a distance of at least 73 mm and, from fractographic evidence, no more than this amount.

An SEM examination of the region that breached the inner wall was made. Figure I.3 shows that the fracture surface near the inside is essentially featureless. The surfaces that evolved as a consequence of the crack extension during testing subsequently came into intimate contact when the pressure was relieved and were then plastically deformed. The flat facets in Fig. I.3 are the result of this deformation. There is evidence that the fracture surface has a dimple morphology, but this could not be uncontestably confirmed. However, this conclusion can be inferred from the morphology of the fracture surfaces at areas 1 and 5 in Fig. I.1, both of which exhibited a dimple fracture mode below the EB weld crack. Figure I.4 contains SEM photomicrographs of the areas below the EB weld that fractured during the V-7A test. The surfaces exhibit a dimple mode of fracture, indicative of ductile tearing.

In summary, the crack in V-7A extended by ductile tearing until the inner wall was breached by the propagating crack front. The final crack extension that breached the inner wall was about 73 mm long. When the pressure was released, the fracture surfaces came into contact and were plastically deformed, resulting in the flat facets in the fracture surfaces evident in Figs. I.3 and I.4.

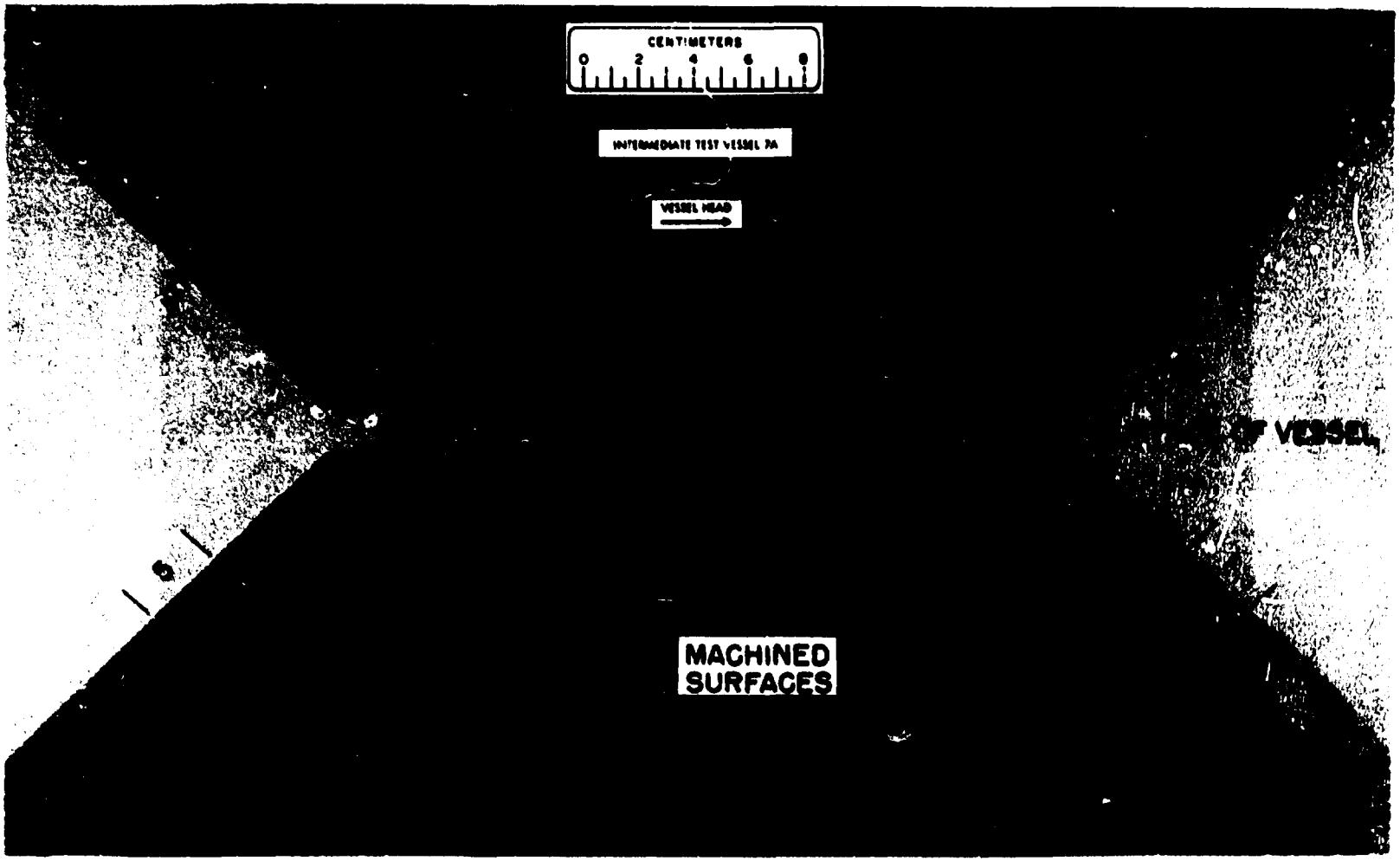

Fig. I.1. Photograph of the fractured surfaces from intermediate test vessel V-7A. The regions of the fracture that were examined by scanning electron microscopy are areas 1 to 5.

PHOTO 2807-77

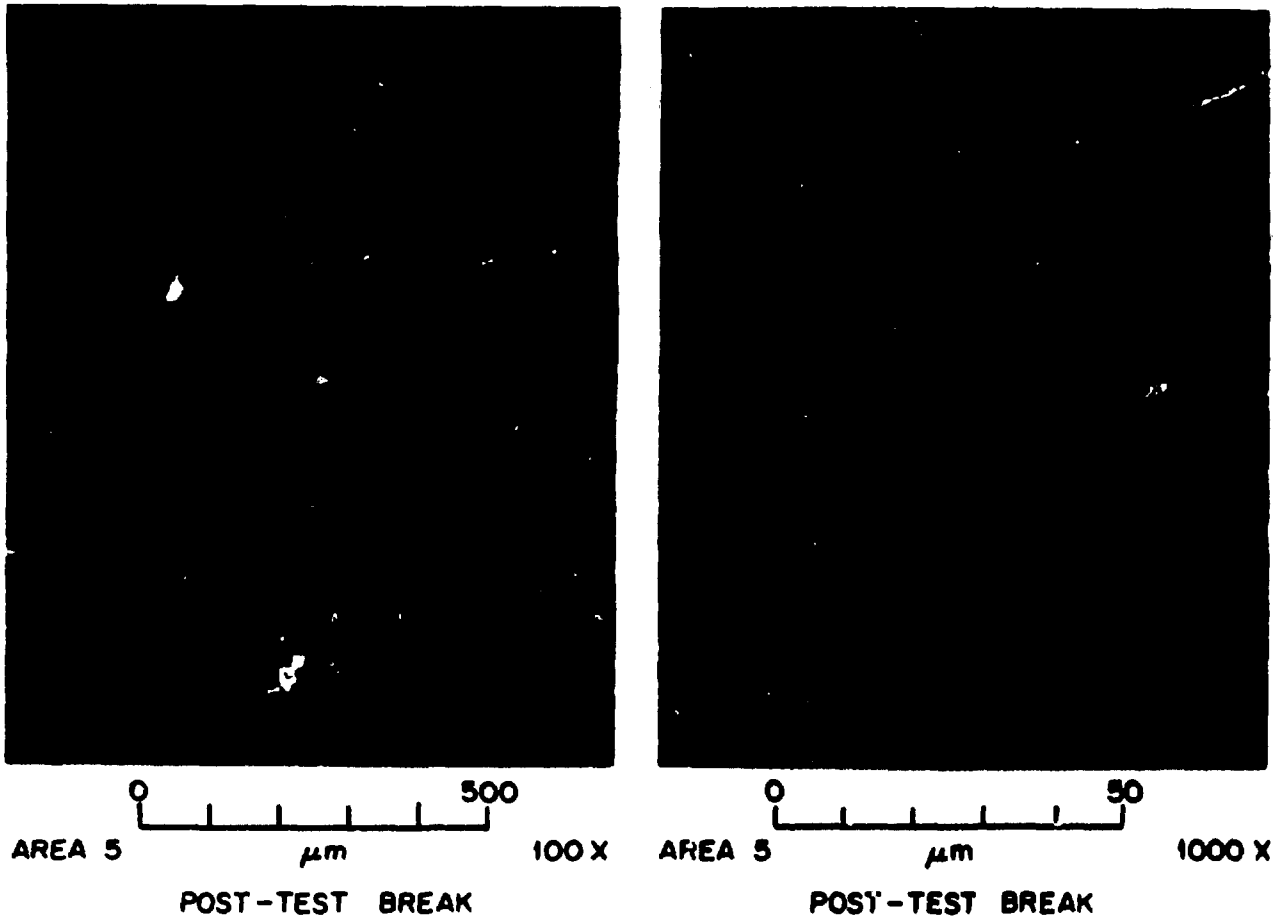

Fig. I.2. SEM photomicrographs of the area of the V-7A fracture surface that was separated after the test at extremely low temperatures. The fracture occurred at low temperature by the cleavage mode. These photomicrographs are representative of the SEM appearance of brittle fracture in this A533, grade B, class 1 material. Original reduced 26%.

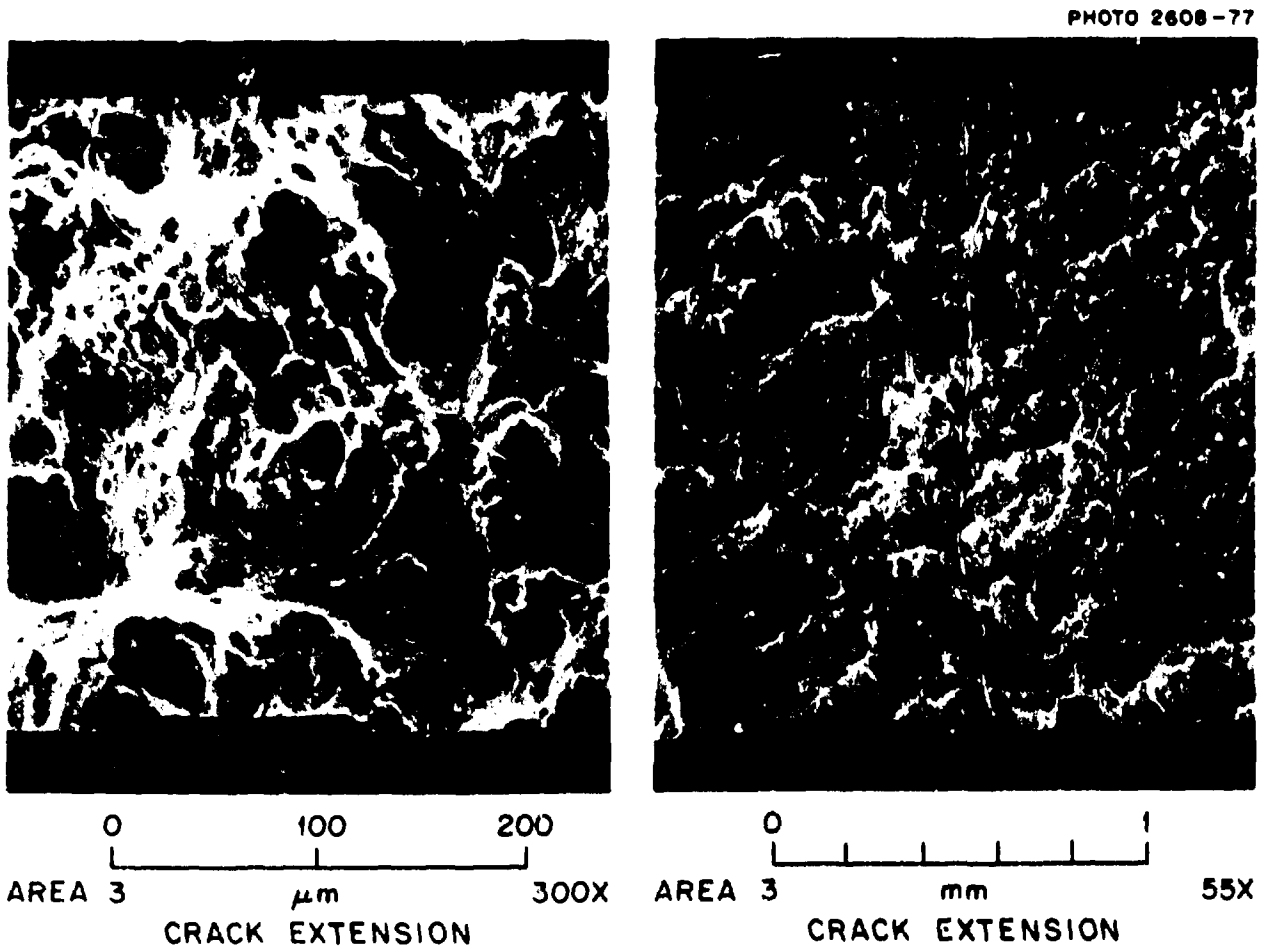

Fig. I.3. SEM photomicrographs of the region of the crack in V-7A that breached the inner wall (area 3 in Fig. I.1). The fracture surface was flat facets, indicative of an area that was plastically deformed. This deformation undoubtedly occurred when the internal pressure was released and the two surfaces were brought into intimate contact. Original reduced 27%.

PHOTO 2609-77

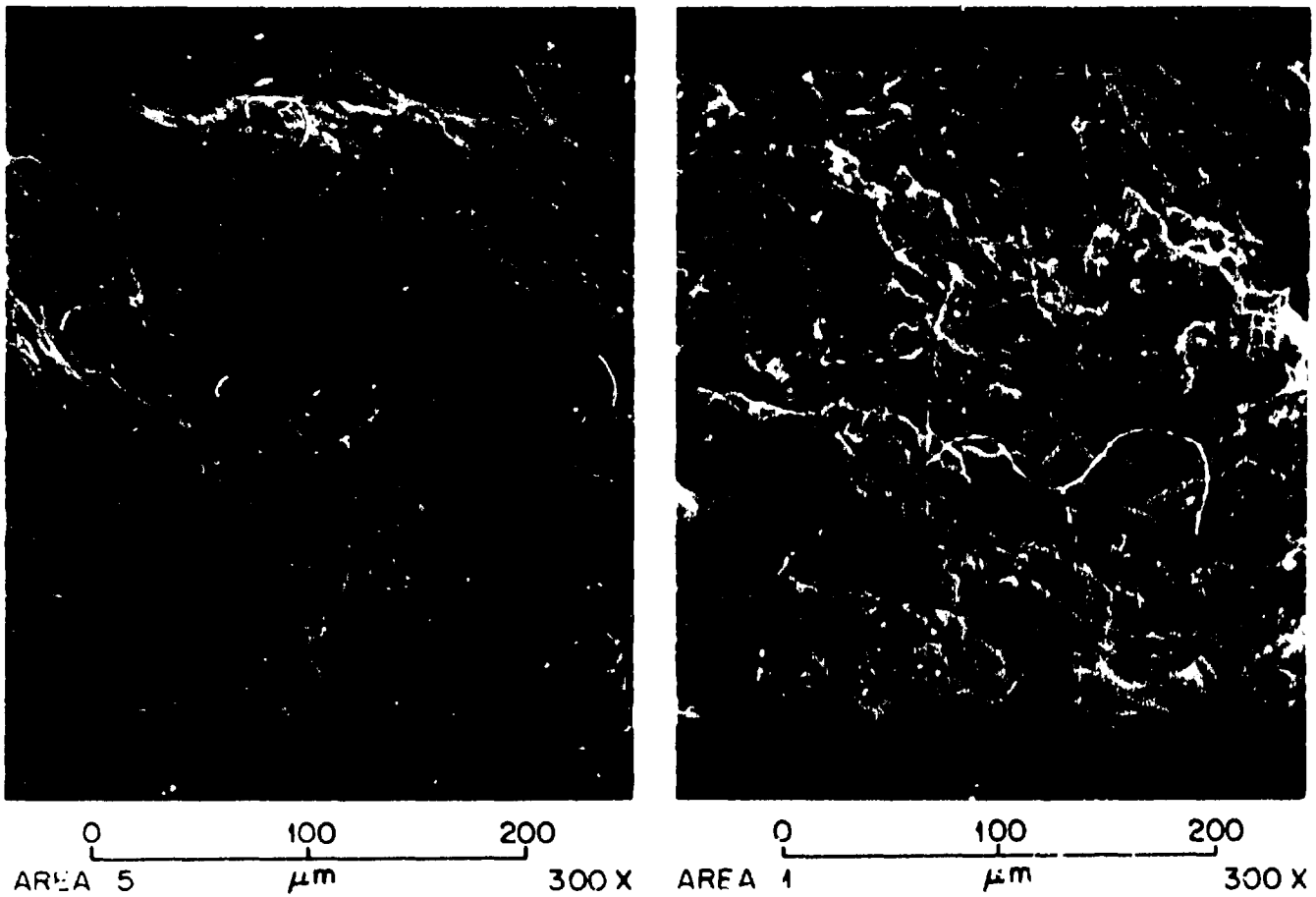

Fig. I.4. SEM photomicrographs representative of the regions within the wall of the V-7A vessel where the cracks extended and arrested (areas 1 and 5 in Fig. I.1). The dimpled appearance of the fracture surface is indicative of ductile tearing. The flat facets are undoubtedly due to the plastic deformation that occurred when the pressure was released and the fracture surfaces were brought into intimate contact. Original reduced 21.5%.